



**HAL**  
open science

# Structural and functional study of the respiratory syncytial virus nucleocapsid

Lorène Gonnin

► **To cite this version:**

Lorène Gonnin. Structural and functional study of the respiratory syncytial virus nucleocapsid. Structural Biology [q-bio.BM]. Université Paris-Saclay, 2023. English. NNT : 2023UPASL047 . tel-04138758

**HAL Id: tel-04138758**

**<https://theses.hal.science/tel-04138758v1>**

Submitted on 23 Jun 2023

**HAL** is a multi-disciplinary open access archive for the deposit and dissemination of scientific research documents, whether they are published or not. The documents may come from teaching and research institutions in France or abroad, or from public or private research centers.

L'archive ouverte pluridisciplinaire **HAL**, est destinée au dépôt et à la diffusion de documents scientifiques de niveau recherche, publiés ou non, émanant des établissements d'enseignement et de recherche français ou étrangers, des laboratoires publics ou privés.

# Structural and functional study of the respiratory syncytial virus nucleocapsid

*Étude structurale et fonctionnelle de la nucléocapside du virus  
respiratoire syncytial*

## Thèse de doctorat de l'université Paris-Saclay

École doctorale n°577, structure et dynamique des systèmes vivants (SDSV)  
Spécialité de doctorat : Biologie moléculaire et cellulaire  
Graduate School : Life Sciences and Health  
Référent : Université de Versailles-Saint-Quentin-en-Yvelines

Thèse préparée dans les unités de recherche **VIM (Université Paris-Saclay, UVSQ, INRAE)** et **IBS (CEA, CNRS, UGA)**  
sous la direction de **Jean-François ÉLÉOUËT**, directeur de recherche,  
la co-direction de **Irina GUTSCHE**, directrice de recherche,  
le co-encadrement de **Marie GALLOUX**, directrice de recherche  
et le co-encadrement de **Ambroise DESFOSES**, chargé de recherche

Thèse soutenue à Jouy-en-Josas, le 1<sup>er</sup> juin 2023, par

**Lorène GONNIN**

## Composition du Jury

Membres du jury avec voix délibérative

### **Marie-Anne RAMEIX-WELTI**

Professeure des universités, praticienne hospitalière,  
Université Paris-Saclay et Institut Pasteur

Présidente

### **Petr CHLANDA**

Directeur de recherche, BioQuant, Université  
d'Heidelberg

Rapporteur & Examineur

### **Célia PLISSON-CHASTANG**

Directrice de recherche, Centre de Biologie  
Intégrative de Toulouse

Rapporteur & Examinatrice

### **Louis-Marie BLOYET**

Chargé de recherche, Centre International de  
Recherche en Infectiologie, Lyon

Examineur



**Titre :** Étude structurale et fonctionnelle de la nucléocapside du virus respiratoire syncytial

**Mots clés :** virus respiratoire syncytial, nucléocapside, encapsidation, cryo-microscopie électronique

**Résumé :** Le virus respiratoire syncytial (VRS) est la première cause de bronchiolites et de pneumonies chez les jeunes enfants. Il est également responsable d'infections respiratoires sévères chez les personnes âgées ou immunodéprimées. Il n'existe pas de vaccin ni de traitement spécifique contre le VRS. Le VRS est un virus enveloppé dont le génome est un ARN simple-brin de polarité négative contenant 10 gènes codant pour 11 protéines virales. Le génome viral est constamment encapsidé par de multiples copies de la nucléoprotéine virale N, constituant un complexe N-ARN en forme d'hélice, appelé nucléocapside. Au cours du cycle viral, la nucléocapside est utilisée comme matrice par la polymérase virale L pour (i) transcrire les ARN messagers viraux, et (ii) répliquer génomes et antigénomes. Les activités de la polymérase L dépendent de ses cofacteurs viraux, la phosphoprotéine P et la protéine M2-1, anti-terminateur de la transcription. La protéine P peut être vu comme le chef d'orchestre de la multiplication du virus, capable d'interagir avec la polymérase L, la nucléocapside, la protéine M2-1, mais également avec la protéine N néosynthétisée, permettant ainsi son maintien sous forme monomérique et non liée à l'ARN, nommée N<sup>0</sup>.

Les étapes de transcription et de répllication se déroulent au sein d'usines virales, dans le cytoplasme de la cellule infectée. Les usines virales sont des organelles dépourvues de membranes, formées par séparation de phase liquide, dont la morphogénèse dépend de l'expression des protéines N et P. Les protéines N et P et leurs interactions jouent par conséquent un rôle central non seulement pour le fonctionnement de la polymérase mais également dans la formation des usines virales. Toutefois, les mécanismes régulant la spécificité d'encapsidation des ARN génomique et antigénomique viraux, dépendant de la transition N<sup>0</sup>-P vers N-ARN, restent mal caractérisés. De plus, les informations structurales de haute résolution sont limitées à la structure cristallographique d'anneaux N-ARN du VRS.

Dans ce contexte, mes travaux de thèse visaient à obtenir des données fonctionnelles et structurales sur la nucléocapside du VRS, suivant deux axes principaux : (i) l'étude du rôle de l'ARN dans l'encapsidation par la protéine N et (ii) la détermination de la structure de la nucléocapside du VRS par cryo-microscopie électronique.

Partant de la capacité à purifier une protéine N recombinante exprimée chez *E. coli* sous forme monomérique et non liée à l'ARN, j'ai dans un premier temps étudié la capacité de cette protéine à encapsider différents ARN synthétiques *in vitro*. Les données obtenues ont permis de montrer que l'encapsidation peut se déclencher en présence d'ARNs de 7 nucléotides, mais que 11 nucléotides sont nécessaires pour former des complexes N-ARN stables *in vitro*. Cependant, la nature de l'extrémité 5' des ARNs ne permet pas d'expliquer la spécificité d'encapsidation. Enfin, ces travaux ont permis de montrer que l'encapsidation de l'ARN par la protéine N est indispensable pour la reconstitution de pseudo-usines virales *in vitro*.

En parallèle, la purification de nucléocapsides exprimées en cellules d'insectes nous a permis de déterminer la structure par cryo-microscopie électronique de plusieurs assemblages N-ARN (nucléocapside hélicoïdale, nucléocapside hélicoïdale à deux têtes, nucléocapside hélicoïdale coiffée d'un anneau, et double-anneaux N-ARN). Plus spécifiquement, nos données ont permis de révéler que la nucléocapside du VRS présente une symétrie non-canonique, avec un assemblage en unité asymétrique composée de 16 protomères de N. Cet assemblage particulier conduit à une variation dans l'accessibilité de l'ARN le long de l'hélice. Enfin, nous avons montré que cette symétrie non-canonique dépendait du bras C-terminal de la protéine N, puisque son raccourcissement entraîne la formation d'une nucléocapside hélicoïdale de symétrie canonique.

**Title:** Structural and functional study of the respiratory syncytial virus nucleocapsid

**Keywords:** respiratory syncytial virus, nucleocapsid, encapsidation, cryo-electron microscopy

**Abstract:** Respiratory syncytial virus (RSV) is the leading cause of bronchiolitis and pneumonia in young children. It is also responsible for severe respiratory infections in elderly or immunocompromised people. There is no vaccine or specific treatment for RSV.

RSV is an enveloped virus with a single-stranded negative-sense RNA genome containing 10 genes coding for 11 proteins. The viral genome is constantly encapsidated by multiple copies of the viral nucleoprotein N, constituting a helical N-RNA complex, called the nucleocapsid. During the viral cycle, the nucleocapsid is used as a template by the viral polymerase L to (i) transcribe viral messenger RNAs, and (ii) replicate genomes and antigenomes. The activities of the polymerase L require interaction with its main cofactor, the phosphoprotein P, as well as the transcription anti-terminator protein M2-1. P can be seen as the hub of the virus multiplication, able to interact with the polymerase L, the nucleocapsid, M2-1, but also with the neosynthesised N, allowing its maintenance in a monomeric and RNA-free form, called N<sup>0</sup>.

Viral transcription and replication steps take place in viral factories, in the cytoplasm of the infected cells. Viral factories are membrane-less organelles formed by liquid-liquid phase separation, whose morphogenesis depends on the expression of N and P. N, P, and their interactions, therefore, play a central role not only in the function of the polymerase L but also in the formation of viral factories. However, the mechanisms regulating the specificity of viral genomic and antigenomic RNA encapsidation, dependent on the N<sup>0</sup>-P to N-RNA transition, remain poorly characterised. Furthermore, high-resolution structural information is limited to the crystallographic structure of RSV N-RNA rings.

In this context, my thesis work aimed at obtaining functional and structural data on the RSV nucleocapsid, following two main axes: (i) the study of the role of RNA in the encapsidation by N and (ii) the determination of the structure of the RSV nucleocapsid by cryo-electron microscopy.

Starting from the ability to purify a recombinant monomeric and RNA-free N<sup>0</sup> expressed in *E. coli*, I first studied the propensity of this protein to encapsidate different synthetic RNAs *in vitro*. The data obtained showed that encapsidation can be triggered in the presence of a 7 nucleotides-long RNA, but that 11 nucleotides are required to form stable N-RNA complexes *in vitro*. Secondly, the nature of the 5' end of the RNAs does not explain the specificity of encapsidation. Finally, we have shown that RNA encapsidation by the N protein is essential for the reconstitution of pseudo-viral factories *in vitro*.

In parallel, the purification of nucleocapsids expressed in insect cells allowed us to determine the cryo-electron microscopy structures of several N-RNA assemblies (helical nucleocapsid, double-headed helical nucleocapsid, ring-capped helical nucleocapsid, and N-RNA double ring). Specifically, our data revealed that the RSV nucleocapsid exhibits a non-canonical symmetry, with an asymmetric unit composed of 16 N protomers. This particular assembly leads to a variation in the RNA accessibility along the helix. Finally, we have shown that this non-canonical symmetry depends on the C-terminal arm of the N protein since its truncation leads to the formation of a helical nucleocapsid of canonical symmetry.



## Remerciements

Après 3 ans et demi de thèse au sein de deux équipes, entre Jouy-en-Josas, Grenoble et un petit peu Umeå, il est temps pour moi de remercier les personnes avec qui j'ai travaillé et avec lesquelles j'ai passé ces incroyables années. Une thèse scientifique ça ne se fait pas tout seul et j'ai eu la chance de rencontrer beaucoup de personnes fabuleuses qui m'ont accompagnée tout au long de mon parcours. Alors c'est parti !

Tout d'abord je voudrais remercier Marie, mon encadrante de l'équipe BMP, depuis mon stage de M2 j'ai énormément appris à tes côtés. Ceux qui travaillent avec toi savent à quel point j'ai eu de la chance de t'avoir eue à mes côtés, merci pour ta patience, ton énergie, ton enthousiasme et de m'avoir portée jusqu'ici. Ensuite je remercie Jean-François, mon co-directeur de thèse, merci de m'avoir accompagnée pendant plus de 3 ans sur ce sujet de thèse passionnant. Je retiens ta curiosité insatiable, ta disponibilité et tes conseils toujours très avisés. Je remercie tous les membres passés et présents de l'équipe BMP qui s'agrandit à vue d'œil : Charles-Adrien, Charlotte, Christophe, Didier, Fortune, Julien, Laura, Lucas et Maxime. Merci à Monika pour les discussions toujours intéressantes. Merci à Jenna, reine de la biologie moléculaire, qui a été là depuis le début.

Un grand merci à toutes les personnes de l'unité VIM, cette unité de virologie et d'immunologie avec qui les échanges sont toujours riches. Une pensée pour les copains doctorants et doctorantes de l'unité : Adrien, Basile, Carla, Célia, Claire, Clara, Elise, Lena, Lise, Mantasha, Joelton et Soraya, courage vous êtes sur la bonne voie ! Merci à toi Mélissa, partenaire de rigolades sans failles et une mention spéciale à Vincent qui prend la relève. Je n'oublie pas les anciens thésards : Jessica, Joëlle et Raphaël. Merci à toi Hortense pour ces supers bons moments passés ensemble.

Maintenant je souhaite remercier ma deuxième équipe d'adoption : le groupe MICA. J'ai passé plusieurs mois à vos côtés et c'était très intense et joyeux. Merci à ma co-directrice de thèse Irina, d'avoir accepté une doctorante virologue qui n'y connaissait vraiment pas grand-chose en microscopie électronique ; et de m'avoir accompagnée tout au long de cette

thèse, notamment de m'avoir donné l'opportunité de me frotter à la cryo-tomographie pendant quelques mois à Umeå, c'était une super expérience, qui n'est pas finie ! Bien sûr je souhaite remercier Ambroise qui m'a encadrée sur la reconstruction des hélices, tu as été d'une grande patience avec moi et toujours d'une grande aide. Merci à tous les membres du groupe MICA et associés avec qui j'ai passé de supers moments à l'IBS : Karine, Lindsay, Lorenzo, Madalen, Maria, Moritz, Yoan, Benoit, Hélène, Leandro et Quentin.

Je souhaiterais remercier Linda qui dirige la plateforme de microscopie d'Umeå, qui m'a accueillie pendant quelques mois au côté d'Irina. Merci à tous les membres de son équipe : Hugh, Niklas, Suresh et Mehmethan. Un immense merci à Selma et Lars qui ont été d'une aide incroyable. Merci à toi Lorenzo, partenaire de cette aventure suédoise, avec qui j'ai passé de supers moments.

Je remercie les membres de mon jury qui ont accepté d'évaluer mon travail : Petr Chlanda, Célia Plisson-Chastang, Louis-Marie Bloyet et Marie-Anne Rameix-Welti.

Je souhaiterais remercier les membres de mon comité de thèse : Christina Sizun, Jean Millet et Ludovic Sauguet pour leurs conseils scientifiques toujours précis et leur bienveillance.

Un grand merci à mes parents et à ma sœur qui ont toujours été là pour moi dans les moments difficiles mais aussi dans les moments heureux.

J'ai aussi une pensée pour Natan et Prunille avec lesquels j'ai partagé les deux premières années de ma thèse et un confinement.

J'aimerais remercier mes amis qui ont été à mes côtés au cours de ces années et avec qui j'ai pu partir en vacances, en weekends, aller à l'escalade, courir, débattre et passer de supers soirées ! Une mention très spéciale pour les PPP, mes amies depuis presque 10 ans déjà : Armelle, Camille, Célia, Ella, Jeanne, Manon et Margot. Avec une pensée particulière pour Jeanne avec qui je partage mes joies et mésaventures de doctorante. Enfin je remercie Julia avec qui je partage une amitié indéfectible.

# Table of contents

<b>Part I: Introduction</b>	<b>3</b>
<b>Chapter I: Generalities on the respiratory syncytial virus</b>	<b>3</b>
1. History and classification	3
2. Epidemiology, RSV-associated diseases, and therapeutics	5
2.1. RSV circulation in humans	5
2.2. RSV infection and associated disease	8
2.3. Therapeutic development against RSV	10
3. Viral particle organisation	12
4. Respiratory Syncytial Virus life cycle	15
4.1. Viral entry: attachment and membrane fusion	17
4.2. Transcription and replication	20
4.3. Assembly and budding of the virion	23
4.4. Immune response control during the viral cycle	25
<b>Chapter II: RSV polymerase machinery</b>	<b>27</b>
1. RSV polymerase protein and its viral cofactors: the phosphoprotein and the M2-1 protein	27
1.1. Structure of the L protein	27
1.2. Function and characteristics of the P protein	30
1.3. Structure and role of the M2-1 protein	34
2. Inclusions bodies	36
3. Nucleoprotein and nucleocapsid	38
3.1. N-RNA oligomers	40
3.2. Monomeric N protein	45
3.3. Transition from the N <sup>0</sup> -P to the N-RNA form	51
<b>Chapter III: Cryo-EM at a glance</b>	<b>53</b>
1. Negative stain EM and sample preparation for cryo-EM	55
2. From the electron to the image	56
3. Image processing principles for single-particle analysis	59
4. Reconstruction of helical objects	63
5. Cryo-electron tomography	65
<b>Thesis goals</b>	<b>67</b>
<b>Part II: Results</b>	<b>69</b>
<b>Chapter I: Study of the specificity of RNA encapsidation by the nucleoprotein</b>	<b>69</b>
1. Introduction	69
2. Article 1: Importance of RNA length for <i>in vitro</i> encapsidation by the nucleoprotein of human respiratory syncytial virus	72
3. Discussion	87
<b>Chapter II: Structural analysis of the RSV nucleocapsid by cryo-EM</b>	<b>93</b>
1. Introduction	93
2. Article 2: Structural landscape of the respiratory syncytial virus nucleocapsids	97
3. Initial study of RSV nucleocapsid assembly in infected cells by cryo-electron tomography	131
<b>Part III: Conclusion and perspectives</b>	<b>135</b>
<b>References</b>	<b>141</b>

<b>Résumé en français de la thèse intitulée : « Étude structurale et fonctionnelle de la nucléocapside du virus respiratoire syncytial »</b>	<b>175</b>
1. Introduction	175
1.1. Généralités sur le virus respiratoire syncytial	175
1.2. Organisation de la particule virale et cycle viral du VRS	176
1.3. La nucléoprotéine et la nucléocapside au cœur cycle viral du VRS	179
2. Les objectifs de la thèse	181
3. Résultats	182
3.1. Étude de la spécificité d'encapsulation des ARNs par la nucléoprotéine du VRS	182
3.2. Analyse structurale de la nucléocapside du VRS par cryo-ME	185
4. Conclusion	188
<b>Review: Interactions between the Nucleoprotein and the Phosphoprotein of Pneumoviruses: Structural Insight for Rational Design of Antivirals</b>	<b>189</b>
<b>Article: Depletion of TAX1BP1 Amplifies Innate Immune Responses during Respiratory Syncytial Virus Infection</b>	<b>209</b>

## Part I: Introduction

The first chapter of the introduction aims to present the epidemiological context of the respiratory syncytial virus and an overview of its viral cycle. The second chapter presents in more detail the viral proteins that are essential for viral RNA synthesis, ending with the nucleoprotein and the nucleocapsid that constitute the core of my thesis topic. Finally, the third chapter aims to give an overview of cryo-electron microscopy.

### Chapter I: Generalities on the respiratory syncytial virus

#### **1. History and classification**

In 1956, a virus was isolated from nasal secretions of sick young chimpanzees and called Chimpanzee Coryza Agent (CCA) (Morris et al., 1956). A year later, the respiratory syncytial virus (RSV), so called because of its ability to form syncytia areas in human tissue cultures (Chanock et al., 1957), was isolated from young infants with severe lower respiratory illness and was described as undistinguishable from CCA virus. In the following years, the first evidence of an association between acute respiratory illness in infants and RSV infection was provided (Beem et al., 1960).

RSV belongs to the *Mononegavirales* order which is composed of enveloped viruses with a non-segmented, linear, single-strand, negative-sense RNA genome. Originally this order was divided into three families: *Filoviridae*, *Paramyxoviridae*, and *Rhabdoviridae*. The order now contains eight families including the *Pneumoviridae* family to which RSV belongs. Before 2016, pneumoviruses were classified in the *Paramyxoviridae* family, and the *Pneumovirinae* subfamily. Since pneumoviruses are as distant from paramyxoviruses as they are from filoviruses, the sub-family was elevated to family status (Afonso et al., 2016). The *Mononegavirales* order comprises many pathogens that are a significant threat to human and



animal health, for instance, Ebola and Marburg viruses (*Filoviridae*), measles, Nipah, Sendai, and mumps viruses (*Paramyxoviridae*), or rabies virus (*Rhabdoviridae*) (Figure 1).

The *Pneumoviridae* family is subdivided into two genera: *Metapneumovirus* and *Orthopneumovirus*. The *Metapneumovirus* genus includes the avian and human metapneumoviruses (AMPV and HMPV, respectively). The *Orthopneumovirus* genus comprises the three subgroups of human RSV (A2, B1, and S2), the bovine respiratory syncytial virus (BRSV) responsible for pneumonia in calves which causes significant economic losses on farms (Valarcher and Taylor, 2007) and the murine pneumonia virus (MPV). Although not included in the taxonomic classification of the ICTV (International Committee on Taxonomy of Viruses), ovine respiratory syncytial virus (ORSV), close to the BRSV was identified in sheep with respiratory tract disease (Mallipeddi and Samal, 1993). Swine and canine orthopneumoviruses (SOV and CPV respectively), sharing 90% nucleotide identity with MPV, were detected in pigs (Hause et al., 2016; Richard et al., 2018) and dogs (Song et al., 2021).

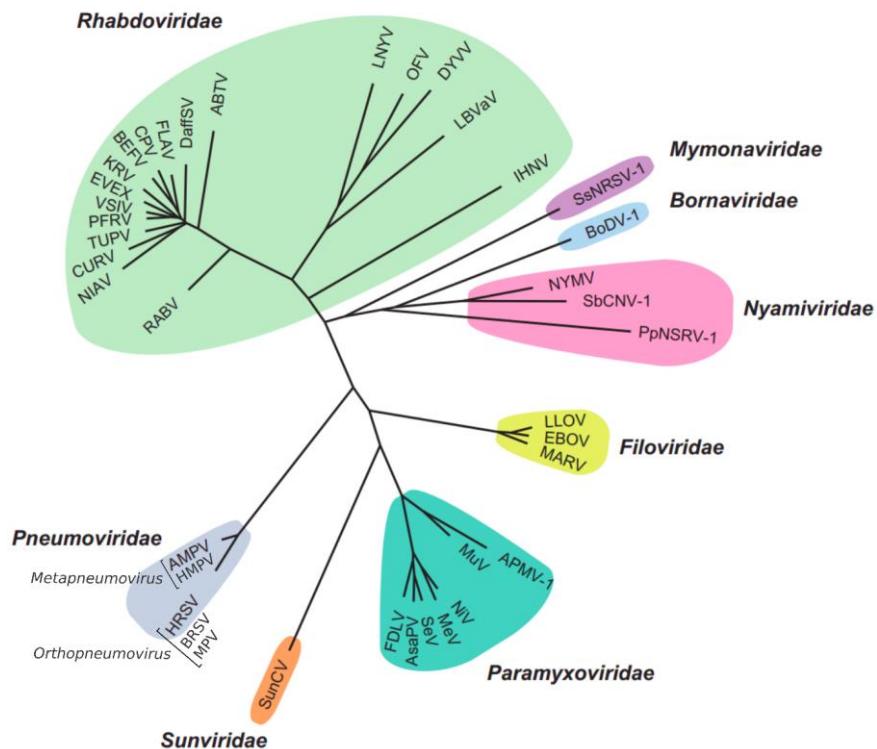


**Figure 1.** Phylogenetic tree of the *Mononegavirales* order. The tree was based on the alignment of amino acid sequences of the RNA polymerases. Figure adapted from Ortega et al., 2019.

## **2. Epidemiology, RSV-associated diseases, and therapeutics**

### *2.1. RSV circulation in humans*

RSV is the leading cause of bronchiolitis and pneumonia in infants (PERCH study group, 2019). Almost all children will be infected with RSV by the age of 2 (Glezen, 1986). In older children and adults, reinfections with RSV are very common throughout life and usually cause only mild symptoms. However, in the elderly and immunocompromised, RSV can cause severe respiratory infections that can lead to death (Shi et al., 2020). The estimated RSV disease burden is similar to seasonal influenza A in the elderly and high-risk adults (adults with lung or heart conditions) (Falsey et al., 2021). Noteworthy, HMPV also causes acute lower respiratory diseases, but mainly in children aged 2-5 years (Falsey et al., 2003).

In 2019, the estimated number of acute RSV-associated acute lower respiratory infections in children under 5 years of age was 33 million, with approximately 10 % of these leading to hospitalisations and about 100,000 deaths of children under 5 years of age. The vast majority of these deaths occur in low-income countries (Li et al., 2022) (Figure 2). In high-income countries, the mortality rate of RSV is low. However, because of hospitalisations of the most severe cases, the burden of RSV on the emergency departments remains high. For example, in the United States (US) between 2000 and 2004 and during the RSV circulation season (November to April), RSV was associated with 20 % of hospitalisations of children for acute respiratory illness (Hall et al., 2009).

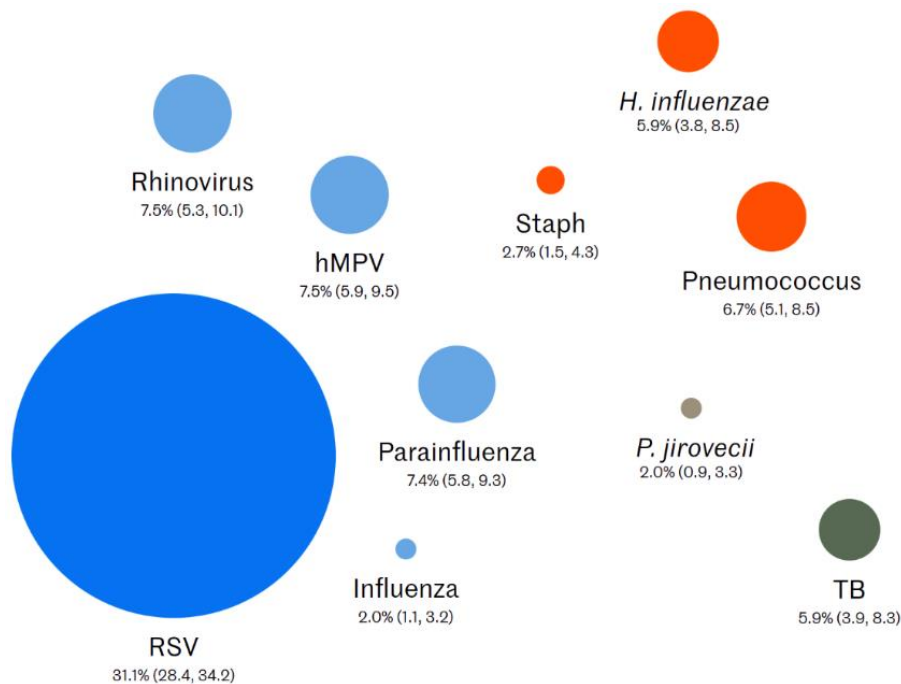


**Figure 2.** Top causes of severe Pneumonia in children, in order of importance: RSV, rhinovirus, HMPV, parainfluenza viruses, pneumococcus, *Haemophilus influenzae*, tuberculosis, *Staphylococcus aureus*, influenza viruses, and *Pneumocystis jirovecii*. Percentages are average for all ages of hospitalised children with pneumonia from 7 different countries (the Gambia, Mali, Kenya, Zambia, South Africa, Bangladesh, and Thailand). Figure adapted from the <http://perchresults.org/>, PERCH, 2019.

The occurrence of RSV epidemics depends on latitude. In temperate climates, seasonal epidemics occur during winter periods when the absolute humidity is the lowest, associated with low temperatures (Midgley et al., 2017). However, in tropical climates, RSV outbreaks are less steady and may occur all year round; and may be associated with the rainy seasons (Paynter, 2015).

Of note, the COVID-19 pandemic and associated policies to limit the transmission of the SARS-CoV-2 (severe acute respiratory syndrome coronavirus 2), such as social distancing, lockdowns, school and day-care centre closures, travel limitations and the wearing of masks have also limited the spreading of other respiratory viruses, such as parainfluenza viruses, influenza A, human rhino- and entero-viruses, RSV and HMPV (Nawrocki et al., 2021). As a consequence, the seasonality pattern of these viruses changed and predictions showed a

potential increase in the severity of future RSV and influenza outbreaks (Baker et al., 2020). Preliminary data from the 2022-2023 RSV outbreak tend to confirm these predictions. In France and in the US, a clear increase in hospitalisation rates were associated with RSV in young children this season (Bulletin épidémiologique bronchiolite, semaine 2. Saison 2022-2023; CDC, <https://www.cdc.gov/rsv/research/rsv-net/dashboard.html>, accessed: 01/23/2023) (Figure 3).

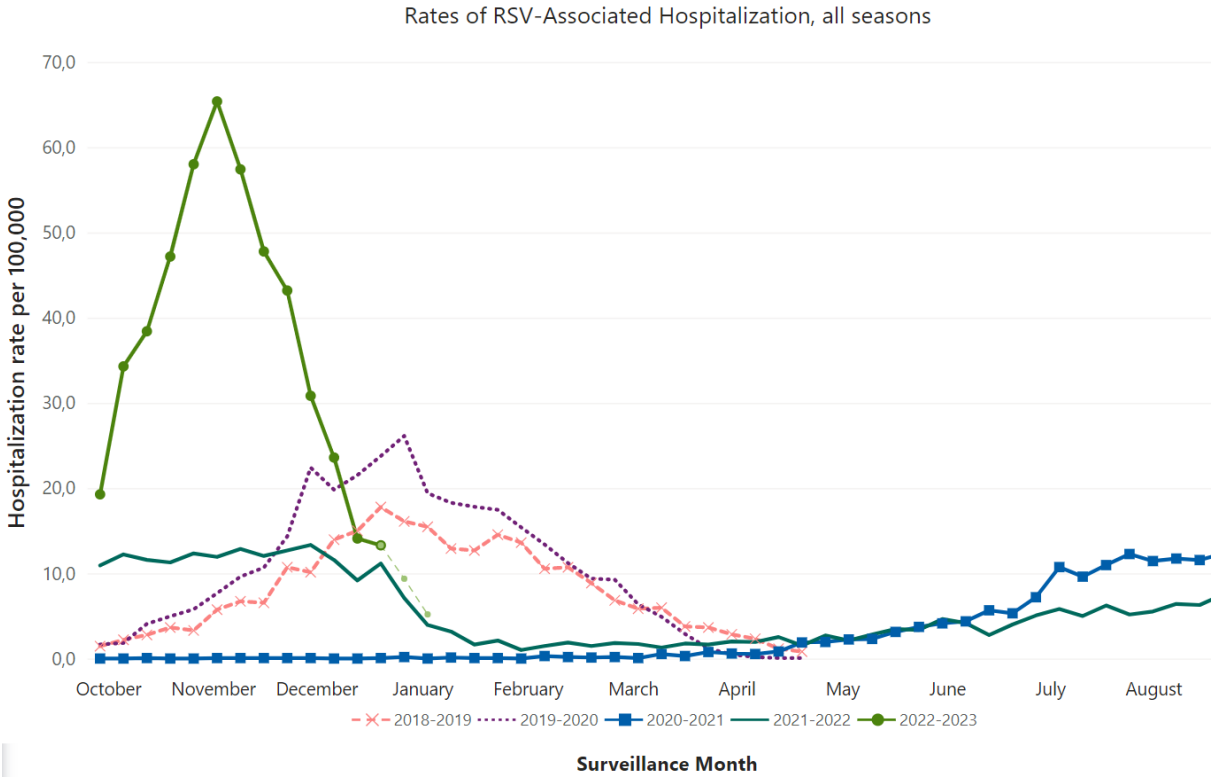


**Figure 3.** The hospitalisation rate of children of 0-4 years old for RSV-associated diseases over 11 months, since 2018 in the US. Data updated the 01/08/2023. Figure adapted from <https://www.cdc.gov/rsv/research/rsv-net/dashboard.html>, accessed: 01/23/2023.

## *2.2. RSV infection and associated disease*

RSV disseminates through respiratory droplets and secretions from infectious people or by self-contamination following contact with contaminated surfaces. RSV infects nasopharyngeal mucous or eyes. Incubation time varies from 2 to 8 days and infected people will be contagious for up to 8 days (Hall and Douglas, 1981).

RSV infection starts in the upper respiratory tract and can provoke symptoms like rhinorrhoea and sneezing due to mucosal inflammation. In some cases, mostly infants experiencing first RSV infection and the elderly, RSV infection can spread to the lower respiratory tract and causes bronchiolitis (inflammation of the bronchioles) or pneumonia (infection of the lungs). Of note, syncytia formation in respiratory epithelial cells was reported in natural infection by RSV (Neilson and Yunis, 1990). RSV replicates actively in ciliated cells of the bronchioles and in type I pneumocytes (Johnson et al., 2007; Welliver et al., 2007; Zhang et al., 2002). RSV was also detected in alveolar macrophages (Midulla et al., 1989). In addition, it was demonstrated that RSV can infect olfactory sensory neurons in mice (Bryche et al., 2020).

Primary RSV infection occurs during the first RSV season the child will experience, correlating with the decline in maternal antibodies. Indeed, the presence of maternal IgG in the serum of infants is associated with less severe infections and lower risks of hospitalisation (Piedra et al., 2003). Maternal antibodies transferred to the infants through the placenta and later breast milk thus seem to be the main explanation for the protection of infants from RSV infection during the first weeks/months of life (Chu et al., 2014).

The severity of RSV disease is linked to both a high viral load (El Saleeby et al., 2011), and an inappropriate and exacerbated immune response. This disproportionate response leads to the infiltration in the arterioles of neutrophils, monocytes, and T cells and airway obstruction caused by abundant mucus production and accumulation of epithelial and inflammatory cell debris (Johnson et al., 2007; McNamara et al., 2003; McNamara et al., 2004; McNamara et al., 2005). Specifically, in infants, the major determinant of RSV disease is the immaturity of the immune system before the age of 2 years. The TLR-mediated (toll-like receptors) response resulting in a Th2 and Th17-type immunity response (stimulating eosinophilic and neutrophilic

inflammations), compared to a mature Th1 immunity response in adults (Lukens et al., 2010). It is noteworthy that in the long term, RSV bronchiolitis in the first year of life is recognised as a cause of recurrent respiratory illness with an increased prevalence of asthma, persistent wheezing, and allergies in infants (Sigurs et al., 2010).

Practically, every older child and adults possess serum antibodies specifically directed against RSV. However, those antibodies are not sufficient to prevent reinfection that occurs every 2 or 3 years in older children or adults (Hall et al., 1991). The presence of serum-neutralising antibodies only partially correlates with protection against RSV infection. Interestingly, the presence of high level of mucosal nasal IgA (Immunoglobulin A) is associated with reduced infection in RSV infection challenge. However, serum and mucosal antibody levels decrease considerably a few months after infection (Habibi et al., 2015). These observations may explain the lack of effective long-term protective immunity against RSV.

In the elderly, RSV infection can lead to severe disease. The underlying causes are certainly multifactorial, one of them being the decrease and/or dysregulation of innate immune responses in this population (Malloy et al., 2013). However, there is no clear explanation for RSV disease severity in this population.

### *2.3. Therapeutic development against RSV*

The antiviral strategy of choice to prevent infection remains vaccination. However, in the sixties clinical trials with a formalin-inactivated vaccine in children were catastrophic, resulting in two deaths and the enhancement of the disease in vaccinated young children after a natural RSV infection (Chin et al., 1969; Fulginiti et al., 1969; Kapikian et al., 1969; Kim et al., 1969). The enhanced disease was due to an inappropriate immune response of vaccinated infants (Polack et al., 2002), including the induction of non-neutralising antibodies and inflammatory responses (Widjaja et al., 2016). This significantly inhibited the development of RSV vaccines, particularly those for young children. The SARS-CoV-2 pandemic, which led to intense vaccine research and the emergence of messenger RNA (mRNA) vaccines, also conducted to the recent development of RSV RNA vaccines with mRNA encoding a stabilised prefusion form of the RSV fusion protein F (mRNA-1345). This vaccine is currently in phase 3 clinical trial in older adults, and Moderna announced in January 2023 that its vaccine induces more than 80 % protection against symptoms associated with RSV disease and will seek global market authorisation in 2023. Several other RSV vaccines are also in phase 3 clinical trials. Four subunit vaccines using the stabilised prefusion F protein as an antigen are currently under development for either older adults (RSVPreF, Pfizer), both infants and older adults (RSVPreF3/GSK3844766A, GSK), or pregnant women (RSVPreF3/GSK3888550A, GSK; RSVPreF, Pfizer). Recombinant vectors vaccines are also in development for older adults, coding for the prefusion F protein (AD26.RSV.PreF, Johnson & Johnson) or coding for 4 viral genes F, G, N, and M2 (MVA-BN RSV, Bavarian Nordic) (Mazur et al., 2023).

In addition, there is still no effective treatment for RSV infection. Treatments mostly consist in supportive care for hospitalised infants with RSV bronchiolitis (from nasal suction and supplemental oxygen to hydration and nutrition by intravenous fluids and invasive ventilation). A preventive treatment, palivizumab, consisting in humanised monoclonal antibodies directed against F, injected before the RSV circulation season (five injections are necessary), is available (The IMPact-RSV Study Group, 1998). However, its effectiveness remains limited and its high cost restricts it to children at risk in developed countries (Homaira et al., 2014). A new monoclonal antibody targeting an antigenic site of F in its pre-fusion state

and presenting an extended half-life, nirsevimab, received marketing authorisation from the European Commission in November 2022. Clinical trials showed that a unique dose of nirsevimab protects healthy and pre-term infants (Hammit et al., 2022), with the same safety profile as palivizumab (Domachowske et al., 2022). Finally, other antiviral approaches are also developed, mostly targeting the F protein, but also the L and N proteins. A nanobody, ALX-0171 targeting F, was shown to present significant efficacy in the reduction of nasal and lung RSV viral load in cotton rats (Detalle et al., 2016). Nonetheless, in phase 2 clinical trial, ALX-0171 fails to show an improvement in the clinical response of the treated group compared to the placebo group in hospitalised children with RSV lower respiratory tract infection (Cunningham et al., 2021). A molecule targeting F in its prefusion state, JNJ-53718678, was also shown to inhibit the development of acute lower respiratory tract infection in neonatal lambs (Roymans et al., 2017) and to reduce clinical disease severity in healthy RSV challenged adults (Stevens et al., 2018). GS-5806, an RSV fusion inhibitor, demonstrated a reduction of symptoms and viral load in healthy adults challenged with RSV (DeVincenzo et al., 2014) but not in hematopoietic-cell transplant patients (Marty et al., 2020).

Many inhibitors preventing RSV replication by targeting L are being developed, but few are reaching phase 2 clinical trials. Among them, ALS-008176, a cytidine nucleoside analogue, and PC786, a non-nucleoside L protein inhibitor, showed efficacy in reducing both the symptoms and the viral load in treated group compared to the placebo group in healthy adults inoculated with RSV (DeVincenzo et al., 2022, 2015). Molecules targeting N are also in development. ALN-RSV0A, a small interfering RNA, was shown to induce *in vitro* and *in vivo* viral titre reduction (Alvarez et al., 2009), and in phase 2 clinical trial, and a reduction of the risk to develop bronchiolitis obliterans syndrome in lung transplant patients (Gottlieb et al., 2016). RSV604 and EDP-938, targeting N (Challa et al., 2015; Rhodin et al., 2021), demonstrate efficacy in reducing symptoms and viral load in healthy adults inoculated with RSV (Ahmad et al., 2022). Nevertheless, none of these antiviral molecules is approved for clinical use yet.

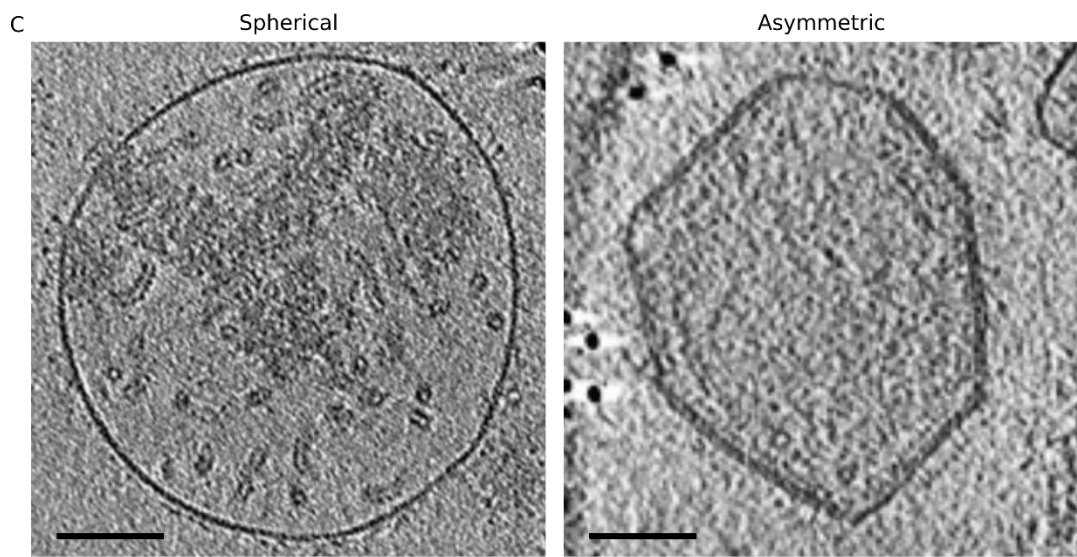
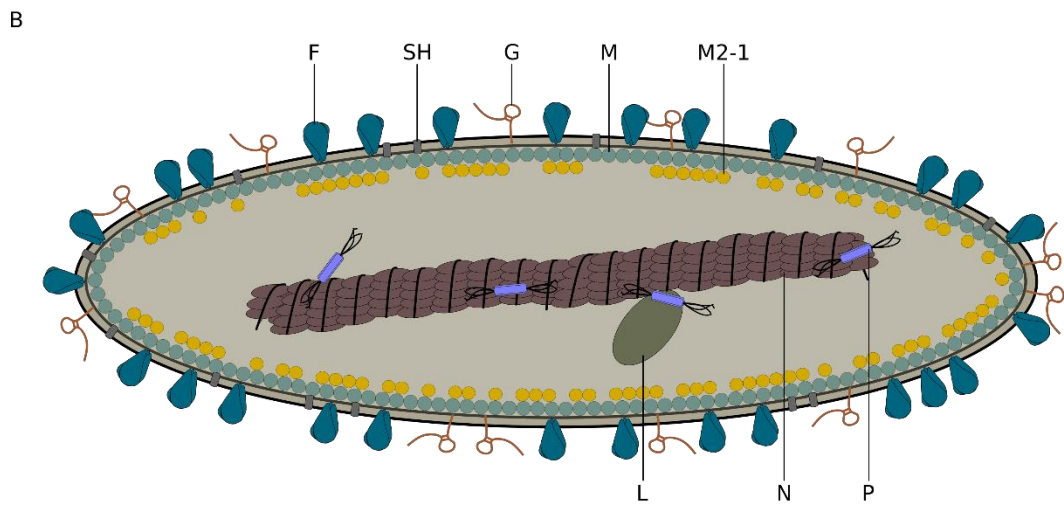
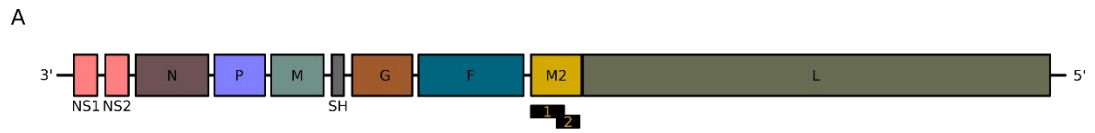


### **3. Viral particle organisation**

The RSV genome is a single negative-stranded RNA of about 15.2 kb, containing ten genes coding for eleven proteins: eight structural proteins, M2-2 protein, and two non-structural proteins (NS1 and NS2) involved in the control of host immune response. The M2 gene contains two overlapping open reading frames (ORF) leading to the translation of the M2-1 and M2-2 proteins (Fearn and Collins, 1999) (Figure 4A, B).

RSV viral particles vary in morphology and size, from filamentous (length from 200 nm to 2  $\mu$ m), to asymmetric, or spherical (diameter from 100 nm to 1  $\mu$ m) (Liljeroos et al., 2013) (Figure 4C).

RSV is an enveloped virus whose membrane is derived from the plasma membrane of the host cell. The virus envelope contains three transmembrane proteins; the glycoprotein (G), which participates in the attachment of the virion to the host cell (Levine et al., 1987), the fusion protein (F), which interacts with receptors at the cell surface and is responsible for the membrane fusion between the host cell and the virion (Walsh and Hruska, 1983), and the small hydrophobic protein (SH), a pentameric ion channel (Gan et al., 2012) which function is not yet fully elucidated but could modulate the immune response. There are contradictory studies regarding the effect of SH on the production of the cytokine Interleukin-1  $\beta$  (IL-1 $\beta$ ) (Russell et al., 2015; Triantafilou et al., 2013).



Filamentous



**Figure 4. RSV virion.** (A) Schematic of the RSV genome organisation, each box represents a gene, and the two ORF of the M2 gene are represented as black boxes. (B) Schematic of an RSV particle, the structural proteins are annotated. (C) Three RSV virion morphologies are shown, images are from tomographic reconstructions (from Kiss et al., 2014). Scale bars 100 nm.

Inside the virion, the matrix protein (M) (essential for the assembly and the budding of the virion) lines the membrane (Marty et al., 2004). RSV RNA genome is constantly enwrapped by the nucleoprotein (N) forming a helical left-handed nucleocapsid (NC) (Bakker et al., 2013) which is the template for the transcription and the replication of the viral genome, carried out by the viral polymerase (L). In the virion, the NC is associated with L and the phosphoprotein (P), an essential cofactor of L (Grosfeld et al., 1995). Evidence supports that the protein M2-1, which is promoting transcription elongation (Collins et al., 1996), could constitute a layer underneath the M layer (Conley et al., 2022; Kiss et al., 2014) (Figure 4B). The M2-2 protein is involved late replication promotion (Bermingham and Collins, 1999).

#### **4. Respiratory Syncytial Virus life cycle**

The RSV viral cycle is entirely cytoplasmic. Attachment of the viral particle and fusion between the viral envelope and the cell plasma membrane are mediated by G and F. The fusion allows the release of the ribonucleoprotein complex (RNP, composed of NC, L, P, and M2-1) in the cytoplasm (Figure 5). The membrane fusion mediated by F is pH-independent (Srinivasakumar et al., 1991), and could occur at the plasma membrane or in endosomes after macropinocytosis (Krzyzaniak et al., 2013). However, the exact sequence of events from particle attachment to membrane fusion is not yet well known.

After the release of RNPs in the cytoplasm of the infected cells, the transcription of viral mRNAs and replication of genomes and antigenomes are initiated by the viral polymerase L which is responsible for all RNAs synthesis activities (RNA-dependent RNA polymerase, mRNAs capping and methyltransferase). Those steps take place in viral factories that are membraneless liquid organelles, called inclusion bodies (IBs) (Garcia et al., 1993; Norrby et al., 1970; Rincheval et al., 2017) (Figure 5). The role of the different proteins constituting RNPs will be detailed in Chapter II of the introduction.

IBs contain the neosynthesised genomes and antigenomes that are encapsidated by N as well as viral mRNAs that are not encapsidated. The viral mRNAs are then exported from IBs to the cytoplasm where viral proteins are synthesised by the cellular machinery of the host cell. Finally, the assembly of viral particles takes place at the plasma membrane where new virions are budding and released (Figure 5).

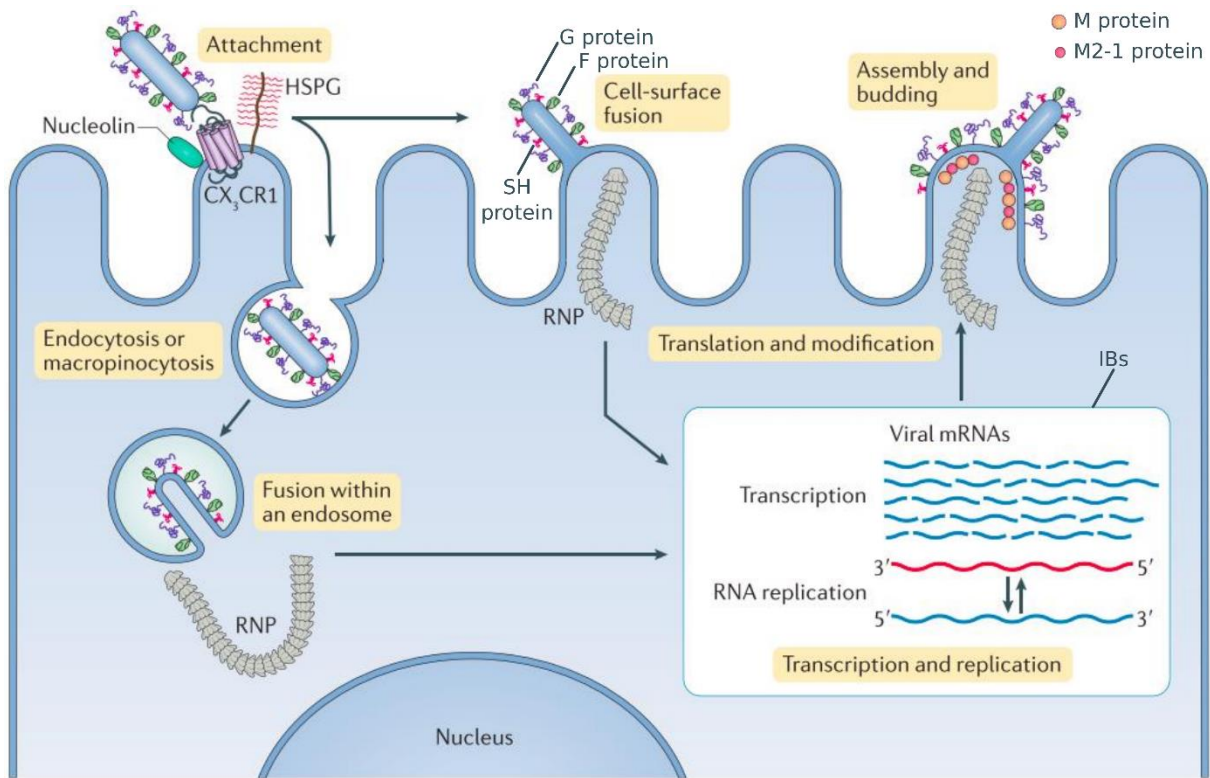


**Figure 5. RSV viral cycle.** Scheme illustrating the viral cycle of RSV. Adapted from Battles and McLellan, 2019. RNP, ribonucleoprotein complex. IBs, inclusion bodies. HSPG, heparan sulfate proteoglycan.

#### 4.1. Viral entry: attachment and membrane fusion

RSV viral cycle starts with the attachment of the virion to the host cell membrane. The attachment is principally mediated by G (Figure 6A) (Levine et al., 1987). The G protein is a highly-glycosylated protein, that exists in two forms: a full-length transmembrane form that mediates attachment and a secreted truncated form that could act as a decoy for the immune system (Figure 6B) (Bukreyev et al., 2008; Hendricks et al., 1987). The transmembrane full-length protein consists of an N-terminal cytoplasmatic tail, a transmembrane part, and the ectodomain. The ectodomain comprises a first sequence-variable mucin-like region bearing *N*- and *O*-linked glycans, a conserved domain containing 4 cysteines forming 2 disulfides bonds and a CX<sub>3</sub>C motif (Doreleijers et al., 1996; Tripp et al., 2001), a heparin-binding domain (Feldman et al., 1999), and finally the second mucin-like region at the C-terminal part (Langedijk et al., 1996). G is the less conserved protein of RSV, with the mucin-like domains presenting the most variability and determining subgroup affiliations (Mufson et al., 1985). Duplication and insertion events occur in this area and lead to the emergence of new subgroups (Hirano et al., 2014; Trento et al., 2010).

Different studies demonstrated that G can attach to different host membrane factors, such as glycosaminoglycans (Krusat and Streckert, 1997) and the receptor CX<sub>3</sub>CR1 of the airway-ciliated epithelial cells or of type I alveolar pneumocytes (Chirkova et al., 2015; Jeong et al., 2015; Johnson et al., 2015). The exact role of those factors is not demonstrated yet, considering that RSV deleted of the genes coding for G and SH proteins can successfully grow in cell culture, despite being attenuated especially *in vivo* (Karron et al., 1997).

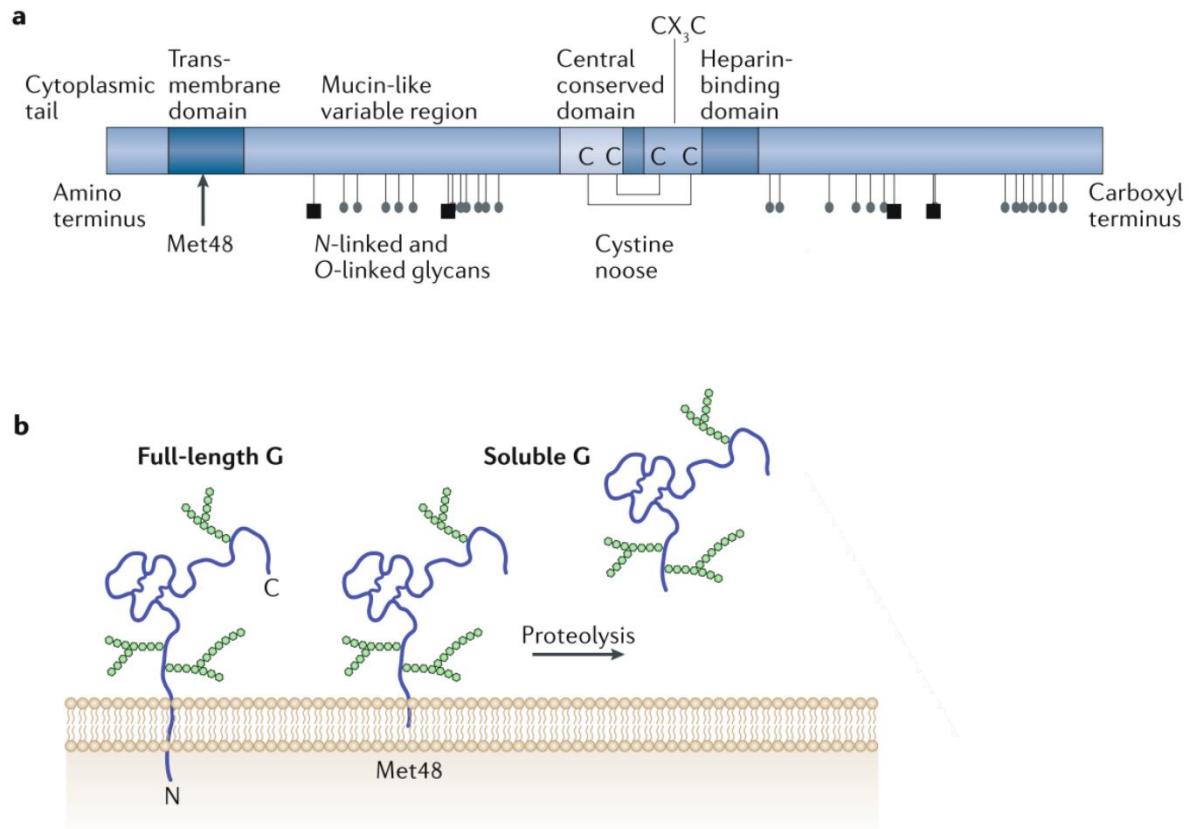


**Figure 6. Structure of the RSV G protein.** (A) Schematic of the RSV G protein organisation, each box represents a domain of the protein, post-translational modifications are indicated underneath. (B) Schematic of the 2 forms of G, the full-length G protein anchored to the membrane and the soluble G protein after proteolysis. Green hexagons represent the O-linked glycans. Figure adapted from Battles and McLellan, 2019.

Unlike G, F is essential for virion attachment and entry into host cells, responsible for the fusion between the viral and host cell membranes. Several receptors of F were described, glycosaminoglycans (Feldman et al., 2000), intercellular adhesion molecule 1 (ICAM1) (Behera et al., 2001), the nucleolin (Tayyari et al., 2011), and epidermal growth factor receptor (EGFR) (Currier et al., 2016).

F is a class I fusion protein, synthesised as an inactive monomer that undergoes post-translational modifications (N-linked glycans are added) and a maturation process consisting



of two events. One event is the cleavage at two polybasic sites by a furin-like protease generating two subunits linked by two disulphide bonds (Zimmer et al., 2001). The other is the trimerisation of the monomer (McLellan et al., 2013) (Figure 7). It is not known which stage occurs first between cleavage and trimerisation. At the virion surface, F is organised in trimers, in a prefusion state. The prefusion state is unstable and the refolding to the postfusion trimer seems to happen without any triggering events and is irreversible (Liljeroos et al., 2013). From the prefusion to postfusion trimer, an intermediate state is formed, called pre-hairpin intermediate, where the fusion peptide is exposed and can bind membranes. Further refolding is necessary to bring the membrane together to initiate the fusion (McLellan et al., 2013; Zhao et al., 2000).

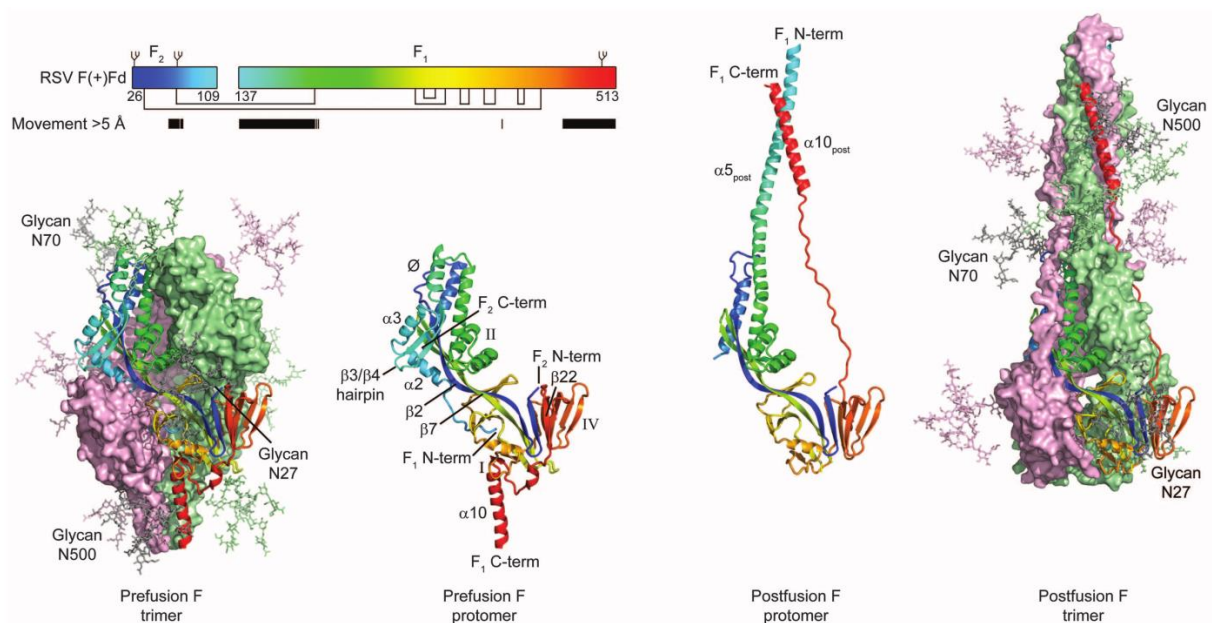


**Figure 7. Prefusion and postfusion structures of the RSV F protein.** Top left, schematic of the RSV cleaved F protein organisation showing the two F subunits. Black lines represent the disulphide bonds and black boxes the amino acids that are moving more than 5 Å between the pre and postfusion forms. Bottom left, the prefusion F in the trimeric structure where two protomers are shown as surface and one as ribbons. Right, the postfusion F in the trimeric structure where two protomers are shown as surface and one as ribbons. Glycans are modelled and displayed as sticks. The colouring of the atomic models matches the schematic. Figure from McLellan et al., 2013.



#### 4.2. Transcription and replication

The L protein processes all the enzymatic activities required for both transcription and replication of the viral genome, RNA synthesis by the RNA-depend RNA polymerase (RdRp), cap addition by the polyribonucleotidyl transferase (PRNTase), and cap methylation by the methyltransferase (MTase). Of note, the RSV genome is constantly encapsidated by N. If encapsidation protects the viral genome from RNAses and from detection by immune sensors which could prevent virus multiplication, it also impairs the direct access of the genome to the viral polymerase. Thereby, when the transcription or the replication occurs the NC should be transiently opened allowing L to gain access to the RSV genome or antigenome (Galloux et al., 2012; García-Barreno et al., 1996; Mallipeddi et al., 1996; Slack and Easton, 1998; Tran et al., 2007).

Transcription of viral mRNAs starts with the recognition of the 3' end "leader" sequence of the genome, located upstream the first gene. For transcription, L initiates RNA synthesis on the 3<sup>rd</sup> nucleotide (Tremaglio et al., 2013). The *de novo* RNA synthesis, meaning that no primer is required to initiate the synthesis, is thought to be mediated by the priming loop of the capping domain of L. The leader sequence is synthesised and released by L. Then L re-initiates RNA synthesis on the first "gene start" signal. Transcription is sequential, each gene being individually transcribed through special sequences flanking each gene: 3' "gene start" and 5' "gene end", which are the sites of initiation and termination of transcription, respectively (Kuo et al., 1996) (Figure 8). Viral mRNAs are capped and polyadenylated by the L (Barik, 1993; Liuzzi et al., 2005). The "gene end" signal induces polyadenylation and the release of mRNAs. The polyadenylated tail is formed by the stuttering of L on a stretch of a U-rich sequence. The capping and methylation of viral mRNA are indistinguishable from that of cellular mRNAs (though the capping pathway is different). The cap exhibits triple methylation, *N*-7-methylation on the guanosine allowing the recognition by the EIF4F (eukaryotic translation initiation factor 4F) cellular complex, for the translation into viral proteins (Filipowicz et al., 1976). And 2'-*O*-methylation on the two first nucleotide residues of the mRNA, constituting a molecular signature of the "self", protecting against the recognition by the host cytoplasmic sensors such as RIG-I (retinoic acid-inducible gene) and MDA5 (melanoma differentiation-associated protein

5) (Devarkar et al., 2016; Züst et al., 2011). Synthesised viral mRNAs are then translated by the cellular machinery.

During transcription, L re-initiates mRNA synthesis at the next "gene start" signal (Fearn and Collins, 1999). L is poorly processive, and can "fall-off" the genome, creating a gradient of viral mRNAs, with the most transcribed gene being the closest to the 3' end of the genome (Barik, 1992). However, the existence of this gradient was recently questioned by studies showing that the mRNA level is not dependent on gene position and varies with the RSV genotype (Donovan-Banfield et al., 2022; Piedra et al., 2020). Although M2-1 is not strictly necessary for the synthesis of genomes and antigenomes *in vitro*, it enhances drastically L processivity and is necessary for transcription of mRNAs in cells (Collins et al., 1996; Grosfeld et al., 1995).

Replication is initiated on the 3' end terminal nucleotide of the "leader" sequence of the genome (negative sense) or on the 3' end terminal nucleotide of the "trailer" sequence of the antigenome (positive sense) to synthesis the antigenome or the genome, respectively (Braun et al., 2017; Mink et al., 1991) (Figure 8). During the replication, L ignores the "gene start" and "gene end" signals to proceed to the end of the genome or antigenome. Just like the genome, the antigenome is encapsidated by N during its synthesis and will be used in turn for the synthesis of multiple new genomes.

The switch from transcription to replication is not yet fully understood but is enhanced by M2-2 (Jin et al., 2000). A high level of monomeric N in the cytoplasm of the infected cell was also hypothesised to be a signal for switching to replication. However, it was observed that an increased level of N enhances replication but also transcription of mRNAs at the same time (Fearn et al., 1997). Since L initiates both transcription and replication on the "leader" sequence, but at a different position, the question arises as to how L discriminates between the two activities. Studies have given some insight into this mechanism. Based to the high affinity of L for ATP and GTP, regardless of the RNA template, an increase in ATP level leads to more initiation at the 1<sup>st</sup> base and less at the 3<sup>rd</sup> base. The opposite result is obtained when the level of GTP is increased. Rising the level of CTP increases initiation on 1<sup>st</sup> base but has no effect on the initiation at the 3<sup>rd</sup> base, indicating that L may have 2 binding sites for nucleoside

triphosphate (NTP). Thus, the discrimination of the initiation site could depend on the NTP to which L is bound (Cressey et al., 2018; Kuo et al., 1997; Noton et al., 2010; Noton and Fearn, 2011) (Figure 8).

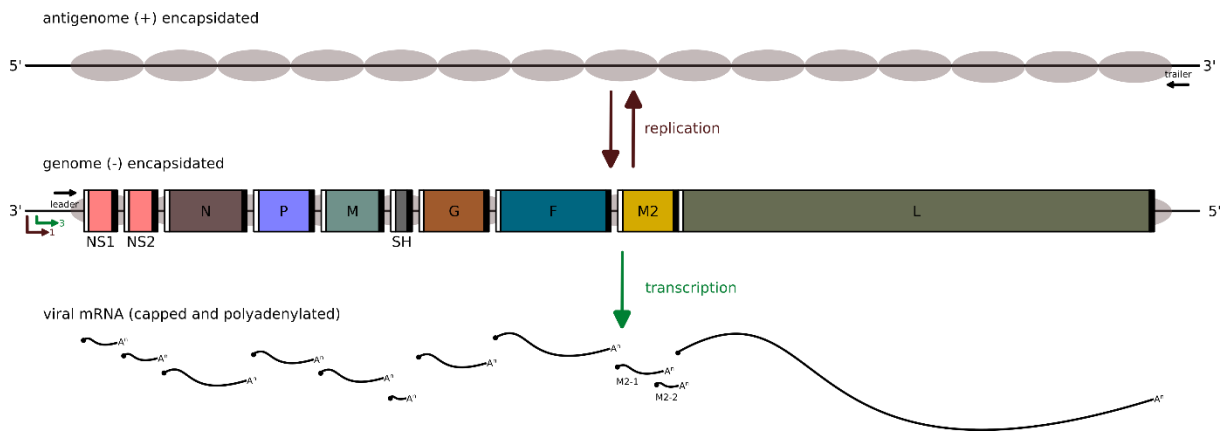


**Figure 8. RSV transcription and replication.** Scheme illustrating the transcription and replication mechanisms in RSV. Each gene is coloured differently, with the name of the protein encoded by the corresponding gene. The M2 gene is coding for 2 different proteins; M2-1 and M2-2 illustrated as 2 different mRNAs. Each gene is flanked by "gene start" and "gene end" signals represented as white and black boxes, respectively. The genome and antigenome are encapsidated by N proteins, materialised by oval shapes. Initiation sites on the 3' end of the genome are depicted by a red arrow for replication (1<sup>st</sup> nucleotide) and a green arrow for transcription (3<sup>rd</sup> nucleotide).

### *4.3. Assembly and budding of the virion*

Viral particles bud at the apical surface of the polarised epithelial cells and form filamentous particles (Ke et al., 2018; Roberts et al., 1995). Assembly of the virions takes place at the plasma membrane (Ke et al., 2018), and requires P, M, and F (Figure 5). Although M is not essential for the initial steps of filament formation (Mitra et al., 2012), M assembly starts through dimerisation and further oligomerisation is necessary for the maturation and release of virions (Bajorek et al., 2014; Förster et al., 2015). Recently, a study using cryo-electron tomography on RSV virions showed that M assembled as dimers form a helical lattice that is oriented relative to the virion lipid bilayer (Conley et al., 2022).

The exact mechanisms underlying the transport of the viral proteins from the cytoplasm and the IBs to the plasma membrane, as well as those of virion assembly, remain elusive. M being shown to colocalise with the IBs (Ghildyal et al., 2002; Meshram et al., 2016; Mitra et al., 2012), it was suggested that M could be implicated in the transport of NC to the budding site (Mitra et al., 2012). Other observations suggested that M2-1 may mediate the interaction between M and NC (Li et al., 2008). The current model of RSV assembly relies on the interaction between the cytoplasmic tail of F and M, which is expected to drive the formation of filamentous virions at the membrane. P should act as a coordinator interacting both with M and NC (Meshram et al., 2016; Shaikh et al., 2012). Indeed, a region on the N-terminal domain of P (residues 39 to 57) was identified as critical for the formation of virus-like-particles (Meshram and Oomens, 2019). Recently M was shown to interact directly with P, through multiple binding sites localised between the N-terminal and oligomerisation domains of P (Bajorek et al., 2021).

More recent studies also support early assembly events in the cytoplasm. Indeed, G was shown to colocalise within vesicles with genomic RNA, forming filamentous structures in the cytoplasm of RSV-infected cells (Blanchard et al., 2020; Vanover et al., 2017; Vijayakrishnan et al., 2022, bioRxiv preprint). Based on these data, a second model of RSV assembly emerged, with cytoplasmic structures that may be transported by a microtubule-dependent mechanism at the plasma membrane. Of note, it was also shown that RSV assembly at the apical face of

polarised cells depends on the apical recycling endosomes of the infected cells (Brock et al., 2003).

#### *4.4. Immune response control during the viral cycle*

The non-structural proteins NS1 and NS2 are the major viral proteins that suppress the host's innate immune response. It was shown that, although these proteins are dispensable for RSV replication, deletion of NS1 or NS2 induces a strong reduction of the viral titre in cell culture (Teng et al., 2000; Teng and Collins, 1999).

NS1 and NS2 inhibit type I and type III interferon response and subsequent interferon production (Spann et al., 2005; Swedan et al., 2011). Both NS1 and NS2 are interfering with the MAVS (mitochondrial antiviral signalling protein) signalling pathway. NS2 is able to block the MAVS signalling pathway by interacting with the CARD (caspase recruitment domain) domain of RIG-I (Ling et al., 2009). NS1 is able to bind directly MAVS and thus blocking its interaction with RIG-I and further interferon production (Boyapalle et al., 2012).

Moreover, a study showed that NS1 is also localised in the nucleus of infected cells and could play a role in the transcription regulation of the host cell genes (Pei et al., 2021). It was further demonstrated that NS1 interacts directly with the mediator complex subunit 25 (MED25) (Dong et al., 2022). The mediator complex is making the bridge between the RNA polymerase II and transcription factors, this NS1-MED25 interaction could be involved in the transcription regulation of some of the host cell genes.



## Chapter II: RSV polymerase machinery

As previously mentioned, during the viral cycle the genomic and antigenomic RNA are encapsidated, and L must be able to access the genomic RNA in order to perform transcription and replication. The mechanisms involved in the specific encapsidation of viral genome and those underlying genome access are still poorly established. However, in recent years, studies of protein-protein interactions and atomic structures of proteins belonging to the RSV RNP have led to new hypotheses. Furthermore, these steps take place in cytoplasmic IBs, but the activity and/or role of proteins and their interaction modes in these structures are insufficiently understood. The existing structural data on L, P, M2-1, and N, as well as data on IBs, are detailed in the following paragraphs.

### **1. RSV polymerase protein and its viral cofactors: the phosphoprotein and the M2-1 protein**

#### *1.1. Structure of the L protein*

RSV L protein consists of 2165 amino acids (250 kDa) and is composed of 5 domains: the RdRp, the PRNTase domain responsible for the cap synthesis on the 5' end of viral mRNAs, the connector domain (CD), the MTase domain which is instigating the methylation of the cap of the viral mRNAs, and the C-terminal domain (CTD) (Gilman et al., 2019) (Figure 9).

Very recently, the cryo-EM structures of RSV and HMPV L proteins, in complex with the tetrameric P, were reported, two RSV structures at 3.2, and 3.7 Å resolution, and one HMPV structure at a resolution of 3.7 Å (Gilman et al., 2019; Cao et al., 2020; Pan et al., 2020, respectively). The data showed that L structure is conserved within the *Pneumoviridae* family. Interestingly, these structures revealed that each one of the four C-terminal parts of P tetramer adopts a unique conformation upon binding to L, associated with a distinct site of fixation on L (Figure 9). This asymmetric interaction could be related to the different roles of P during the transcription and replication, bringing the NC to L, and participating in the local and temporary



disassembly of the NC for L to gain access to RNA. More specifically, the structures reveal that 2 out of 4 P of the tetramer are making vast contacts with L while the 2 others are making limited contacts with L and are mainly interacting with the other P protomers. Those P-P interactions are not only at the oligomerisation domain ( $P_{OD}$ ) but also outside of it, forming a bundle of three  $\alpha$ -helices from the C-terminal part of three different P protomers (Figure 9).

It is noteworthy that, although L was purified as a full-length protein, only the RdRp and the capping domains were solved for both RSV and HMPV. The absence of the other domains in the cryo-EM maps could be explained by their potential flexibility, as shown for L of the vesicular stomatitis virus (VSV, *Rhabdoviridae* family) (Rahmeh et al., 2010).

The RdRp is divided into 4 subdomains called palm, fingers, thumbs, and support region. Together with the cap domain the RdRp forms a doughnut-like configuration (Figure 9) that is shared among the RNA polymerases. The RdRp and capping domain are creating a cavity, where the majority of the RdRp catalytic motifs are located at the bottom, and the capping domain motifs at the top. Six conserved catalytic motifs (A to F) are described in the RdRp (Jácome et al., 2015; Poch et al., 1989), 5 out of 6 belong to the palm domain, and one is in the fingers domain. The 6 conserved motifs are implicated in the accommodation of incoming NTP and RNA templates, and the overall flexibility of the RdRp (Garriga et al., 2013). The capping domain possesses 5 conserved motifs (A to E) and a flexible priming loop that could be implicated in the synthesis initiation (Liang et al., 2015). In the VSV L protein structure, this loop occupies the RdRp catalytic site, whereas for RSV and HMPV L structures, it is flipped and leaves the RdRp catalytic site empty. The two alternative positions of the loop could reflect different states of activity of the polymerase, the initiation state when the loop occupies the RdRp site (Liang et al., 2015), and the elongation state when the loop is lifted up (Gilman et al., 2019; Pan et al., 2020).

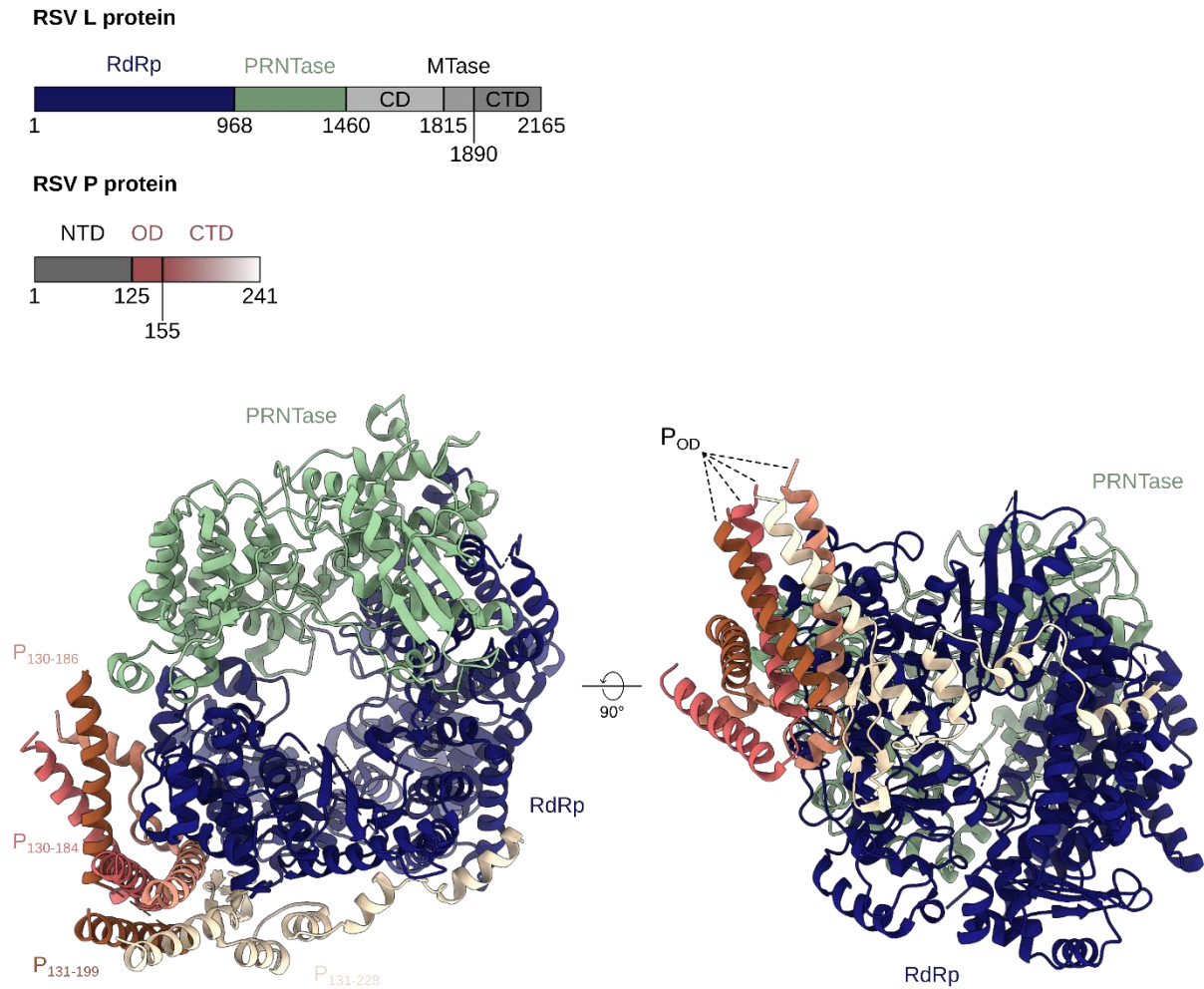


**Figure 9. Cryo-EM structure of RSV L-P complex.** Top, schematic view of the RSV L and P proteins sequences. L protein is divided into 5 domains, RdRp (blue), PRNTase (green), CD, MTase, and CTD (grey). The P protein is divided into 3 domains, NTD (grey), OD (red), and CTD (red gradient). L and P proteins schematics are not drawn to scale. Bottom, atomic model of the L-P complex as ribbons (PDB: 6PZK, Gilman et al., 2019). The RdRp and PRNTase domains are coloured as on the schematic (top). Each P protein of the tetramer is coloured in a different shade of pink.

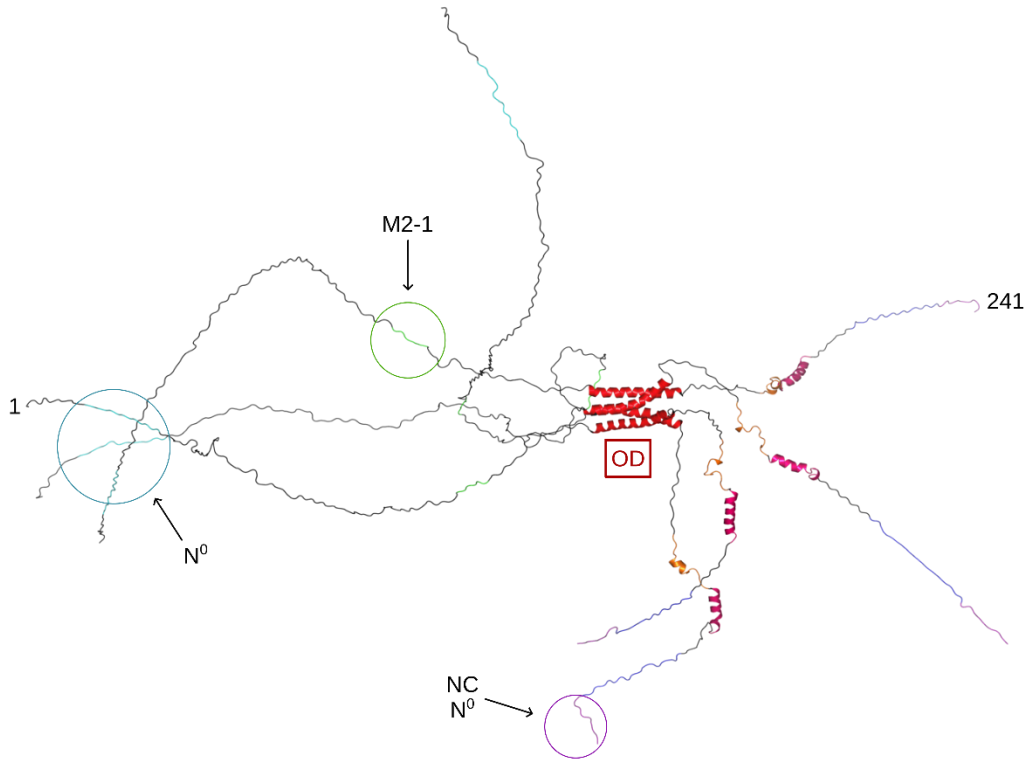
## *1.2. Function and characteristics of the P protein*

The phosphoprotein P is a key viral protein which is involved in many protein-protein interactions, acting as a hub. First, P is the essential cofactor of L, recruiting the NC to L (Garcia-Barreno et al., 1996; Mallipeddi et al., 1996; Slack and Easton, 1998). In particular, the nine C-terminal residues of P were identified as essential for the binding to the NC and RNA synthesis (Tran et al., 2007; Galloux 2012). This interaction is mediated by hydrophobic and acidic residues of P and a hydrophobic pocket on the N-terminal domain of N (Galloux et al., 2012; Ouizougoun-Oubari et al., 2015; Shapiro et al., 2014; Tran et al., 2007). Second, P also acts as a molecular chaperone to maintain the neosynthesised N protein in its monomeric form, constituting the N<sup>0</sup>-P complex (Esneau et al., 2019; Galloux et al., 2015). Third, P is responsible for the recruitment of M2-1 and of the cellular protein phosphatase 1 (PP1) to IBs (Blondot et al., 2012; Mason et al., 2003; Richard et al., 2018; Tran et al., 2009). Finally, P was shown to interact with M during the virion assembly (Bajorek et al., 2021). A review detailing the pneumoviruses N-P interactions (Decool et al., 2021), of which I am co-first author, can be found in the appendix.

RSV P protein is composed of 241 residues (27 kDa) and forms tetramers through a central oligomerisation domain (P<sub>OD</sub>, residues 125 to 155) (Castagné et al., 2004; Gilman et al., 2019; Llorente et al., 2008, 2006; Pereira et al., 2017). The structure of HMPV P<sub>OD</sub> showed that P protomers are ordered in parallel conformation (Leyrat et al., 2013). On both sides of the P<sub>OD</sub>, the N and C-terminal domains (P<sub>NTD</sub> and P<sub>CTD</sub>, respectively) are intrinsically disordered but could fold upon binding with other proteins (Castagné et al., 2004; Noval et al., 2016; Pereira et al., 2017; Simabuco et al., 2011) (Figure 10A). P is phosphorylated on several serine amino acids, in particular on the S116, S117, S229, S232, and S237 (Barik et al., 1995; Navarro et al., 1991; Sanchez-Seco et al., 1995). The phosphorylation/dephosphorylation of P depends on the cellular phosphatases PP1 and PP2A (Asenjo et al., 2005), and casein kinase II (Mazumder and Barik, 1994). However, phosphorylation of P may not be essential for the transcription and replication of viral RNA (Lu et al., 2002; Villanueva et al., 2000), and the role of these post-translational modifications remain to be determined.

The structural study of P by NMR (nuclear magnetic resonance) demonstrated the presence of transient  $\alpha$ -helices in the P<sub>NTD</sub> and more stable  $\alpha$ -helices in P<sub>CTD</sub> (Peirera et al., 2017). The transient  $\alpha$ -helices of P<sub>NTD</sub> were shown to correspond to the domains of interaction with N<sup>0</sup> and M2-1 (Galloux et al., 2015; Mason et al., 2003; Tran et al., 2009; Blondot et al., 2012). Furthermore, the NMR study showed that the P<sub>CTD</sub> domain identified as NC binding domain (Galloux et al., 2012) was unlikely to fold into  $\alpha$ -helices and probably stay disordered upon interaction (Pereira et al., 2017) (Figure 10A). The cryo-EM structure of the RSV L-P complex revealed that both P<sub>OD</sub> and P<sub>CTD</sub>, through  $\alpha$ -helices, interact with L (Gilman et al., 2019) (Figure 10B).

A



B

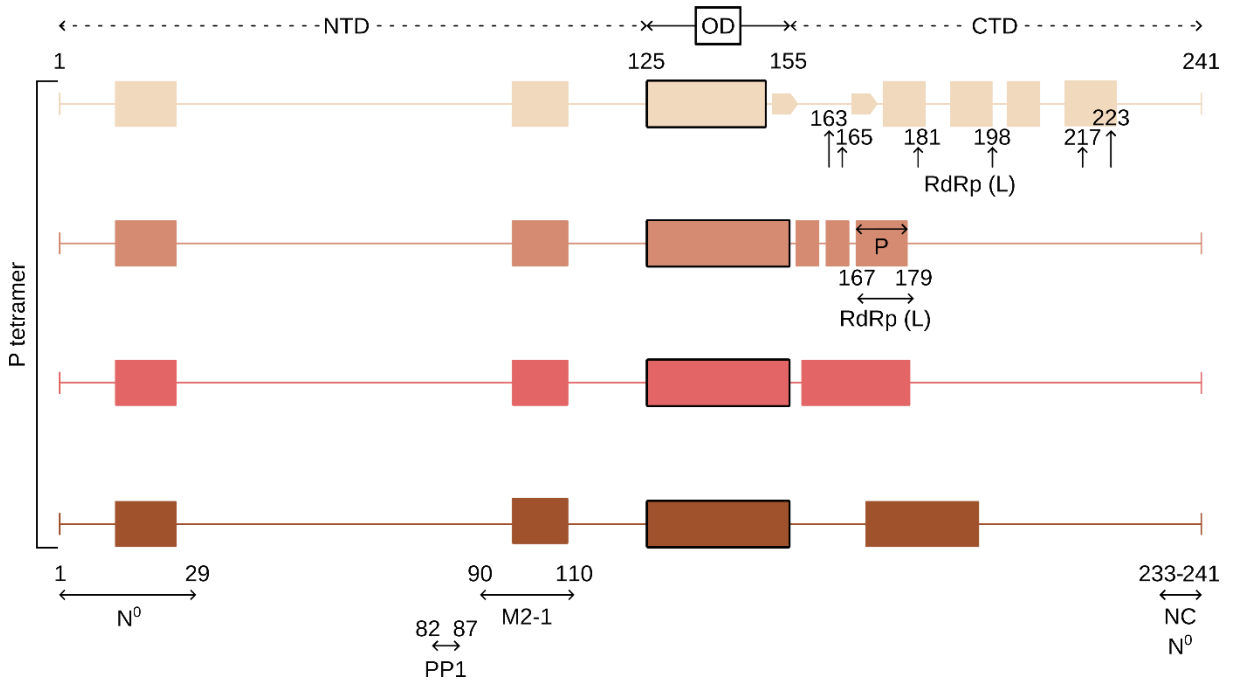


**Figure 10. Binding sites between P and the proteins implicated in viral RNA synthesis.** (A) Model of the RSV P tetramer, regions of interaction with N and M2-1 proteins are identified by the circles, adapted from Pereira et al., 2017. (B) Schematic view of a tetramer of P, each P protomer is coloured as in Figure 9. For each P protomer, the boxes represent transient or permanent (outlined in black)  $\alpha$ -helices. The  $\beta$ -sheets are represented as boxed arrows. The CTD of each P protomer presents a singular folding according to the atomic structure of the L/P complex established by Gilman et al., 2019 (PDB: 6PZK). At the top, the three domains of P, NTD, OD, and CTD, are indicated. The domains interacting with viral proteins and the cellular phosphatase PP1 are indicated with black arrows.

### *1.3. Structure and role of the M2-1 protein*

The M2-1 protein is a transcription factor (Collins et al., 1996, 1995). It was shown that M2-1 increases the processivity of L by acting as an anti-terminator of transcription, critical for mRNA synthesis (Collins et al., 1996; Fearn and Collins, 1999; Hardy and Wertz, 1998; Sutherland et al., 2001). Furthermore, M2-1 was found to be associated with viral mRNA in specific substructures of the inclusion bodies called IBAGs (inclusion bodies associated granules) (Rincheval et al., 2017). More recently, it was shown that M2-1 also binds to specific cellular mRNAs during infection (Braun et al., 2021). Nonetheless, M2-1 is also described as a structural protein forming a layer underneath M in the viral particle (Conley et al., 2022; Kiss et al., 2014; Liljeroos et al., 2013).

The M2-1 protein, composed of 194 residues (22 kDa), forms stable tetramers. Each protomer is composed of a zinc-binding domain (ZBD, residues 7 to 25), followed by a tetramerisation  $\alpha$ -helical domain (residues 32 to 49), a core domain (residues 69 to 172), and twenty last C-terminal residues that are unstructured (Blondot et al., 2012; Tanner et al., 2014) (Figure 11). M2-1 also presents two sites of phosphorylation (S58 and S61) modulating its function (Cartee and Wertz, 2001). M2-1 is an RNA binding protein that preferentially binds to viral mRNA, but also interacts with P (Cartee and Wertz, 2001; Cuesta et al., 2000; Mason et al., 2003; Rincheval et al., 2017; Tran et al., 2009). The RNA and P binding sites are overlapping on the M2-1 core domain (Blondot et al., 2012; Tanner et al., 2014). It was further shown that P recruits the phosphorylated form of M2-1 to IBs, but also induces its dephosphorylation by recruiting the phosphatase PP1. Dephosphorylation of M2-1 allows RNA binding, and its concentration in IBAGs (Richard et al., 2018). These data demonstrated the critical role of phosphorylation/dephosphorylation cycle for M2-1 activity. Crystal structures of M2-1 tetramer in the presence of P or RNA were determined, showing that the P peptide (residues 90 to 110) interacts with three  $\alpha$ -helices from the core domain of M2-1 (Selvaraj et al., 2018) (Figure 11). Recently, a crystal structure of M2-1 with a double-stranded positive-sense RNA revealed that the ZBD may be a secondary RNA binding site (Gao et al., 2020).

Overall, available data suggest that M2-1 may bind the nascent viral mRNA during the transcription, preventing premature RNA release and promoting mRNA elongation, and may act as a post-transcriptional regulator by holding the mRNA in the IBs (Rincheval et al., 2017). It is likely that M2-1 also plays a role, after the export of the viral mRNAs to the cytoplasm, in mRNA stabilisation and translation (Bouillier et al., 2019).

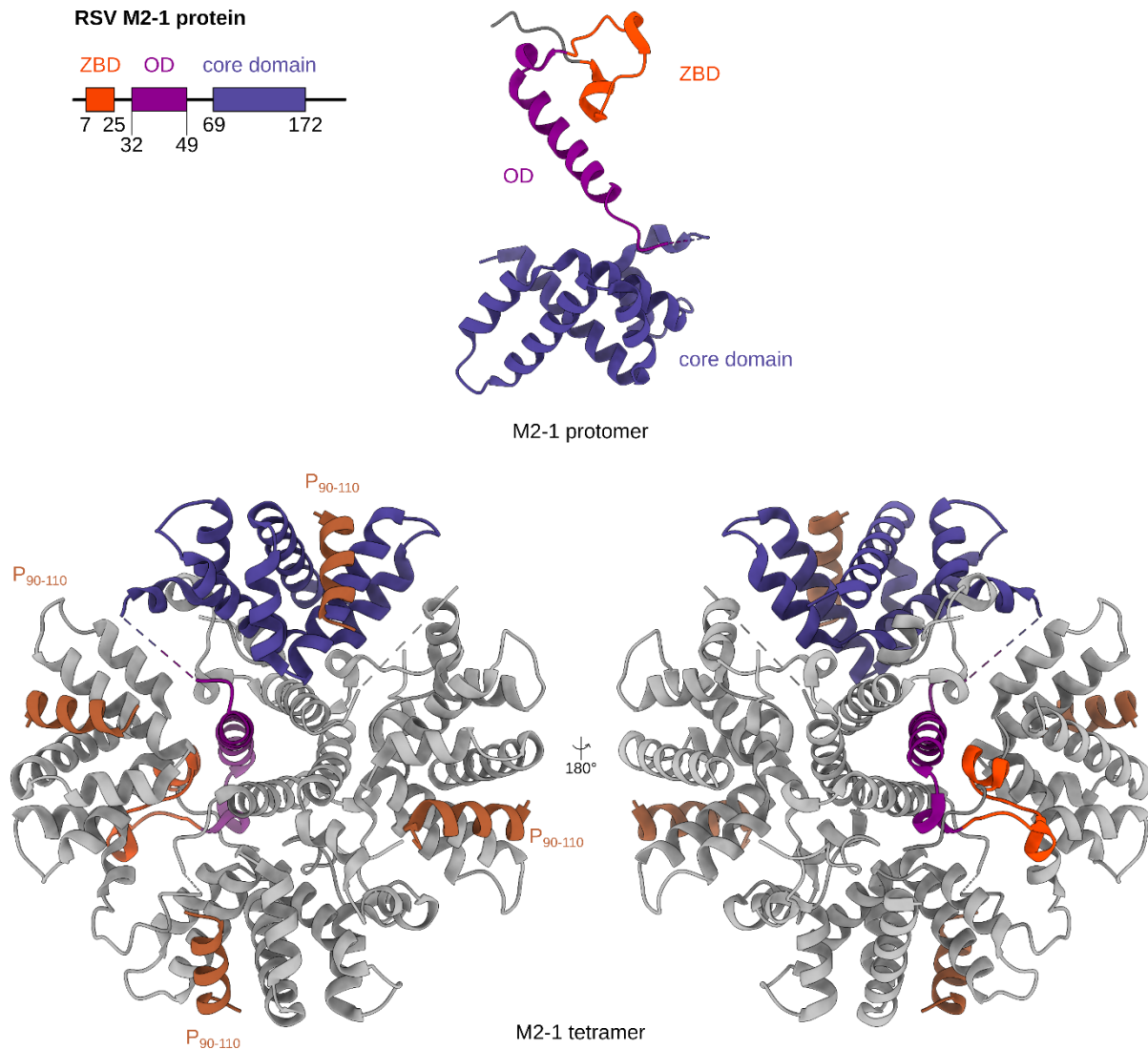


**Figure 11. RSV M2-1-P<sub>90-110</sub> complex structure.** Top left, schematic view of the RSV M2-1 protein sequence. M2-1 is divided into 3 domains, the zinc binding domain (ZBD, orange), the oligomerisation domain (OD, purple) and the core domain (blue). Top right, the atomic model of the M2-1 protomer as ribbons (PDB: 6G0Y, Selvaraj et al., 2018), the protomer is coloured as on the schematic (top left). Bottom, the atomic model of the M2-1-P<sub>90-110</sub> complex as ribbons (PDB: 6G0Y, Selvaraj et al., 2018). The P<sub>90-110</sub> peptide is coloured in dark orange. M2-1 tetramer, 3 out of 4 M2-1 protomer are coloured in grey and one as on the schematic (top left).



## 2. Inclusions bodies

Transcription and replication steps occur in membrane-less viral factories called inclusion bodies (IBs) found in the cytoplasm of RSV-infected cells (Norrby et al., 1970) (Figure 12A). IBs are a signature of infection by *Mononegavirales*, observed in the cytoplasm of cells infected by HMPV (Cifuentes-Muñoz et al., 2017), rabies virus (Lahaye et al., 2009), VSV (Heinrich et al., 2010), measles virus (MeV) (Zhou et al., 2019), Nipah virus (NiV) (Ringel et al., 2019), parainfluenza virus 5 (PIV5) (Carlos et al., 2009), human parainfluenza 3 (HPIV3) (Zhang et al., 2017), Ebola virus (EBOV) (Hoenen et al., 2012), and Marburg virus (MARV) (Kolesnikova et al., 2000).

RSV IBs contain N, P, L, and M2-1 and viral RNA (Rincheval et al., 2017) (Figure 12B). It was shown that NS2 and M could also be recruited in IBs (Ghildyal et al., 2002; Weber et al., 1995). In addition, many cellular proteins are associated with IBs: the chaperones HSP70 (heat shock protein 70) and HSP90 (Munday et al., 2015; Radhakrishnan et al., 2010), MDA5 and MAVS, which are two proteins implicated in the innate immune response (Lifland et al., 2012), actin and actin-binding proteins (Jeffree et al., 2007; Kipper et al., 2015), the poly(A)-binding protein (PABP) and the eukaryotic translation initiation factor 4 G (eIF4G) which are two proteins involved in the initiation of the translation (Rincheval et al., 2017), and the phosphatase PP1 (Richard et al., 2018).

RSV IBs condensate by liquid-liquid phase separation and are very dynamic structures (Galloux et al., 2020; Risso-Ballester et al., 2021) (Figure 12C). It was determined that the minimal elements responsible of IBs morphogenesis are N et P (Garcia et al., 1993; Garcia-Barreno et al., 1996; Galloux et al., 2020). Interestingly, RSV IBs enclose sub-compartments, especially IBAGs, that include exclusively M2-1 proteins and newly synthesised viral mRNA (Rincheval et al., 2017) (Figure 12B). Such sub-compartmentation was not yet observed for other *Mononegavirales*.

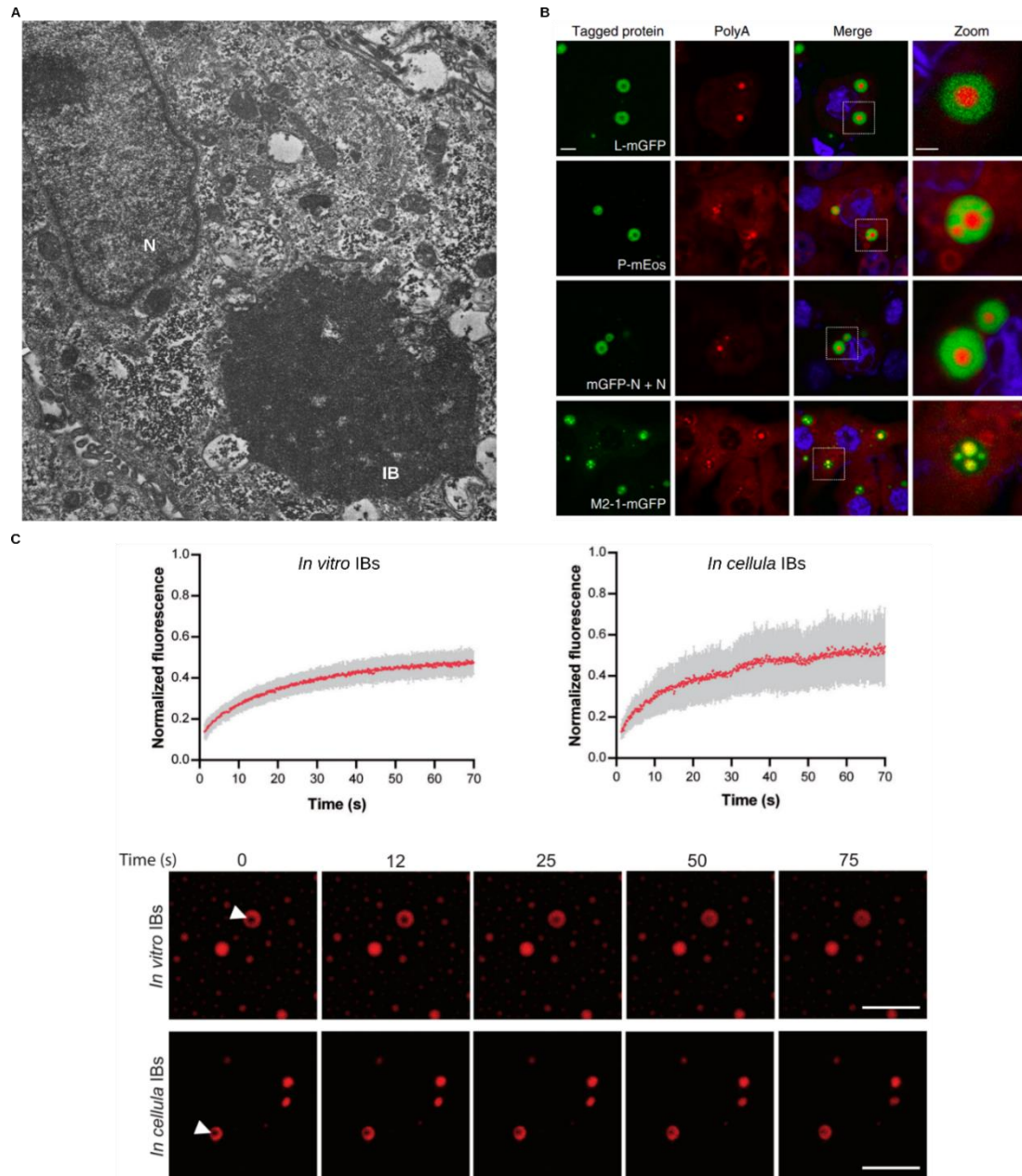


**Figure 12. RSV inclusion bodies.** (A) Negative stain EM section of RSV-infected cells. Magnification X24,000. N: nucleus, IB: inclusion body. Adapted from Norrby et al., 1970. (B) Confocal microscopy images of cells transfected with plasmids coding for N, P, L and M2-1 proteins, tagged with the GFP (green fluorescent protein). When indicated, cells were stained with Hoechst 33342 (merge). FISH (fluorescent in situ hybridisation) analyses were performed to detect the poly(A) RNA. Scale bars 5  $\mu$ m and 2  $\mu$ m for the zoomed images (fourth column). Adapted from Rincheval et al., 2017. (C) Top, graphs of FRAP (fluorescent recovery after photobleaching) performed on *in vitro* (left) or *in cellula* (right) IBs (cells were transfected with plasmids coding for the P and N-mCherry proteins). Bottom, time-lapse images of FRAP performed on *in vitro* IBs or on *in cellula* IBs, scale bars 10  $\mu$ m. Adapted from Galloux et al., 2020.

### 3. Nucleoprotein and nucleocapsid

The RSV nucleoprotein N, composed of 391 amino acids (44 kDa), is present in two forms during the viral cycle, a monomeric form, called N<sup>0</sup>; and an oligomeric form bound to viral RNA, called the NC. N<sup>0</sup> is neosynthesised, competent for the encapsidation of newly synthesised genomes and antigenomes, and maintained RNA-free by the P, which acts as a molecular chaperone. Thus, P (i) prevents N from binding to cellular RNAs and (ii) recruits N<sup>0</sup> to L to encapsidate nascent genomes and antigenomes. The oligomeric form consists of N protomers enwrapping genomes and antigenomes and used as a template by L for transcription and replication (Moyer et al., 1991; Yu et al., 1995).

In 2009, the crystal structure of RSV decameric N-RNA ring at 3.3 Å resolution was obtained (Tawar et al., 2009). The N protein is composed of two globular domains, the NTD (N-terminal domain, residues 37 to 252), and the CTD (C-terminal domain, residues 253 to 359), mainly composed of  $\alpha$ -helices. These globular domains are linked by a hinge region, with their interface forming a RNA binding groove. N has also two extensions, the N-terminal arm (residues 1 to 36), upstream of the NTD, and the C-terminal arm (residues 360 to 391), downstream of the CTD, which are both essential for the oligomerisation of N along the RNA (Esneau et al., 2019; Murphy et al., 2003; Tawar et al., 2009) (Figure 13). This structure also showed that each RSV N binds exactly 7 nucleotides.

Among the *Mononegavirales* order, the *Paramyxoviridae* and *Filoviridae* families are the closest to the *Pneumoviridae* family (Afonso et al., 2016). The N proteins (termed NP for the *Filoviridae* family) of these viruses present a similar structural organisation with two globular domains separated by a hinge region and involved in RNA binding, and the N- and C-terminal arms. The main difference lies in the presence of an additional C-terminal extension after the C-terminal arm of the N proteins of the *Paramyxoviridae* and *Filoviridae* families, called N<sub>tail</sub>.

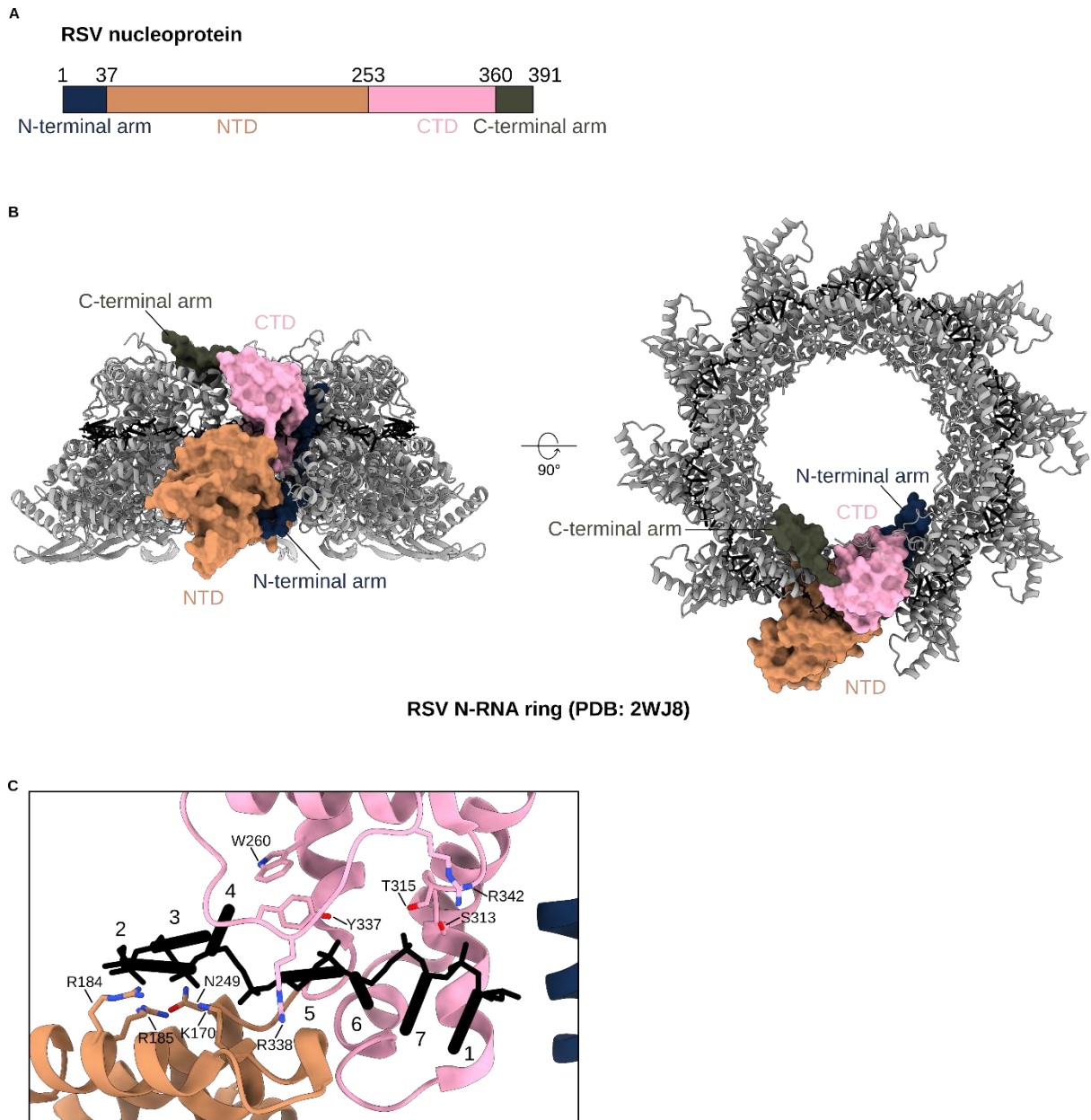


**Figure 13. RSV N-RNA ring structure.** (A) Schematic view of the RSV N sequences divided into an N-terminal arm (blue), NTD (orange), CTD (pink), and C-terminal arm (khaki). (B) Atomic model of the RSV N-RNA ring (PDB: 2WJ8, Tawar et al., 2009), one protomer is shown as a surface coloured as in A. The others are shown as ribbons, coloured in grey. RNA is in black. (C) Close up on the RNA binding to an N protomer, bases are annotated from 1 to 7 and coloured in black. Residues of the N proteins implicated in RNA binding are shown as sticks.

### 3.1. N-RNA oligomers

During the viral cycle, the genomes and antigenomes are constantly encapsidated by N, forming helical NCs. Encapsidation is required for efficient transcription and replication. Encapsidation also allows (i) to protect viral RNA from recognition by cellular nucleases or by immune sensors such as RIG-I, and (ii) to prevent RNA from folding into secondary structures (Blumberg et al., 1983; Bitko and Barik, 2001; Khattar et al., 2001; Hornung et al., 2006; Nilsson-Payant et al., 2021).

Similarly to the NCs of the *Paramyxoviridae* family, RSV NCs display a helical “herringbone” appearance when observed by electron microscopy (EM) (Figure 14). However, the NCs of RSV appear to be highly flexible compared to the *Paramyxoviridae* family ones. The diameter of RSV NC is between 14 and 17 nm (Bhella et al., 2002; Liljeroos et al., 2013), and its variable pitch is estimated to fall between 68 and 74 Å (Bhella et al., 2002; Bakker et al., 2013). Nonetheless, the high-resolution structure of the helical RSV NC is still missing. An atomic model of RSV left-handed NC helix was proposed (Bakker et al., 2013) based on the N-N lateral contacts observed in the structure of the decameric N-RNA ring (Tawar et al., 2009).

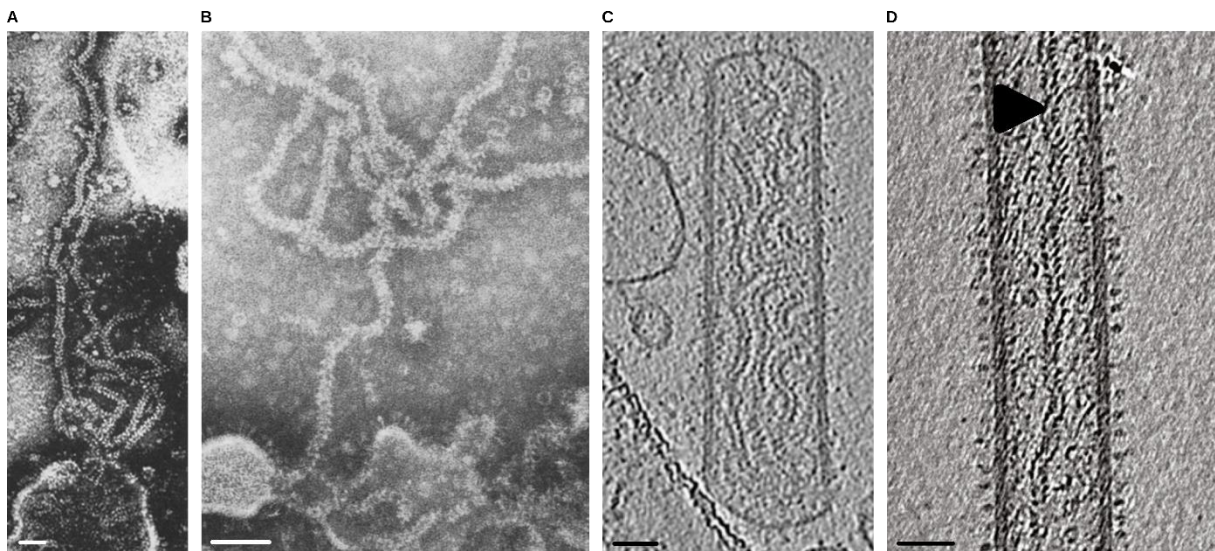


**Figure 14. RSV native nucleocapsids.** (A) NC filaments from a disrupted RSV particle, adapted from Bloth and Norrby, 1967. (B) NC filaments from a disrupted RSV particle, adapted from Bächli and Howe, 1973. (C) Filamentous RSV particle containing NCs, adapted from Liljeroos et al., 2013. (D) Filamentous RSV particle containing NCs (black triangle), adapted from Conley et al., 2022. (A) and (B) are negative stain EM images. (C) and (D) images are slices through tomograms. Scale bars 50 nm.

N-RNA ring structure of RSV (Tawar et al., 2009) gave insights into the N-RNA assembly mechanism of the *Pneumoviridae* family. RSV N-RNA ring is exhibiting a diameter of about 15 nm, close to the one of the HMPV N-RNA ring (16 nm) (Renner et al., 2016), in the range of the diameters observed for RSV NC. The N-RNA ring assembly is mediated by the RNA and the N- and C-terminal arms that are making lateral interactions with the surrounding protomers. The N-terminal arm sticks along the NTD and CTD of the previous N protomer while the C-terminal arm lies on the CTD domain of the following N protomer (Figure 13B). Of note, the assembly of the HMPV N-RNA ring and secondary structure of N are very comparable to RSV (Renner et al., 2016) despite the relatively low percentage of sequence homology, around 60 %, between N amino sequences of RSV strain ATCC VR26 and HMPV strain CAN 97-83.

The RNA is placed outside of the N-RNA ring. RSV N does not follow the “rule of six” which was previously observed for paramyxoviruses (Calain and Roux, 1993; Kolakofsky et al., 1998). Indeed, the structure of N-RNA rings revealed that each RSV N binds 7 nucleotides (Tawar et al., 2009), which provided insight into previous results demonstrating that the RSV genome does not have to be a multiple of 6 to be replicated efficiently (Samal and Collins, 1996). Note that the length of the genome is not determinant as it does not need to be a multiple of 7 either. The RNA backbone is stretched and adopts a conformation where 4 bases are pointing outwards (bases 5 to 7, and 1) and 3 bases inwards (bases 2 to 4) (Figure 13C).

It is noteworthy that RSV N-RNA rings were considered as artefacts of N overexpression in recombinants systems, either in *E. coli* (Tawar et al., 2009) or in insect cells (Bhella et al., 2002; MacLellan et al., 2007). However, a recent study showed that N-RNA rings may be present in viral particles (Conley et al., 2022). These N-RNA rings could be the result of the encapsidation of truncated viral RNAs or of the non-specific encapsidation of cellular RNAs.

Comparison of the N-RNA oligomer structures of the *Pneumoviridae* family with the N-RNA oligomer structures of the *Paramyxoviridae* and *Filoviridae* families reveals a strong homology of the oligomerisation mechanism of N. The overall appearance of the left-handed NCs of these three families is also analogous. The diameter of the paramyxoviruses NCs is between 15 and 20 nm (Gutsche et al., 2015; Ker et al., 2021; Shan et al., 2021; Song et al., 2019;

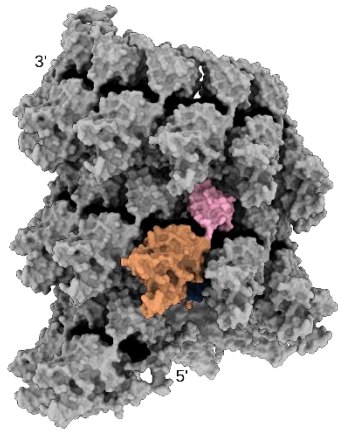


Zhang et al., 2021; Zinzula et al., 2021), close to the pneumoviruses one. In contrast, filovirus NCs exhibit a larger diameter of around 30 nm (Fujita-Fujiharu et al., 2022; Sugita et al., 2018). Although EBOV and MaV demonstrate similar oligomerisation features, MaV forms a singular double helix (Fujita-Fujiharu et al., 2022) (Figure 15). Of note, the cryo-EM structure arrangement of MaV as a double helix is different from the NC structures coming from intact viruses, where no double helix is observed (Bharat et al., 2011; Wan et al., 2017).

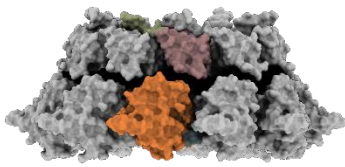
Previously published data suggest that the interactions between the protomers inside the N-RNA rings are similar between the three families and comparable to the ones in the corresponding helical NCs. The N-terminal arm is always essential for the oligomerisation, binding the inside of the CTD of the neighbouring protomer, mainly through hydrophobic interactions. For the viruses of the *Pneumo*- and *Paramyxoviridae* families, the C-terminal arm binds the next promoters at the top of the CTD. Nonetheless, for the *Filoviridae* family, the C-terminal interaction is quite different, with multiple hydrophobic interactions between two  $\alpha$ -helices from two adjacent CTD protomers. RNA binding is similar, the RNA forming a belt on the outside of the helix or the ring, buried at the interface of the NTD and CTD of each protomer. The RNA is stabilised by the interaction with positively charged residues from the NTD and CTD (Figure 15).

The flexibility of the NC is variable and depends on the virus and the family. The expression and purification method used can impact the coiling (Heggeness et al., 1980; Schoehn et al., 2004) and can lead to the formation of rings rather than helices (Alayyoubi et al., 2015; Cox et al., 2009). Subsequently, if the N protein is full-length or truncated of its N<sub>tail</sub> for the *Paramyxo*- and *Filoviridae* families, the conformation of the helix will be impacted. Indeed, the helix is more rigid without the N<sub>tail</sub>, indicating the key role of the N<sub>tail</sub> for the flexibility of the NC (Desfosses et al., 2011; Fujita-Fujiharu et al., 2022; Zhang et al., 2021). Moreover, along the same NC filament different condensation stages can be observed (Shan et al., 2021) with uncoiled parts (Sugita et al., 2018). Finally, in the *Paramyxoviridae* family, clam-shaped structures were observed for Newcastle disease virus (NDV), Sendai virus (SeV), and NiV (Song et al., 2019; Zhang et al., 2021; Ker et al. 2021). The clam-shaped structures correspond to two helical NCs packed back to back, forming a double-headed helical NC.

A

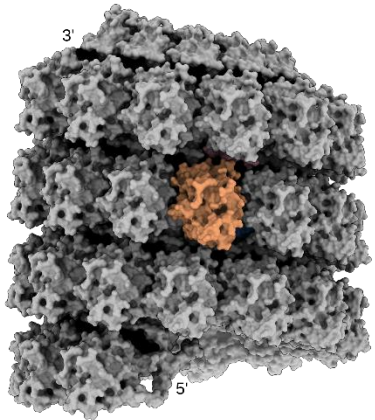


150 Å  
Model of RSV nucleocapsid (PDB: 4BKK)

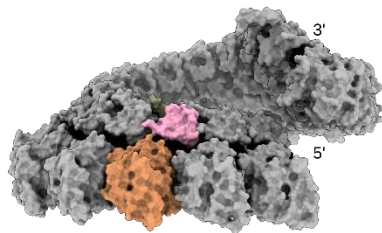


150 Å  
HMPV N-RNA ring (PDB: 5FVC)

C

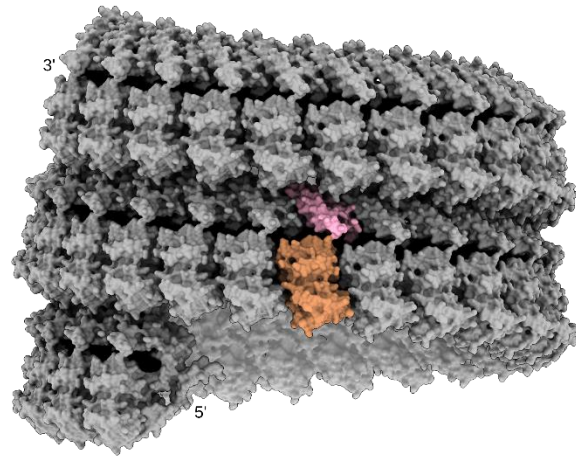


200 Å  
MeV nucleocapsid (PDB: 4UFT)

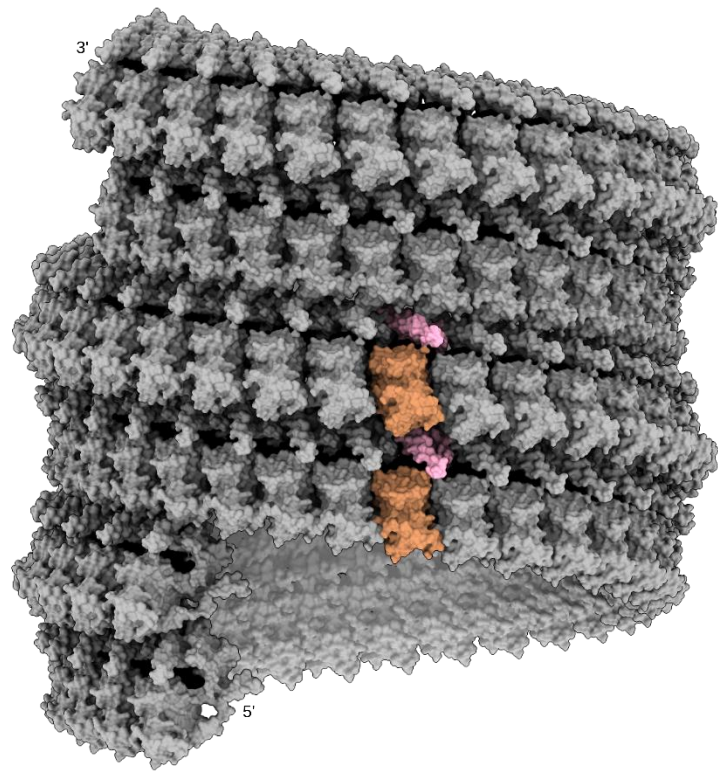


200 Å  
NiV nucleocapsid (PDB: 7NT5)

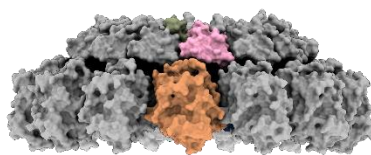
B



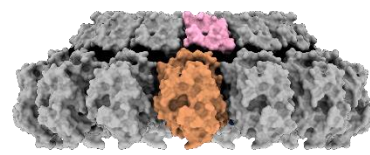
300 Å  
EBOV nucleocapsid (PDB: 5Z9W)



300 Å  
MaV nucleocapsid (PDB: 7F1M)



200 Å  
PIV5 ring (PDB: 4XJN)



200 Å  
MuV ring (PDB: 7EWQ)



**Figure 15. Structure of the N-RNA nucleocapsids and rings among the *Pneumoviridae*, *Filoviridae*, and *Paramyxoviridae* families.** (A) Top, model of RSV NC (PDB: 4BKK, Bakker et al., 2013) shown as surface, one protomer is coloured as in Figure 13. Bottom, atomic model of HMPV N-RNA ring crystal structure (PDB: 5FVC, Renner et al., 2016) shown as surface, one protomer is coloured as in Figure 16. (B) Top, atomic model of EBOV NC structure (PDB: 5Z9W, Sugita et al., 2018) shown as surface, one protomer is coloured as in Figure 13. Bottom, atomic model of MaV NC structure (PDB: 7F1M, Fujita-Fujiharu et al., 2022) shown as surface, one protomer is coloured as in Figure 13. (C) Top, atomic model of MeV NC structure (PDB: 4UFT, Gutsche et al., 2015) shown as surface, one protomer is coloured as in Figure 13. Bottom, left to right, atomic model of NiV N-RNA ring structure (PDB: 7NT5, Ker et al., 2021) shown as surface, one protomer is coloured as in Figure 13. Atomic model of PIV5 N-RNA ring structure (PDB: 4XJN, Alayyoubi et al., 2015) shown as surface, one protomer is coloured as in Figure 16. Atomic model of MuV N-RNA ring structure (PDB: 7EWQ, Shan et al., 2021) shown as surface, one protomer is coloured as in Figure 13. RNA is in black.

### 3.2. Monomeric N protein

The structural data of the pneumovirus N<sup>0</sup>-P complex primarily originate from the 1.9 Å crystal structure of HMPV N<sup>0</sup>-P fusion protein (Renner et al., 2016) (Figure 16) and the biochemical studies of RSV N<sup>0</sup>-P-like complexes in solution (Esneau et al., 2019; Galloux et al., 2015). The obtention of a monomeric N is not straightforward because N has a strong propensity to bind to host RNA upon heterologous recombinant expression, and to oligomerise. Thus, in order to purify a monomeric, RNA-free N protein, and to obtain soluble N<sup>0</sup>-P-like complexes, different strategies based on the association of P (or P fragments) with mutated or truncated N proteins were used for several *Mononegavirales* (Aggarwal et al., 2018; Dong et al., 2022; Guryanov et al., 2016; Kirchdoerfer et al., 2015; Leyrat et al., 2011; Yabukarski et al., 2014; Zhu et al., 2017).

HMPV N<sup>0</sup>-P crystal structure was obtained by fusing the N-terminal 40 residues of P (P peptide) to the C-terminal part of N (Renner et al., 2016). This structure revealed that the P peptide forms two  $\alpha$ -helices sticking to the CTD of N through hydrophobic interactions (Renner et al., 2016). The binding site of the P peptide partially overlaps the binding sites of the N-terminal arm of N<sub>i+1</sub> and the C-terminal arm of N<sub>i-1</sub> in the N-RNA ring (Figure 16B). These data thus unveiled that P acts as an N<sup>0</sup> chaperone by impairing N oligomerisation. Moreover, this study showed that N undergoes conformational changes between the N<sup>0</sup>-P complex and the N-RNA ring, with the NTD getting closer to the CTD by 10 degrees between the N<sup>0</sup>-P (open conformation) and the N-RNA ring (closed conformation) (Figure 17A). Finally, the last conformational change comes from the C-terminal arm position. In the N<sup>0</sup>-P complex, the C-terminal arm is positioned along the CTD, whereas in the N-RNA ring it lies on the top of the CTD of the following N protomer (Figure 16B). The specific folding of the C-terminal arm within the N<sup>0</sup>-P complex, blocks the access to the RNA binding site. Indeed, in the N<sup>0</sup>-P conformation, the residues D373 and E375 could interact with residues R186, and R260/W261, respectively. These interactions can no longer exist upon N oligomerisation as R186 and W261 are interacting with the RNA, and R260 interacts with the N-terminal arm of the N<sub>i+1</sub> protomer (Renner et al., 2016) (Figure 16B).

Concerning the RSV N<sup>0</sup>-P complex, several strategies were used to purify and characterise a soluble N<sup>0</sup> protein: truncation of the N-terminal arm of N (El Omari et al., 2008), mutation of two residues of N (K170 and R185) implicated in RNA binding (Galloux et al., 2015) or co-expression of GST-P40 (Glutathione S-transferase linked to the 40 N-terminal residues of P) with N deleted of its N-terminal arm (N<sub>31-391</sub>) (Esneau et al., 2019).

The study by Galloux et al., 2015 allowed to determine that the residues 1-29 form the minimal domain of P required to interact with N<sup>0</sup>, with 11 residues identified as critical for the interaction with N<sup>0</sup>. Of note, this study also suggested that the last C-terminal residues of P, which were identified as the NC binding domain of P, were also able to interact with N<sup>0</sup>.

The study by Esneau et al., 2019 revealed the role of the RSV N<sup>0</sup> C-terminal arm in preventing RNA binding. Models based on small-angle X-ray scattering (SAXS) analysis revealed two alternative conformations of N<sup>0</sup>: an open conformation where the C-terminal arm blocks the access of the RNA groove, and a close conformation with the C-terminal arm being highly flexible and adopting different conformations. In conclusion, this study confirmed the strong homology of the binding sites of the P peptide on N<sup>0</sup> and of the flexibility of the C-terminal arm between HMPV and RSV N<sup>0</sup>-P complexes (Esneau et al., 2019).

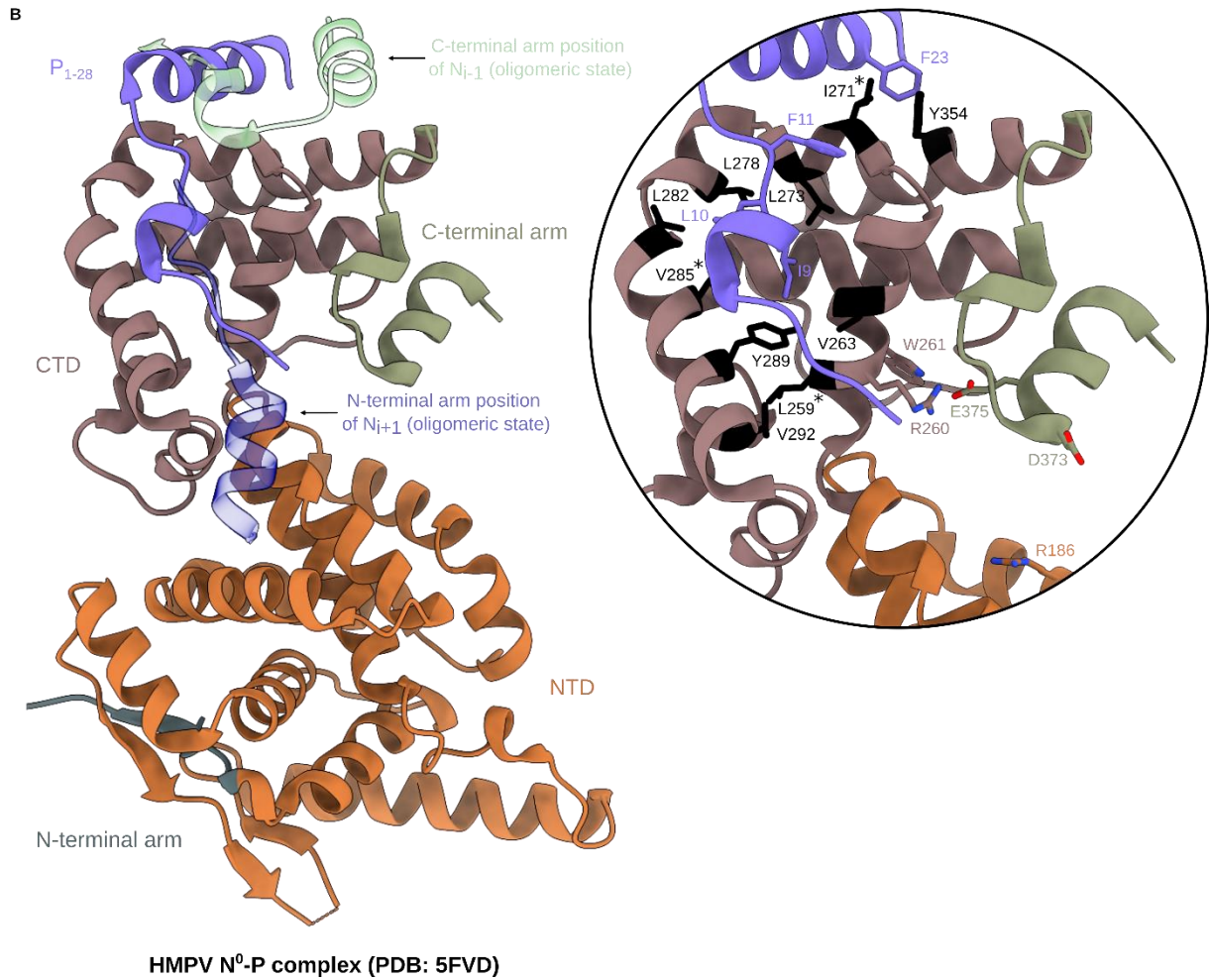
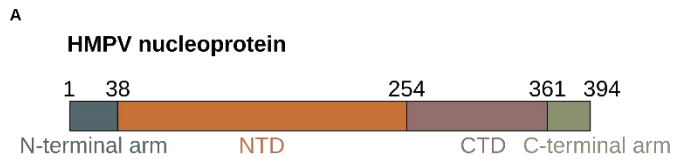


**Figure 16. Crystal structure of HMPV N<sup>0</sup>-P complex.** (A) Schematic view of HMPV N sequence divided into an N-terminal arm (blue), NTD (orange), CTD (pink), and C-terminal arm (green). (B) Atomic model of HMPV N<sup>0</sup>-P complex as ribbons (PDB: 5FVD, Renner et al., 2016). The N-terminal arm, NTD, CTD, and C-terminal arm are coloured as in (A), P<sub>1-28</sub> (the 28 N-terminal residues of the P) is in purple. The N-terminal arm of the N<sub>i+1</sub> and C-terminal arm of the N<sub>i-1</sub> from HMPV N-RNA ring crystal structure (PDB: 5FVC, Renner et al., 2016) are overlaid on N<sup>0</sup>-P complex and coloured in transparent blue and transparent green, respectively. The close-up shows (i) hydrophobic residues of the N<sub>CTD</sub>, as sticks and coloured in black, both implicated in the interaction with P<sub>1-28</sub>, and conserved among the *Pneumoviridae* family, (ii) hydrophobic residues of P<sub>1-28</sub>, as sticks and coloured in purple, interacting with N<sub>CTD</sub> and (iii) residues of the NTD (R186), CTD (R260 and W261) and of the C-terminal arm (E373 and E375) of N, as sticks that could interact with each other and have a role in keeping the C-terminal arm along the CTD in the open conformation. The black stars are pointing to the corresponding residues of RSV N, identified as implicated in the interaction with the P peptide, in the N<sup>0</sup>-P complex (Esneau et al., 2019).

Crystal structures of N<sup>0</sup>-P complexes of NiV, EBOV, HMPV, MeV, MARV, PIV5, and HPIV3 revealed a very similar interaction between the N-terminal part of P (or its homolog VP35, viral protein 35, for the *Filoviridae* family) and the N<sub>CTD</sub>. The P/VP35 peptide is adopting a comparable conformation of one or two  $\alpha$ -helices (Aggarwal et al., 2018; Dong et al., 2022; Guryanov et al., 2016; Kirchdoerfer et al., 2015; Leung et al., 2015; Renner et al., 2016; Yabukarski et al., 2014; Zhu et al., 2017) (Figure 17).

As described for HMPV, the P peptide binding site overlaps with the binding site of the N-terminal arm of the neighbouring protomer, impairing N oligomerisation. Furthermore, for HMPV, MeV, and NiV, the second  $\alpha$ -helix of the P peptide sits at the top of the CTD domain of the N protein, overlapping with the binding site of the C-terminal arm of the neighbouring protomer in the oligomeric state (Guryanov et al., 2016; Renner et al., 2016; Yabukarski et al., 2014). Noteworthy, EBOV and MaV VP35 peptides adopt a slightly different binding conformation compared to the P peptides of Pneumo- and Paramyxoviruses (Kirchdoerfer et al., 2015; Zhu et al., 2017). Interestingly for PIV5 only, the N-terminal end of the P-peptide is placed in the RNA binding site (Aggarwal et al., 2018) (Figure 17). Interactions between the P/VP35-peptide and the N protein are mainly of hydrophobic nature among the three families. These observations reveal differences in the mechanism of chaperone activity of P between viruses.

Of note, for all the N<sup>0</sup>-P complexes mentioned except hPIV3, the structures of N-RNA complexes were also solved, showing that the global arrangement of N is kept between the two forms. Still, two conformations are observed, an open (N<sup>0</sup>-P) and a closed (N-RNA) conformation, which is a characteristic found among these three families (Figure 17). It was hypothesised that N<sup>0</sup> is the preferable adopted conformation upon synthesis (Aggarwal et al., 2018; Kirchdoerfer et al., 2015) even without the presence of the P/V35 peptide. It is the interaction with RNA that might induce the rearrangement and stabilises the closed conformation.

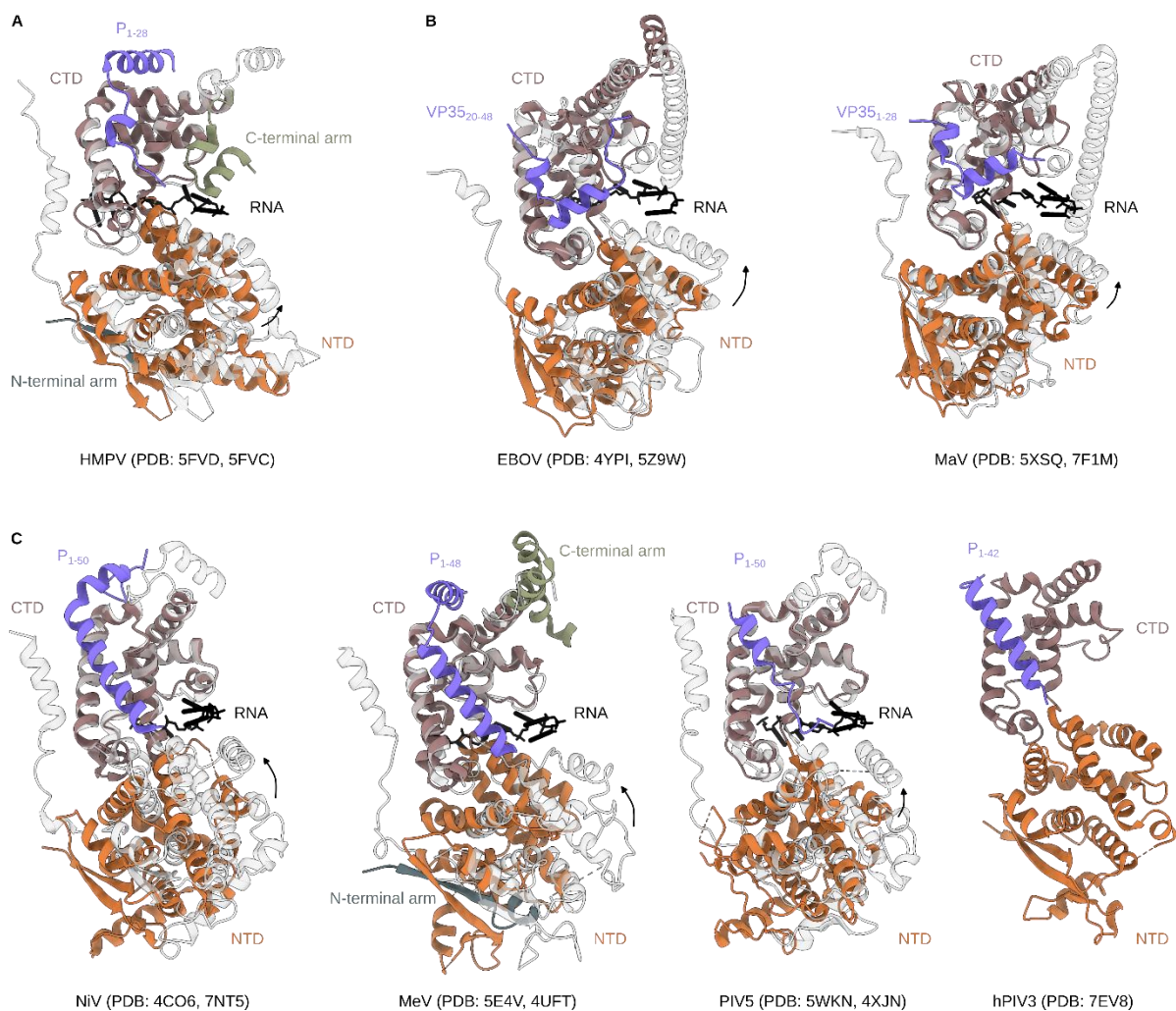


**Figure 17. Crystal structures of N<sup>0</sup>-P complexes of the *Pneumoviridae*, *Filoviridae*, and *Paramyxoviridae* families.** (A) Superimposition of HMPV N<sup>0</sup>-P complex (PDB: 5FVD, Renner et al., 2016) and HMPV N-RNA ring crystal structure (PDB: 5FVC, Renner et al., 2016). (B) Left, superimposition of EBOV NP<sup>0</sup>-VP35 complex (PDB: 4YPI, Leung et al., 2015) and EBOV NP-RNA complex (PDB: 5Z9W, Sugita et al., 2018). Right, superimposition of MaV NP<sup>0</sup>-VP35 complex (PDB: 5XSQ, Zhu et al., 2017) and MaV NP-RNA complex (PDB: 7F1M, Fujita-Fujiharu et al., 2022). (C) Left to right; superimposition of NiV N<sup>0</sup>-P complex (PDB: 4CO6, Yabukarski et al., 2014) and NiV N-RNA complex (PDB: 7NT5, Ker et al., 2021). Superimposition of MeV N<sup>0</sup>-P complex (PDB: 5E4V, Guryanov et al., 2016) and MeV N-RNA complex (PDB: 4UFT, Gutsche et al., 2015). Superimposition of PIV5 N<sup>0</sup>-P complex (PDB: 5WKN, Aggarwal et al., 2018) and PIV5 N-RNA complex (PDB: 4XJN, Alayyoubi et al., 2015). HPIV3 N<sup>0</sup>-P complex (PDB: 7EV8, Dong et al., 2022). For (A), (B), and (C), the atomic models are shown as ribbons, the N<sup>0</sup>-P/VP35 complexes are coloured as in Figure 13 and N-RNA complex structures are coloured transparent grey, RNA is in black. The CTD of the N-RNA complexes are aligned with the CTD of the N<sup>0</sup>-P complexes; except for HPIV3, where no N-RNA complex structure is available. The black arrows are pointing the hinge motion of the NTD toward the CTD from the N<sup>0</sup>-P complex (open conformation) to the N-RNA complex (closed conformation).

### 3.3. Transition from the N<sup>0</sup>-P to the N-RNA form

Despite the fact that monomeric and oligomeric structures of N were obtained, the mechanisms involved in the transition from the N<sup>0</sup>-P to the N-RNA form are not elucidated. This transition depends on concomitant N oligomerisation and RNA binding. P is essential to maintain N in its monomeric form, but the mechanisms that lead to the detachment from N<sup>0</sup> are not characterised. In particular, the temporality between the detachment of P, oligomerisation of N proteins, and binding to the RNA is not known and could be specific to each viral family.

For paramyxoviruses, the study by Milles et al., 2016, about MeV, showed that RNA is required to initiate oligomerisation, but the use of a short RNA demonstrates that oligomerisation can proceed further without RNA. In addition, this study provided insight into the temporality of the encapsidation mechanism, by revealing that the binding of N proteins to RNA occurs first, followed by the assembly of RNA-bound N proteins.

For filoviruses, the study by Kirchdoerfer et al., 2015 on the EBOV NP<sup>0</sup>-VP35 complex has given insight into the N<sup>0</sup>-P to N-RNA transition mechanism. The NP<sup>0</sup>-VP35 complex (NP<sub>1-450</sub>, N- and C-terminal arms present, and VP35<sub>1-80</sub>) can form oligomers *in vitro* without RNA by purifying away the VP35-peptide. Moreover, this oligomerisation is reversible, the addition of an excess of VP35<sub>1-80</sub> to NP<sub>1-450</sub> oligomers leading to the formation of NP<sup>0</sup>-VP35 complexes. Nonetheless, oligomer dissociation is impossible when NP<sub>1-450</sub> oligomers are purified with RNA, indicating that oligomerisation and RNA binding are coupled mechanisms. The study by Peng et al., 2016, on the contrary, showed that oligomerisation could not start without RNA.

Overall, these studies tend to demonstrate that RNA may be essential to initiate the oligomerisation of the N proteins of paramyxo- and filoviruses and to obtain stable oligomers, but that further oligomerisation is more dependent on the N-N interactions within the NCs.





## Chapter III: Cryo-EM at a glance

Cryo-electron microscopy (cryo-EM), X-ray crystallography and NMR spectroscopy are the three main techniques for determining the structure of biological macromolecules. Obtaining structural information is a key step to better understand the macromolecular function. Over the last decade, cryo-EM has undergone significant developments, such as improvement of the microscope stability, implementation of direct electron detectors, automated data acquisition, innovative computational algorithms and introduction of user-friendly data processing software, which have greatly increased the number of structures of biological macromolecules solved by cryo-EM.

In transmission electron microscopy (TEM), electrons pass through the biological sample to create images that are 2D projections of the 3D object. The term “cryo” of cryo-EM refers to the fact that the biological sample is hydrated and enclosed in a fine vitreous ice layer, with the ice layer being preserved by cooling all the instruments near the temperature of liquid nitrogen.

We will mostly talk about single-particle analysis of cryo-EM images, which allows the 3D reconstruction from the 2D projections of purified macromolecules, but also, very briefly, about cryo-electron tomography (cryo-ET), which enables studying larger biological complexes in their native environment.

The process of determining the structure of a macromolecule by cryo-EM begins by applying the purified macromolecules to the dedicated support, which is then blotted and plunged into liquid ethane. The grid is then placed in the microscope for data collection, followed by data processing (Figure 18).

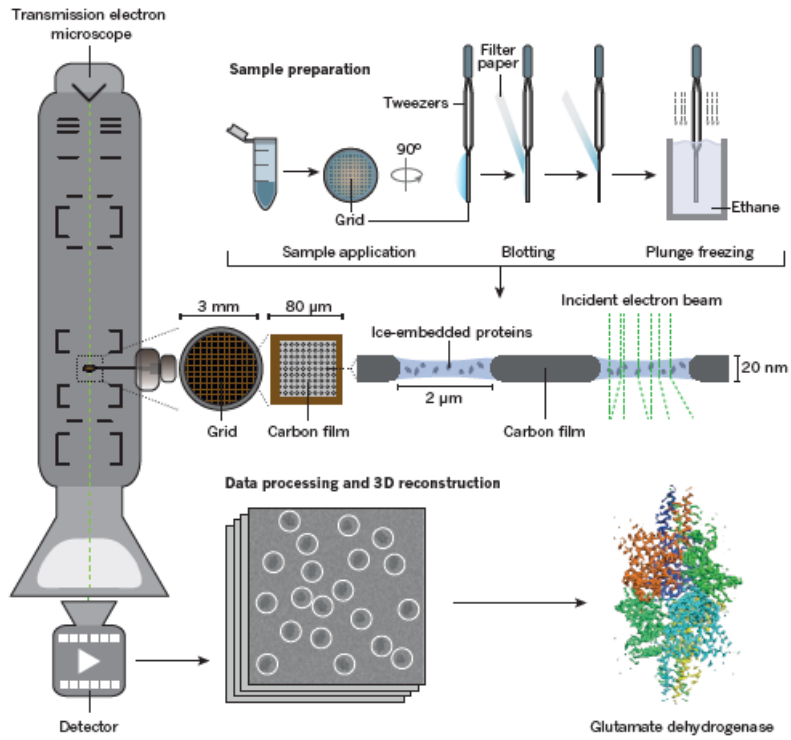


**Figure 18. Scheme depicting the main steps for structure determination by cryo-EM.** Glutamate dehydrogenase is used as an example of a structure solved by cryo-EM. From Fernandez-Leiro and Scheres, 2016.

## **1. Negative stain EM and sample preparation for cryo-EM**

Before starting cryo-EM data collection, the simplest and quickest way to assess the quality of the sample is by negative stain electron microscopy (ns-EM). Ns-EM provides information on sample homogeneity, overall shape, size and symmetry of the macromolecule. The preparation of the ns-EM grid consists of placing the sample on the carbon-coated grid, quickly blotting the excess of sample solution and replacing it with a solution of heavy metal salt, blotting again and finally letting the grid air dry. The heavy metal salt solution allows to significantly increase the contrast of the obtained images which facilitates the visualisation of the macromolecules. However, the staining may introduce artefacts and the 3D structure of the macromolecules may be altered in particular by the drying steps. Therefore, ns-EM is used as a quality control step before proceeding to cryo-EM data collection aimed to obtain the 3D structure of macromolecules.

Electron microscopes are operated in a high vacuum to avoid the scattering of the electron by molecules present in the air. However, the high vacuum is not compatible with biological materials conservation because these are usually present in an aqueous state. Moreover, biological materials are very sensitive to radiation damage, and the energy deposited by the electrons is cleaving the chemical bonds of the macromolecules. In order to both maintain the sample in a hydrated state despite the high vacuum and to limit the effects of radiation damage, the solution of purified macromolecules is frozen quickly into a fine vitreous ice layer (Dubochet and McDowell, 1981; Dubochet et al., 1982). To do so, the sample is deposited on the grid covered by a carbon or a gold film containing holes where the sample will be kept after the blotting of excess liquid with filter paper (Figure 18). The freezing should be quick enough and the ethane cold enough to create a non-crystalline ice layer where the purified macromolecules are trapped in a close-to-native state.

## 2. From the electron to the image

The term "resolution" is defined in microscopy as the smallest distance between two points of the specimen that can be distinguished without ambiguity. In EM, electrons are accelerated in the column of the microscope by an electric field that is typically ranging from 100 to 300 kV. The electrons thus generated have wavelengths that are shorter than the distance between the atoms in a protein, the resolution is thereby not limited by the electron wavelength.

After their emission, the electrons are accelerated and focused by the electromagnetic lenses (Figure 19A). When hitting the sample, the incident electron can pass through the sample without interacting with the sample, in this case, the electrons are unscattered. In other cases, the transmitted electron is simply deflected and does not suffer energy loss, it is called elastic scattering. The incident electron can be scattered after interacting directly with the electrons or the nuclei of the specimen leading to energy loss, it is called inelastic scattering. In this case, the energy is transmitted to the specimen and alters its structure (Figure 19B).

The contrast of the images formed in cryo-EM comes from the addition of two types of contrast. There is the amplitude contrast resulting from the absorption of some of the incident electrons by the specimen, and the phase contrast appearing from the elastic scattering, each electron following a different path in the specimen. In cryo-EM the electrons interact poorly with the biological macromolecules, thus the amplitude contrast is weak. However, electrons experience scattering and thus undergo a phase shift that can be converted into amplitude variations and recorded by the detection system (Figure 19C). Furthermore, in order to obtain a better contrast of the images, the images are recorded at different defocus, to do so the image plane is placed at a different position from the exact focus. The created defocus induces an additional phase shift in the transmitted electrons, enhancing the image contrast. Energy filters placed in the column of the microscope are also used to stop the electrons that interact inelastically with the specimen and do not contribute productively to the image contrast.

Because the electron microscope is not a perfect operating system, aberrations created by the lenses, beam incoherence, sample instability, temperature changes or defaults in the

vacuum, affect the image formation and thereby a sharp dot in the sample will appear blurry in the image. The defaults of the electron microscope are described by a function called the point spread function (PSF) and are considered during image processing.

One of the main breakthroughs in cryo-EM data collecting was the development of direct electron detectors (Faruqi, 2009; Milazzo et al., 2010) that allow the direct conversion of the electron in voltage recorded by a pixel matrix. The quick conversion in digital signals coupled with the high speed of these detectors, improved the speed and accuracy of data collection, and offers the possibility to record movies that can be dose-fractionated, i.e. each frame can be filtered or removed according to the electron dose received.

The energy deposited by the electrons interacting with the specimen induces movement of the grids but also in the vitreous ice and molecular vibration in the specimen that impacts the image quality. The movement can be minimised by using grids that deform less (Naydenova et al., 2020; Russo and Passmore, 2016). Finally, as images are recorded as movies, the frames are realigned during the image processing to correct the beam-induced movement.

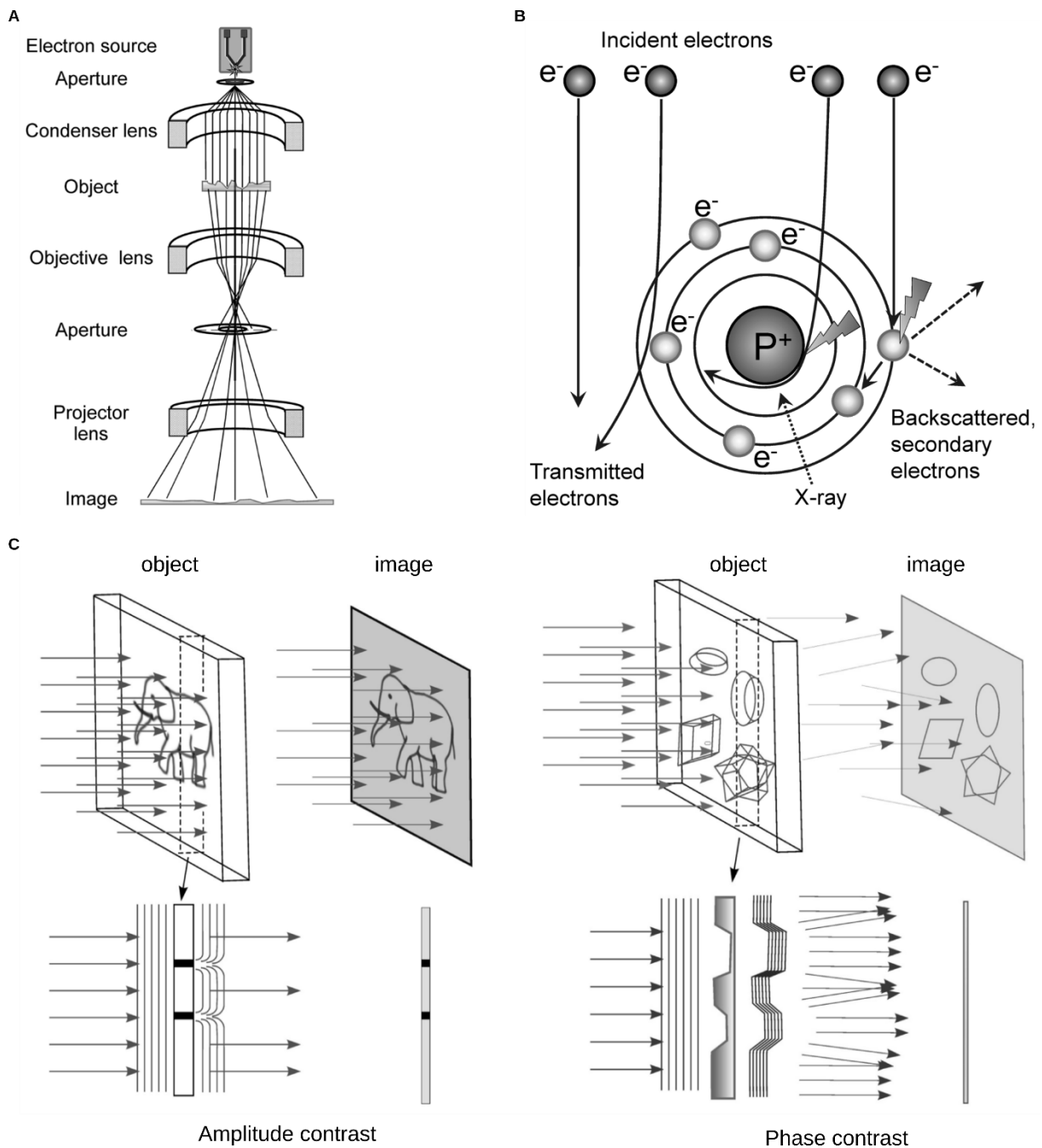


**Figure 19. Image formation in ME.** (A) Scheme of a simplified electron microscope. (B) Scheme of the different modes of interaction of the incident electrons with the specimen. From left to right, the electron can pass through the specimen without interacting with it; or can be deflected by the electron cloud without energy loss (elastic scattering); or interact with the nucleus or atomic electrons leading to energy loss (inelastic scattering). (C) Illustration of the amplitude (left) and phase (right) contrasts. The arrows represent the electron beam. For the amplitude contrast, a part of the incident beam is absorbed in the specimen, the intensity of the beam is changed. For the phase contrast, the wavefront is no more parallel but the intensity is not changed. Adapted from Orlova and Saibil, 2011.

### **3. Image processing principles for single-particle analysis**

Since the 2D images exhibit low contrast, it is necessary to collect thousands of images in order to average the similar images of the specimen to increase the signal over noise and then perform alignment of them (Frank, 1975).

The image processing for determining the 3D structure of a macromolecule by single particle analysis consists of three major steps, the pre-processing, the processing itself and the refinement and model building.

First, the pre-processing starts with the motion correction. As mentioned before, the beam-induced movements can be corrected, and the frames composing a movie can be realigned by correcting the global movement and the local movement of the particles in the frame (Li et al., 2013; Zivanov et al., 2019). The first frames of the movies, where the beam-induced movement may be too important to be corrected, are usually removed (leading to information loss because the first frames contain high-resolution information since they undergo less radiation damage). The result of the alignment of all the frames of the movie is the micrograph where the high frequencies were restored by the motion correction. A filter is also applied to the movie frames so that the first frames containing the high-resolution information have more weight in the reconstruction without removing the last images that have undergone radiation damage but still exhibit lower-resolution information (Grant and Grigorieff, 2015).

Once the frames of the movies are re-aligned and combined to give the micrographs, the CTF estimation and correction can be done. The equivalent of the PSF in the reciprocal space is an oscillatory function called the contrast transfer function (CTF). The CTF of the imaging system illustrates how well the microscope translates phase fluctuations in the object into amplitude modulations in the image; it depends on the spacial frequency, the defocus, the wavelength of the incident electron, and the spherical aberrations of the objective lens. In practice, the wavelength of the incident electrons and the spherical aberration constant are known, so that only the defocus and the potential additional aberrations, such as the astigmatism of the optical system, remain to be determined. The defocus depends on the



position of the specimen in the microscope column, the more precisely this position can be estimated, the better the resolution of the reconstruction will be. CTF correction allows a partial recovery of the amplitude of spatial frequencies that were diminished in the micrograph (Rohou and Grigorieff, 2019).

The final step of the pre-processing is particle selection and extraction from the micrographs. Particle picking can be automated using cross-correlation between models and the micrograph. It is also possible to use a neural network-based program that can be trained for particle picking (Bepler et al., 2019; Tegunov and Cramer, 2018; Wagner et al., 2019).

The projection-slice theorem is the theoretical basis for the reconstruction of a 3D object from 2D projections. The projection-slice theorem states that in the reciprocal space, each 2D projection of an object corresponds to a central section in the 3D Fourier transform (FT) (Figure 20A). The section is oriented perpendicularly to the direction of the projection. In theory, by recording enough images of different projections of the object, it is possible to get access to the original structure by filling the 3D FT space with these differently oriented 2D FT slices. Moreover, if the object presents a symmetry, the number of views needed will be diminished compared to a non-symmetrical object because the symmetrical object in several different orientations offers the same projection (De Rosier and Klug, 1968) (Figure 20B).

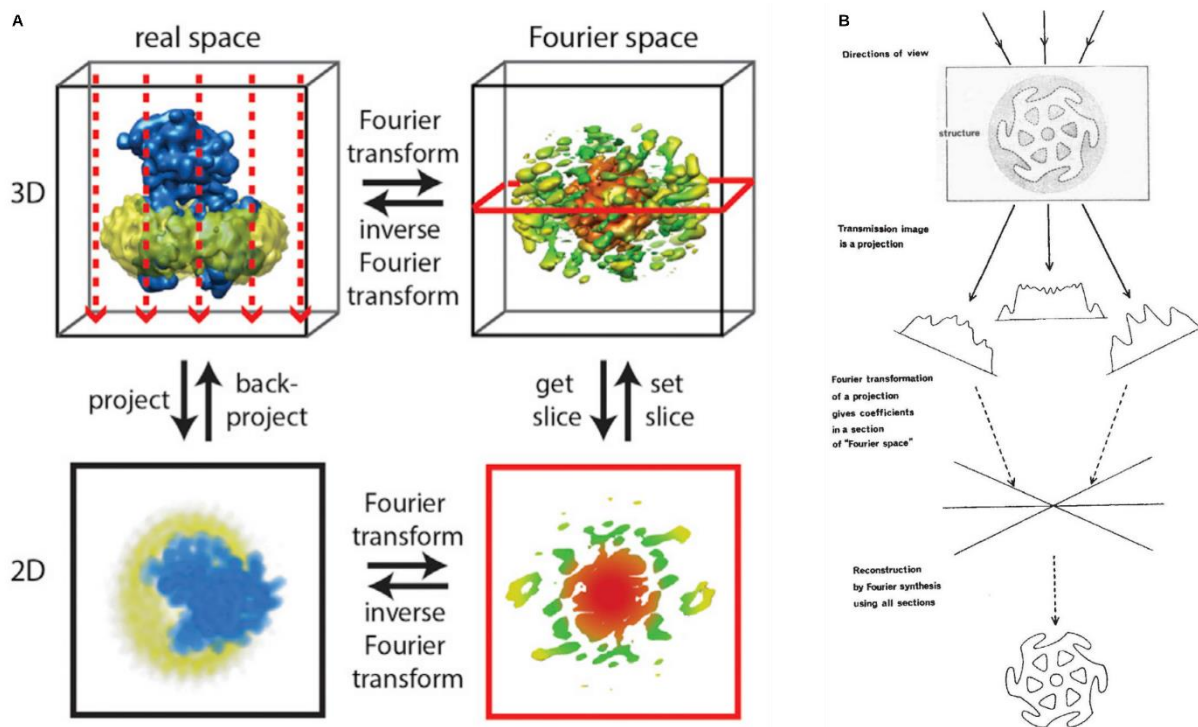


**Figure 20.** (A) Illustration of the projection-slice theorem. From Nogales and Scheres, 2015. (B) Illustration of the major steps for the reconstruction of a 3D object from the projections. From De Rosier and Klug, 1968.

Once the particles are extracted from the micrographs, the processing starts with their 2D classification. 2D classification assembles particles having the same orientations, and by averaging the particles in each class, the signal-to-noise ratio is increased. 2D classification also allows the cleaning of the data set by removing particles that are not well-defined or are false positives. 2D classification is usually done with algorithms using maximum likelihood classification.

The particles selected from the 2D classes are used to create the *ab initio* 3D model. Algorithms combining stochastic gradient descent and maximum likelihood greatly simplify and accelerate the *ab initio* 3D reconstruction and 3D classification (Punjani et al., 2017). From the initial 3D model, 3D refinement is performed using software which adopts a Bayesian approach (Scheres, 2012; Punjani et al., 2017). The 3D model will be refined, first by comparing

projections of the *ab initio* 3D model to the experimental images giving information about the relative orientation of the images. Each image is assigned to several projections with a different probability. Then, the images are recombined by back projection using the prior information and a new model is generated and used for the next iteration. At the last iteration, two sets of data are separated, refined independently and compared with the Fourier Shell Correlation (FSC) to evaluate the resolution of the final map (Chen et al., 2013). Of note, 3D classification can be used to separate two different states (or more) of a macromolecule from the same data set and obtain a 3D reconstruction for each one. Finally, the 3D map is used for pseudo-atomic or atomic model building and refinement.

#### 4. Reconstruction of helical objects

The biological helical object is constituted by the periodic repetition of a subunit along a unique axis. The helical symmetry can be described with two parameters, the pitch ( $P$ ), which is the distance between two subsequent turns (a rotation of 360 degrees on the  $z$  axis) and the rise ( $\Delta z$ ), which is the distance to go from one subunit to the next along the  $z$  axis. Starting with these two parameters, the helical twist ( $\Delta\phi$ ), which is the angle allowing the passage from one subunit to the next along the  $z$  axis, can be determined by dividing  $360^\circ$  by the number of subunits/turn (which is the pitch divided by the rise) (Figure 21).

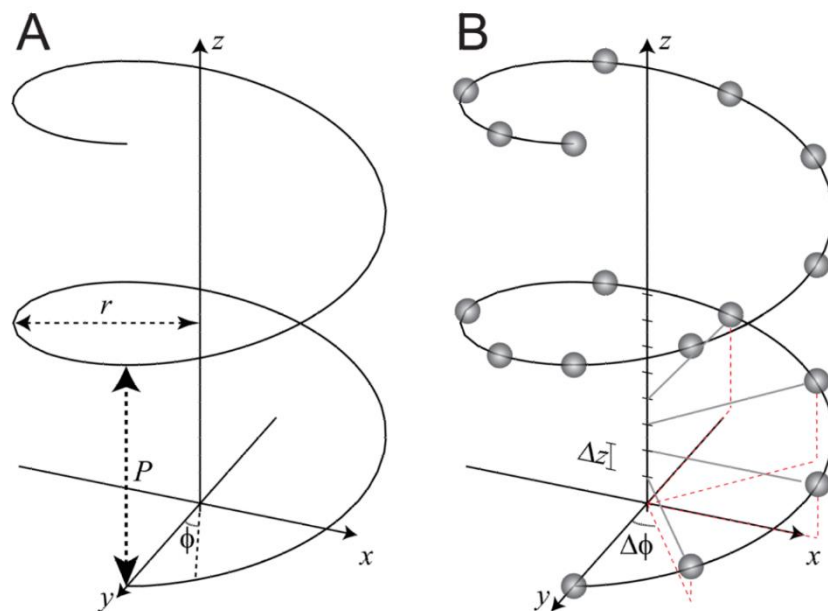


**Figure 21. Helix geometry.** (A) A continuous helix is defined by two parameters, the pitch ( $P$ ) and the radius ( $r$ ). (B) A helix composed of repeated subunits is characterised by the  $P$  and the rise  $\Delta z$ . The helical twist ( $\Delta\phi$ ) can be calculated,  $\Delta\phi = 360/(P/\Delta z)$ . The  $z$  axis corresponds to the axis of the helix. From Diaz et al., 2010.

The helical reconstruction and determination of the helical parameters are traditionally performed in Fourier space using the description of the FT of a helical object done by Cochran et al., 1952 and by Klug et al., 1958. By analysing the Fourier diffraction pattern of the helical object, consisting of layer lines that are the resultant of the periodic repetition of the subunit, it is possible to index the FT of the helix and determine the pitch and the rise of the helix. Current helical reconstruction procedures combine the determination of the helical parameters by layer line indexing with the classical single particle analysis approaches (Egelman, 2010). The helix is divided into segments that are extracted and then 2D classified. Indexation of the helical parameters is made on the FT of the images belonging to the same 2D class. However, this process is rarely precise, notably because the segments are tilted in the specimen or because of ambiguities in the helical symmetry. In order to validate the helical parameters estimated during the indexation, 3D reconstruction is performed. A high resolution 3D reconstruction with detailed side chains of amino acid will confirm the helical parameters determined earlier. Furthermore, now data processing software have implemented local research of the helical parameters to correct the uncertainty of the helical indexation (He and Scheres, 2017).

## 5. Cryo-electron tomography

A macromolecule structure obtained by single particle analysis is often insufficient to understand the overall mechanism of a protein, it misses the protein partners, and more generally the cellular environment; cryo-ET is a way to access that information. The workflow for tomography differs from the one of single particle analysis. First, the sample preparation is different, in cryo-ET sample preparation and optimisation can be a considerable bottleneck. To obtain the structure of macromolecules in their native environment, methods were developed to vitrify thicker material, such as eukaryotic cells that can be deposited or grown on EM grids, frozen and then sliced thin enough to be imaged. The method of choice to image the interior of the cell with limited deformation is cryo-FIB (focused ion beam) milling, allowing to create lamella from the cell. However, this method is quite time-consuming and requires special equipment. Furthermore, since only a part of the cells is retained in the lamella, the localisation of the region of interest can be hazardous. Thus, correlative light and electron microscopy can be used by integrating fluorescent labelling of proteins or regions of interest in the cells. The fluorescent signal is used to map the grid and guide the subsequent FIB milling on the designated regions (Klumpe et al., 2021).

Second, data collection differs because the sample will be recorded at different tilt angles. During the tilt series collection, the sample is usually tilted from  $-60$  to  $+60^\circ$  (Hagen et al., 2017; Turoňová et al., 2020), which results in a missing wedge of information in Fourier Space. The tomograms recorded at the highest angles present the lowest signal/noise ratio of the series because the electron path in the specimen is increased.

During the data processing, the tilt series are aligned for tomogram reconstruction. The defocus estimation is more complicated compared to single particle analysis because of the defocus variation in each image frame due to the sample tilt. Finally, sub-tomogram averaging can be performed when the tomograms contain a repeated protein or macromolecule that can be extracted as a 3D object and then treated as in single particle analysis, while taking into account the missing wedge (Castaño-Díez et al., 2012; Himes and Zhang, 2018; Tegunov et al., 2021; Tegunov and Cramer, 2018).



## Thesis goals

The NC is the template for the viral polymerase to transcribe the viral mRNAs and replicate the genome. The NC is the result of the oligomerisation of N along the entire genomic (or antigenomic) RNA, forming a helical N-RNA complex. In 2009, the structure of decameric N-RNA rings obtained upon expression of N in *E. coli* and encapsidation of short cellular RNA was solved by X-ray crystallography (Tawar et al., 2009), giving significant information about N-RNA association and N oligomerisation. In 2013, a low resolution ns-EM study of helical NC purified from insect cells resulted in a model of a left-handed NC helix, based on the lateral N-N interactions observed in the crystal structure of the N-RNA rings (Bakker et al., 2013). However, no high-resolution structure of the helical RSV NC is available, and the mechanisms involved in the control of the specific encapsidation of genomes and antigenomes remain unknown.

In this context, the global goal of my thesis was to obtain functional and structural information on the RSV NC. A better comprehension of the structure, assembly, and function of NCs should not only provide insight into the mechanism of virus replication, but should also pave the way for the development of new antiviral strategies.

My project was divided into two complementary parts: (i) the study of the role of RNA in the mechanisms driving its specific encapsidation by N, (ii) the determination of RSV NC structure by cryo-EM.

Concerning the first objective, the aim was (i) to obtain a monomeric, functional, and RNA-free N protein, in order (ii) to perform *in vitro* encapsidation assays and biochemical and biophysical characterisation of N-RNA complexes. This work was performed mostly during the two first years of my thesis, within the BMP team at the INRAE of Jouy-en-Josas for the major part, with the collaboration of the Chemical Biology and Nucleic Acid Chemistry group in the IBMM Montpellier, which provided all the synthetic RNAs used in the study, and with the Microscopic Imaging of Complex Assemblies (MICA) group in the IBS Grenoble who



characterised different assemblies by ns-EM. This study was published in August 2022 in the *Journal of Biological Chemistry*. Of note, during this period, I also tried to isolate monomeric N protein in order to solve the structure of the N<sup>0</sup> protein by X-ray crystallography, in collaboration with the Viral Replication Machines group at the IBS of Grenoble. However, we did not manage to obtain crystals of the protein.

The second objective of my PhD was to express the N protein in eukaryotic cells in order to purify NCs and solve their structure using cryo-EM, and obtain information on N-RNA assembly. This work allowed us to solve structures of four different N-RNA assemblies: helical NC, double-headed NC, ring-capped NC, and double-ring. A manuscript summarising this work is currently under review. The expression and purification of the N-RNA assemblies were performed within the BMP team, and the samples characterised by ns-EM by the MICA group to provide feedback required for sample optimisation. Once the sample preparation was optimised for cryo-EM, the data collection and processing were performed within the MICA group. During this period, I also had the opportunity to participate in the first attempts to visualise native RSV NC produced in infected cells using cryo-FIB milling and cryo-ET. This work was initiated at the Umeå Centre for Electron Microscopy in Sweden, during the last year of my thesis.

## Part II: Results

### Chapter I: Study of the specificity of RNA encapsidation by the nucleoprotein

#### 1. Introduction

The first challenge to perform *in vitro* RNA encapsidation assays is to isolate a monomeric N, that is stable, RNA-free, and competent for encapsidation. Indeed, the *Mononegavirales* nucleoproteins present a strong propensity to oligomerise and interact with RNA when overexpressed in recombinant systems. During the viral cycle, P is acting as a chaperone to maintain N in a monomeric form and deliver it to the nascent genome (or antigenome). Strategies to mimic this mechanism were used to isolate and purify N<sup>0</sup> (or N<sup>0</sup>-like) of several *Mononegavirales* viruses (Aggarwal et al., 2018; Dong et al., 2022; Guryanov et al., 2016; Kirchdoerfer et al., 2015; Leyrat et al., 2011; Milles et al., 2016; Renner et al., 2016; Yabukarski et al., 2014; Zhu et al., 2017).

Among *Mononegavirales*, *in vitro* RNA encapsidation by N was first studied for the VSV (*Rhabdoviridae* family) (Blumberg et al., 1983). This study revealed that a purified monomeric N can oligomerise alone or in presence of RNA to form nucleocapsid-like particles (NCLPs). Furthermore, they demonstrated that (i) the leader RNA sequence is preferentially encapsidated compared to other viral sequences, (ii) the presence of a 5' end methylated cap does not impair encapsidation, and (iii) the repetition of adenosines can promote encapsidation. Moyer and colleagues later showed that the minimal RNA length to trigger encapsidation was 10 nucleotides, and 19 nucleotides for optimal encapsidation (Moyer et al., 1991). They have also created NCLPs, by *in vitro* encapsidation, that could be used to synthesise a positive-sense RNA.

Measles N<sup>0</sup>-P complex (*Paramyxoviridae* family) was also purified and used for *in vitro* encapsidation assays (Milles et al., 2016). The authors demonstrated that the addition of a short 6-mer RNA (corresponding to the 5' end of the viral genome or a poly-adenosine RNA), induced the formation of NCLPs. The cryo-EM structures of those NCLPs were solved (Desfosses et al., 2019) giving insights into the RNA encapsidation mechanism, with (i) the N<sub>NTD</sub>

and N<sub>CTD</sub> undergoing significant reorientation from the N<sup>0</sup>-P complex to the NCLPs, and (ii) residues of N implicated in RNA encapsidation being identified.

Concerning RSV, different strategies were developed to stabilise N<sup>0</sup>, such as preventing the oligomerisation by truncating the N-terminal arm (El Omari *et al.*, 2008; Esneau *et al.*, 2019), mutating the amino acids that bind to RNA (Galloux *et al.*, 2015), or co-expressing N with a P fragment (Esneau *et al.*, 2019). These strategies allowed to gain information on the minimal domain of P required to stabilise N<sup>0</sup> (Galloux *et al.*, 2015) and on the structure of the complex in solution by SAXS (Esneau *et al.*, 2019). However, the study of RNA encapsidation by N requires purification of a non-mutated full-length N protein.

One of my PhD objectives was to isolate a recombinant full-length RSV N protein in order to investigate the role of RNA in the specificity of encapsidation. Five different constructions consisting in the fusion protein between N and the 40 first amino acids of P, associated with a histidine tag (HIS) and a TEV cleavage site were generated. The construct HIS-TEV-N-GSGSGSGS-P40, named N-P40, was selected for further analysis by RNA encapsidation assays.

Of note, in the course of this period, Gao and colleagues published a study on RNA encapsidation by the RSV N protein (Gao *et al.*, 2020). By co-expressing full-length N with the N-terminal part of P (residues 1-126), they managed to isolate a monomeric RNA-free N protein that was competent for *in vitro* RNA encapsidation. They demonstrate that a 7-mer was the minimal length to trigger the encapsidation when the sequence was a poly-adenosine. They also investigated the importance of the sequence of RNA for encapsidation and claimed that some positions are critical to trigger encapsidation; positions 1, 4, 5, and 6 may have more effect on N-RNA complex formation than positions 2, 3, and 7. Finally, they showed that *in vitro* encapsidation led to the formation of ring-like particles visible in ns-EM whatever the length of RNA used, and did not manage to form helical N-RNA complexes *in vitro*.

In this context, I further investigated the ability of RSV N to encapsidate RNA depending on RNA length and the 5' end modifications (Figure 22). In parallel, we also studied the importance of RNA encapsidation for the formation of RSV inclusion bodies *in vitro* (Figure 22). This work was published in August 2022 in the Journal of Biological Chemistry.

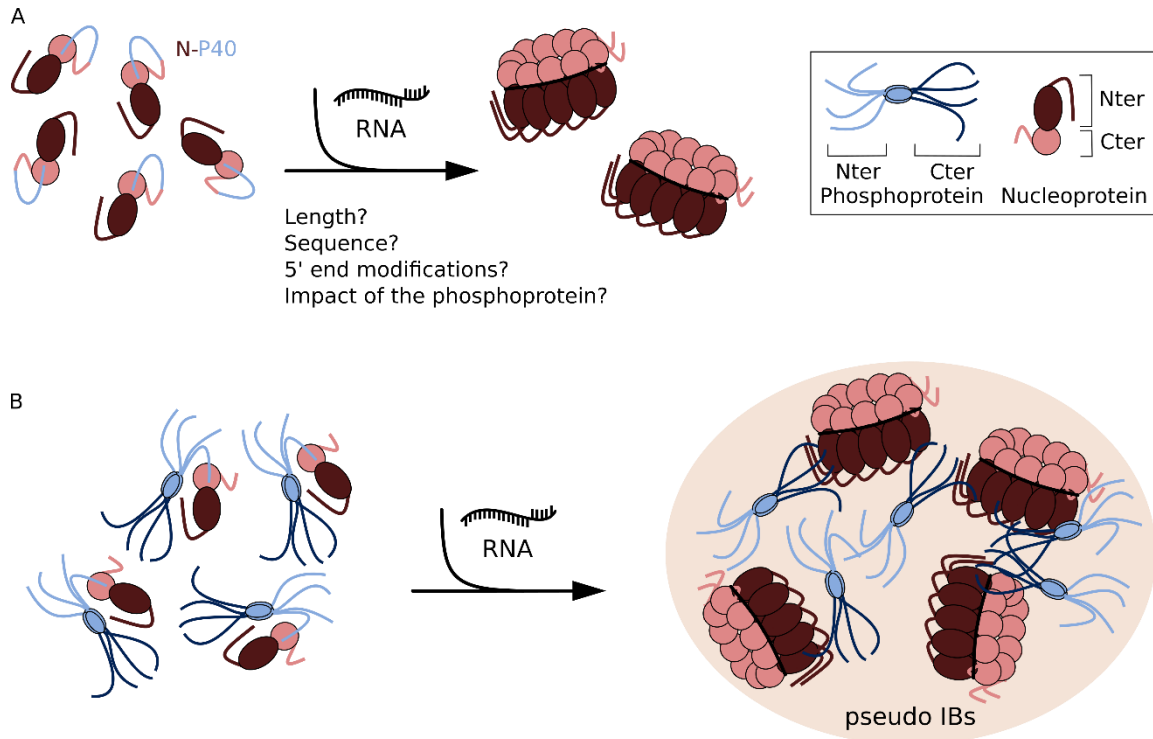


**Figure 22. Scheme of the study's problematic.** (A) Investigation of essential elements required to obtain stable RNA encapsidation by N. (B) Role of RNA encapsidation for *in vitro* formation of pseudo-IBs.

**2. Article 1: Importance of RNA length for *in vitro* encapsidation by the nucleoprotein of human respiratory syncytial virus**

# Importance of RNA length for *in vitro* encapsidation by the nucleoprotein of human respiratory syncytial virus

Received for publication, April 23, 2022, and in revised form, July 21, 2022. Published, Papers in Press, August 3, 2022.  
<https://doi.org/10.1016/j.jbc.2022.102337>

Lorène Gonnin<sup>1</sup>, Charles-Adrien Richard<sup>1</sup>, Irina Gutsche<sup>2</sup>, Didier Chevet<sup>1</sup>, Joris Troussier<sup>3</sup>, Jean-Jacques Vasseur<sup>3</sup>,  
Françoise Debart<sup>3</sup>, Jean-François Eléouët<sup>1,\*</sup>, and Marie Galloux<sup>1,\*</sup>

From the <sup>1</sup>INRAE, UVSQ, VIM, Université Paris-Saclay, Jouy-en-Josas, France; <sup>2</sup>CEA, CNRS, IBS, University of Grenoble Alpes, Grenoble, France; and <sup>3</sup>IBMM, ENSCM, CNRS, UMR, Université de Montpellier, Montpellier, France

Edited by Karin Musier-Forsyth

Respiratory syncytial virus has a negative-sense single-stranded RNA genome constitutively encapsidated by the viral nucleoprotein N, forming a helical nucleocapsid which is the template for viral transcription and replication by the viral polymerase L. Recruitment of L onto the nucleocapsid depends on the viral phosphoprotein P, which is an essential L cofactor. A prerequisite for genome and antigenome encapsidation is the presence of the monomeric, RNA-free, neosynthesized N protein, named N<sup>0</sup>. Stabilization of N<sup>0</sup> depends on the binding of the N-terminal residues of P to its surface, which prevents N oligomerization. However, the mechanism involved in the transition from N<sup>0</sup>-P to nucleocapsid assembly, and thus in the specificity of viral genome encapsidation, is still unknown. Furthermore, the specific role of N oligomerization and RNA in the morphogenesis of viral factories, where viral transcription and replication occur, have not been elucidated although the interaction between P and N complexed to RNA has been shown to be responsible for this process. Here, using a chimeric protein comprising N and the first 40 N-terminal residues of P, we succeeded in purifying a recombinant N<sup>0</sup>-like protein competent for RNA encapsidation *in vitro*. Our results showed the importance of RNA length for stable encapsidation and revealed that the nature of the 5' end of RNA does not explain the specificity of encapsidation. Finally, we showed that RNA encapsidation is crucial for the *in vitro* reconstitution of pseudo-viral factories. Together, our findings provide insight into respiratory syncytial virus viral genome encapsidation specificity.

The *Mononegavirales* order includes many human pathogenic viruses such as those responsible for rabies, measles, mumps, haemorrhagic fevers due to Ebola or Nipah viruses, and respiratory diseases induced by human respiratory syncytial virus (HRSV), metapneumovirus (HMPV), or parainfluenza viruses (1). All these viruses have a negative-sense single-stranded RNA genome that is constitutively encapsidated by the nucleoprotein N, forming the nucleocapsid (NC). This NC serves as a template for the viral polymerase L

responsible for both viral transcription and replication (2, 3). For the vast majority of these viruses, transcription and replication are cytoplasmic, occurring in viral factories which are viro-induced organelles called inclusion bodies (IBs) (4–8).

Among *Mononegavirales*, HRSV is the prototype of the *Pneumoviridae* family and the *Orthopneumovirus* genus (9, 10). HRSV is the most common cause of acute lower respiratory infections in young children worldwide (11–13). It is also recognized as a major cause of severe respiratory infections in immunocompromised and elderly people (14–16). Currently, no vaccine is available, and the only specific treatment against HRSV is prophylactic, consisting of injection of humanized monoclonal antibodies directed against the fusion protein F (palivizumab, Sinagis) (17). However, the efficacy of this treatment is controversial and its high cost limits its prescription to at-risk children. The HRSV genome is approximately 15.2 kb long and contains 10 genes encoding 11 proteins (2). Replication and transcription rely on 4 of these proteins: the RNA-dependent RNA polymerase L which exhibits all the enzymatic activities required for viral replication and transcription, its cofactor, the phosphoprotein P responsible for the recruitment of L on the NC, the nucleoprotein N involved in genome and antigenome encapsidation, and the transcription factor M2-1 that has been described as an “antiterminating” factor during transcription and interacts with P and viral mRNA.

During transcription, the polymerase L recognizes the leader sequence at the 3' end of the genome, and the polymerase is guided by the *gene start* (*gs*) and *gene end* (*ge*) sequences flanking each gene in the viral genome. The neosynthesized viral mRNAs are capped and methylated at the 5' end and polyadenylated at the 3' end by the polymerase. It is noteworthy that the synthesis of all viral mRNAs depends on the presence of the M2-1 protein, which is required for L processivity along the genome (18, 19). The mechanism of action of M2-1 is still poorly understood. However, it has recently been shown that RSV mRNAs concentrate with M2-1 in specific subcompartments of IBs called IBs-associated granules (8), suggesting that the M2-1–mRNA interaction may promote the release of mRNAs from the polymerase L.

On the contrary, replication of the viral genome only depends on L, P, and the NC. In that case, the polymerase

\* For correspondence: Marie Galloux, [marie.galloux@inrae.fr](mailto:marie.galloux@inrae.fr); Jean-François Eléouët, [jean-francois.eleouet@inrae.fr](mailto:jean-francois.eleouet@inrae.fr).

## RNA encapsidation by the RSV nucleoprotein

recognizes the *leader* or the *trailer* sequences at the 3' end of the genome or antigenome respectively, and the RNA synthesis starts at the first nucleotide and the polymerase proceeds through the *ge* and *gs* sequences to the end of the genome (or antigenome) (20, 21). Genomes and antigenomes, which have a triphosphate 5' end (22, 23), are directly encapsidated by the N protein during their synthesis, forming helical NC (24) which can both be incorporated in progeny virions (25, 26). Encapsidation of genome and antigenome thus prevents the formation of double strand RNAs but also their degradation as well as their detection by cellular sensors of the innate immune system. The structure of N expressed in *Escherichia coli* and purified as N-RNA rings composed of 10 protomers revealed that each N protomer interacts with 7 nucleotides (27). The RNA binds within a groove formed by the interface between the 2 globular domains of N ( $N_{\text{NTD}}$  and  $N_{\text{CTD}}$ ) that are separated by a flexible hinge region. The N protein also possesses 2 N- and C-terminal extensions (N- and C-arms) that are involved in N oligomerization: the N-arm of the  $N_i$  protomer binds to the  $N_{i-1}$  protomer, whereas the C-arm of  $N_i$  binds to the top of the  $N_{\text{CTD}}$  of the  $N_{i+1}$  protomer (24, 27). RNA encapsidation therefore depends on both direct interaction with RNA and the ability of N to oligomerize, 2 mechanisms that are closely coupled. When expressed alone, the *Mononegavirales* N proteins all show a strong tendency to encapsidate cellular RNAs. This implies that viral replication depends on the ability to maintain a pool of RNA-free monomeric N, termed  $N^0$ , available for the specific encapsidation of genomic and antigenomic RNAs. It is now well established that all these viruses share a common mechanism, with the neosynthesized N being maintained in the  $N^0$  form by P which acts as a molecular chaperone (28–36). Specifically for HRSV, and by analogy to the  $N^0$ -P complex of the HMPV whose crystal structure has been solved (31), the binding of the 28 N-terminal residues of P to the  $N_{\text{CTD}}$  surface overlaps with the binding sites of both the N- and C-arms of the  $N_{i+1}$  and  $N_{i-1}$  protomers in the oligomeric form, preventing self-oligomerization of N (30, 37). Notably,  $N^0$  is characterized by a rotation of  $N_{\text{NTD}}$  relative to  $N_{\text{CTD}}$  compared to the oligomeric form and a stacking of the C-terminal arm of N into the positively charged RNA groove that blocks RNA binding (30). However, the mechanism involved in the switch from  $N^0$  to N-RNA, which regulates specific encapsidation of genomes and antigenomes remains poorly characterized.

In addition to their critical role in viral polymerase function, N and P have been shown to be the scaffold proteins responsible for IBs morphogenesis (38, 39). It has recently been shown that IBs are liquid organelles formed by liquid-liquid phase separation induced by N–P interaction (39, 40). Importantly, the P protein (241 residues long), which forms tetramers through its central oligomerization domain (residues 131–151) flanked by highly disordered N- and C-terminal domains ( $P_{\text{NTD}}$  and  $P_{\text{CTD}}$  respectively) that are involved in multiple protein–protein interactions, plays a central role in regulating polymerase activity as well as in IBs formation. The  $P_{\text{NTD}}$  interacts with  $N^0$  (37), M2-1 (41), the cellular phosphatase PP1 (41), and the viral matrix protein M responsible

for virion assembly (42), whereas  $P_{\text{CTD}}$  is involved in the interaction with L (43, 44) and NC (45, 46) and is critical for IBs formation (39). Both the length of the  $P_{\text{CTD}}$  and its interaction with N complexed to RNA are required for efficient IBs morphogenesis. However, the importance of N oligomerization and of RNAs in the morphogenesis of IBs remains to be characterized.

In this study, we investigated the specificity of RNA encapsidation by HRSV N. Using a fusion protein between the full-length N and the peptide derived from the first 40 N-terminal residues of P (P40) responsible for chaperone activity on  $N^0$ , we managed to purify a recombinant monomeric and RNA-free N-P40 chimeric protein. The resulting N-P40 protein was competent for *in vitro* RNAs encapsidation, the length of RNAs being critical for stable oligomerization, and invariably leading to the formation of N-RNA rings under the conditions tested. Furthermore, using this N-P40 protein, we revealed that RNA encapsidation is critical for the morphogenesis of pseudo-IBs *in vitro*.

## Results

### Production of a $N^0$ -like recombinant protein

Recently, a strategy based on coexpression of  $P_{\text{NTD}}$  with His-tagged N in *E. coli* allowed the purification of a  $N^0$ - $P_{\text{NTD}}$  complex competent for encapsidation (47). Given the low affinity of P peptide for N (37), which could lead to the loss of peptide upon purification and thus to N aggregation, we chose here to use a strategy based on the expression of a fusion protein between His-tagged full-length N and the 40 N-terminal residues of P (P40) in *E. coli* (Fig. 1A). This approach was previously used to determine the crystal structure of the  $N^0$ -P complexes of HMPV (31), measles virus (34), and parainfluenza virus 5 (32). After purification of this chimeric protein in the presence of 1 M NaCl, the sample was analyzed by size-exclusion chromatography, following the absorbance at 260 and 280 nm, and compared to the profile of purified WT N ( $N_{\text{wt}}$ ) forming N-RNA rings (46). The elution profile of N-P40 showed 2 peaks (Fig. 1B). The major P1 peak with  $A_{260\text{nm}}/A_{280\text{nm}}$  ratio >1 and apparent mass of ~500 kDa (estimated from the Superdex 200 calibration profile), of slightly smaller size than N-RNA rings, that could correspond to N-RNA oligomers or aggregates. A minor P2 peak presented  $A_{260\text{nm}}/A_{280\text{nm}}$  ratio <1 and apparent mass of ~50 kDa, as expected for monomeric RNA-free N-P40 protein. The fractions of P1 or P2 peaks were pooled, and samples were analyzed by SDS-PAGE stained with Coomassie blue and by band shift assay on native agarose gel and compared to the sample corresponding to purified  $N_{\text{wt}}$ . As shown on Figure 1C (upper panel), as analyzed by SDS-PAGE, the presence of a single band with a molecular weight close to 45 kDa for  $N_{\text{wt}}$  sample and of 50 kDa for P1 and P2 peaks were observed, consistent with the expected mass of the  $N_{\text{wt}}$  and the N-P40 protein, respectively. On native agarose gel, the  $N_{\text{wt}}$  complexed to RNA and thus negatively charged clearly migrated within the gel. The N-P40 from the P1 peak migrated with a single band, close to the band observed for  $N_{\text{wt}}$ , suggesting that N-P40 could

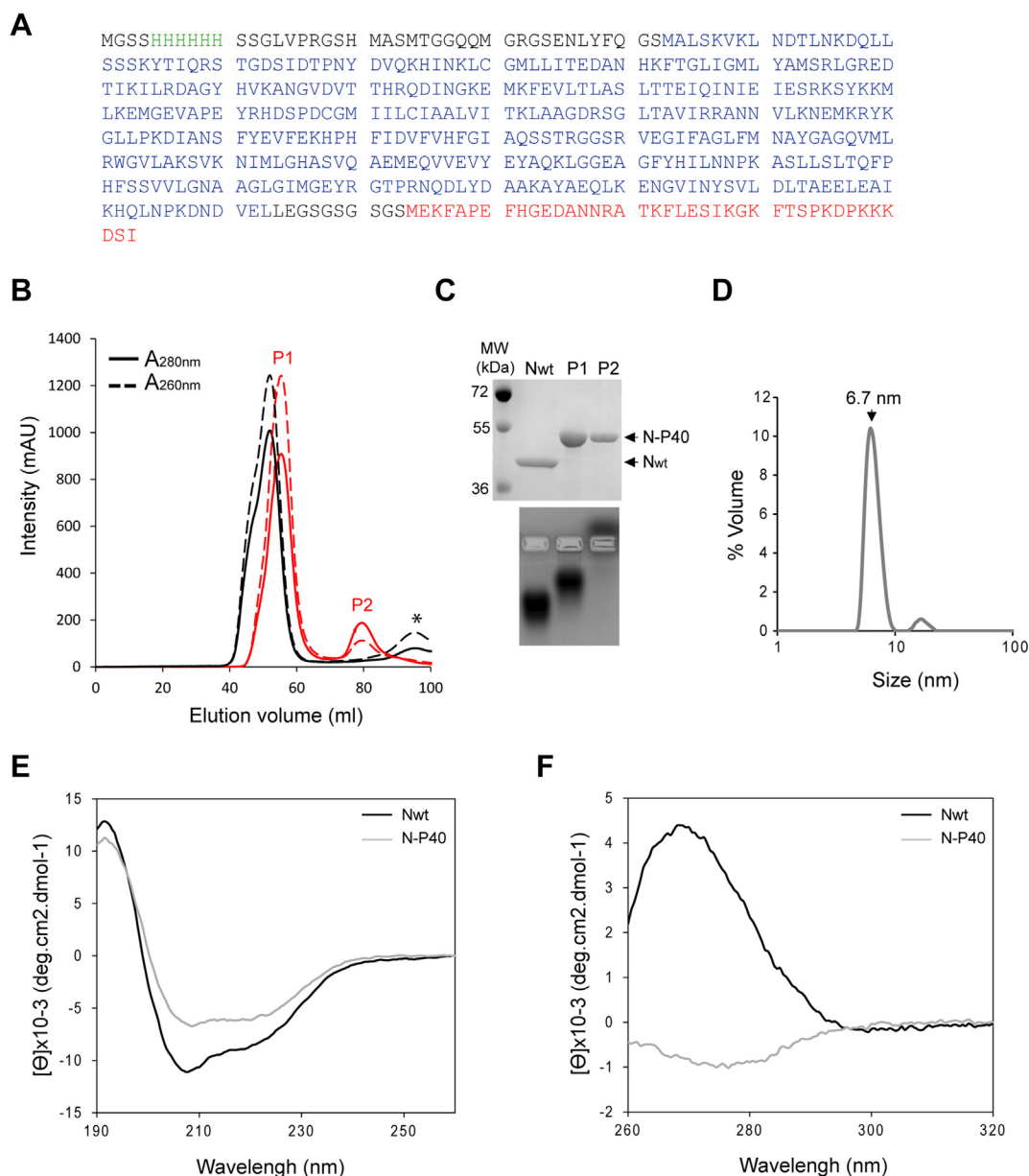


**Figure 1. Purification and characterization of recombinant N-P40 fusion protein.** *A*, amino acid sequence of the N-P40 fusion protein. The N-terminal 6xHis tag is in green, the N sequence is in blue, and the sequence of P40 is in red. Amino acids in black correspond to additional residues and linkers. *B*, gel filtration profile of purified N-P40 (red) and N<sub>wt</sub> (black). The curves corresponding to absorbance at 260 nm and 280 nm are presented as dash and solid lines, respectively. P1 and P2 indicate the 2 peaks detected for the gel filtration profile of N-P40. The asterisk indicates the peak corresponding to the C-terminal fragment of P used for N<sub>wt</sub> purification (46). *C*, the fractions corresponding to the peak of purified N<sub>wt</sub> and to the peaks P1 and P2 of the gel filtration profile of N-P40 were pooled, and the samples were analyzed by SDS-PAGE colored with Coomassie blue (upper panel) and by migration on native agarose gel (lower panel). *D*, dynamic light scattering (DLS) analysis of the N-P40 protein isolated from the gel filtration peak P2, showing a homogenous peak close to 6.7 nm, corresponding to N-P40 monomer and a minor peak of oligomers near 17 nm in diameter (Fig. 1D). *E* and *F*, far-UV (*E*) and near-UV CD (*F*) spectra of N<sub>wt</sub> corresponding to N-RNA rings in black and N-P40 in gray.

oligomerize as rings (Fig. 1C, lower panel). On the contrary, N-P40 from the P2 peak poorly migrated within the gel and in the opposite direction.

We then focused on the sample from P2 peak which was dialyzed to 300 mM NaCl and concentrated up to 1.5 mg/ml. Dynamic light scattering (DLS) analysis of the sample revealed the presence of a major protein peak near 6.7 nm in diameter that should correspond to monomers and a minor peak of oligomers near 17 nm in diameter (Fig. 1D). These data revealed that in our conditions, N-P40 tended to aggregate or

oligomerize upon concentration and led us to work with a protein concentration of 1 mg/ml. We finally analyzed the secondary and tertiary structures of N-P40 by circular dichroism (CD), using as previously N<sub>wt</sub> purified as N-RNA rings as a control. The far-UV spectra of both N-P40 and N<sub>wt</sub> showed peaks at 208 and 222 nm, typical of secondary structures with predominant  $\alpha$ -helical content (Fig. 1E). The peak intensity shift observed for N-P40 revealed a lower helical content than N<sub>wt</sub>. This observation correlates with the insertion of linkers in the N-P40 constructs, which are expected to



## RNA encapsidation by the RSV nucleoprotein

be unfolded. The near-UV CD allows the detection of signals from aromatic residues engaged in a rigid chiral environment, consistent with the presence of a tertiary structure. The detection of a broad signal around 280 nm for the N-P40 protein can be attributed to the signal from Tyr and Trp residues and validates that the protein has a tertiary structure (Fig. 1F). In comparison, the spectrum obtained for N<sub>wt</sub> revealed an intense positive signal between 260 and 280 nm, which can be attributed to the presence of RNA masking the signals from the aromatic residues of N.

Overall, these results show that N-P40 can be purified as a monomeric and RNA-free protein and that the fusion of P40 does not have a major impact on N folding. This latter observation correlates with previous results showing that binding of P40 to N does not induce major conformational changes in N (30).

### N-P40 is competent for encapsidation of RNAs

We then assessed the capacity of the N-P40 protein to encapsidate RNA *in vitro*. As each N<sub>wt</sub> protomer has been shown to interact with seven nucleotides within purified N-rings formed of 10 or 11 protomers (27), we first tested the ability of N-P40 to encapsidate a 70-nucleotide long (70-mer) RNA or DNA of similar sequence. The RNA sequence that we used was the antileader sequence (the 5' end of the antigenomic RNA), which is the initial RNA sequence synthesized by the polymerase using the genomic RNA as a template (Table 1). Encapsidation of RNA by N-P40 was analyzed using a band shift assay on native polyacrylamide and agarose gels, using N<sub>wt</sub> rings as a control. As shown in Figure 2A, while only slight migration was observed for purified N-P40, a clear band shift was observed when N-P40 was incubated with RNA. However, the protein seemed to poorly interact with DNA. In parallel, the samples were observed by negative stain electron

microscopy (ns-EM). As expected, images of N-P40 alone showed only very small species (Fig. 2C). While N-P40 incubated with 70-mer RNA formed ring-shaped N-RNA assemblies, only aggregates were observed for the sample of N-P40 incubated with DNA (Fig. 2C). These results suggest that, although N could interact with DNA, the affinity is not sufficient to allow the regular and constrained assembly of N on nucleotides, which, based on the crystal structure, implies twists on the ribose-phosphate chain (27). Using the same approach, we confirmed that N-P40 was also capable of encapsidating shorter 14-mer RNAs and forming N-RNA rings (Fig. 2, B and C). Furthermore, as the first nucleotides could initiate RNA encapsidation, we investigated the impact of substitutions of the 2 first nucleotides on the capacity of N to encapsidate 14-mer RNAs (Table 1). However, we observed that N-P40 similarly encapsidated 14-mer RNAs of different sequences (Fig. 2B), suggesting that the first nucleotides are not critical for starting RNA encapsidation.

Our results thus show that, although fused to N, the P40 peptide is not sufficient to prevent RNA encapsidation *in vitro*. Furthermore, while N-P40 specifically encapsidated RNAs over DNA, no specificity in RNA length was observed under the conditions tested. It is noteworthy that, as previously observed by Gao *et al.* (47), *in vitro* encapsidation of RNA did not result in the formation of helical NCs but only in N-RNA rings.

### Investigation of the minimal RNA length required for encapsidation

Using the same antileader sequence of HRSV, we further studied the minimal RNA length required for encapsidation, using 5- to 11-mer oligonucleotides (Table 1). As shown in Figure 3A, no band shift of N-P40 was detected on native polyacrylamide or agarose gels in the presence of 5- and 6-mer

**Table 1**  
RNAs sequences

RNAs length	5' end modification	RNA sequence <sup>a</sup>
70-mer <sup>b</sup>	OH	5'-ACGCGAAAAAAUAGCGUACAACAACUUGCAUAAACCAA AAAAUGGGGCAAAUAAGAAUUUGAUAAAGUAC-3'
14-mer (a)		5'-ACGCGAAAAAAUGC-3'
14-mer (b)		5'-GGGCGAAAAAAUGC-3'
14-mer (c)		5'-GUGCGAAAAAAUGC-3'
11-mer		5'-ACGCGAAAAAA-3'
10-mer		5'-ACGCGAAAAA-3'
9-mer		5'-ACGCGAAAA-3'
8-mer		5'-ACGCGAAA-3'
7-mer		5'-ACGCGAA-3'
6-mer		5'-ACGCGA-3'
5-mer		5'-ACGCG-3'
11-mer	PPP	5'-ACGCGAAAAAA-3'
10-mer		5'-ACGCGAAAAA-3'
9-mer		5'-ACGCGAAAA-3'
8-mer		5'-ACGCGAAA-3'
7-mer		5'-ACGCGAA-3'
11-mer	<sup>7m</sup> Gppp	5'-ACGCGAAAAAA-3'
10-mer		5'-ACGCGAAAAA-3'
9-mer		5'-ACGCGAAAA-3'
8-mer		5'-ACGCGAAA-3'
7-mer		5'-ACGCGAA-3'

<sup>a</sup> All the sequences correspond to HRSV antileader sequence except those of the 14-mer b and c indicated in italics.

<sup>b</sup> Corresponding 70-mer DNA was used in the study.

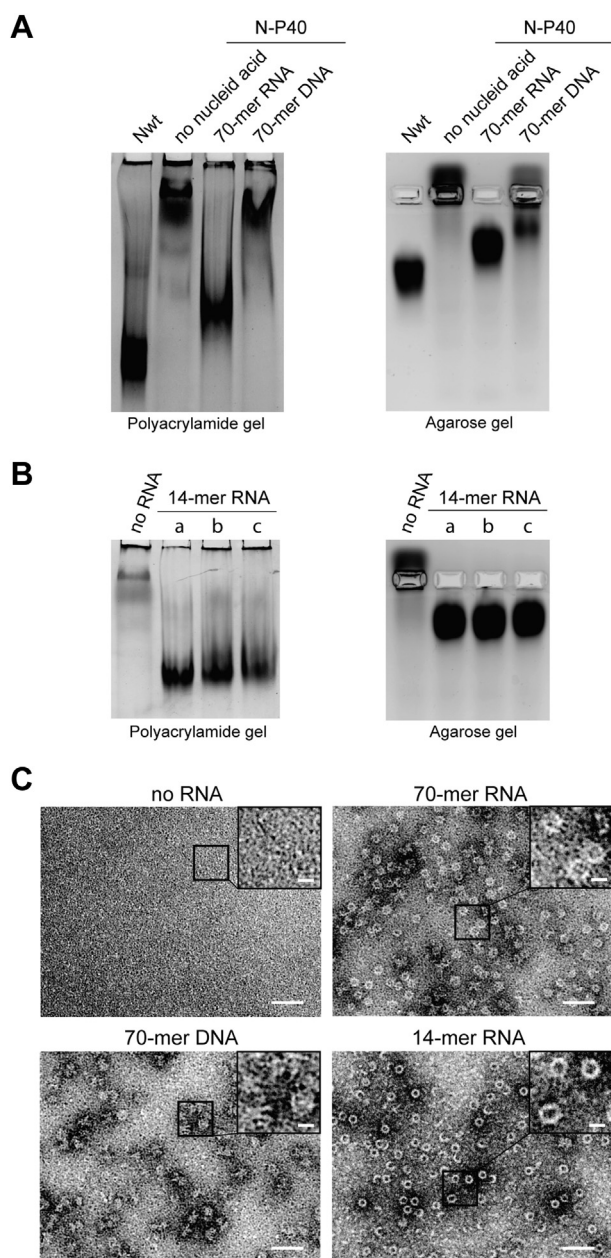


**Figure 2. The N-P40 fusion protein is competent for RNA encapsidation.** A, analysis of N-P40 migration alone or incubated in the presence of 70-mers RNA or DNA (see 70-mer sequence in Table 1) by native polyacrylamide (left) or agarose (right) gel electrophoresis. Polyacrylamide and agarose gels were stained with *Coomassie blue* or *amido black* respectively. N<sub>wt</sub> corresponds to purified recombinant RNA-N rings, used as control. B, analysis of 14-mer RNAs (see sequences Table 1) encapsidation by N-P40 on native polyacrylamide (left) or agarose (right) gels. C, images of N-P40 alone or incubated in the presence of 70-mer RNA, 70-mer DNA, or 14-mer RNA, as observed by ns-EM. The scale bar represents 50 nm. Magnifications of selected areas (indicated by black squares) are presented at the right top of each panel. The scale bar represents 10 nm. ns-EM, negative stain electron microscopy.

RNAs. Similar N-P40 band shifts were observed in the presence of 10- and 11-mer oligonucleotides compared with N-P40 incubated with 14-mer RNAs. Finally, intermediate band shift profiles were observed for N-P40 incubated in the presence of 7-, 8-, and 9-mer RNAs. Yet, according to ns-EM observations, incubation of N-P40 with 7-mer and 11-mer

RNAs both led to the formation of N-RNA rings, similar to the ones observed with the 14-mer and 70-mer RNAs (Fig. 3B). To clarify these results, we next investigated the stability of the N-P40–RNA complexes by incubating the samples overnight in the presence of RNase A followed by dialysis. Migration analysis of the samples on a native agarose gel showed no band shift for N-P40 incubated with 6- to 10-mer RNAs, suggesting RNA digestion, whereas a band shift was still observed for N-P40 in the presence of 11-mer and 14-mer RNAs (Fig. 3C), indicating that RNA was protected from digestion. Further analysis of the samples was performed by measuring the  $A_{260\text{nm}}/A_{280\text{nm}}$  ratio and by investigating structural changes of N-P40 by DLS and near-UV CD. Before RNase A treatment, all samples displayed an  $A_{260\text{nm}}/A_{280\text{nm}}$  ratio close to 1.2, similar to the value measured for N<sub>wt</sub> (Table 2). After RNase A treatment,  $A_{260\text{nm}}/A_{280\text{nm}}$  ratios were  $<1$  for N-P40 samples incubated with 6- to 10-mer RNAs (Table 2), validating RNA digestion upon RNase A treatment. Of note, the  $A_{260\text{nm}}/A_{280\text{nm}}$  ratio of these samples remained higher than that obtained for purified N-P40. For N-P40 incubated in the presence of 11- and 14-mer RNAs, the  $A_{260\text{nm}}/A_{280\text{nm}}$  ratios were close to 1. These data suggested that, although the RNAs were partially digested by RNase A, N-P40 was still associated with RNAs, preventing complete RNA degradation. In parallel, determination of the hydrodynamic diameter (Dh) of the samples by DLS revealed that N-P40 incubated in the presence of 6- to 10-mer RNAs displayed a Dh between 6.7 and 9 nm after RNase treatment, close to the Dh obtained under the same conditions for N-P40 alone, whereas those of N-P40 incubated with 11- and 14-mer RNAs were 14.2 and 14.4 nm, respectively, similar to the Dh of N<sub>wt</sub> (Table 2). Furthermore, the near-UV CD spectra showed that only the N-P40 sample incubated with 11-mer RNA exhibited a positive peak around 260 nm, whereas the spectra with 7- to 10-mer RNAs were similar to purified N-P40 alone or displayed only a weak signal around 260 nm (Fig. 3D). These data correlate with absorbance and Dh measurements, suggesting that RNase A treatment induced degradation of RNAs shorter than 11-nucleotides long and N rings disassembly.

Altogether, these results reveal that stable RNA encapsidation by N-P40 depends on RNA length, with the minimal length to stabilize N-P40–RNA complexes being 11-mer RNAs.

#### Impact of 5' end modification of RNAs on encapsidation

One of the differences between RNAs lies in post-transcriptional modifications, notably at the 5' end. Genomic and antigenomic RNAs have been described as having a 5' triphosphate (ppp) (22, 23), whereas viral mRNAs are capped and methylated by L during their synthesis (3). Therefore, we investigated whether posttranscriptional modifications of the 5' end of RNAs could impact the ability of N to encapsidate RNAs. Again, N-P40 was incubated in the presence of synthetic 7- to 11-mer RNAs with either a 5' ppp or a N7 and 2'-O methylated cap structure (<sup>7m</sup>Gppp) (Table 1), followed by native agarose gel electrophoresis

## RNA encapsidation by the RSV nucleoprotein

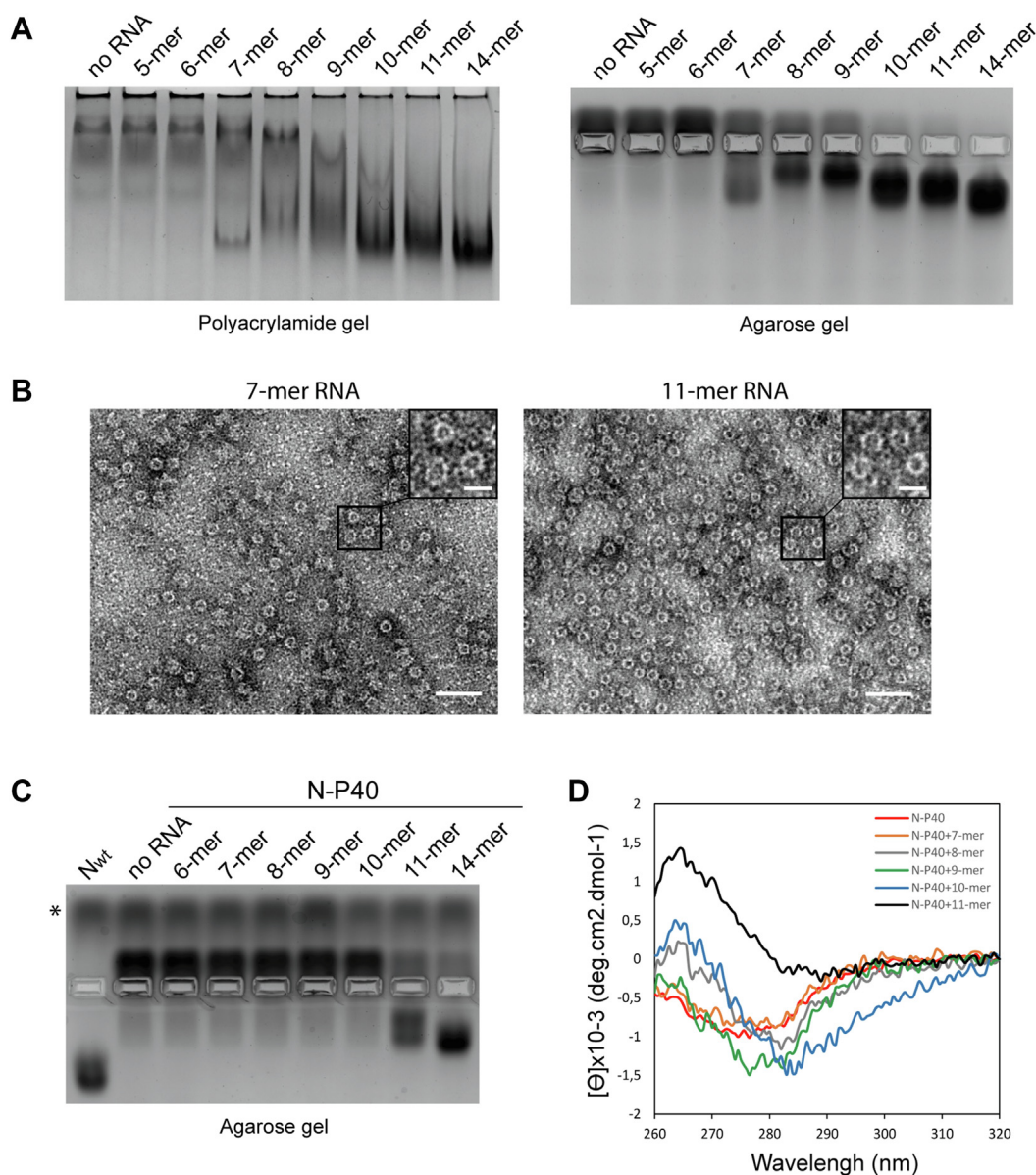


**Figure 3. Formation of stable RNA-N complexes by N-P40 depends on RNA length.** *A*, analysis of N-P40 migration alone or incubated in the presence of 5- to 11-mer RNAs, compared to 14-mer RNAs, by native polyacrylamide (*left*) or agarose (*right*) gel electrophoresis. Polyacrylamide and agarose gels were stained with *Coomassie blue* or *amido black* respectively. *B*, images of N-P40–RNA complexes formed upon incubation of N-P40 in the presence of 7- and 11-mer RNAs with 5' OH, as observed by ns-EM. The scale bar represents 50 nm. Magnifications of selected areas (indicated by *black squares*) are presented at the right top of each panel. The scale bar represents 20 nm. *C*, analysis of N-P40 migration alone or incubated in the presence of 5- to 11-mer RNAs, after treatment with RNase A, by native agarose gel electrophoresis. Gel was stained with *amido black*. The *asterisk* indicates the band corresponding to RNase A. *D*, near-UV CD spectra of N-P40 alone or incubated in the presence of 7- to 11-mer RNAs, after treatment with RNase A. ns-EM, negative stain electron microscopy.

analysis. Results showed that the presence of ppp or <sup>7m</sup>Gppp at the 5' end inhibited the ability of N to encapsidate 7- and 8-mer RNAs compared to 5' OH RNAs (Figs. 3A and 4A). However, N-P40 was still able to encapsidate 9-, 10-, and 11-mer RNAs, and no difference was observed between 5' end ppp or capped RNAs. Interestingly, independently of the length and the capping of the RNAs, N-P40–RNA rings could always be detected by ns-EM (Fig. 4B), suggesting that this method of observation may stabilize ring-shaped assemblies and highlights the importance of using multiple complementary techniques for the analysis of RNA encapsidation by N.

One more time, we investigated the impact of RNAs' 5' end modification on the stability of N-P40-11-mer RNA complexes upon RNase A treatment. Surprisingly, although band shifts were still observed (Fig. 4C), N-P40 samples incubated with 5' ppp and 5' <sup>7m</sup>Gppp RNAs displayed  $A_{260\text{nm}}/A_{280\text{nm}}$  ratios of 0.9 and 1, respectively, and DLS analysis revealed the presence of different populations (not shown). Furthermore, while the near-UV CD spectrum of N-P40 incubated with 5' <sup>7m</sup>Gppp RNAs was similar to the spectrum of N-P40 complexed with 5'OH RNA, the spectrum of N-P40 incubated with 5' ppp RNAs clearly differed from those of N-P40 alone or incubated with 5' OH RNAs (Fig. 4D).



**Table 2**  
Characterization of 5' OH RNA–N-P40 complexes after RNase A treatment

Proteins and RNAs	A <sub>260nm</sub> /A <sub>280nm</sub>	Dh (nm) <sup>a</sup>
Nwt <sup>b</sup>	1.24	15.75
N-P40	0.67	7.9
N-P40 + 6-mer RNA	0.79	8.9
N-P40 + 7-mer RNA	0.9	8.7
N-P40 + 8-mer RNA	0.88	6.7
N-P40 + 9-mer RNA	0.87	7.6
N-P40 + 10-mer RNA	0.94	9
N-P40 + 11-mer RNA	1.03	14.2
N-P40 + 14-mer RNA	1	14.4

<sup>a</sup> Hydrodynamic diameter determined by DLS. Data representative of 2 independent experiments.

<sup>b</sup> Purified as N-RNA rings.

These results revealed that modification of the 5' end of RNAs only partially impairs encapsidation but is not a critical factor for the specificity of encapsidation, 5' end modifications delay RNAs encapsidation maybe by creating steric hindrance.

### Impact of full-length P protein on the stability of RNAs encapsidation

As our results were obtained in the presence of only a short peptide of P, we then assessed if full-length P protein could modulate the stability of RNAs encapsidation. By analysis on native agarose gel, we first showed that coincubation of P with N-P40 allowed to observe the formation of a complex, revealing that P was able to interact with N-P40, although this interaction appeared weak compared to the interaction between P and N<sub>w<sub>t</sub></sub> (Fig. 5A). This result suggests that P could bind to N either by displacing P40 binding on N or through the binding of the C-terminal extremity of P on N<sub>NTD</sub>. In the presence of 14-mer RNA, a band of strong intensity, similar to the band observed in presence of N<sub>w<sub>t</sub></sub>, was observed, showing that P does not prevent RNA encapsidation by N-P40. We therefore studied the impact of P on encapsidation depending on RNA length. As previously, no band shift was detected in the presence of 5- and 6-mers. In the presence of 7- to 9-mers, a band of weak intensity migrating slightly faster and at the same level than the bands of strong intensity observed in the presence of 10-, 11-, and 14-mers was observed (Fig. 5B, upper panel). These data reveal that in the presence of RNA, the full-length P does not improve the stability of the monomeric N compared to the P40 peptide. Of note, upon treatment with RNase A, the band observed in the presence of 8- and 9-mers was not detected, and a clear decrease of intensity of the band observed in the presence of 10-mer RNA was observed (Fig. 5B, lower panel). Finally, in the presence of 5' end ppp or 7<sup>m</sup>Gppp RNAs, a band of strong intensity was observed only in the presence of 11-mer RNAs.

Altogether, these results reveal that the presence of P does not drastically impact RNA encapsidation or the stability of the oligomers.

### Role of RNA encapsidation on pseudo-IBs morphogenesis in vitro

We have previously shown that *in vitro* coincubation of purified recombinant fluorescent N-RNA rings (mCherry-N<sub>w<sub>t</sub></sub>)

with P can lead to the formation of liquid droplets that exhibit properties similar to cellular IBs formed during infection. We also identified the key properties of P required for pseudo-IBs morphogenesis, that is, oligomerization, P<sub>CTD</sub> length and flexibility, and interaction of the C-terminus of P with N (39). However, this study did not decipher the role of N oligomerization and of the presence of RNAs in this process. Furthermore, although our data suggested that the N/P ratio maybe important for optimal IBs formation, these results remained preliminary, and a systematic study of the impact of N/P ratio and concentration on the morphogenesis of IBs was missing. As phase separation is known to be facilitated by increased protein concentration (48–52), we here decided to limit the protein concentrations to avoid spontaneous pseudo-IBs formation. Using a fixed minimum concentration of 3.5 μM for mCherry-N<sub>w<sub>t</sub></sub> or P, the addition of the second partner at a 1:1 ratio allowed us to observe the formation of small droplets of 1 to 5 μm in diameter (Fig. 6). A fixed low P concentration limited the size and number of droplets that remained similar whatever the concentration of mCherry-N (Fig. 6A). On the other hand, in a fixed low N concentration condition, the number and size of droplets increased proportionally to the addition of P until reaching a plateau for a P/N ratio ≥4 (Fig. 6B). These results correlate with our previous observations (39) but also revealed that P concentration is a limiting factor for IBs formation.

To study the impact of N-P40 oligomerization in the presence of RNAs on pseudo-IBs morphogenesis, we then investigated whether pseudo-IBs could form when N-P40 was incubated with a 70-mer RNA in the presence of P-BFP. Since no droplets were observed with a 3 μM concentration of N-P40 in the presence of an excess of P-BFP (15 μM) and 70-mer RNA at 50 μM, we then screened for the optimal conditions allowing pseudo-IBs formation, with a minimum concentration of proteins. Pseudo-IBs of 10 to 15 μm in diameter were observed in the presence of 3.5 μM of P-BFP, 70-mer RNAs (50 μM), and a minimum of 4-fold excess of N-P40 (13.5 μM). Of note, pseudo-IBs of only 2 to 3 μm in diameter were observed when coincubating P-BFP with N<sub>w<sub>t</sub></sub> (RNA-N rings) in the same conditions (Fig. 7A). It is noteworthy that no droplets were detected when incubating P-BFP in the presence of either RNAs or N-P40 alone (Fig. 7A). We then assessed the impact of RNA length on pseudo-IBs morphogenesis by incubating N-P40 with RNAs of various lengths before the addition of P-BFP, under the same conditions. As shown in Figure 7B, the addition of 14-mer RNA resulted in the formation of droplets similar to those observed in the presence of 70-mer RNA. More interestingly, droplet size decreased when N-P40 was incubated with 11-mer and 8-mer RNAs, and only aggregates were observed in the presence of 6-mer RNA. Furthermore, whereas RNase A treatment of N-P40 incubated with 11-mer RNA still allowed to observe droplets, only aggregates were detected for the sample with 8-mer RNA (Fig. 7C). This result correlates with data showing the instability of N oligomerization in the presence of short RNAs. Finally, pseudo-IBs similar to those obtained in the presence of

## RNA encapsidation by the RSV nucleoprotein

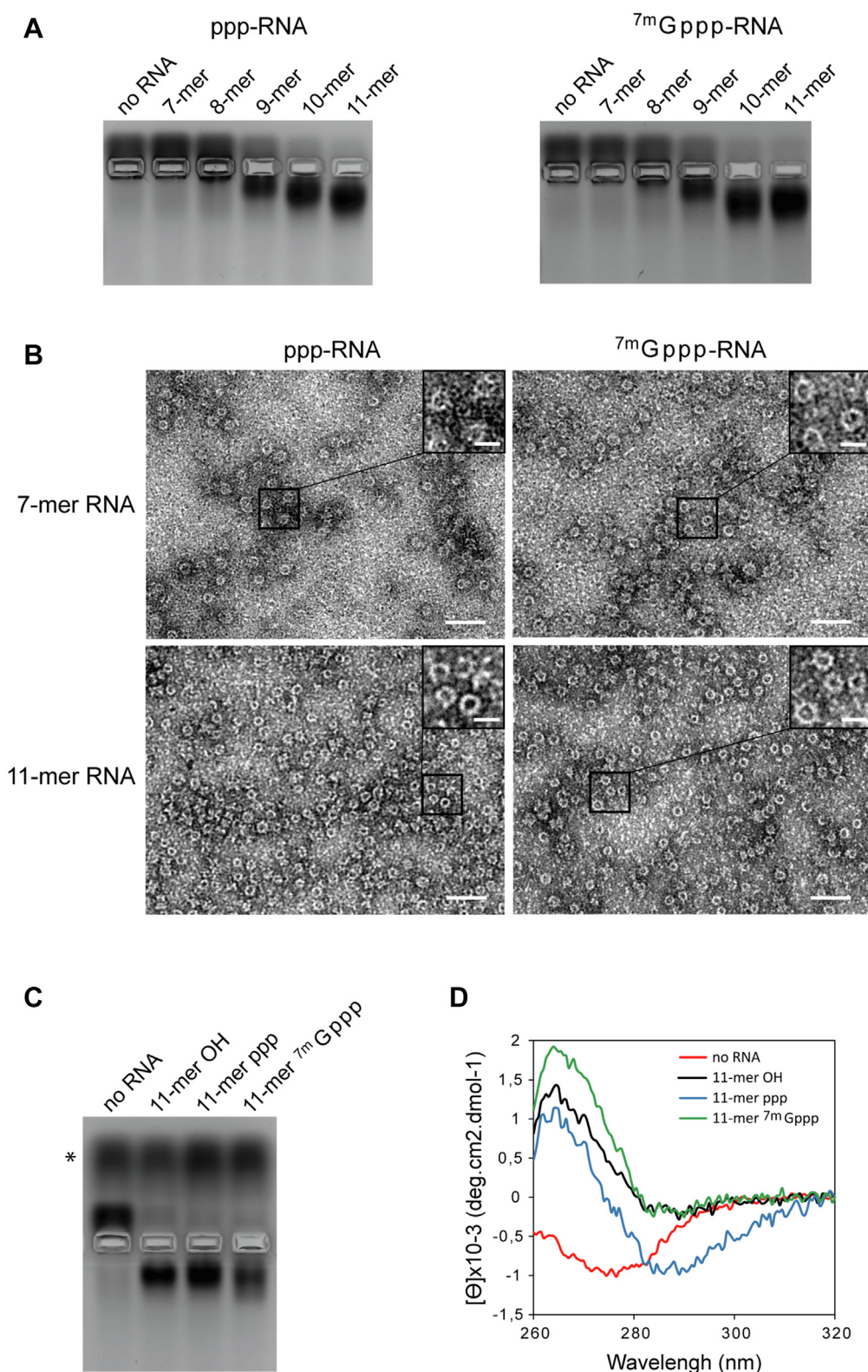


**Figure 4. Impact of RNA 5' end modifications on the ability of N-P40 to encapsidate RNAs.** *A*, analysis of N-P40 migration alone or incubated in the presence of 7- to 11-mer RNAs with 5' ppp (left) or 5'<sup>m</sup>Gppp (right) by native agarose gel electrophoresis. Gels were stained with *amido black*. *B*, images of N-P40-RNA complexes formed upon incubation of N-P40 in the presence of 7- and 11-mer RNAs with 5' ppp or 5'<sup>m</sup>Gppp, as observed by ns-EM. The scale bar represents 50 nm. Magnifications of selected areas (indicated by *black squares*) are presented at the right top of each panel. The scale bar represents 20 nm. *C*, comparison of the migration of N-P40 alone or incubated in the presence of 11-mer RNAs with 5' OH, ppp, or  $7^m$ Gppp after RNase A treatment by native agarose gel electrophoresis, gel stained with *amido black*. *D*, near-UV CD spectra of N-P40 alone or incubated in the presence of 11-mer RNAs with 5' OH, ppp, or  $7^m$ Gppp after RNase A treatment. ns-EM, negative stain electron microscopy.

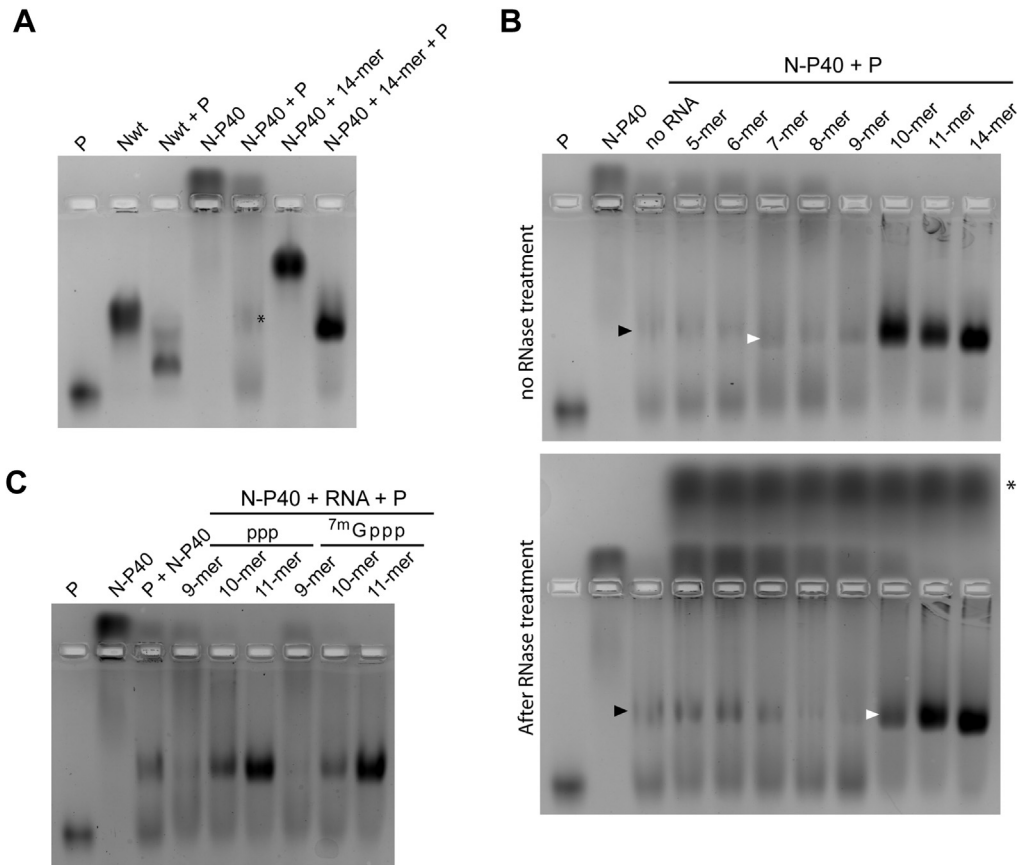


**Figure 5. Impact of full-length P on the stability of RNA encapsidation.** A, migration on native agarose gel of P, N<sub>wt</sub> or N-P40 in the absence or presence of 14-mer RNA alone or coincubated in the absence or the presence of 14-mer RNA. The *asterisk* indicates the band corresponding to P–N-P40 complex migration. B and C, analysis by native agarose gel electrophoresis of P and N-P40 migration alone or incubated in the presence of 7- to 11-mer RNAs (B) before (*upper panel*) or after treatment (*lower panel*) by RNase A or with 9- to 11-mer RNAs displaying 5' ppp or 7<sup>m</sup>Gppp (C). The *black* and *white* arrows indicate the bands corresponding the migration of P–N-P40 and P–N-P40–RNA complexes, respectively. The *asterisk* indicates the band corresponding to RNase A.

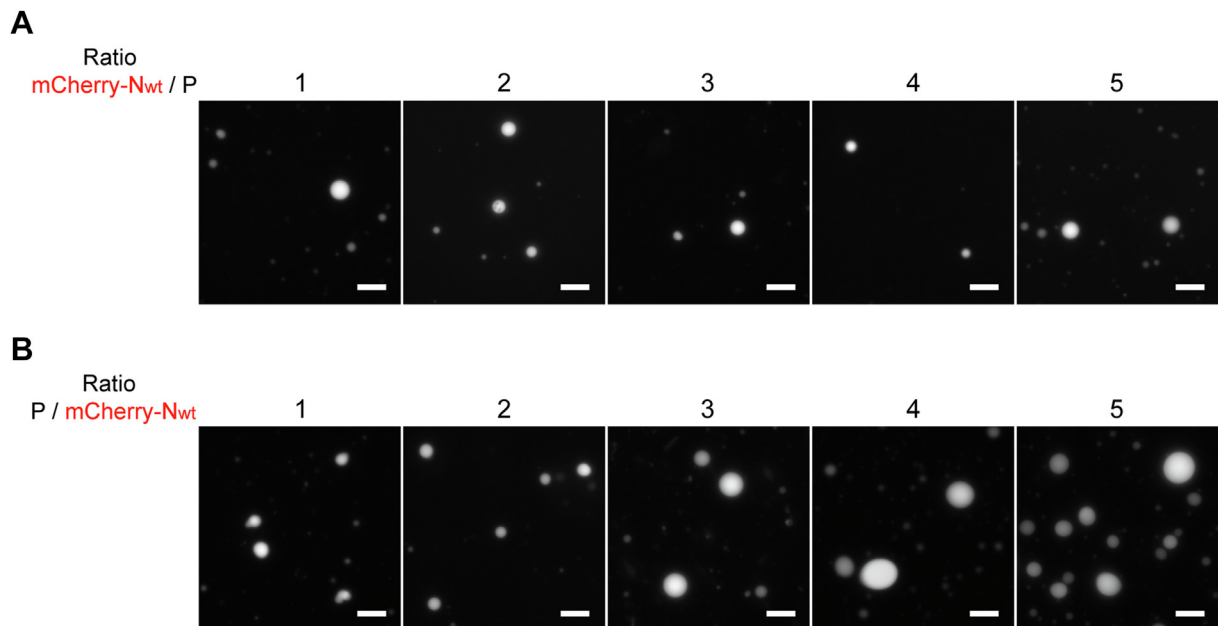


**Figure 6. Impact of N<sub>wt</sub> and P concentration and ratio on pseudo-IBs formation.** Recombinant mCherry-N<sub>wt</sub> (corresponding to mCherry-N-RNA rings) and P proteins were coincubated in the presence of 15% Ficoll and the formation of droplets was observed by fluorescence microscopy. A, P concentration was fixed to 3.5 μM, and mCherry-N<sub>wt</sub> was added up to a ratio mCherry-N<sub>wt</sub>/P of 5; B, mCherry-N<sub>wt</sub> concentration was fixed to 3.5 μM, and P concentration increased up to a ratio P/mCherry-N<sub>wt</sub> of 5. The scale bar represents 10 μm. IB, inclusion body.



## RNA encapsidation by the RSV nucleoprotein

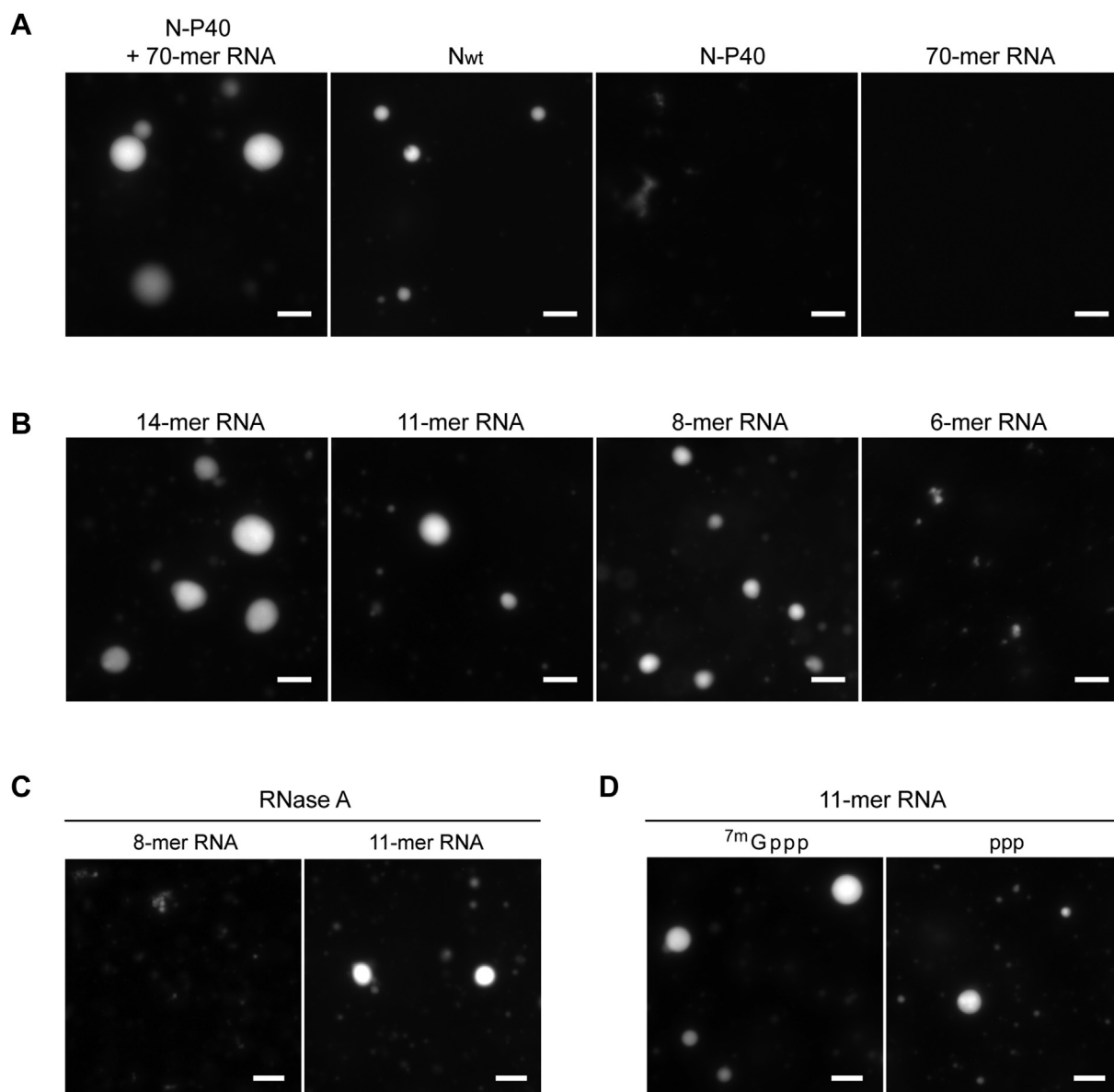


**Figure 7. N oligomerization is needed for the formation of pseudo-IBs.** *A*, recombinant P-BFP (3.5  $\mu\text{M}$ ) was incubated in the presence of either N-P40 preincubated with 70-mer RNA (13.5 and 50  $\mu\text{M}$ , respectively), N<sub>wt</sub> (13.5  $\mu\text{M}$ ), N-P40 (13.5  $\mu\text{M}$ ), or 70-mer RNA (50  $\mu\text{M}$ ). *B*, recombinant P-BFP (3.5  $\mu\text{M}$ ) was incubated in the presence of N-P40 (13.5  $\mu\text{M}$ ) preincubated with 14-mer, 11-mer (5' end OH), 8-mer, or 6-mer RNAs (50  $\mu\text{M}$ ). *C*, recombinant P-BFP (3.5  $\mu\text{M}$ ) was incubated in the presence of N-P40 (13.5  $\mu\text{M}$ ) preincubated with 8-mer and 11-mer RNAs (50  $\mu\text{M}$ ) followed by treatment with RNase A. *D*, recombinant P-BFP (3.5  $\mu\text{M}$ ) was incubated in the presence of N-P40 (13.5  $\mu\text{M}$ ) preincubated with 5' ppp or <sup>7m</sup>Gppp 11-mer RNAs (50  $\mu\text{M}$ ). For each condition, the formation of droplets was analyzed by fluorescence microscopy. The scale bar represents 10  $\mu\text{m}$ . IB, inclusion body.

11-mer RNA with 5' OH were observed in the presence of 11-mer RNAs with 5' ppp and <sup>7m</sup>Gppp (Fig. 7D).

Altogether, our data revealed that coincubation of P with monomeric N does not allow pseudo-IBs morphogenesis *in vitro*, and that the addition of short RNAs is not sufficient to induce phase separation. Overall, these results showed that N oligomerization in the presence of RNA is critical for the morphogenesis of pseudo-IBs.

### Discussion

Like for the majority of viruses belonging to the *Mono-negavirales* order, HRSV replication and transcription take place within cytoplasmic viral factories called IBs that

concentrate the viral and cellular proteins required for these activities, as well as neosynthesized antigenomic and genomic RNAs and viral mRNAs. Replication leads to the synthesis and amplification of full-length negative-sense genomic and positive sense antigenomic RNAs, which are encapsidated by N in its RNA-free form N<sup>0</sup>, forming the so-called NCs, in contrast to viral mRNAs. This specificity of encapsidation of viral genomes and antigenomes by N remains unexplained. Given the strong tendency of N<sup>0</sup> to oligomerize on RNAs, some particular mechanisms might regulate the specificity of viral RNA encapsidation and thus the transition from N<sup>0</sup> to N-RNA. The aim of this work was to investigate whether specificity of encapsidation could be explained either by the sequence or the nature of the 5' end of RNAs. Here, using a chimeric protein

composed of full-length N and P40, a peptide corresponding to the 40 N-terminal residues of P, we showed that this construct is competent for RNA encapsidation *in vitro*, even in the presence of full-length P protein. This first observation shows that P is not sufficient to prevent RNA encapsidation by N, suggesting the existence of another factor that could regulate the transition from monomeric N<sup>0</sup> to N-RNA assembly in infected cells, most likely by enhancing the stability of N<sup>0</sup>. In agreement with a recent publication by Gao *et al.* (47), our results also confirmed that RNA as short as 7-mer can be encapsidated, and that N oligomerization on RNAs always leads to the formation of N-RNA rings *in vitro*. We showed that the minimum length for stable encapsidation was 11 nucleotides, revealing that RNA length is critical for the stability of N-RNA oligomers. However, we cannot exclude that the presence of P40 fused to the C-terminus of N may partially alter N oligomerization. In contrast to measles virus for which helical NC can form *in vitro* using recombinant N protein and 6-mer RNAs (4), our data suggest that additional factors such as viral or cellular partners or posttranslational modifications maybe required for proper HRSV N oligomerization along RNA to obtain helical NCs.

Currently, the specificity of encapsidation of viral genomic and antigenomic RNAs by N is unknown. The difference between the 5' ends of mRNAs (capped) and genomic and antigenomic RNAs (ppp) could explain this mechanism. However, we found that the presence of either ppp or <sup>7m</sup>Gppp at the 5' end instead of OH only partially impedes the ability of N to encapsidate RNAs, most probably by creating steric hindrance. In light of the recent discovery of subcompartments called IBs-associated granules within IBs, that specifically concentrate M2-1 and viral mRNA (8), we hypothesize that the exclusion of viral mRNA complexed to M2-1 from the polymerase complex could contribute, at least in part, to the segregation of mRNAs and thereby specificity of genome encapsidation by N. Our study highlighted the absence of encapsidation of short 5' ppp RNAs. This observation suggests that the 5' ppp end of genomes and antigenomes should be exposed and detected by sensors of the cellular innate immune system such as RIG-I. Recently, cryo-EM studies of Newcastle disease virus, Sendai, Nipah, and cetacean morbillivirus have revealed heterogeneity in NC assembly, with the presence of double-headed helical structures (53–56). Such an assembly could hide the 5' end of antigenomes and genomes, thus preventing 5' ppp detection by cellular sensors. However, further investigation will be needed to decipher the accessibility and protection of the 5' end of viral genomes.

Finally, we investigated the importance of P, N oligomerization, and RNAs in the morphogenesis of pseudo-IBs *in vitro*. The tetrameric RSV P protein has intrinsically disordered regions involved in multiple transient interactions known to be critical for phase separation and is a major scaffolding component of IBs (39). When P was mixed with a monomeric N<sup>0</sup>-like protein (N-P40) and RNAs are too short to be encapsidated, no phase separation was observed, indicating that the presence of RNA-N oligomers is critical for pseudo-

IBs formation. Interestingly, the length of encapsidated RNAs seems to modulate the size of pseudo-IBs. These observations correlate with the fact that RNAs have been shown to play a major role in liquid-liquid phase separation mechanisms (49, 50). Further characterization of IBs morphogenesis in the presence of RSV helical NC should be of great interest, as the size and high flexibility of these structures could modulate IBs morphogenesis. A recent cryo-electron tomography study of RSV-infected cells has revealed the presence of N rings in filamentous RSV particles (57), showing for the first time the heterogeneity of N assembly in the cell. The role of these structures during viral cycle, that is, IBs morphogenesis, control of the innate immune response to infection, and virion assembly remains to be determined.

## Experimental procedures

### Plasmid constructs

The gene sequence of the nucleoprotein N was amplified without stop codon by PCR using Pfu DNA polymerase (Stratagene) and cloned in the pET28a+ vector, at BamHI and XhoI sites. The oligonucleotides used were as follows: 5'-GCCGCCGATCCATGGCTCTTAGAAAG TCAAG TTG-3' (BamHI) and 5'-GAGGAGCTCGAGAAG CTCTACATCATTATCTTTTGG-3' (XhoI). The sequence-coding TEV cleavage site was then introduced at the BamHI site after annealing of the oligonucleotides 5'-GATCCGAGAACCT ATATTTCCAGG-3' and 5'-GATCCCTGGAAATATAGG TTCTCG-3'. Finally, the sequence coding for the 40 N-terminal residues of P was PCR amplified using the oligonucleotides 5'-GAGGAGCTCGAGGGTAGCGGTAGCGGTAG CCGTAGCATGGAAAAGTTTGC TCTGAATTCC-3' (containing the sequence coding for 4 Gly/Ser, underlined) and 5'-GAG GAGCTCGAGTTAGATACTATCTTTTTT CTTCCCATC-3' (with a stop codon at the 3' end, underlined) and inserted at the XhoI site. The viral sequences derived from the human RSV strain ATCC VR-26 (GenBank accession number: AY911262.1). The final plasmid allows the expression of the fusion protein 6xHis-N-4xgs-P40 containing a TEV cleavage site upstream of the N sequence. For expression and purification of recombinant mCherry-N, N, and P-BFP proteins, the previously described pET-mCherry-N, pET-N, and pET-P-BFP plasmids were used (37, 39).

### Expression and purification of the recombinant proteins

The *E. coli* BL21 (DE3) bacteria strain (Novagen) were transformed by the pET-N-P40 plasmid. Cultures were grown at 37 °C in 2xYT medium containing 50 µg/ml kanamycin. After 8 h, an equal volume of 2xYT medium containing 50 µg/ml kanamycin was added to the cultures, and protein expression was induced by the addition of 80 µg/ml IPTG overnight at 28 °C. Bacteria were then harvested by centrifugation. Pellets were resuspended in lysis buffer (20 mM Tris-HCl, pH 8, 500 mM NaCl, 0.1% Triton X-100, 10 mM imidazole, 4 mM benzamidine, 1 mg/ml lysozyme, and complete protease inhibitor cocktail (Roche)). After incubation on



## RNA encapsidation by the RSV nucleoprotein

ice for 30 min, the lysates were sonicated, benzonase (Novagen) (final concentration 5 U/ml) and RNase A (final concentration of 1 U/ml) were added to the lysate, followed by incubation for 30 min at room temperature, finally NaCl was added (up to a concentration of 1 M). After centrifugation at 10,000 *g* for 30 min at 4 °C, the lysates were incubated with chelating Sepharose Fast Flow beads (GE Healthcare) charged with Ni<sup>2+</sup>, for 1 h at 4 °C. Beads were washed with washing buffers (20 mM Tris–HCl, pH 8, 1 M NaCl, 4 mM benzamidine) with increasing imidazole concentrations (10, 50, and 100 mM), before elution of the protein using 600 mM imidazole. Purified proteins were then loaded on a Hi-Load 16/600 Superdex 200 column (GE Healthcare) and eluted in 20 mM Tris–HCl, pH 8.5, 1 M NaCl. Then, the purified protein was dialyzed against 10 mM Tris–HCl, pH 8.5, with decreasing NaCl concentrations (500 and 300 mM) buffers, for 4 h at each step, at 4 °C. Finally, the purified protein was concentrated using a centrifugal concentrator with a MWCO of 10 kDa (vivaspin turbo 4, Sartorius). WT mCherry-N, N, and P-BFP proteins were expressed and purified as previously described (39).

### Synthesis of RNA substrates

RNA sequences were chemically synthesized on a solid support using an ABI 394 automated synthesizer with 2'-*O*-pivaloyloxymethyl 3'-*O*-phosphoramidite ribonucleosides and with 2'-*O*-methyl 3'-*O*-phosphoramidite adenosine to obtain <sup>7m</sup>GpppA<sub>m</sub>-RNA (ChemGenes Corp.) (58). After RNA assembly, depending on the desired 5' end of the RNA, 3 different processes were applied. For 5' OH-RNA sequences, the solid support was directly subjected to a basic treatment (28% aqueous ammonia solution at r.t for 3 h) to recover the crude RNA material. In the other 2 cases, the 5'-hydroxyl group was phosphorylated and the resulting *H*-phosphonate derivative was oxidized and activated to a phosphoroimidazolide derivative to react with pyrophosphate or GDP, yielding ppp-RNA (59) or Gppp-RNA (60), respectively. After deprotection and release from the solid support by the same ammonia treatment as for 5'-OH RNA, all RNA substrates were purified by IEX-HPLC (>95% pure) and their identity was confirmed by MALDI-TOF spectrometry. *N*7-methylation of the cap structure (Gppp) was performed using human (guanine-*N*7)-MTase to obtain <sup>7m</sup>Gppp-RNA (60).

### RNA–N-P40 complexes formation

RNA oligonucleotides (15 μM) and purified N-P40 protein (10 μM) in 20 mM Tris–HCl, pH 8.5, 300 mM NaCl buffer were coincubated for 30 min at room temperature. The presence of RNA was assessed by measuring the A<sub>260nm</sub>/A<sub>280nm</sub> absorption ratio. For RNase treatment, samples were incubated overnight at 4 °C in the presence of RNase A (PureLink, Invitrogen), then dialyzed against 10 mM NaP, 300 mM NaF, pH 8.5, for 3 h at 4 °C. After dialysis, the A<sub>260nm</sub>/A<sub>280nm</sub> absorption ratio was measured.

### Band shift on native polyacrylamide and agarose gels

50% sucrose loading buffer was added to the samples before loading either on native 4% native polyacrylamide gel or on native 1% agarose gel. For polyacrylamide native gel analysis, migration was performed in 0.2 × TBE (pH 8.0 for 2 h at 200 V at 4 °C), and gels were stained with Coomassie blue. For agarose native gel analysis, migration was performed in 1× Tris–Glycine buffer during 1 h 30 at 80 V before staining with amido black 10B.

### Dynamic light scattering

Size measurement of purified N-P40 alone or incubated with RNAs was performed at 20 °C using a helium-neon laser wavelength of 633 nm and detection angle of 173° with a Zetasizer Nano (Malvern). Ten measurements were made, with an acquisition time of 10 s for each measurement. Hydrodynamic diameters were calculated using the Zetasizer software provided by the instrument manufacturer (<https://www.malvernpanalytical.com/fr/support/product-support/software/Zetasizer-Nano-software-update-v3-30>). The results were presented as size distribution (nm).

### CD spectroscopy

CD experiments were performed on a J-810 spectropolarimeter (Jasco) in a thermostated cell holder at 20 °C. Spectra of N-P40 and RNA–N-P40 complexes were measured after dialysis against 10 mM NaP, 300 mM NaF, pH 8.5 buffer, and at concentrations of 10 μM. Far-UV spectra (190–260 nm) were recorded in a 0.5 mm path-length quartz cell using a bandwidth of 2 nm and an integration time of 1 s. Near-UV spectra (260–320 nm) were recorded in a 10 mm path-length quartz cell using a bandwidth of 2 nm and an integration time of 1 s. Each spectrum was the average of 3 scans, with a scan rate of 100 nm/min and 50 nm/min for far-UV and near-UV spectra, respectively. Correction by subtracting the signal from the buffer was made and the spectra were smoothed with the fast Fourier transform filter (Jasco Software), and data were treated as previously described (37).

### Negative stain electron microscopy observations of N-P40–RNA complexes

Three microliters of sample were applied to the clean side of carbon on a carbon–mica interface and stained with 2% sodium silicotungstate. Micrographs were recorded on a Thermofisher Scientific Tecnai T12 microscope operated at 120 kV with a Gatan Orius 1000 camera. Images were recorded at a nominal magnification of 23000× resulting in a pixel size of 2.8 Å.

### In vitro assay of pseudo-IBs formation

As previously described (39), mCherry-N and P proteins or P-BFP and WT N or N-P40 recombinant proteins alone or in the presence of RNAs in 20 mM Tris–HCl pH 8.5, 150 mM NaCl buffer were coincubated at different P/N molecular ratio on glass slides, and the molecular-crowding agent Ficoll was

added on the droplets of solution. Then, coverslips were laid on the droplets. For RNase treatment, N-P40 recombinant protein was preincubated in the presence of 8-mer and 11-mer RNAs, then incubated half an hour at room temperature in the presence of RNase A (PureLink, Invitrogen). Pseudo-IBs were then observed with a Nikon TE200 inverted microscope equipped with a Photometrics CoolSNAP ES2 camera. Images were processed using MetaVue software (Molecular Devices, <https://www.nikonusa.com/fileuploads/pdfs/MetaVue.pdf>) and ImageJ software (<https://imagej.nih.gov/ij/index.html>).

## Data availability

All data are contained within the article.

**Acknowledgments**—We thank Stephane Duquerroy (Institut Pasteur, France) for the scientific discussions related to this work. Protein purification benefited from the purchase of a gel filtration system funded by the Région Ile de France, France (DIM OneHealth 2018). For electron microscopy observations, this work used the EM platform of the Grenoble Instruct-ERIC center (ISBG; UAR 3518 CNRS-CEA-UGA-EMBL) within the Grenoble Partnership for Structural Biology (PSB), supported by the French Agence Nationale de la Recherche (ANR-10-INBS-0005-02) and financed within the University Grenoble Alpes graduate school, France and the specific program ANR-17-EURE-0003. The electron microscope facility is supported by the Auvergne-Rhône-Alpes Region, the Fondation Recherche Médicale (FRM), the fonds FEDER, and the GIS-Infrastructures en Biologie Santé et Agronomie (IBISA). This work was carried out with the financial support of the French Agence Nationale de la Recherche, France, specific programs ANR DecRisP n° ANR-19-CE11-0017 and ANR RSVFact n° ANR-21-CE15-0030-02.

**Author contributions**—L. G., J.-F. E., and M. G. methodology; L. G., C.-A. R., I. G., D. C., J. T., J.-J. V., and F. D. investigation; M. G. writing—original draft; J.-F. E. and M. G. writing—review and editing.

**Conflict of interest**—The authors declare that they have no conflicts of interest with the contents of this article.

**Abbreviations**—The abbreviations used are: DLS, dynamic light scattering; HMPV, human metapneumovirus; HRSV, human respiratory syncytial virus; IB, inclusion body; NC, nucleocapsid; ns-EM, negative stain electron microscopy.

## References

- Rima, B., Collins, P., Easton, A., Fouchier, R., Kurath, G., Lamb, R. A., et al. (2018) Problems of classification in the family Paramyxoviridae. *Arch. Virol.* **163**, 1395–1404
- Collins, P. L., and Crowe, J. E. (2007) Respiratory syncytial virus and metapneumovirus. In: Knipe, D. M., Howley, P. M., eds. *Fields Virology*, 5th Ed., Lippincott Williams & Wilkins, Philadelphia: 1601–1646
- Fearn, R., and Plemper, R. K. (2017) Polymerases of paramyxoviruses and pneumoviruses. *Virus Res.* **234**, 87–102
- Guseva, S., Milles, S., Jensen, M. R., Salvi, N., Kleman, J. P., Maurin, D., et al. (2020) Measles virus nucleocapsid and phosphoproteins form liquid-like phase-separated compartments that promote nucleocapsid assembly. *Sci. Adv.* **6**, eaaz7095
- Heinrich, B. S., Maliga, Z., Stein, D. A., Hyman, A. A., and Whelan, S. P. J. (2018) Phase transitions drive the formation of vesicular stomatitis virus replication compartments. *mBio* **9**, e02290-17
- Nikolic, J., Le Bars, R., Lama, Z., Scrima, N., Lagaudriere-Gesbert, C., Gaudin, Y., et al. (2017) Negri bodies are viral factories with properties of liquid organelles. *Nat. Commun.* **8**, 58
- Zhou, Y., Su, J. M., Samuel, C. E., and Ma, D. (2019) Measles virus forms inclusion bodies with properties of liquid organelles. *J. Virol.* **93**, e00948-19
- Rincheval, V., Lelek, M., Gault, E., Bouillier, C., Sitterlin, D., Blouquit-Laye, S., et al. (2017) Functional organization of cytoplasmic inclusion bodies in cells infected by respiratory syncytial virus. *Nat. Commun.* **8**, 563
- Afonso, C. L., Amarasinghe, G. K., Banyai, K., Bao, Y., Basler, C. F., Bavari, S., et al. (2016) Taxonomy of the order Mononegavirales: update 2016. *Arch. Virol.* **161**, 2351–2360
- Rima, B., Collins, P., Easton, A., Fouchier, R., Kurath, G., Lamb, R. A., et al. (2017) ICTV virus taxonomy profile: pneumoviridae. *J. Gen. Virol.* **98**, 2912–2913
- Shi, T., McAllister, D. A., O'Brien, K. L., Simoes, E. A. F., Madhi, S. A., Gessner, B. D., et al. (2017) Global, regional, and national disease burden estimates of acute lower respiratory infections due to respiratory syncytial virus in young children in 2015: a systematic review and modelling study. *Lancet* **390**, 946–958
- Nair, H., Nokes, D. J., Gessner, B. D., Dherani, M., Madhi, S. A., Singleton, R. J., et al. (2010) Global burden of acute lower respiratory infections due to respiratory syncytial virus in young children: a systematic review and meta-analysis. *Lancet* **375**, 1545–1555
- Pneumonia Etiology Research for Child Health Study Group (2019) Causes of severe pneumonia requiring hospital admission in children without HIV infection from Africa and Asia: the PERCH multi-country case-control study. *Lancet* **394**, 757–779
- Falsey, A. R., Hennessey, P. A., Formica, M. A., Cox, C., and Walsh, E. E. (2005) Respiratory syncytial virus infection in elderly and high-risk adults. *N. Engl. J. Med.* **352**, 1749–1759
- Asner, S., Stephens, D., Pedulla, P., Richardson, S. E., Robinson, J., and Allen, U. (2013) Risk factors and outcomes for respiratory syncytial virus-related infections in immunocompromised children. *Pediatr. Infect. Dis. J.* **32**, 1073–1076
- Shah, J. N., and Chemaly, R. F. (2011) Management of RSV infections in adult recipients of hematopoietic stem cell transplantation. *Blood* **117**, 2755–2763
- Collins, P. L., and Melero, J. A. (2011) Progress in understanding and controlling respiratory syncytial virus: still crazy after all these years. *Virus Res.* **162**, 80–99
- Collins, P. L., Hill, M. G., Camargo, E., Grosfeld, H., Chanock, R. M., and Murphy, B. R. (1995) Production of infectious human respiratory syncytial virus from cloned cDNA confirms an essential role for the transcription elongation factor from the 5' proximal open reading frame of the M2 mRNA in gene expression and provides a capability for vaccine development. *Proc. Natl. Acad. Sci. U.S.A.* **92**, 11563–11567
- Fearn, R., and Collins, P. L. (1999) Role of the M2-1 transcription antitermination protein of respiratory syncytial virus in sequential transcription. *J. Virol.* **73**, 5852–5864
- Noton, S. L., and Fearn, R. (2015) Initiation and regulation of paramyxovirus transcription and replication. *Virology* **479–480**, 545–554
- Noton, S. L., Tremaglio, C. Z., and Fearn, R. (2019) Killing two birds with one stone: how the respiratory syncytial virus polymerase initiates transcription and replication. *PLoS Pathog.* **15**, e1007548
- Hefti, E., and Bishop, D. H. (1975) The 5' nucleotide sequence of vesicular stomatitis viral RNA. *J. Virol.* **15**, 90–96
- Hefti, E., and Bishop, D. H. (1975) The 5' sequence of VSV viral RNA and its *in vitro* transcription product RNA. *Biochem. Biophys. Res. Commun.* **66**, 785–792
- Bakker, S. E., Duquerroy, S., Galloux, M., Loney, C., Conner, E., Eleouet, J. F., et al. (2013) The respiratory syncytial virus nucleoprotein-RNA complex forms a left-handed helical nucleocapsid. *J. Gen. Virol.* **94**, 1734–1738

## RNA encapsidation by the RSV nucleoprotein

25. Samal, S. K., and Collins, P. L. (1996) RNA replication by a respiratory syncytial virus RNA analog does not obey the rule of six and retains a nonviral trinucleotide extension at the leader end. *J. Virol.* **70**, 5075–5082
26. Cowton, V. M., McGivern, D. R., and Fearn, R. (2006) Unravelling the complexities of respiratory syncytial virus RNA synthesis. *J. Gen. Virol.* **87**, 1805–1821
27. Tawar, R. G., Duquerroy, S., Vonnrhein, C., Varela, P. F., Damier-Piolle, L., Castagne, N., *et al.* (2009) Crystal structure of a nucleocapsid-like nucleoprotein-RNA complex of respiratory syncytial virus. *Science* **326**, 1279–1283
28. Leyrat, C., Yabukarski, F., Tarbouriech, N., Ribeiro, E. A., Jr., Jensen, M. R., Blackledge, M., *et al.* (2011) Structure of the vesicular stomatitis virus N(0)-P complex. *Plos Pathog.* **7**, e1002248
29. Yabukarski, F., Lawrence, P., Tarbouriech, N., Bourhis, J. M., Delaforge, E., Jensen, M. R., *et al.* (2014) Structure of Nipah virus unassembled nucleoprotein in complex with its viral chaperone. *Nat. Struct. Mol. Biol.* **21**, 754–759
30. Esneau, C., Raynal, B., Roblin, P., Brule, S., Richard, C. A., Fix, J., *et al.* (2019) Biochemical characterization of the respiratory syncytial virus N(0)-P complex in solution. *J. Biol. Chem.* **294**, 3647–3660
31. Renner, M., Bertinelli, M., Leyrat, C., Paesen, G. C., Saraiva de Oliveira, L. F., Huiskonen, J. T., *et al.* (2016) Nucleocapsid assembly in pneumoviruses is regulated by conformational switching of the N protein. *eLife* **5**, e12627
32. Aggarwal, M., Leser, G. P., Kors, C. A., and Lamb, R. A. (2018) Structure of the paramyxovirus parainfluenza virus 5 nucleoprotein in complex with an amino-terminal peptide of the phosphoprotein. *J. Virol.* **92**, e01304–e01317
33. Zhu, T., Song, H., Peng, R., Shi, Y., Qi, J., and Gao, G. F. (2017) Crystal structure of the Marburg virus nucleoprotein core domain chaperoned by a VP35 peptide reveals a conserved drug target for Filovirus. *J. Virol.* **91**, e00996-17
34. Guryanov, S. G., Liljeroos, L., Kasaragod, P., Kajander, T., and Butcher, S. J. (2015) Crystal structure of the measles virus nucleoprotein core in complex with an N-terminal region of phosphoprotein. *J. Virol.* **90**, 2849–2857
35. Kirchdoerfer, R. N., Abelson, D. M., Li, S., Wood, M. R., and Saphire, E. O. (2015) Assembly of the Ebola virus nucleoprotein from a chaperoned VP35 complex. *Cell Rep.* **12**, 140–149
36. Dong, X., Wang, X., Xie, M., Wu, W., and Chen, Z. (2022) Structural basis of human parainfluenza virus 3 unassembled nucleoprotein in complex with its viral chaperone. *J. Virol.* **96**, e0164821
37. Galloux, M., Gabiane, G., Sourimant, J., Richard, C. A., England, P., Moudjou, M., *et al.* (2015) Identification and characterization of the binding site of the respiratory syncytial virus phosphoprotein to RNA-free nucleoprotein. *J. Virol.* **89**, 3484–3496
38. Garcia, J., Garcia-Barreno, B., Vivo, A., and Melero, J. A. (1993) Cytoplasmic inclusions of respiratory syncytial virus-infected cells: Formation of inclusion bodies in transfected cells that coexpress the nucleoprotein, the phosphoprotein, and the 22K protein. *Virology* **195**, 243–247
39. Galloux, M., Risso-Ballester, J., Richard, C. A., Fix, J., Rameix-Welti, M. A., and Eleouet, J. F. (2020) Minimal elements required for the formation of respiratory syncytial virus cytoplasmic inclusion bodies in vivo and in vitro. *mBio* **11**, e01202–e01220
40. Risso-Ballester, J., Galloux, M., Cao, J., Le Goffic, R., Hontonnou, F., Jobart-Malfait, A., *et al.* (2021) A condensate-hardening drug blocks RSV replication *in vivo*. *Nature* **595**, 596–599
41. Richard, C. A., Rincheval, V., Lassoued, S., Fix, J., Cardone, C., Esneau, C., *et al.* (2018) RSV hijacks cellular protein phosphatase 1 to regulate M2-1 phosphorylation and viral transcription. *PLoS Pathog.* **14**, e1006920
42. Bajorek, M., Galloux, M., Richard, C. A., Szekely, O., Rosenzweig, R., Sizun, C., *et al.* (2021) Tetramerization of phosphoprotein is essential for respiratory syncytial virus budding while its N terminal region mediates direct interactions with the matrix protein. *J. Virol.* **11**, 1225
43. Sourimant, J., Rameix-Welti, M. A., Gaillard, A. L., Chevret, D., Galloux, M., Gault, E., *et al.* (2015) Fine mapping and characterization of the L-polymerase-binding domain of the respiratory syncytial virus phosphoprotein. *J. Virol.* **89**, 4421–4433
44. Gilman, M. S. A., Liu, C., Fung, A., Behera, I., Jordan, P., Rigaux, P., *et al.* (2019) Structure of the respiratory syncytial virus polymerase complex. *Cell* **179**, 193–204.e14
45. Tran, T. L., Castagne, N., Bhella, D., Varela, P. F., Bernard, J., Chlironczyk, S., *et al.* (2007) The nine C-terminal amino acids of the respiratory syncytial virus protein P are necessary and sufficient for binding to ribonucleoprotein complexes in which six ribonucleotides are contacted per N protein protomer. *J. Gen. Virol.* **88**, 196–206
46. Galloux, M., Tarus, B., Blazevic, I., Fix, J., Duquerroy, S., and Eleouet, J. F. (2012) Characterization of a viral phosphoprotein binding site on the surface of the respiratory syncytial nucleoprotein. *J. Virol.* **86**, 8375–8387
47. Gao, Y., Cao, D., Ahn, H. M., Swain, A., Hill, S., Ogilvie, C., *et al.* (2020) *In vitro* trackable assembly of RNA-specific nucleocapsids of the respiratory syncytial virus. *J. Biol. Chem.* **295**, 883–895
48. Banani, S. F., Lee, H. O., Hyman, A. A., and Rosen, M. K. (2017) Biomolecular condensates: organizers of cellular biochemistry. *Nat. Rev. Mol. Cell Biol.* **18**, 285–298
49. Alberti, S., Gladfelter, A., and Mittag, T. (2019) Considerations and challenges in studying liquid-liquid phase separation and biomolecular condensates. *Cell* **176**, 419–434
50. Alberti, S., Saha, S., Woodruff, J. B., Franzmann, T. M., Wang, J., and Hyman, A. A. (2018) A user's guide for phase separation assays with purified proteins. *J. Mol. Biol.* **430**, 4806–4820
51. Shimobayashi, S. F., Ronceray, P., Sanders, D. W., Haataja, M. P., and Brangwynne, C. P. (2021) Nucleation landscape of biomolecular condensates. *Nature* **599**, 503–506
52. Brocca, S., Grandori, R., Longhi, S., and Uversky, V. (2020) Liquid-liquid phase separation by intrinsically disordered protein regions of viruses: roles in viral life cycle and control of virus-host interactions. *Int. J. Mol. Sci.* **21**, 9045
53. Song, X., Shan, H., Zhu, Y., Hu, S., Xue, L., Chen, Y., *et al.* (2019) Self-capping of nucleoprotein filaments protects the Newcastle disease virus genome. *eLife* **8**, e45057
54. Zhang, N., Shan, H., Liu, M., Li, T., Luo, R., Yang, L., *et al.* (2021) Structure and assembly of double-headed Sendai virus nucleocapsids. *Commun. Biol.* **4**, 494
55. Ker, D. S., Jenkins, H. T., Greive, S. J., and Antson, A. A. (2021) CryoEM structure of the Nipah virus nucleocapsid assembly. *Plos Pathog.* **17**, e1009740
56. Zinzula, L., Beck, F., Klumpe, S., Bohn, S., Pfeifer, G., Bollschweiler, D., *et al.* (2021) Cryo-EM structure of the cetacean morbillivirus nucleoprotein-RNA complex. *J. Struct. Biol.* **213**, 107750
57. Conley, M. J., Short, J. M., Burns, A. M., Streetley, J., Hutchings, J., Bakker, S. E., *et al.* (2022) Helical ordering of envelope-associated proteins and glycoproteins in respiratory syncytial virus. *EMBO J.* **41**, e109728
58. Parey, N., Baraguey, C., Vasseur, J. J., and Debart, F. (2006) First evaluation of acyloxymethyl or acylthiomethyl groups as biolabile 2'-O-protections of RNA. *Org. Lett.* **8**, 3869–3872
59. Zlatev, I., Lavergne, T., Debart, F., Vasseur, J. J., Manoharan, M., and Morvan, F. (2010) Efficient solid-phase chemical synthesis of 5'-triphosphates of DNA, RNA, and their analogues. *Org. Lett.* **12**, 2190–2193
60. Thillier, Y., Decroly, E., Morvan, F., Canard, B., Vasseur, J. J., and Debart, F. (2012) Synthesis of 5' cap-0 and cap-1 RNAs using solid-phase chemistry coupled with enzymatic methylation by human (guanine-N(7))-methyl transferase. *RNA* **18**, 856–868

### 3. Discussion

Although this study clearly showed that RNA length is critical for stable encapsidation, our results did not fully decipher the role of 5' end modifications and RNA sequence in the specificity of encapsidation by N. One of the main differences between genomic/antigenomic RNA and viral mRNA relies on the 5' end modifications. Since the presence of 5' ppp or 5' <sup>7m</sup>Gppp did not impair the encapsidation by N *in vitro* (except for the smallest RNAs but likely by steric hindrance), we wondered if in the context of IBs, the encapsidation of the viral mRNAs by N could be prevented by the specific interaction of viral mRNA with M2-1 (Cartee and Wertz, 2001; Cuesta et al., 2000; Tran et al., 2009). This hypothesis could be supported by the recent observation of substructures within the IBs, called IBAGs (IB-associated granules), where M2-1 and viral mRNAs concentrate (Rincheval et al., 2017). Previously, two RNA binding sites were identified in M2-1, located within the zinc-binding and core domains (Tanner et al., 2014). In 2020, the X-ray crystallography structure of M2-1 in complex with short 7-mer RNA confirmed these results and revealed that the zinc-binding domain recognises adenosine through a base-stacking interaction and that the core binding domain interacts with the phosphate backbone of RNA (Gao et al., 2020). Based on the cryo-EM structure of the L-P complex (Gilman et al., 2019) and the respective position of M2-1 and L on P, the authors suggested that viral mRNA could interact directly with M2-1 during sorting of the catalytic site of RdRp. This mechanism could almost explain the absence of encapsidation of viral mRNA by N. During the course of our study, we thus wondered if M2-1 could present higher affinity than N for RNA with 5' end modifications.

To test this hypothesis, we analysed the migration of the HIS-M2-1 protein (Tran et al., 2009) alone or incubated in presence of short RNA displaying 5' OH, 5' ppp, or 5' <sup>7m</sup>Gppp, by native agarose gel electrophoresis, as for RNA encapsidation assays. Interestingly, whereas M2-1 presented poor affinity for 5' OH RNAs shorter than 9-mer, a clear shift of M2-1 migration was observed in the presence of 7-mer RNAs displaying 5' ppp or 5' <sup>7m</sup>Gppp ends (Figure 23). These results may suggest that, contrary to what we observed for the N protein, 5' ppp or 5' <sup>7m</sup>Gppp ends could favour the interaction with HIS-M2-1 (Figure 23). To our knowledge, it is the first study of the interaction between M2-1 and 5' <sup>7m</sup>Gppp end RNAs. These observations

pave the way for further investigation of the affinity and binding of 5' <sup>7m</sup>Gppp RNA on M2-1. Further work is required to determine more precisely whether the affinity of M2-1 to the RNA increases in the presence of 5' ppp or 5' <sup>7m</sup>Gppp ends. And more globally, whether or not M2-1 may interact directly with the 5' ppp or 5' <sup>7m</sup>Gppp of viral mRNA.

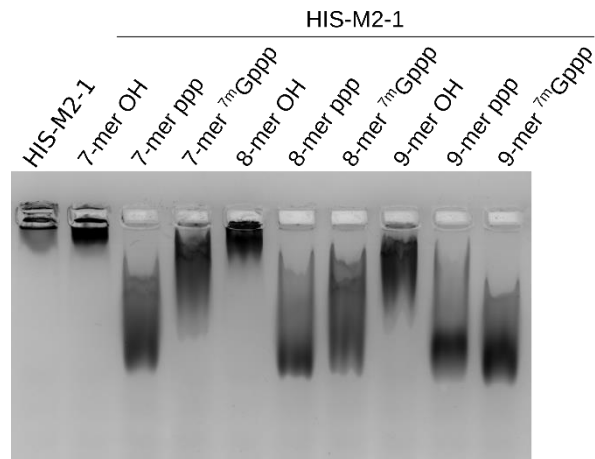


**Figure 23. Study of the interaction between M2-1 and RNA.** Analysis of HIS-M2-1 migration alone or in the presence of 7- to 9-mer RNAs with 5' OH, 5' ppp, or 5' <sup>7m</sup>Gppp ends by native agarose gel electrophoresis. Agarose gel was stained with amido black.

Finally, in order to gain information on the structural changes required for the transition from N<sup>0</sup>-P to N-RNA complexes, crystallisation assays of N-P40 were performed. However, SEC-MALLS analysis and ns-EM revealed that N-P40 aggregated over 1.5 mg/ml and at a NaCl concentration under 300 mM.

We tried several other N<sup>0</sup>-P complex constructions in order to isolate an N<sup>0</sup> that could remain monomeric at high concentrations. Notably, one of the constructs was a fusion protein between N deleted of its N-terminal arm (NΔ30) and the first 29 amino acids of P. Despite the stability of the NΔ30-P29 fusion at high concentration and the optimisation of the crystal growth conditions, the crystals obtained did not diffract.



To obtain a prediction of RSV N<sup>0</sup> folding, we decided to use AlphaFold2 (AF2). AF2 is an artificial neural network-based program that can predict 3D protein structures (Jumper et al., 2021). To perform the prediction, we used the full-length N protein sequence and the 40 N-terminal amino acids of P (P40) of the RSV A long strain, with the two proteins treated as separate sequences. Five models were predicted using ColabFold, <https://colab.research.google.com/github/sokrypton/ColabFold/blob/main/AlphaFold2.ipynb>, v1.5.1.

First, we assessed the predictions by looking at the predicted local distance difference test (pLDDT) per position. The pLDDT allows to estimate the local distance differences of all the atoms that are in the model, with a score from 0 to 100 (Mariani et al., 2013). A pLDDT > 90 indicates that the modelling is highly accurate; between 70 and 90 the modelling is considered good; between 50 and 70 the modelling should be treated with caution, and a pLDDT < 50 indicates that the predictions are not relevant or that the corresponding domain could be a disorder region. For the structure predictions of the N-P40 complex, the score was globally the same between the five models for the N protein sequence, with models 4 and 5 (ranks 4 and 5) having a slightly lower score at the C-terminal part of the sequence. Concerning the P protein sequence, the score was very comparable for the 4 first models, but model 5 exhibits a lower score (Figure 24A). Interestingly the pLDDT was overall > 80, and often > 90 along the sequences, indicating that the predicted reliability of the 3D structure is overall very good. Second, we looked at the PAE (predicted aligned error) plots for each model. While the pLDDT is a good indicator of the accuracy of the model locally, the PAE gives a score to assess the prediction of the relative position of the different domains (a low score, in blue, indicates that the relative domain position predictions are of good quality) (Figure 24B). Models 1 to 3 exhibit the same PAE plot globally and indicate that the confidence of the relative position of the 2 domains of N (NTD and CTD), but also the relative position of P40 to N is quite good. Model 1 was chosen as the “best” model (Figure 24C), but models 2 and 3 were almost similar.

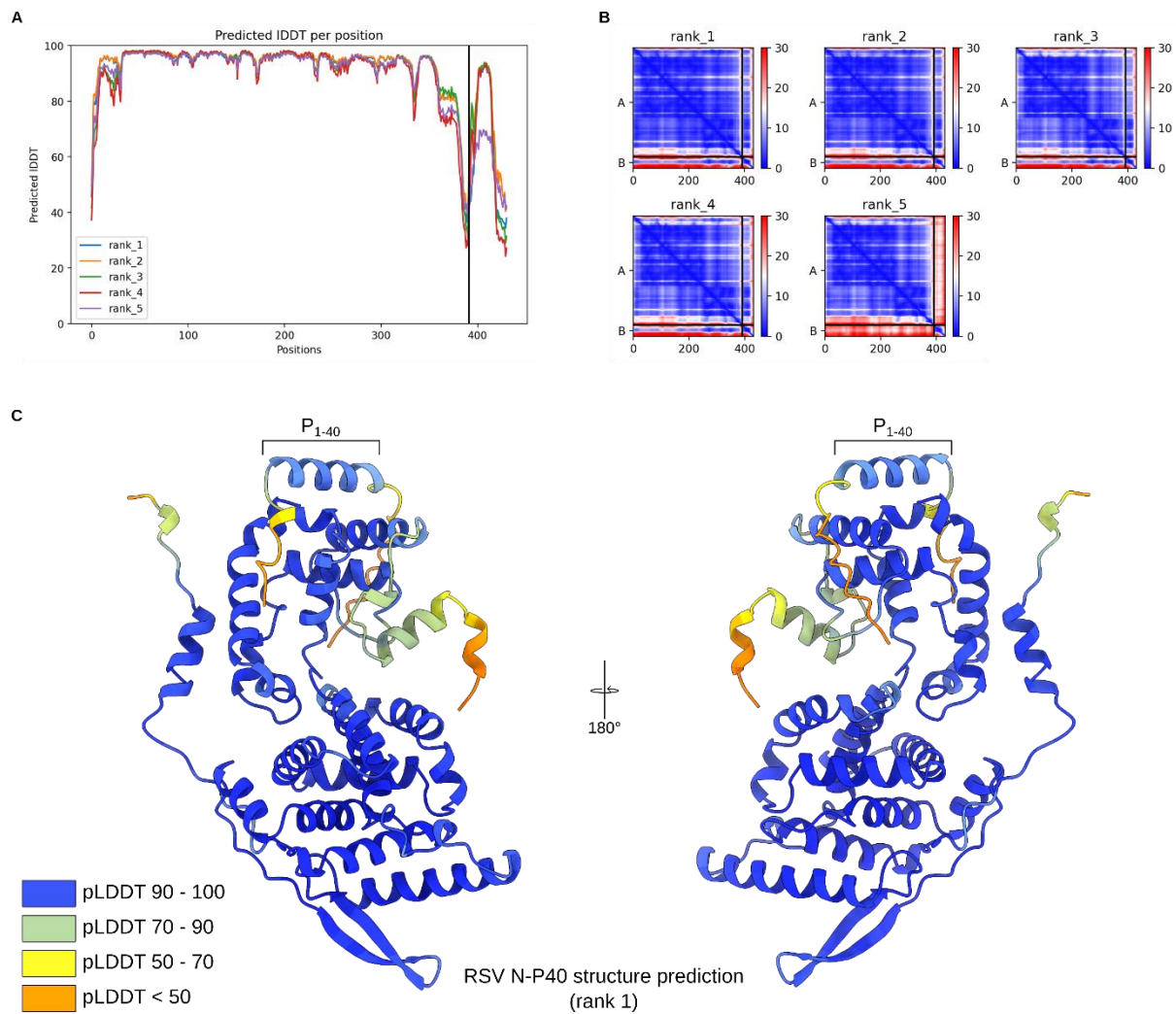


**Figure 24. Structure prediction of RSV N-P40 complex using AlphaFold 2.** (A) pLDDT per position plot for the five N-P40 complex models (rank 1 to 5). Positions 1 to 391 correspond to N, and positions 392 to 432 to P<sub>1-40</sub>. (B) PAE plots for each N-P40 complex model (rank 1 to 5), A corresponds to N and B to P<sub>1-40</sub>. (C) Atomic model of the N-P40 complex model 1, coloured depending on the pLDDT score.

The predicted RSV N-P40 complex structure closely resembles the crystal structure of the HMPV N<sup>0</sup>-P complex (Renner et al., 2016) (Figure 25A) and of the model generated based on SAXS analysis (Esneau et al., 2019). Remarkably, in this model the position of the C-terminal arm of N is matching the one of the HMPV N<sup>0</sup>-P complex, i.e. folded against the N<sub>CTD</sub>. The position of the P<sub>1-40</sub> is also highly comparable. In the RSV N-RNA ring, the C-terminal arm is

interacting at the top of the adjacent N protomer (Tawar et al., 2009). The superimposition of the predicted RSV N-P40 complex structure with one protomer from the N-RNA ring crystal structure highlights the probable high flexibility of the C-terminal arm of N (Figure 25B).

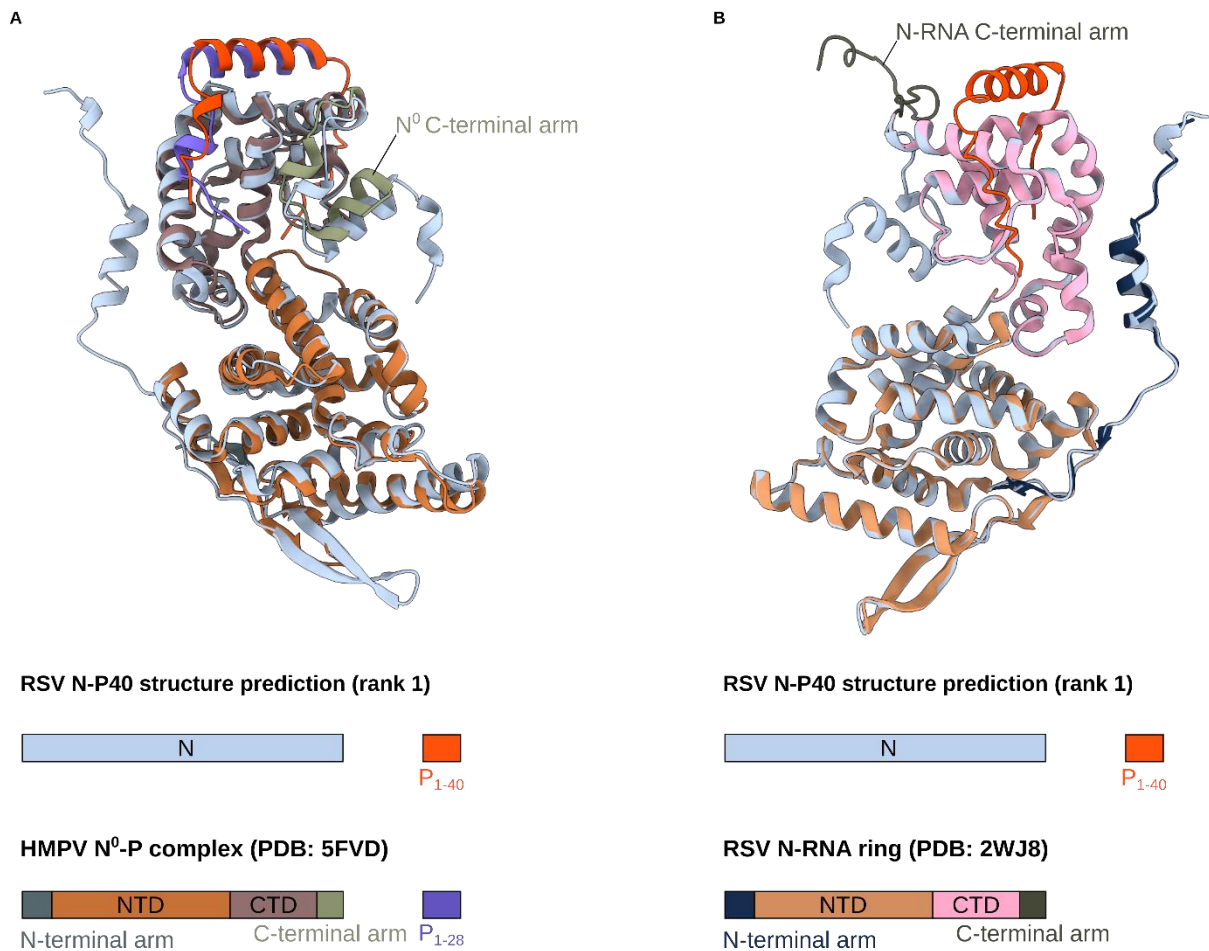


**Figure 25. Comparison of the predicted structure of RSV N-P40 complex with the crystal structures of the HMPV N<sup>0</sup>-P complex and RSV N from N-RNA rings.** (A) Superimposition of RSV N-P40 complex predicted structure (rank 1) with the HMPV N<sup>0</sup>-P complex (PDB: 5FVD, Renner et al., 2016). (B) Superimposition of RSV N-P40 complex predicted structure (rank 1) with a N protomer of RSV N-RNA rings (PDB: 2WJ8, Tawar et al., 2009).



In order to further understand N oligomerisation, and in addition to the *in vitro* encapsidation study, we initiated a structural study of the RSV NC by cryo-EM. The aim was to obtain structural data about N oligomerisation and RNA encapsidation.

## Chapter II: Structural analysis of the RSV nucleocapsid by cryo-EM

### **1. Introduction**

Numerous helical NC structures of *Mononegavirales* have been solved by cryo-EM (Fujita-Fujiharu et al., 2022; Gutsche et al., 2015; Jenni et al., 2022; Ker et al., 2021; Riedel et al., 2019; Shan et al., 2021; Song et al., 2019; Sugita et al., 2018; Zhang et al., 2021; Zinzula et al., 2021). For the *Pneumoviridae* family high resolution structural data are limited to the N-RNA ring crystal structures of RSV (Tawar et al., 2009) and HMPV (Renner et al., 2016). Cryo-EM and cryo-ET images of RSV NCs are available (Bhella et al., 2002; Bakker et al., 2013; Liljeroos et al., 2013), but the resolution remains insufficient to accurately characterise the NC of pneumoviruses.

The first challenge to determine RSV NCs structure was to isolate recombinant NCs of high quality. Here, the baculovirus expression system was used to produce recombinant RSV N protein in insect cells. Indeed, the expression of the RSV N protein in *E. coli* only yielded N-RNA rings (Tran et al., 2007).

The first protocol used was adapted from Bhella and colleagues' publication, which allowed to isolate for the first time helical NC (Bhella et al., 2002). Briefly, after expression of RSV N using the baculovirus system, insect cells (Sf9 line) were lysed before ultracentrifugation of the supernatant in a caesium chloride (CsCl) gradient. After extraction of the band of interest from the CsCl gradient and analysis by acrylamide gel electrophoresis, the sample containing N was dialysed to remove the CsCl. The sample was then deposited on either a sucrose gradient or a glycerol cushion, followed by ultracentrifugation. Observation of the samples by ns-EM showed our ability to isolate helical NC. However, the helices were very short and highly curved (Figure 26), thus not of sufficient quantity and quality to perform cryo-EM structural analysis.

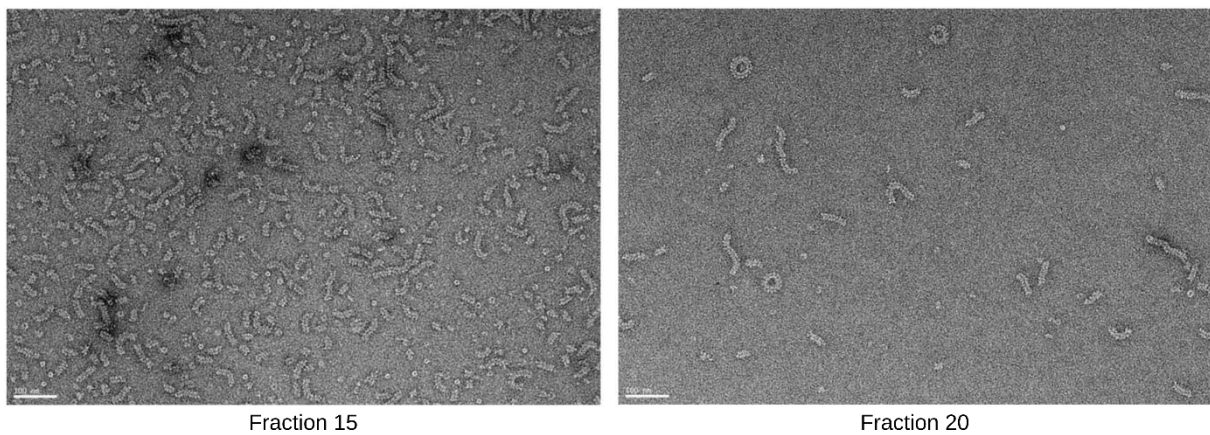


**Figure 26.** ns-EM images of the fractions 15 (left) and 20 (right) of purified RSV NC-like on a sucrose gradient. Scale bars 100 nm.

We continued to optimise the protocol to obtain helices at higher concentrations, and we succeeded but the helices still appeared very curved in ns-EM images (Figure 27A). Furthermore, after dialysis to remove the sucrose and concentration of the sample, cryo-EM images revealed almost completely unwound helices (Figure 27B).

After several attempts to improve the purification protocol and grid preparation for cryo-EM data collection, we decided to adopt a protocol based on the strategy used to purify the RSV N-RNA rings (Tawar et al., 2009). To do so, the GST-P<sub>CTD</sub> (C-terminal residues 161 to 241 of the RSV P protein) was expressed in *E. coli* and purified on glutathione-sepharose beads. After the expression of the N protein in insect cells, the cell lysate was incubated on the GST-P<sub>CTD</sub> beads. After washes and GST cleavage in the presence of thrombin, the NCs were collected and concentrated using a column. This second protocol has the advantage of being quicker, simpler (no ultracentrifugation and no need for a dialysis to remove the sucrose before cryo-EM grid preparation), and restraining NC manipulation. This protocol made it possible to obtain helical NC with a higher concentration but with the disadvantage of getting a lot of single rings in the sample (Figure 27). In order to improve the quality of the preparation and to reduce the number of single rings, optimisations in the production and purification protocols were made, including the use of High Five insect cells instead of the Sf9 line for N expression, which increased drastically the quantity of purified NC (Figure 28). Irina Gutsche and Maria Bacia-

Verloop of the MICA group carried out extensive grid preparation and optimisation in order to obtain good-quality cryo-EM grids for data collection.

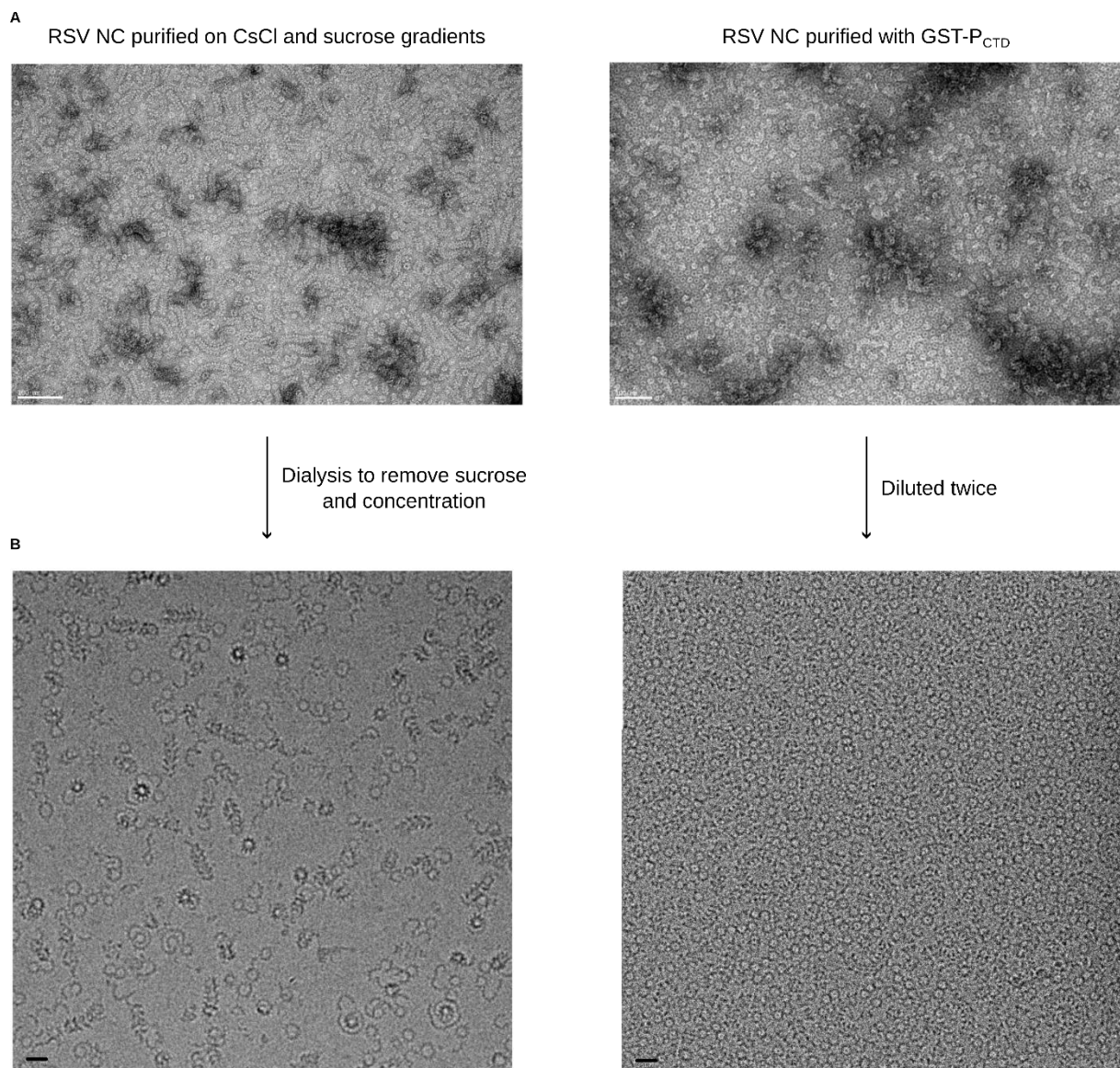


**Figure 27.** (A) Ns-EM images of purified RSV NC-like on a sucrose gradient (left) and of purified RSV NC-like with GST-P<sub>CTD</sub> (right). Scale bars 100 nm. (B) Cryo-EM images of purified RSV NC-like on a sucrose gradient after dialysis and concentration (left) and of purified RSV NC-like with GST-P<sub>CTD</sub> diluted twice (right). Scale bars 20 nm.

Interestingly, different objects were observed in the images: helical NC, double-rings, double-headed NC and ring-capped NC and were processed independently (Figure 28). I worked for several months in the MICA group, under the co-supervision of Ambroise Desfosses to carry out the data processing. Structural determination revealed that RSV helical NCs adopt a unique non-canonical symmetry involving differential access to RNA along the helix. We showed that this flexibility is driven by the C-terminal arm of N by determining the structures of the mutant N1-370 NC that adopted both helical and stack assemblies. Of note, the N1-370 mutant (N protein deleted of the 22 C-terminal amino acids) was purified using the same protocol as N wild-type. This work was the subject of an article, currently under review.

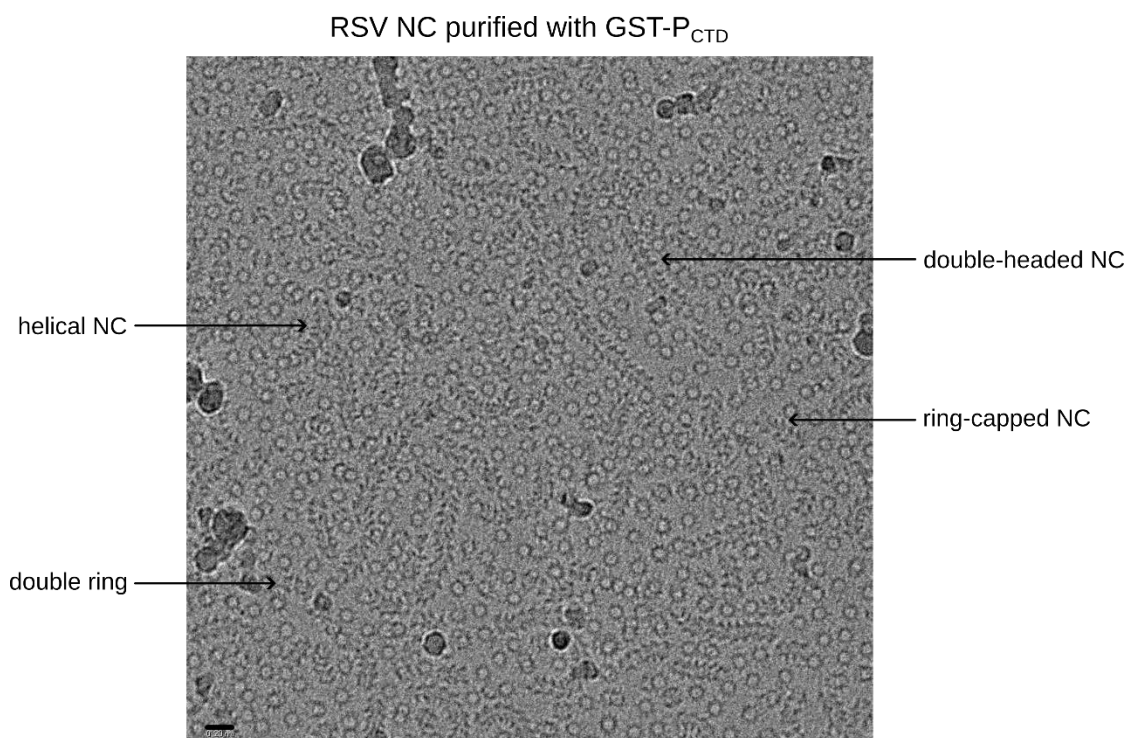


**Figure 28.** Cryo-EM image of purified RSV NC-like assemblies with GST-P<sub>CTD</sub>. Scale bar 20 nm.

## **2. Article 2: Structural landscape of the respiratory syncytial virus nucleocapsids**

# 1 Structural landscape of the Respiratory Syncytial Virus nucleocapsids

2 Lorène Gonnin<sup>1,2</sup>, Ambroise Desfosses<sup>1\*</sup>, Maria Bacia-Verloop<sup>1</sup>, Didier Chevret<sup>2</sup>, Marie Galloux<sup>2</sup>,  
3 Jean-François Éléouët<sup>2</sup> and Irina Gutsche<sup>1\*</sup>

## 4 Affiliations

5 <sup>1</sup>Institut de Biologie Structurale, Univ Grenoble Alpes, CEA, CNRS, IBS, 71 Avenue des martyrs, F-  
6 38044 Grenoble, France

7 <sup>2</sup>VIM, Paris-Saclay University, INRAE, 78350 Jouy-en-Josas, France

8 \*corresponding authors: [irina.gutsche@ibs.fr](mailto:irina.gutsche@ibs.fr), [ambroise.desfosses@ibs.fr](mailto:ambroise.desfosses@ibs.fr)

## 9 Abstract

10 Human Respiratory Syncytial Virus (RSV) is a prevalent cause of severe respiratory infections in  
11 children and the elderly. The viral genome, enwrapped by the nucleoprotein N into a helical  
12 nucleocapsid (NC), is a template for the viral RNA synthesis and a scaffold for the virion assembly.  
13 Although the structures of NC filaments representative of the other major families of the  
14 *Mononegavirales* order have been solved, a detailed understanding of the RSV NCs is missing.  
15 This cryo-electron microscopy (cryo-EM) analysis highlights the polymorphism of the RSV  
16 nucleocapsid-like assemblies. We reveal in particular the non-canonical arrangement of the RSV  
17 NC helix, composed of 16 N per asymmetric unit, and the resulting systematic variations in the  
18 RNA accessibility. We demonstrate that this unique helical symmetry originates from recurring  
19 longitudinal interactions by the C-terminal arm of the RSV N, whose truncation abrogates the inter-  
20 turn contacts. We report the cryo-EM structures of the full-length helical NC filaments, double-  
21 headed NCs, ring-capped NCs and double-decameric N-RNA rings, as well as those of the  
22 alternative assemblies formed by a C-terminally truncated N mutant. In addition, we demonstrate  
23 the functional importance of the interface involved in the formation of the double-headed and the  
24 ring-capped interactions. We put all these findings in the context of the RSV RNA synthesis  
25 machinery and delineate the structural basis for its further investigation.

## 26 Introduction

27 Human respiratory syncytial virus (RSV) is the most frequent cause of bronchiolitis and  
28 pneumonia in infants and a major cause of childhood death in low-income settings <sup>1,2</sup>. Reinfection  
29 can occur throughout life and is often serious in elderly and immunocompromised. Yet, RSV  
30 remains one of the only major etiological agents of the lower respiratory tract infections-related  
31 mortality for which no licensed vaccine is yet available, with treatment limited to supportive care.  
32 Development of effective therapeutics requires a better understanding of the RSV synthesis  
33 machinery. RSV belongs to the *Mononegavirales* order with the non-segmented negative strand  
34 RNA genome fully coated by the viral nucleoprotein N. The resulting helical nucleocapsid (NC)  
35 shields the viral genetic material from recognition by the innate immune system while serving as  
36 template for replication and transcription by the viral RNA polymerase complex, thereby  
37 constituting a potential drug target.

38 Alongside RSV and human Metapneumovirus (hMPV), belonging to the *Pneumoviridae*  
39 family, *Mononegavirales* contains other important human pathogens such as the *Rhabdoviridae*

40 rabies, the *Filoviridae* Ebola (EV) and Marburg (MaV), and the *Paramyxoviridae* measles (MeV),  
41 mumps (MuV) and Nipah (NiV) viruses. *Pneumoviridae* are equally distant to *Paramyxo-* and  
42 *Filoviridae*<sup>3</sup>. In particular, as far as the NCs are concerned (i) each paramyxo- and filoviral N binds  
43 precisely 6 nucleotides, whereas pneumoviral N binds 7<sup>4</sup>; (ii) the genome size of paramyxo- but  
44 not pneumo- and filoviruses is a strict multiple of 6 nucleotides; (iii) paramyxo- and filo- but not  
45 pneumoviral genomes require bipartite promoters separated by an exact multiple of 6 nucleotides  
46<sup>5</sup>; (iv) paramyxo- and filoviral N possess a very long C-terminal extension involved in replication  
47 and transcription, whereas the pneumoviral N features only a short C-terminal arm (*i.e.* the length  
48 of MeV N is 525, EV NP 739 and RSV N 391 amino acids respectively)<sup>6</sup>. Removal of the C-  
49 terminal extension rigidifies and condenses the helical paramyxo- and filoviral NCs by  
50 strengthening the contacts between successive turns, thus facilitating their structural analysis by  
51 cryo-electron microscopy (cryo-EM) and tomography (cryo-ET).

52 Despite a recent massive increase in the number of medium and high resolution cryo-EM  
53 structures of the helical paramyxo- and filoviral NCs<sup>7-16</sup>, a detailed cryo-EM characterisation of the  
54 pneumoviral NCs is still lacking. Here we present an exhaustive cryo-EM analysis of the structural  
55 landscape of RSV NCs in solution. We reveal in particular the non-canonical helical symmetry of  
56 the RSV NC, with 16 nucleoproteins per asymmetric unit, and demonstrate that this unique  
57 organisation results from inter-turn interactions by the C-terminal arm of N and leads to periodic  
58 variations in the RNA accessibility along the NC filament.

## 59 Results

### 60 RSV nucleocapsids are flexible and polymorphic

61 The current structural information about RSV NCs comes mostly from the 3.3 Å resolution  
62 X-ray crystal structure of decameric N-RNA rings<sup>4</sup> (N<sub>10</sub> ring, PDB: 2WJ8), a negative stain electron  
63 tomography analysis of purified helical NCs<sup>17</sup> and two cryo-ET studies of the RSV virion<sup>18,19</sup>. Our  
64 cryo-EM images of recombinant RSV N purified from insect cells displayed a polymorphic  
65 ensemble in which ring-like particles and filaments could be distinguished and classified (Figure  
66 1a, b). A map of a bottom-to-bottom assembly of two decameric N-RNA rings, termed N<sub>10</sub> double  
67 ring, was derived from the ring-like classes. In parallel, the filaments were split into sets of classes  
68 showing either continuous or discontinuous course. The former were used for 3D reconstruction of  
69 a helical NC and its ~1.5-turn subsection, whereas the latter yielded reconstructions of a double-  
70 headed NC and a ring-capped NC. Thus, five different 3D maps - a double ring, a helical NC and  
71 its short subsection, a double-headed NC and a ring-capped NC - were obtained from the same  
72 data set (Figure 1c-g; Supplementary Figure 1).

### 73 Unique tripartite stabilisation of the RSV N oligomerisation inside a conserved N-hole

74 The 2.86 Å resolution map and the resulting atomic model of the N<sub>10</sub> double ring show that  
75 the N protomer and the entire N<sub>10</sub> ring are identical to the crystal structure, with 0.5-Å RMSD over  
76 378 backbone residues and the density of the last twelve residues (380-391) largely disordered.  
77 Accordingly, the RNA binding groove formed by the interface between the N-terminal and the C-  
78 terminal domains of N (NTD and CTD), and the “4-bases-in, 3-bases-out” RNA conformation  
79 remain unaltered.



80 Similarly to other *Mononegavirales*<sup>20,21</sup>, the N- and C-terminal extensions of RSV N, termed  
81 NTD-arm (residues 1-36) and CTD-arm (residues 360-391) (Figure 1h), interact with the laterally  
82 adjacent N protomers thereby stabilising their oligomeric assembly on the RNA strand by  
83 subdomain swapping (Figure 2a). The visible part of the CTD-arm of  $N_i$  lies on top of the CTD of  
84  $N_{i+1}$  implying that in a helical NC it should be situated in between consecutive turns<sup>4</sup>. In parallel, the  
85 NTD-arm of  $N_{i+1}$  inserts into a compact fold of the CTD of  $N_i$  from the ring interior and extends  
86 towards the CTD-arm of  $N_{i-1}$ . In this regard, a “latch-bolt type” interaction formed by an insertion of  
87 a loop from the NTD of  $N_{i-1}$  into an  $N_i$  cavity, termed N-hole, has been recently described for  
88 paramyxoviral NCs<sup>12,13,21</sup>, and is also present in filoviral NCs (Supplementary Figure 2). The  
89 structures of RSV and hMPV  $N_{10}$  rings<sup>22</sup> (PDB: 5FVC) indicate that pneumoviral NCs do actually  
90 possess a cognate N-hole formed by an Supplementary NTD-arm-proximal loop (residues 19-32 in  
91 RSV N), together with two short loops from the NTD (86-92) and the CTD (300-307). Likewise, in  
92 RSV and hMPV rings, a short loop from the NTD of  $N_{i-1}$  (residues 230-238 in RSV N) protrudes into  
93 the N-hole of  $N_i$  (Figure 2a, b), which demonstrates that the N-hole based interaction is conserved  
94 between *Paramyxo*-, *Filo*- and *Pneumoviridae* families (Supplementary Figure 2).

95 Deeper into the N-hole matter, the first atomic model of an RSV NC helix (PDB: 4BKK),  
96 derived from a crystal structure fit into a tomography-based featureless 68-Å pitch spiral,  
97 suggested a fascinating direct interaction between three consecutive protomers<sup>17</sup>. Specifically,  
98 R234 of  $N_{i-1}$  was predicted to bind both D221 of  $N_i$  and Y23 from  $N_{i+1}$ . Such a tripartite interaction  
99 between  $N_{i-1}$ ,  $N_i$  and  $N_{i+1}$  does not exist in paramyxo- and filoviral NCs, and to our knowledge has  
100 not been explicitly investigated for the hMPV  $N_{10}$  ring. Examination of our RSV double ring  
101 structure verifies the presence of the tripartite Y23-D221-R234 interaction and shows that it occurs  
102 inside the N-hole of  $N_i$  which carries D221; the loop 230-238 of  $N_{i-1}$  provides R234 while Y23 is  
103 contributed by the loop 18-32 of  $N_{i+1}$ , whereas Y23 on the equivalent loop of  $N_i$  points into the N-  
104 hole of  $N_{i-1}$  so that to bind R234 of  $N_{i-2}$  (Figure 2a). Surprisingly, despite a great resemblance  
105 between the RSV and the hMPV N-RNA rings, the latter contains no tripartite contact (Figure 2b).  
106 Indeed, although all loops are in place and Y23 is conserved, in hMPV N both D221 and R234 are  
107 replaced by serines making the interaction impossible (Figure 2c). Thus, an additional tripartite  
108 stabilisation of the “latch-bolt type” interaction seems to be a signature of the RSV NCs.

### 109 **Molecular determinants of the longitudinal NTD-NTD interaction**

110 In the double ring, the NTD-NTD stacking of two  $N_{10}$  rings, whose centers of gravity are 67  
111 Å apart, is assured by D1-symmetry-related  $\beta$ -sheets providing two opposing interacting H100  
112 residues and two R101-E122 hydrogen bonds (Figure 3). Interestingly, examination of the crystal  
113 structures of RSV and hMPV rings (Figure 3a-c; Supplementary Figure 3) reveals their bottom-to-  
114 bottom (NTD-NTD) stacking but with a tighter packing, with an inter-ring distance of 61 Å and 60 Å  
115 respectively. This compaction arises from an inter-ring rotation accompanied by a  $\beta$ -sheet insertion  
116 into inter-protomer grooves of the opposite ring (Figure 3a-c), which leads to a difference between  
117 the crystallographic inter-ring interface, based on a K91-D96 interaction, and the solution one.

118 2D classification of segments of filamentous RSV NC produced some 2D class averages  
119 featuring a clear seam, either across the filament stem or close to its end (Figure 1b). Particles with  
120 the stem-crossing seam yielded a 3.9 Å resolution map with a barbed end-to-barbed end junction  
121 of two NC helices (Figure 1e; Supplementary Figure 1), similar to the spiral clams described for  
122 *Paramyxoviridae* Sendai (SeV)<sup>13</sup>, NiV<sup>23</sup> and Newcastle disease (NDV)<sup>10</sup>. The particles with an

123 end-proximal seam gave a 3.8 Å resolution map of a helical NC capped by an N<sub>10</sub> ring (Figure 1d;  
124 Supplementary Figure 1), reminiscent of the semi-spiral clam observed for NiV NCs<sup>23</sup>.  
125 Remarkably, the mode of the longitudinal NTD-NTD interaction in the double rings, the double-  
126 headed and the ring-capped RSV NCs is conserved (Figure 3a, d, e), confirming that the interface  
127 delineated by cryo-EM is more reflective of the native structures than the crystal structure interface  
128 constrained by the crystal packing. In RSV, the NTD-NTD interface is however distinct from the  
129 one in the NiV, SeV and NDV clams, mediated by NTD loops which are absent in pneumoviral N  
130 (Supplementary Figure 4).

131 All *Mononegavirales* NCs are left-handed helices, with the CTDs and the 3'-end of the RNA  
132 oriented towards the pointed end of the filaments and the NTDs and the 5'-end towards the barbed  
133 ends<sup>20</sup>. The paramyxoviral clam-shaped assemblies were proposed to seed the growth of the  
134 double-headed helices from the 5' to the 3' end, protect the 5' end from nucleases<sup>10</sup> and support  
135 encapsidation of several NCs per virion<sup>24</sup>, also documented for RSV<sup>19,25</sup>. Thus, based on our  
136 structures, we designed two double mutants of N – H100E-R101D and H100E-E122R – and  
137 assessed their phenotypes in an RSV minigenome assay. While the first construct behaved  
138 similarly to the wild type N, the H100E-E122R mutation resulted in a circa 90% reduction of the  
139 polymerase activity (Supplementary Figure 5), which suggests a possible functional role of the  
140 NTD-NTD interactions in the RSV RNA synthesis.

#### 141 **Cryo-EM analysis reveals a non-canonical symmetry of the helical RSV NC**

142 Although at first glance, the 2D class averages of the RSV NCs with a continuous filament  
143 course suggest a paramyxoviral-like arrangement with a herringbone appearance and a ~70 Å  
144 pitch, their careful scrutiny shows that every ~1.5 turns (or ~100 Å) densities at either the left- or  
145 the right-hand side of the pattern are shifted inwards (Figure 1b; Supplementary Figure 6). The  
146 power spectrum (PS) of the 2D classes exhibit an expected layer line with the maximum close to  
147 the meridian at ~1/70 Å, attributable to the estimated pitch. Surprisingly however, the PS also  
148 features an additional layer line, with a strong maximum on the meridian, at ~1/100 Å, pinpointing a  
149 periodicity that should correspond to a ~100 Å rise (Supplementary Figure 6). Since geometrically  
150 the rise cannot be larger than the pitch, this implies that the measured value of the rise does not  
151 reflect the axial shift between two consecutive protomers. In principle, the ~100 Å periodicity could  
152 arise from stacking of short ~1.5-turn helices with a 70 Å pitch; however, no discontinuity and no  
153 isolated ~1.5-turn helices were observed in our cryo-EM images despite exhaustive particle picking  
154 and extensive 2D classification. Alternatively, if the NCs are continuous, they would be organised in  
155 ~1.5-turn asymmetric units composed of multiple N protomers.

156 3D reconstructions with a 100 Å rise as a starting value and a variable twist led to a solution  
157 with correct secondary structures of N, and a subsequent isolation of the straightest NCs yielded a  
158 final 3D map at an average resolution of 6.2 Å and a continuous RNA density (Figure 1f;  
159 Supplementary Figure 1; Figure 4; Supplementary Figure 6). This moderate resolution lies in the  
160 short-range order of the helical RSV NC. Indeed, an additional 3D refinement within a mask  
161 enclosing ~1.5 turns resulted in a 3.5 Å average resolution map of a five protomer-subsection in  
162 the middle of the mask, which however rapidly deteriorates towards the mask periphery due to a  
163 progressive loss of regularity (Figure 1g; Supplementary Figure 1). The structure of the N-RNA  
164 protomer is again largely the same as in the crystal, with RMSD less than 1 Å over 378 backbone  
165 residues for each of the five protomers, and the inter-protomer contacts maintained.

166 The determined helical parameters and an inspection of the map and the model of the NC  
167 helix (Figure 1f; Supplementary Figure 1; Figure 4a, b) allows to interpret the peculiar experimental  
168 class averages and the PS (Supplementary Figure 6). Indeed, the RSV NC reveals itself as a right-  
169 handed “super-helix”, defined by a 105.3 Å rise and a 149.5° twist, generated by helical repetition  
170 of asymmetric units composed of 16 N protomers forming a ~1,5 turns left-handed spiral staircase.  
171 Inside each asymmetric unit, the protomer arrangement is similar to that observed in paramyxoviral  
172 helical NCs. Amazingly however, the position and the orientation of the protomers relative to the  
173 filament axis as well as the axial shift between two consecutive protomers undergo a specific and  
174 coordinated variation (Figure 4c). For example, the tilt of the protomers varies between ~40° for the  
175 most “standing” (N<sub>6</sub> and N<sub>7</sub>) and ~65° for the most “lying” (N<sub>11</sub>, N<sub>12</sub> and N<sub>13</sub>), whereby the most lying  
176 subunits are the closest to the helical axis. The combination between the helical parameters and  
177 the variation profile of the protomer poses in the asymmetric unit engenders an axial alternation of  
178 regions where two neighbouring turns are the closest to each other and regions where they are  
179 spread further apart. This alternation occurs circa every 105 Å/1.5 turns/16 protomers and  
180 manifests itself by clamping the helix on a side, thereby increasing the gaps above and below the  
181 clamps. The helical propagation of the clamps and gaps confers the RSV NC its unique  
182 appearance, accentuated by an inward shift of the densities corresponding to projections of the  
183 most lying subunits in the 2D class averages (Figure 4; Supplementary Figure 6). The variation of  
184 the protomer tilt is visible even on the five protomer-subsection of the helix (Supplementary Figure  
185 1). The numbering of the protomers in the asymmetric unit is done based on the correspondence  
186 between their axial tilts in the double-headed NC, where the first barbed-end subunit is clearly  
187 identified, and in the helical NC (Supplementary Figure 7).

## 188 **Periodic variations of RNA accessibility and the CTD-arm-mediated inter-turn interactions in** 189 **helical RSV NCs**

190 One consequence of this NC organisation is particularly conspicuous: in the configuration  
191 where the lower-turn protomers are lying and shifted inwards and the upper-turn protomers  
192 standing above, the RNA of the lying protomers is hidden inside the clamps; in contrast, in the  
193 standing-protomer configuration the RNA appears exposed (Figure 5). Another striking observation  
194 (Figure 5) is that three consecutive “nearly standing” protomers in the lower turn interact with the  
195 upper turn through their CTD-arms, which are therefore better defined than in the other protomers  
196 where they are not constrained. Indeed, inspection of the CTD-arm densities in the five protomer-  
197 subsection and in the entire asymmetric unit shows that the definition of the CTD-arm of each  
198 protomer N<sub>i</sub> depends on the position and orientation of the protomer(s) located immediately above  
199 (*i.e.* N<sub>i+10</sub>, N<sub>i+11</sub> and N<sub>i+12</sub>) (Figure 5). Although modelling of the CTD-arm after the residue 379  
200 <sup>4</sup> would be unreliable, a rigid body fit into the subsection map indicates that the three “nearly  
201 standing” subunits of the helical RSV NCs do show densities extending beyond. The CTD-arms of  
202 the subunits N<sub>2</sub> and N<sub>3</sub> (equivalent to N<sub>18</sub> and N<sub>19</sub> in Figures 4 and 5) seem to contact almost the  
203 same zones in the subunits N<sub>13</sub> and N<sub>14</sub>, (*i.e.* N<sub>29</sub> and N<sub>30</sub>) respectively, whereas the CTD-arm of the  
204 subunit N<sub>4</sub> (*i.e.* N<sub>20</sub>) falls nearly in between the upper subunits N<sub>14</sub> and N<sub>15</sub> (*i.e.* N<sub>30</sub> and N<sub>31</sub>)  
205 because of the singular helical symmetry of the RSV NC (Figure 5).

## 206 Shortening of the CTD-arm transforms the RSV NCs into paramyxoviral-like canonical 207 helices

208 Since the structure of the helical RSV NC demonstrates the involvement of the CTD-arm in  
209 the longitudinal contacts, we supposed that shortening of this arm may abrogate inter-turn  
210 interactions and thereby transform the non-canonical helix with asymmetric units composed of 16  
211 N arranged in  $\sim 1.5$  turns into a classical helix with one N per asymmetric unit (Supplementary  
212 Figure 6). Considering the previously published data on the major role played by the last 20  
213 residues of N in the RSV polymerase activity and the critical requirement of the N residue L370 for  
214 the stabilisation of the N<sup>0</sup>P complex <sup>26</sup>, we opted for a C-terminally truncated N1-370 construct. The  
215 most glaring differences with the cryo-EM images of the full-length (FL) N-RNA were the  
216 appearance of two new types of filaments - the herringbone-like helices and a major population of  
217 unforeseen rigid stacks of rings (Figure 6; Supplementary Figure 1). The class averages and the  
218 PS of the helical NC formed by the N1-370 mutant are similar to those of paramyxoviral NCs, and  
219 the helical parameters of the resulting 4.3 Å resolution 3D map, 6.58 Å rise and  $-36^\circ$  twist, closely  
220 agree with the ones derived from the FL “super-helix” (Supplementary Figure 6). Moreover, the  
221 mutant manifests no longitudinal contacts (Figure 6a-c), validating the structure-based hypothesis  
222 that it is the CTD-arm of the RSV N that, by periodically linking two successive helical turns,  
223 induces the non-canonical symmetry of the RSV NC and the resulting systematic variations in the  
224 RNA accessibility.

225 The rigid polymers coexisting with these helices are D10-symmetric and formed by  
226 alternating bottom-to-bottom and top-to-top packing of N<sub>10</sub> rings (Figure 6d-f). Thus, these stacks  
227 are very different from those observed for digested mumps N-RNA rings packed top-to-bottom <sup>12</sup>.  
228 The ensuing 2.8 Å resolution cryo-EM map shows that the NTD-NTD stacked units are  
229 indistinguishable from the N<sub>10</sub> double rings of FL N until the end of the  $\alpha$ -helix 344-358 and the  
230 beginning of the CTD-arm. In the rings and helical assemblies of the FL N, the CTD-arm of the  
231 subunit N<sub>i</sub> protrudes straight onto the top of the CTD of N<sub>i+1</sub>. However, in the stacked rings of the  
232 N1-370 mutant, the truncated CTD-arm sharply pivots away and, instead of engaging into a lateral  
233 interaction, tucks into an identical site but on a CTD of the opposite ring in the stack. The pivoting  
234 of all CDT-arms tightly locks the adjacent rings together through their CTDs, such as to generate a  
235 polymer built of layers of inversely oriented N<sub>10</sub> rings engaged both in NTD-NTD and CTD-CTD  
236 contacts; the latter are additionally stabilised by binding between CTD-arms of two opposing  
237 protomers, in particular through a Y365-Y365 stacking (Figure 6g, h).

## 238 Discussion

239 The major finding of this work was the non-canonical helical organisation of the RSV NC,  
240 generated by  $\sim 1.5$ -turn asymmetric units composed of 16 N protomers, which undergo a concerted  
241 variation of their poses while remaining in quasi-equivalent environments. This unique symmetry,  
242 together with the great flexibility of the NCs, complicates their high resolution analysis, and is  
243 totally different from those described for other *Mononegavirales* NCs. Excitingly, the arrangement  
244 of the RSV NC is reminiscent of the one proposed for the Dahlemense strain of tobacco mosaic  
245 virus (TMV), and may be similarly considered in terms of a periodic deformation of a regular helical  
246 structure <sup>27</sup>. In the Dahlemense TMV model, the additional meridional reflexions appear on the  
247 layer lines halfway between those of the common TMV and the asymmetric unit contains exactly  
248 two turns. Likewise, for the RSV NC the maximum on the meridian is observed at two thirds of the



249 layer line of the expected pitch and the asymmetric unit contains ~1.5 turns. The exterior distortion  
250 proposed in the Dahlemense TMV model is explained by the inside and outside sets of inter-turn  
251 interaction being incompatible with the same periodicity, whereas the common TMV does not have  
252 any axial outside interactions. The C-terminally truncated RSV NC mutant also has no inter-turn  
253 interactions and features a canonical helical symmetry with equivalent environments for each N  
254 protomer. In contrast, in the FL NC, the CTD-arms at the filament interior are periodically involved  
255 in axial interactions with the upper turn, which induces a global structural reorganisation leading to  
256 tilting and inwards shifting of certain protomers and manifesting itself as a helical distortion at the  
257 NC exterior. Continuing the parallel, the stability of the observed full-length RSV NC structure  
258 would indicate that “the decrease in the free energy upon forming some additional bonds is greater  
259 than the increase in the free energy required to move the subunits into the slightly different, but  
260 quasi-equivalent positions”<sup>27</sup>.

261 The helical NC, together with the RNA polymerase L, its phosphoprotein cofactor P and the  
262 transcription factor M2-1, form the RSV RNA synthesis complex that constitutes the minimal  
263 infectious unit of the virus. P acts as a central hub by tethering L to the NC template, chaperoning  
264 neosynthesised N such as to keep it monomeric and RNA-free (N<sup>0</sup>) for specific nascent RNA  
265 encapsidation, and recruiting M2-1<sup>28</sup>. The matrix protein M is thought to direct RSV assembly and  
266 budding by interacting both with the NC-bound P and with the envelope glycoprotein F<sup>29,30</sup>. Recent  
267 cryo-ET analysis of filamentous RSV virions demonstrated that M is organised in a helical array  
268 that would coordinate helical ordering of glycoprotein spikes<sup>19</sup>. In addition, in *Paramyxoviridae*, M  
269 was shown to directly bind the CTD-arm of N<sup>31,32</sup>. Thus, RSV M may potentially also influence the  
270 helical parameters of the NC upon the viral cycle via a direct or a P-mediated interaction.  
271 Noteworthy, the binding pocket of P on the NC helix is situated far both from the CTD-arm itself  
272 and from its binding site to the upper helical turn<sup>33,34</sup>.

273 In order to bind M or another viral or host factor, the end of the CTD-arm of N would need to  
274 escape outside the NC through an interstice between two turns, as shown for *Paramyxo-* and  
275 *Filoviridae*, which however have a much longer CTD extension. Here we showed that the non-  
276 canonical helical organisation of the RSV NC is engendered by the last 20 residues of the CTD-  
277 arm of N. Considering high similarity between RSV and hMPV N, we suppose that all  
278 *Pneumoviridae* NCs adopt an analogous arrangement. Our structures and the structural homology  
279 between RSV and hMPV N<sup>0</sup>P complexes inferred from biochemical studies<sup>26</sup> suggest that,  
280 similarly to the situation in hMPV<sup>22</sup>, binding of the N-terminal peptide of RSV P to N<sup>0</sup> would hamper  
281 its self-oligomerisation by preventing the CTD-arm from subdomain swapping and flipping it  
282 downwards along the core of N such as to block the RNA binding<sup>22</sup>. In contrast, in the stacked N1-  
283 370 rings, the truncated CTD-arm rotates upwards to dock into dedicated subdomain swapping site  
284 on the opposite N protomer from the ring above. Thus, comparison of these structures indicates  
285 that the CTD-arm is able to explore a large angular space (Figure 6i).

286 While the truncation of the CTD-arm is not supposed to occur *in vivo*, the high rotational  
287 freedom of the CTD-arm hints to a possibility of its reorientation upon interaction with viral or host  
288 factors. One may therefore envision a temporary capping of the pointed end of the NC helix by an  
289 N-RNA ring or a second NC through a CTD-CTD interaction, such as to protect the 3' end of the  
290 RNA from host antiviral responses. This would however imply an uncapping of the 3' end in order  
291 to initiate transcription or replication from the respective promoters that reside at the pointed end of  
292 the NC, by either P or L or another factor. The 5' end, in its turn, would be protected inside the

294 double-helical and 5' ring-capped NCs formed through NTD-NDT interactions. Such top-to-top  
295 and/or bottom-to-bottom assemblies of RSV NCs would be consistent with the observations in the  
296 RSV virion<sup>19,25</sup> and in the infected cells<sup>35</sup>.

297 The most obvious consequence of the non-canonical RSV NC structure is the periodic  
298 variation of the RNA accessibility, the RNA binding groove of N being severely obstructed in the  
299 inwards shifted lying protomers and exposed in the standing ones. While this difference in access  
300 to the RNA should inevitably influence pneumoviral synthesis by L during its gliding along the NC,  
301 the exact mechanistic implications of the observed variations are difficult to conceptualise. Indeed,  
302 because of the limited long-range order of the RSV NC helices, any prediction of the protomer  
303 poses based on the numbering in the clam and semi-clam structures as adopted here can only be  
304 reliable for the protomers located very close to the barbed, 5'-end. Even an attempt to estimate the  
305 tilt of the protomer containing the most 5'-end proximal gene start (GS), at the onset of the gene of  
306 L, would be too error-prone. In addition, considering that the CTD-arm is required both for the inter-  
307 turn interactions, responsible for the non-canonical NC organisation, and for the prevention of the  
308 premature RNA encapsidation by N<sup>0</sup>, the mechanisms behind the strong inhibition of the RSV RNA  
309 polymerase activity by mutations and truncation of the CTD-arm<sup>26</sup> are certainly convoluted.

310 Finally, it is essential to keep in mind that *in cellula* the RSV RNA synthesis occurs in virally  
311 induced cytoplasmic inclusions considered as active viral factories and formed by liquid-liquid  
312 phase separation<sup>36-38</sup>. In line with the structural polymorphism of the purified NCs obtained by  
313 heterologous expression described here, we hypothesise that particular functional states of the  
314 NCs can be enriched in VFs depending on the progress of the viral cycle or the status of certain  
315 cellular pathways. The material properties of biomolecular condensates may also influence the NC  
316 structures. Thus, in future it is essential to combine cryo-EM investigation of the structure-function  
317 relationships of the RSV synthesis machinery *in vitro* with its cryo-ET analysis in the cellular  
318 context.

## 319 **Methods**

### 320 **Plasmids and baculoviruses**

321 The codon-optimized sequence coding for the wild type (WT) N (strain Long) was syn-  
322 thesised (GenScript) and cloned in the pFastBac Dual vector under the control of the polyhedrin  
323 promoter at BamHI and Sall sites. A stop codon was inserted after amino acid residue 370 by site  
324 directed mutagenesis using Q5 Site-Directed Mutagenesis Kit (NEB), in order to express the trun-  
325 cated N1-370 construct. Recombinant baculoviruses were recovered using the Bac-to-Bac bac-  
326 ulovirus expression system (Invitrogen). N WT or N1-370 bacmids were obtained after transforma-  
327 tion of DH10EMBacY bacteria (Geneva Biotech). Recombinant baculoviruses were recovered after  
328 transfection of High Five cells using Cellfectin reagent (ThermoFisher Scientific) and amplification.

329 The plasmid pGEX-PCT (C-terminal residues 161-241 of RSV P protein), used for bacterial  
330 expression of the recombinant GST-PCT, has been described previously<sup>39,40</sup>. Plasmids for  
331 minigenome assay expressing hRSV N, P, M2-1, and L are designated pN, pP, pM2-1 and pL, and  
332 have been described previously<sup>41,42</sup>. The pM/Luc subgenomic minigenome which encodes the  
333 firefly luciferase (Luc) reporter gene under the control of the M/SH gene start sequence has also  
334 been described<sup>43</sup>. The plasmids encoding N mutants pNH100E, pNH100E-R101D, pNH100E-

335 E122R, and pN1-370 were generated using Q5 Site-Directed Mutagenesis Kit (NEB). Primers are  
336 shown in Supplementary Table 1.

### 337 **Protein expression and purification**

338 Recombinant GST-PCT was used for purification of recombinant N expressed in insect  
339 cells. Briefly, *Escherichia coli* BL21 (DE3) bacteria (Novagen) transformed with the pGEX-PCT  
340 plasmid were grown at 37 °C, in 2xYT medium with 100 µg/ml ampicillin. After 7 h, an equal  
341 volume of 2xYT medium with 100 µg/ml ampicillin and 80 µg/ml of isopropyl β-d-1-  
342 thiogalactopyranoside (IPTG) was added to induce protein expression, before overnight incubation  
343 of the culture at 28 °C. Bacteria were harvested by centrifugation at 3000 g for 30 min at 4 °C,  
344 resuspended for 30 min in lysis buffer (Tris 50 mM, NaCl 60 mM, EDTA 1 mM, 0.1 % Triton X-100,  
345 DTT 2 mM, pH 7.8, anti-proteases (Roche)), and sonicated on ice. Benzonase was then added to  
346 the lysate, followed by a 30 min incubation at room temperature. After centrifugation at 10 000 g for  
347 30 min at 4 °C, the supernatant was incubated with Glutathione-Sepharose 4B beads (Cytiva) for 3  
348 h at 4°C. The beads were washed once in the lysis buffer and twice in PBS 1X buffer. Beads were  
349 resuspended in PBS 1X and stored at 4 °C.

350 For expression of N, High Five cells (ThermoFisher Scientific) were infected at a multiplicity  
351 of infection of 2 for 72 h with the baculovirus coding either for the WT RSV N or the N1-370  
352 construct. Cells were washed in TEN buffer (50 mM Tris-HCl, 10 mM EDTA, 150 mM NaCl, pH 7.4)  
353 and centrifuged at 3000 g for 5 min. The cells were resuspended in 10 ml of lysis buffer (TEN  
354 buffer, NP-40 at 0.6 % (v/v), anti-proteases/phosphatases (Roche), RNase (200 µg/ml, Invitrogen),  
355 DNase (5 units/ml, Promega)) and incubated 40 min at 37 °C. The lysate was clarified by  
356 centrifugation at 14 000 g for 15 min at 4 °C, then incubated for 3 h at 4 °C with the GST-PCT  
357 beads previously rinsed in TEN buffer. The GST-PCT beads were then washed once in lysis buffer  
358 and twice in TEN buffer and then incubated in TEN buffer in the presence of thrombin (Sigma), for  
359 72 h at 4 °C. The supernatant was collected and concentrated using a column with a MWCO of  
360 100 kDa (Sartorius).

### 361 **Minigenome assay**

362 BSRT7/5 cells, a cell line derived from the BHK-21 cells, constitutively expressing the T7  
363 RNA polymerase<sup>44</sup>, were used for the minigenome assay. Cells were grown in Dulbecco's modified  
364 Eagle's medium (Lonza) with 2 mM L-glutamine, antibiotics and 10 % fetal bovine serum. Cells at  
365 90 % confluence in 96-well plate were transfected using Lipofectamine 2000 (Invitrogen) according  
366 to manufacturer's instructions with the following plasmid mixture: 62.5 ng of pM/Luc, pP and pN  
367 (WT or N mutants), 31.3 ng of p L, 15.6 ng of pM2-1, and 15.6 ng of pRSV-β-galactosidase  
368 (Promega) for transfection efficiency normalisation. After 24 h, the cells were lysed in luciferase  
369 lysis buffer (30 mM Tris pH 7.9, 10 mM MgCl<sub>2</sub>, 1 mM DTT, 1% Triton X-100, and 15% glycerol).  
370 After addition of the substrate (Luciferase assay system, Promega), the luciferase activities were  
371 determined for each cell lysate with an Infinite 200 Pro (Tecan, Männedorf, Switzerland) and  
372 normalised based on β-galactosidase (β-Gal) expression. Four replicates were carried out and  
373 mean values were calculated. The analysis was done using Excel (Microsoft) and Prism 9  
374 (GraphPad). Expression of WT and mutant N was assessed by Western blot using a rabbit anti-N  
375 antiserum<sup>39</sup> and a mouse monoclonal anti-tubulin antibody (Sigma), revealed by incubation with  
376 anti-rabbit and anti-mouse antibodies coupled to HRP (SeraCare).

### 377 **Cryo-EM data collection**

378 3  $\mu\text{L}$  of the purified FL or truncated RSV NC sample were applied to a glow-discharged  
379 R2/1 300 mesh holey carbon copper grid (Quantifoil Micro Tools GmbH) and plunge-frozen in liquid  
380 ethane using a Vitrobot Mark IV (FEI) operated at 100% humidity at room temperature. Datasets  
381 were recorded at the EM platform of the IBS Grenoble, on a Glacios microscope (Thermo  
382 Scientific) equipped with a K2 summit direct electron detector (Gatan) operated in counting mode.  
383 A summary of cryo-EM data collection parameters can be found in Supplementary Table 2. Movies  
384 were acquired with a total dose of  $42 \text{ e}^-/\text{\AA}^2$  and a defocus range of  $-0.7$  to  $-2.4 \mu\text{m}$ , at  $1.145 \text{ \AA}/\text{pixel}$   
385 at the specimen level. Cryo-EM data on the N1-370 mutant was acquired with using beam-tilt  
386 induced image-shift protocol (9 images for each stage movement). Micrographs were manually  
387 screened based on the presence of particles, amount of contamination and apparent beam-  
388 induced movement, resulting in a total of 11,386 selected micrographs for the FL NCs and 6,312  
389 selected micrographs for N1-370 NCs. A visual inspection of the full-length NC dataset showed the  
390 presence of at least four types of assemblies – helical NCs, double-headed NCs, ring-capped NCs  
391 and double rings – which were processed separately. Similarly, the helical NCs and the stacks  
392 formed by the N1-370 mutant were also processed separately.

### 393 **Image analysis of the non-canonical helical FL RSV NCs**

394 For the helical NCs, an initial manual picking of 800 filaments from a subset of micrographs  
395 was performed with EMAN2 `e2heliboxer.py`<sup>45</sup> and used to create a training dataset for crYOLO<sup>46</sup>,  
396 which was subsequently used for the picking on all micrographs, resulting in 97,280 filaments  
397 traced. The filament coordinates were then used for particle extraction in RELION<sup>47</sup> with a binning  
398 to a boxsize of 128 pixels (corresponding to  $3.04 \text{ \AA}/\text{pixel}$ ) and a  $15 \text{ \AA}$  distance between boxes. A  
399 total of 1,406,835 helical segments were picked and iteratively classified in RELION, keeping the  
400 straightest 2D class averages at each round, which resulted in 544,972 selected segments. The  
401 sum of PS of the aligned segments corresponding to 27 classes selected based on estimated  
402 resolution and number of particles was calculated with RELION and inspected with `bshow`<sup>48</sup>,  
403 showing a similar pattern for all selected classes. Subsequent processing steps were carried out in  
404 cryoSPARC<sup>49</sup>. After estimating the helical rise to  $\sim 100 \text{ \AA}$  from the PS (Supplementary Figure 6),  
405 the helical twist was determined on the imported binned segment selection whereby multiple  
406 helical 3D refinements were run in parallel using as initial symmetry parameters a fixed  $100 \text{ \AA}$  rise  
407 and varying the twist from  $60$  to  $180^\circ$  with a  $10^\circ$  step. The crystal structure of the RSV N-RNA ring  
408<sup>4</sup> was used to validate the 3D maps after refinement, choose the best one for further analysis and  
409 impose the correct handedness. An examination of this intermediate map and of its refined  
410 symmetry parameters ( $\sim 105 \text{ \AA}$  rise and  $\sim 150^\circ$  twist) enabled us to understand that the helical RSV  
411 NC in our cryo-EM images was in fact a right-handed “super-helix”, with an asymmetric unit  
412 corresponding to a left-handed helix composed of  $\sim 16$  adjacent N protomers. Since the rise of this  
413 super-helix was larger than the initially defined distance between successive segments, a new  
414 template-based picking with the projections of this intermediate map was done in cryoSPARC,  
415 using  $105 \text{ \AA}$  as a distance between segments. The picking yielded 769,699 helical segments that  
416 were cleaned down to 546,489 particles by further 2D classification. This cleaned particle set was  
417 further processed in two different ways. First, it was subjected to a heterogeneous refinement  
418 using 5 classes, with no symmetry imposed, in order to select the better resolved and most regular



419 particles. The three most similar classes were combined into a final set of 389,540 segments that  
420 was used for a final helical refinement to an average resolution of 6.2 Å (Fourier Shell Correlation  
421 (FSC) at 0.143), which was sharpened with a B-factor of  $-470 \text{ \AA}^2$  for visualisation and rigid body fit  
422 of the crystal structure. This map reflects the non-canonical helical RSV NC. Second, because of  
423 the flexibility of the super-helix, we decided to focus on one asymmetric unit and performed a  
424 refinement with a mask enclosing 16 N protomers created from the helical map. This resulted in a  
425 final map, with a subsection of five consecutive well-defined protomers at its centre that had an  
426 average resolution of 3.5 Å (FSC at 0.143). The five protomer-subsection map, sharpened with a  
427 B-factor of  $-94 \text{ \AA}^2$ , was used for subsequent model building and structural analysis.

428 The variation of the axial shifts between two consecutive protomers and their distances  
429 from the helical axis (Figure 4c) was calculated based on the coordinates of the centers of gravity  
430 of each protomer obtained from the rigid body-fitted crystal structure. To estimate the tilt of each  
431 protomer relative to the helical axis, two C $\alpha$  atoms (from G106 and H274) were picked on the long  
432 inertia axis and the angle between the vector formed by these two atoms and the helical axis was  
433 computed.

#### 434 **Image analysis of the double-headed helical NCs and ring-capped NCs**

435 Inspection of the cryoSPARC analysis of the 2D classification from the template-based  
436 picking of helical segments, allowed us to identify a 2D class average, corresponding to a class of  
437 10,718 particles, that showed features of a double-headed helix (potentially mixed with ring-capped  
438 helices). This class was used for template-based picking, giving a set of 176,614 particles that was  
439 iteratively cleaned by 2D classification down to 12,699 particles, mostly by removing double ring  
440 side views. From these particles, an *ab initio* reconstruction was calculated, followed by non-  
441 uniform refinement, which gave a  $\sim 7 \text{ \AA}$  resolution map used to create templates to re-pick the  
442 entire dataset. The resulting over 200,000 particles were classified down to 52,127 particles, with a  
443 mixture of classes showing double-headed features and classes showing ring-capped helices.  
444 Because the separation between double-headed helices and ring-capped helices by 2D  
445 classification only did not seem entirely satisfactory, we imported the particles into RELION and  
446 iteratively performed 3D classifications until obtainment of two stable particle subsets (and one  
447 subset discarded as junk particles). This procedure resulted in 22,162 particles of ring-capped  
448 helices and 25,338 particles of double-head helices. These were imported back into cryoSPARC  
449 and used for final non-uniform refinements using the RELION 3D class averages as initial  
450 references. The average resolutions (FSC at 0.143) of the resulting 3D reconstructions of the ring-  
451 capped and the double-headed helices were 3.9 Å and 3.8 Å respectively; finally, the maps were  
452 respectively sharpened with a B-factor of  $-35 \text{ \AA}^2$  and  $-54 \text{ \AA}^2$ .

453 In order to establish the correspondence between the protomers in the double-headed NCs  
454 and in the non-canonical helical NCs (and thereby to allow the numbering of the protomers in the  
455 asymmetric unit of the non-canonical helix as in Figure 4), we matched each of the 16 rigid body-  
456 fitted protomers of the non-canonical NC onto the rigid body-fitted protomers of the double-headed  
457 NCs (alignment done on one protomer) and calculated the RMSD between the two structures over  
458 five consecutive protomers. The lowest RMSD value (3.39 Å) indicated the register of the N  
459 protomers in the double-headed NCs compared to the helical NC.

#### 460 **Image analysis of the RSV N-RNA double rings**

461 In cryoSPARC, manual picking of 50 side views of double rings followed by 2D  
462 classification was used to create a 2D template for automatic picking, giving 23,704 particles after  
463 cleaning by 2D classification. These particles were used for *ab initio* 3D reconstruction followed by  
464 refinement and new particle picking using the refined map projections. Iterative 2D classification  
465 gave a set of 57,896 side views. Ring-like top views were not considered because they could  
466 potentially correspond to single rings or short helices instead of double rings. The selected side  
467 views were cleaned down to 47,212 particles by an additional 3D classification step in order to  
468 remove undetected potential C11-symmetric rings or short helices mixed with the C10-symmetric  
469 double ring side views. A final non-uniform refinement led to a 3D reconstruction at an average  
470 resolution of 2.9 Å (FSC at 0.143), sharpened with a B-factor of -96 Å<sup>2</sup>.

#### 471 **Image analysis of the canonical helices formed by the N1-370 mutant**

472 In cryoSPARC, manual picking of 200 helical segments followed by 2D classification was  
473 used to prepare templates for the filament tracer job. Two rounds of 2D classification and re-  
474 picking were then performed to yield a set of 471,549 helical segments used for initial  
475 reconstruction. Different helical symmetries ranging from 9 to 11 subunits per turn with a starting  
476 pitch of 60 Å were tested by running multiple helical refinements, and only the refinement starting  
477 at 10 subunits per turn gave an interpretable map with visible secondary structures. This map was  
478 used to generate 2D projections for a final template-based filament tracer job, which gave, after  
479 keeping only the straightest helical segments by iterative 2D classification steps, a final set of  
480 329,706 segments. The last refinement was run with a mask enclosing 30% of the segment length,  
481 giving a reconstruction at an average resolution of 4.3 Å (FSC at 0.143), sharpened with a B-factor  
482 of -155 Å<sup>2</sup>. The refined helical parameters - a -36° twist and a 6.58 Å rise – are very similar to the  
483 ones calculated from the helical parameters of the non-canonical helical NC formed by the FL N,  
484 assuming one protomer per asymmetric unit (-35.7° twist and 6.58 Å rise).

#### 485 **Image analysis of the N1-370 mutant stack**

486 A 2D class average corresponding to stacked rings derived from an automatic picking of  
487 helical segments in cryoSPARC was used for template-based particle picking, followed by 2D  
488 classification and re-picking until a stable subset of 81,918 particles was obtained. *Ab initio* 3D  
489 reconstruction followed by refinement with imposed D10 symmetry as well as defocus refinement  
490 gave a final 3D map at an average resolution of 2.8 Å (FSC at 0.143), which was sharpened with a  
491 B-factor of -99 Å<sup>2</sup>.

#### 492 **Map visualisation, local resolution calculation, model building and refinement**

493 For all final maps, the local resolution was calculated in cryoSPARC. The most interpretable  
494 maps were used for further structural analysis. The crystal structure of the N-RNA monomer (PDB:  
495 2WJ8, chain S) was rigid-body fitted in the maps with Chimera<sup>50</sup>. Where appropriate, refinement  
496 was performed using the Phenix software package<sup>51</sup> and manual correction in Coot<sup>52</sup>. At different  
497 processing stages, the structures were inspected with Chimera and bsoft<sup>48</sup>, and figures were done  
498 using ChimeraX<sup>53</sup>.

## 499 **Data Availability**

500 All data presented in this study are included in the published article and its supplementary  
501 information, and are available from the corresponding author on request.

## 502 **Statistics and reproducibility**

503 Data was collected on independent experiments. Statistics details are presented in the  
504 Methods section and in the figure legends where appropriate.

## 505 **References**

- 506 1. Li, Y. *et al.* Global, regional, and national disease burden estimates of acute lower  
507 respiratory infections due to respiratory syncytial virus in children younger than 5 years in  
508 2019: a systematic analysis. *Lancet* **399**, 2047–2064 (2022).
- 509 2. Busack, B. & Shorr, A. F. Going Viral—RSV as the Neglected Adult Respiratory Virus.  
510 *Pathogens* **11**, 1324 (2022).
- 511 3. Afonso, C. L. *et al.* Taxonomy of the order Mononegavirales: update 2016. *Arch. Virol.* **161**,  
512 2351–2360 (2016).
- 513 4. Tawar, R. G. *et al.* Crystal structure of a nucleocapsid-like nucleoprotein-RNA complex of  
514 respiratory syncytial virus. *Science* **326**, 1279–1283 (2009).
- 515 5. Gutsche, I., le Mercier, P. & Kolakofsky, D. A paramyxovirus-like model for Ebola virus  
516 bipartite promoters. *PLOS Pathog.* **16**, e1008972 (2020).
- 517 6. Jamin, M. & Yabukarski, F. *Nonsegmented Negative-Sense RNA Viruses—Structural Data*  
518 *Bring New Insights Into Nucleocapsid Assembly. Advances in Virus Research* **97**, (Elsevier  
519 Inc., 2017).
- 520 7. Gutsche, I. *et al.* Near-atomic cryo-EM structure of the helical measles virus nucleocapsid.  
521 *Science* **348**, 704–7 (2015).
- 522 8. Wan, W. *et al.* Structure and assembly of the Ebola virus nucleocapsid. *Nature* **551**, 394–  
523 397 (2017).
- 524 9. Sugita, Y., Matsunami, H., Kawaoka, Y., Noda, T. & Wolf, M. Cryo-EM structure of the Ebola  
525 virus nucleoprotein-RNA complex at 3.6 Å resolution. *Nature* **563**, 137–140 (2018).
- 526 10. Song, X. *et al.* Self-capping of nucleoprotein filaments protects the newcastle disease virus  
527 genome. *Elife* **8**, 1–19 (2019).
- 528 11. Desfosses, A. *et al.* Assembly and cryo-EM structures of RNA-specific measles virus  
529 nucleocapsids provide mechanistic insight into paramyxoviral replication. *Proc. Natl. Acad.*  
530 *Sci. U. S. A.* **116**, 4256–4264 (2019).
- 531 12. Shan, H. *et al.* Structural plasticity of mumps virus nucleocapsids with cryo-EM structures.  
532 *Commun. Biol.* **4**, 1–11 (2021).
- 533 13. Zhang, N. *et al.* Structure and assembly of double-headed Sendai virus nucleocapsids.  
534 *Commun. Biol.* **4**, 1–10 (2021).

- 535 14. Zinzula, L. *et al.* Cryo-EM structure of the cetacean morbillivirus nucleoprotein-RNA  
536 complex. *J. Struct. Biol.* **213**, (2021).
- 537 15. Fujita-Fujiharu, Y. *et al.* Structural insight into Marburg virus nucleoprotein–RNA complex  
538 formation. *Nat. Commun.* **13**, 1–9 (2022).
- 539 16. Zhou, K. *et al.* Atomic model of Vesicular Stomatitis Virus and Mechanism of Assembly. *Nat.*  
540 *Commun.* **13**, 5980 (2022).
- 541 17. Bakker, S. E. *et al.* The respiratory syncytial virus nucleoprotein-RNA complex forms a left-  
542 handed helical nucleocapsid. *J. Gen. Virol.* **94**, 1734–1738 (2013).
- 543 18. Liljeroos, L., Krzyzaniak, M. A., Helenius, A. & Butcher, S. J. Architecture of respiratory  
544 syncytial virus revealed by electron cryotomography. *Proc. Natl. Acad. Sci. U. S. A.* **110**,  
545 11133–11138 (2013).
- 546 19. Conley, M. J. *et al.* Helical ordering of envelope-associated proteins and glycoproteins in  
547 respiratory syncytial virus. *EMBO J.* 1–13 (2021).
- 548 20. Bloyet, L. M. The nucleocapsid of paramyxoviruses: Structure and function of an  
549 encapsidated template. *Viruses* **13**, (2021).
- 550 21. Li, T. & Shen, Q.-T. Insights into paramyxovirus Nucleocapsids from diverse assemblies.  
551 *Viruses* **13**, (2021).
- 552 22. Renner, M. *et al.* Nucleocapsid assembly in pneumoviruses is regulated by conformational  
553 switching of the N protein. *Elife* **5**, 1–12 (2016).
- 554 23. Ker, D. S., Jenkins, H. T., Greive, S. J. & Antson, A. A. CryoEM structure of the Nipah virus  
555 nucleocapsid assembly. *PLoS Pathog.* **17**, 1–19 (2021).
- 556 24. Cox, R. M. & Plemper, R. K. Structure and organization of paramyxovirus particles. *Curr.*  
557 *Opin. Virol.* **24**, 105–114 (2017).
- 558 25. Loney, C., Mottet-Osman, G., Roux, L. & Bhella, D. Paramyxovirus Ultrastructure and  
559 Genome Packaging: Cryo-Electron Tomography of Sendai Virus. *J. Virol.* **83**, 8191–8197  
560 (2009).
- 561 26. Esneau, C. *et al.* Biochemical characterization of the respiratory syncytial virus N0-P  
562 complex in solution. *J. Biol. Chem.* **294**, 3647–3660 (2019).
- 563 27. Caspar, D. L. D. & Holmes, K. C. Structure of dahlemense strain of tobacco mosaic virus: A  
564 periodically deformed helix. *J. Mol. Biol.* **46**, 99–133 (1969).
- 565 28. Decool, H. *et al.* Interactions between the Nucleoprotein and the Phosphoprotein of  
566 Pneumoviruses: Structural Insight for Rational Design of Antivirals. *Viruses* **13**, (2021).
- 567 29. Ghildyal, R., Ho, A. & Jans, D. A. Central role of the respiratory syncytial virus matrix protein  
568 in infection. *FEMS Microbiol. Rev.* **30**, 692–705 (2006).
- 569 30. Bajorek, M. *et al.* Tetramerization of Phosphoprotein Is Essential for Respiratory Syncytial  
570 Virus Budding while Its N-Terminal Region Mediates Direct Interactions with the Matrix  
571 Protein. *J. Virol.* **95**, (2021).

- 572 31. Schmitt, P. T., Ray, G. & Schmitt, A. P. The C-terminal end of parainfluenza virus 5 NP  
573 protein is important for virus-like particle production and M-NP protein interaction. *J. Virol.*  
574 **84**, 12810–23 (2010).
- 575 32. Ray, G., Schmitt, P. T. & Schmitt, A. P. C-Terminal DxD-Containing Sequences within  
576 Paramyxovirus Nucleocapsid Proteins Determine Matrix Protein Compatibility and Can  
577 Direct Foreign Proteins into Budding Particles. *J. Virol.* **90**, 3650–60 (2016).
- 578 33. Galloux, M. *et al.* Characterization of a Viral Phosphoprotein Binding Site on the Surface of  
579 the Respiratory Syncytial Nucleoprotein. *J. Virol.* **86**, 8375–8387 (2012).
- 580 34. Ouizougoun-Oubari, M. *et al.* A Druggable Pocket at the Nucleocapsid/Phosphoprotein  
581 Interaction Site of Human Respiratory Syncytial Virus. *J. Virol.* **89**, 11129–11143 (2015).
- 582 35. Santangelo, P. J. & Bao, G. Dynamics of filamentous viral RNPs prior to egress. *Nucleic*  
583 *Acids Res.* **35**, 3602–3611 (2007).
- 584 36. Rincheval, V. *et al.* Functional organization of cytoplasmic inclusion bodies in cells infected  
585 by respiratory syncytial virus. *Nat. Commun.* **8**, 1–11 (2017).
- 586 37. Galloux, M. *et al.* Minimal Elements Required for the Formation of Respiratory Syncytial  
587 Virus Cytoplasmic Inclusion Bodies In Vivo and In Vitro. *MBio* **11**, (2020).
- 588 38. Risso-Ballester, J. *et al.* A condensate-hardening drug blocks RSV replication in vivo. *Nature*  
589 **595**, 596–599 (2021).
- 590 39. Castagné, N. *et al.* Biochemical characterization of the respiratory syncytial virus P–P and  
591 P–N protein complexes and localization of the P protein oligomerization domain. *J. Gen.*  
592 *Virol.* **85**, 1643–1653 (2004).
- 593 40. Tran, T.-L. *et al.* The nine C-terminal amino acids of the respiratory syncytial virus protein P  
594 are necessary and sufficient for binding to ribonucleoprotein complexes in which six  
595 ribonucleotides are contacted per N protein protomer. *J. Gen. Virol.* **88**, 196–206 (2007).
- 596 41. Fix, J., Galloux, M., Blondot, M.-L. & Eléouët, J.-F. The Insertion of Fluorescent Proteins in a  
597 Variable Region of Respiratory Syncytial Virus L Polymerase Results in Fluorescent and  
598 Functional Enzymes But with Reduced Activities. *Open Virol. J.* **5**, 103–108 (2011).
- 599 42. Hardy, R. W. & Wertz, G. W. The Product of the Respiratory Syncytial Virus M2 Gene ORF1  
600 Enhances Readthrough of Intergenic Junctions during Viral Transcription. *J. Virol.* **72**, 520–  
601 526 (1998).
- 602 43. Tran, T.-L. *et al.* The Respiratory Syncytial Virus M2-1 Protein Forms Tetramers and  
603 Interacts with RNA and P in a Competitive Manner. *J. Virol.* **83**, 6363–6374 (2009).
- 604 44. Buchholz, U. J., Finke, S. & Conzelmann, K. K. Generation of bovine respiratory syncytial  
605 virus (BRSV) from cDNA: BRSV NS2 is not essential for virus replication in tissue culture,  
606 and the human RSV leader region acts as a functional BRSV genome promoter. *J. Virol.* **73**,  
607 251–9 (1999).
- 608 45. Tang, G. *et al.* EMAN2: an extensible image processing suite for electron microscopy. *J.*  
609 *Struct. Biol.* **157**, 38–46 (2007).



- 610 46. Wagner, T. *et al.* SPHIRE-crYOLO is a fast and accurate fully automated particle picker for  
611 cryo-EM. *Commun. Biol.* **2**, 218 (2019).
- 612 47. Scheres, S. H. W. RELION: implementation of a Bayesian approach to cryo-EM structure  
613 determination. *J. Struct. Biol.* **180**, 519–30 (2012).
- 614 48. Heymann, B. J. Bsoft: Image Processing for Structural Biology. *Bio-protocol* **12**, e4393  
615 (2022).
- 616 49. Punjani, A., Rubinstein, J. L., Fleet, D. J. & Brubaker, M. A. cryoSPARC: algorithms for rapid  
617 unsupervised cryo-EM structure determination. *Nat. Methods* **14**, 290–296 (2017).
- 618 50. Pettersen, E. F. *et al.* UCSF Chimera--a visualization system for exploratory research and  
619 analysis. *J. Comput. Chem.* **25**, 1605–12 (2004).
- 620 51. Adams, P. D. *et al.* PHENIX: a comprehensive Python-based system for macromolecular  
621 structure solution. *Acta Crystallogr. D. Biol. Crystallogr.* **66**, 213–21 (2010).
- 622 52. Emsley, P., Lohkamp, B., Scott, W. G. & Cowtan, K. Features and development of Coot.  
623 *Acta Crystallogr. D. Biol. Crystallogr.* **66**, 486–501 (2010).
- 624 53. Goddard, T. D. *et al.* UCSF ChimeraX: Meeting modern challenges in visualization and  
625 analysis. *Protein Sci.* **27**, 14–25 (2018).
- 626

## 627 **Acknowledgements**

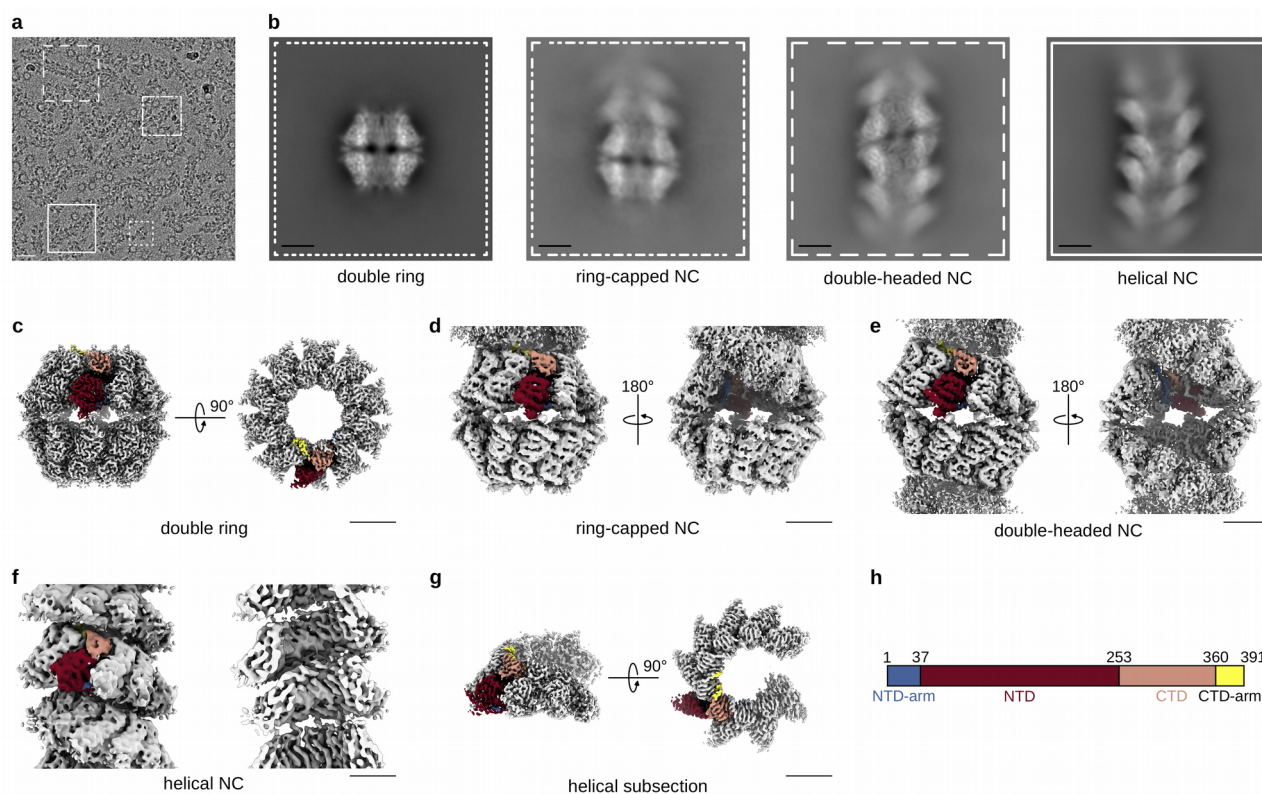
628 We thank Julien Sourimant for providing the pFastBac-N plasmid, Guy Schoehn for  
629 establishing and managing the IBS cryo-electron microscopy platform and for providing training  
630 and support, Lefteris Zarkadas for assistance at the Glacios microscope and Daphna Fenel and  
631 Emmanuelle Neumann for assistance at the negative stain EM platform. This work was funded by  
632 the Agence Nationale de la Recherche (grant ANR DecRisp ANR-19-CE11-0017-01). We used the  
633 platforms of the Grenoble Instruct-ERIC center (ISBG; UAR 3518 CNRS-CEA-UGA-EMBL) within  
634 the Grenoble Partnership for Structural Biology (PSB), supported by FRISBI (ANR-10-INBS-0005-  
635 02) and GRAL, financed within the University Grenoble Alpes graduate school (Ecoles  
636 Universitaires de Recherche) CBH-EUR-GS (ANR-17-EURE-0003). The EM facility is supported  
637 by the Rhône-Alpes Region, the Fondation Recherche Medicale (FRM), the fonds FEDER and the  
638 GIS-Infrastructures en Biologie Sante et Agronomie (IBISA). LG acknowledges the financial support  
639 by the ANR (DecRisp ANR-19-CE11-0017-01) and the Fondation pour la Recherche Médicale  
640 (FRM, FDT202204015081).

## 641 **Author contributions**

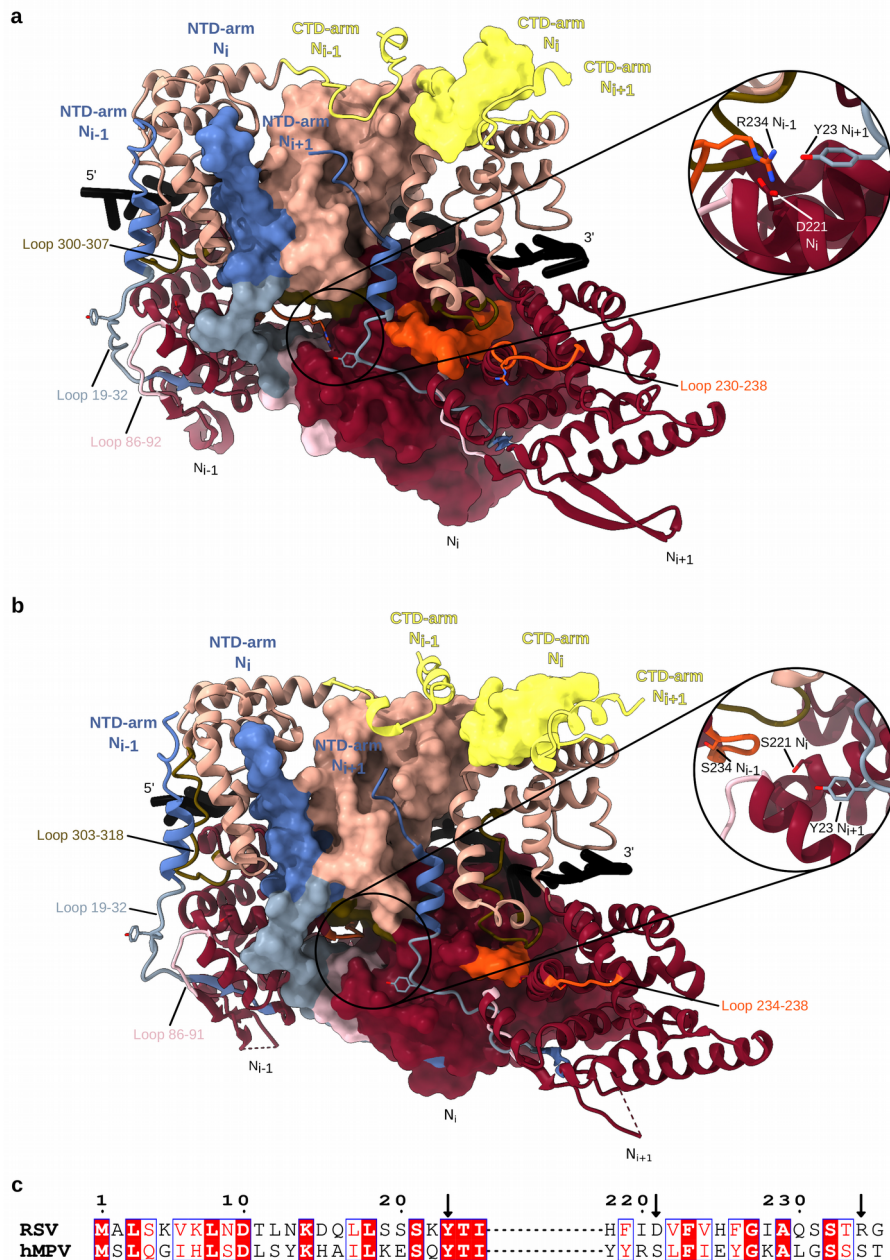
642 LG, MBV, DC, MG and IG performed experiments, LG, AD and IG analysed the cryo-EM  
643 data. LG, JFE and MG analysed the biological data. IG and JFE designed the overall study. IG,  
644 AD, JFE and MG supervised the project. IG wrote the manuscript with contributions of LG, AD, MG  
645 and JFE. LG, AD and IG prepared the figures. All authors read the manuscript prior to submission.

646 **Competing Interests:** The authors declare that there are no competing interests.

## 647 Figures and Legends

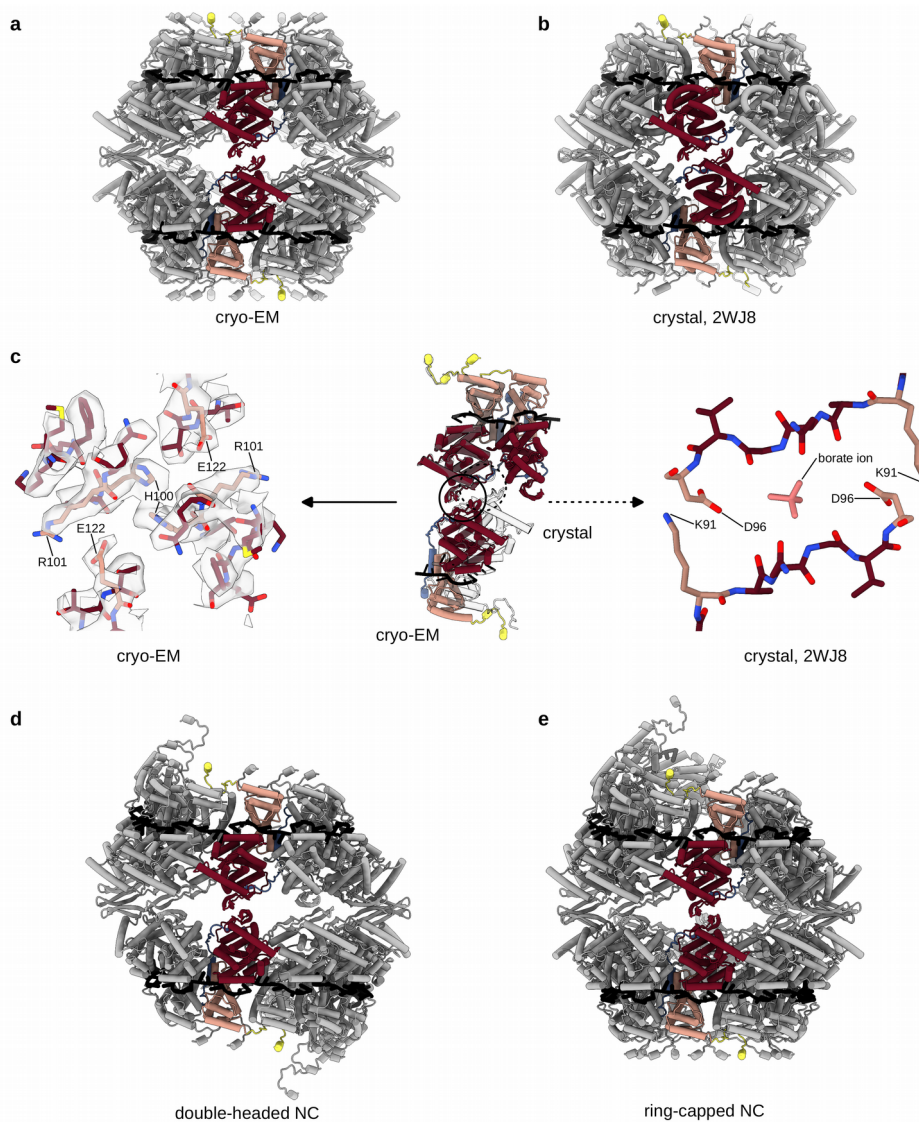


648 **Figure 1: Cryo-EM analysis of RSV NCs.** (a) A representative micrograph of RSV NCs purified  
 649 from insect cells and featuring double rings, ring-capped NCs, double-headed NCs and helical  
 650 NCs. Particles are boxed as an illustration, scale bar 200 Å. (b) Representative 2D classes with the  
 651 outline matching the particles highlighted in (a). (c) Cryo-EM map of the N<sub>10</sub> double ring (side and  
 652 top view). (d) Cryo-EM map of the ring-capped NC (front and back view). (e) Cryo-EM map of the  
 653 double-headed NC (front and back view). (f) Cryo-EM map of the helical NC (front and cut-through  
 654 view). (g) Helical subsection (side and top view). Scale bar, 50 Å in (b-g). (f) Schematic of the RSV  
 655 N sequence divided into an NTD-arm (blue-gray), NTD (rosewood), CTD (old rose) and CTD-arm  
 656 (yellow). In cryo-EM maps in (c-g), one protomer is coloured according to this schematic, with the  
 657 RNA in black.

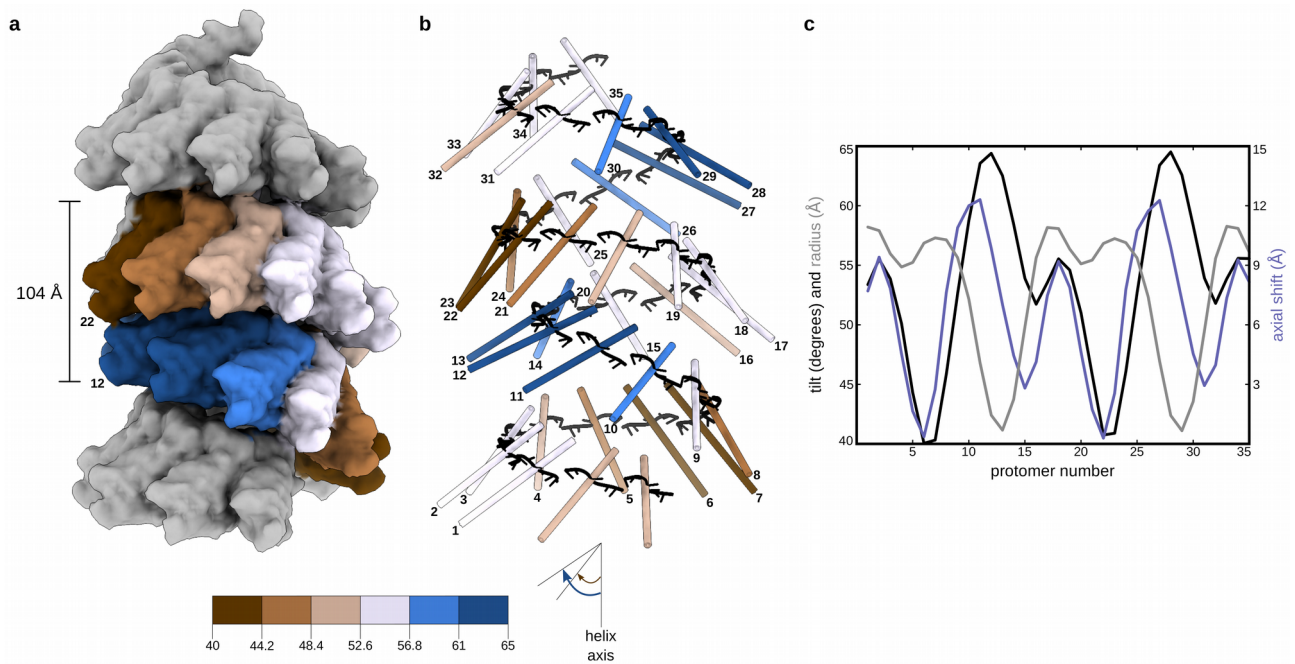


658 **Figure 2: Lateral interactions between N protomers in RSV and hMPV N<sub>10</sub> double rings.** (a)  
 659 Atomic models of three consecutive RSV N protomers are shown, the middle one as a surface and  
 660 the edge ones as ribbons. NTD-arm, NTD, CTD and CTD-arm coloured as in Figure 1, loop 19-32  
 661 in powder blue, loop 86-92 in mimi pink, loop 230-238 in orange and loop 300-307 in olive. The  
 662 close-up of the N-hole of the middle protomer shows the tripartite Y23-D221-R234 interaction. (b)  
 663 Same as (a) but for three protomers from the hMPV N-RNA ring crystal structure (PDB: 5FVC).  
 664 Colouring as in Figure 1 and in (a), loop 19-32 in powder blue, loop 86-91 in mimi pink, loop 234-  
 665 238 in orange and loop 303-318 loop in olive. The close-up shows the absence of a tripartite  
 666 interaction in the N-hole. (c). Pairwise sequence alignment of RSV and hMPV N around the  
 667 residues involved in the tripartite interaction in the RSV N oligomer. Conserved residues in red  
 668 boxes; arrows pointing at residues 23, 221 and 234.

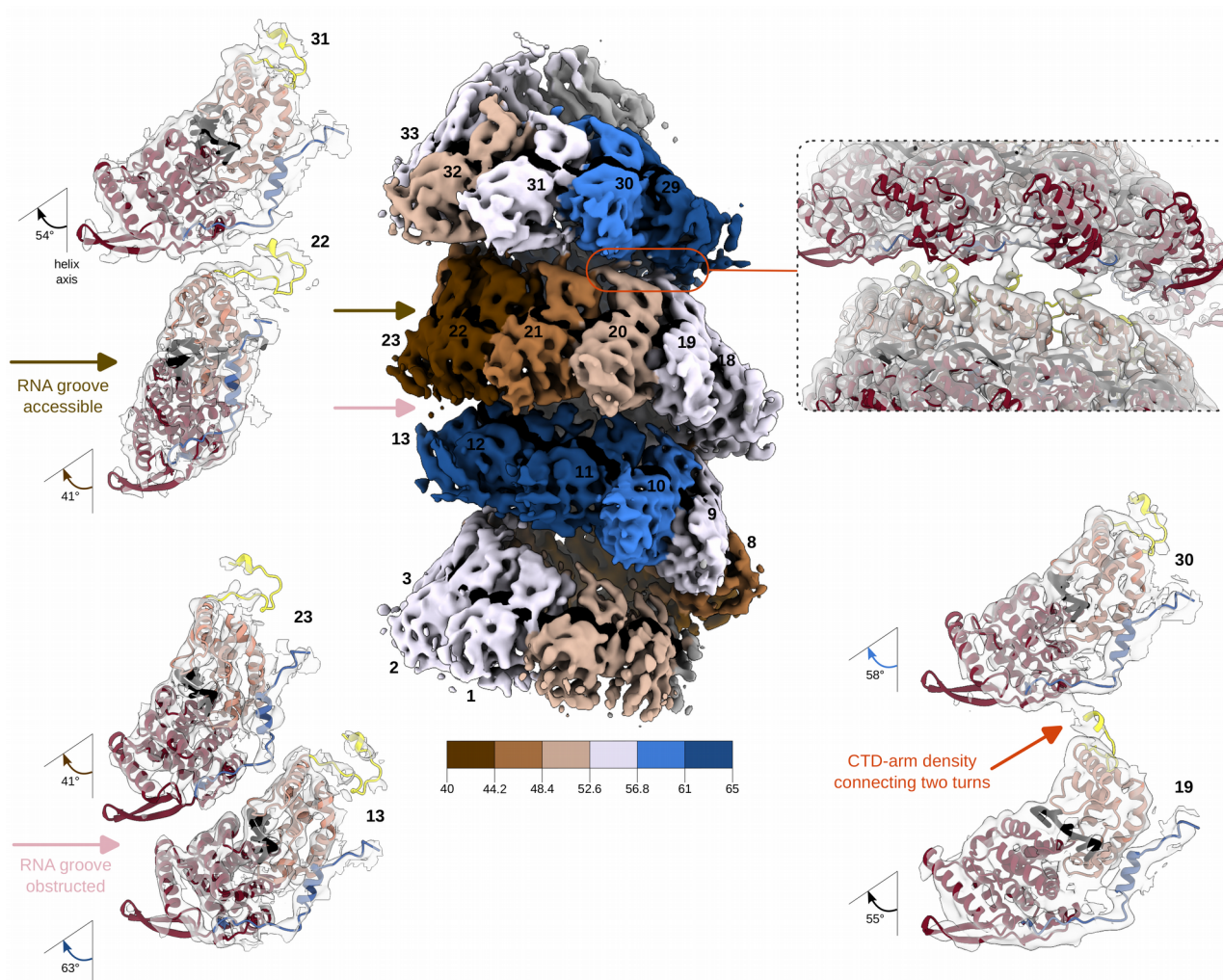




669 **Figure 3. Longitudinal NTD-NTD interactions conserved between RSV N<sub>10</sub> double ring,**  
670 **double-headed and ring-capped NCs but different from the crystal structure of the RSV N<sub>10</sub>**  
671 **double ring.** In each panel, two opposite protomers are coloured as in Figure 1. (a) Atomic model  
672 of the RSV N<sub>10</sub> double ring derived from the cryo-EM map shown as cartoon. (b) Atomic model of  
673 the RSV N<sub>10</sub> double ring crystal structure (PDB: 2WJ8). (c) Alignment of the top rings of the cryo-  
674 EM and crystal structure-based models reveals a rotation between the bottom rings. Two top-ring  
675 protomers and one opposing bottom-ring protomer are shown in the middle of the panel, with the  
676 cryo-EM-based structure coloured as in Figure 1 and the crystal structure in white. A close-up of  
677 the cryo-EM map and the atomic model highlighting the NTD-NTD interactions is on the left, a  
678 close-up of the NTD-NTD interactions in the crystal structure is on the right. The difference  
679 between the crystallographic and the solution inter-ring interfaces may be related to the presence  
680 of a borate ion in the interaction site in PDB: 2WJ8, possibly embarked during the electrophoretic  
681 separation of decameric and undecameric RSV N-RNA rings prior to crystallisation. (d) Atomic  
682 model of the double-headed NC. (e) Atomic model of the ring-capped NC.

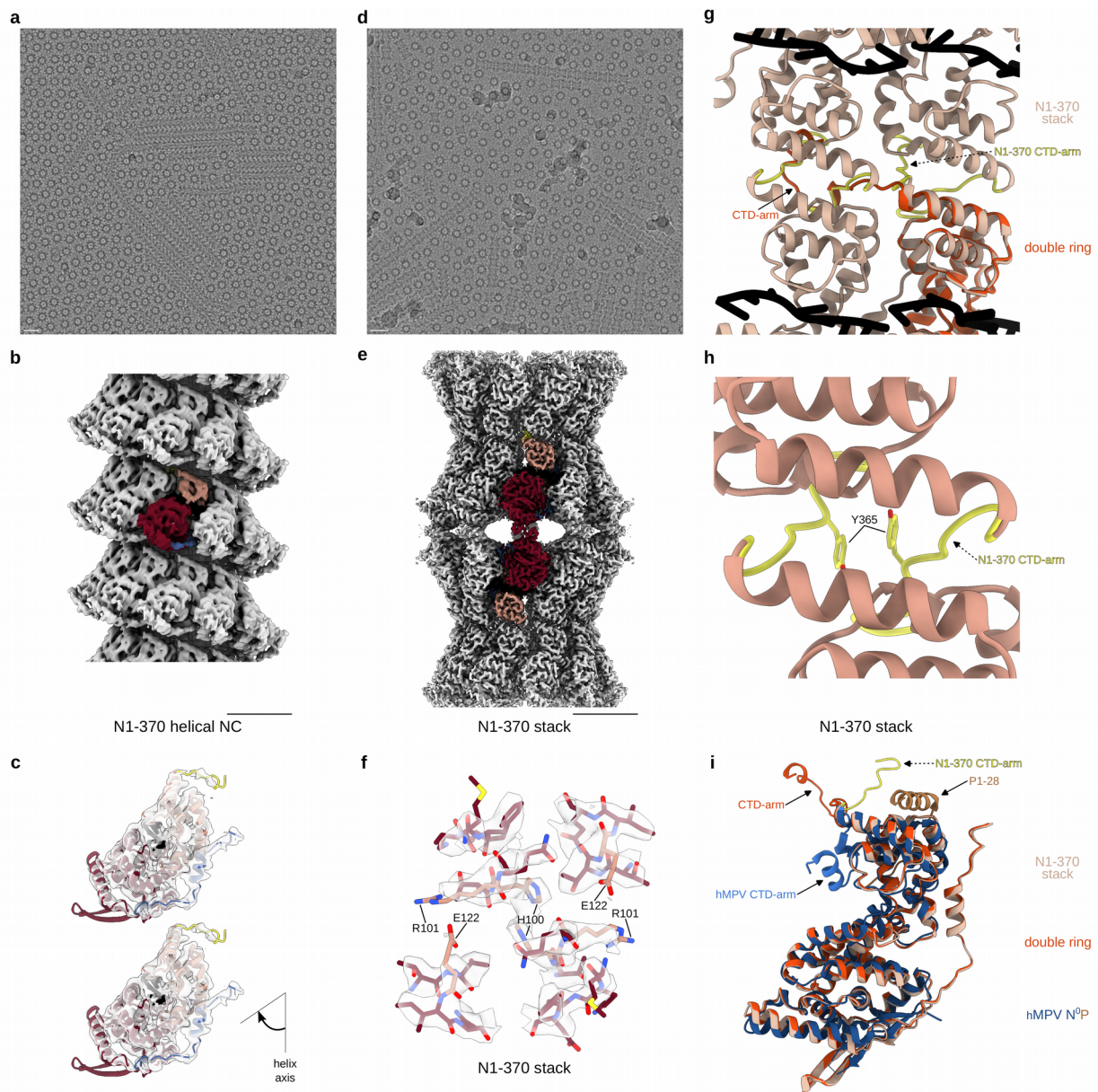


683 **Figure 4. Non-canonical helical symmetry of the RSV NC.** (a). Atomic model of the NC is  
684 filtered to 10 Å resolution and displayed as surface. Protomers in one asymmetric unit are coloured  
685 dependent on their axial tilt following the colour code shown at the schematic underneath, the rest  
686 of the protomers are coloured in grey. (b). Protomers of the model in (a) are shown as sticks  
687 coloured dependent on the protomer axial tilt and numbered 1 to 35. (c) Plot showing the axial tilt  
688 (black), the radial position (grey) and the relative axial shift of each protomer.



689 **Figure 5.** RNA accessibility and CTD-arm-mediated inter-turn interactions in the helical NC. Cryo-  
690 EM map of the helical NC is shown in the middle, coloured as in Figure 4 and as reminded in the  
691 schematic underneath the map, with protomers numbered as in Figure 4. On the left, close-up  
692 views of two sets of opposing protomers from two successive helical turns are shown to illustrate  
693 the difference in the RNA accessibility, with the cryo-EM density in transparent grey and the atomic  
694 model represented as a ribbon and coloured as in Figure 1. On the top right, a similarly-coloured  
695 view of the inter-turn interaction is shown to highlight the densities corresponding to the CTD-arm,  
696 with a corresponding two-protomer close-up underneath. RNA is in black.





697 **Figure 6. Canonical helical NCs and stacked assemblies formed by the N1-370 mutant.** (a) A  
698 representative micrograph of the N1-370 NCs featuring mostly helical NCs and rings, scale bar 200  
699 Å. (b) Cryo-EM map of the canonical N1-370 helical NC, with one protomer coloured as in Figure  
700 1, scale bar 50 Å. (c) Close-up view of protomers from two successive helical turns are shown to  
701 illustrate the position of the CTD-arm and the absence of inter-turn interactions, with the cryo-EM  
702 map in transparent grey and the atomic model represented as a ribbon and coloured as in Figure  
703 1. (d) A representative micrograph of the N1-370 NCs featuring mostly stacks and rings, scale bar  
704 200 Å. (e) Cryo-EM map of the N1-370 stack, with one protomer coloured as in Figure 1, scale bar  
705 50 Å. (f) Close-up of the cryo-EM map of the N1-370 stack and the atomic model highlighting the  
706 NTD-NTD interactions (similar to the ones in the N<sub>10</sub> double ring shown in Figure 3c). (g) Alignment  
707 of the atomic models of the N<sub>10</sub> double ring and the N1-370 stack illustrating the difference in the  
708 orientation of the CTD-arms. One protomer of the N<sub>10</sub> double ring is shown in the bottom-right and  
709 coloured in orange, 4 protomers of the N1-370 stack are shown and colored in beige, with the

710 CTD-arms in yellow. RNA is in black. (h) Close-up of the atomic model of the N1-370 stack  
711 highlighting the CTD-CTD interactions. (i) Alignment of N protomeres of the N<sub>10</sub> double ring  
712 (orange), the N1-370 stack (beige) and the hMPV N<sup>0</sup>P crystal structure (N<sup>0</sup> in blue and P1-28 in  
713 brown) (PDB: 5FVD). Positions of the CDT-arms are indicated.

**Supplementary Table 1. Primer sequences used to generate pN deletion and mutations**

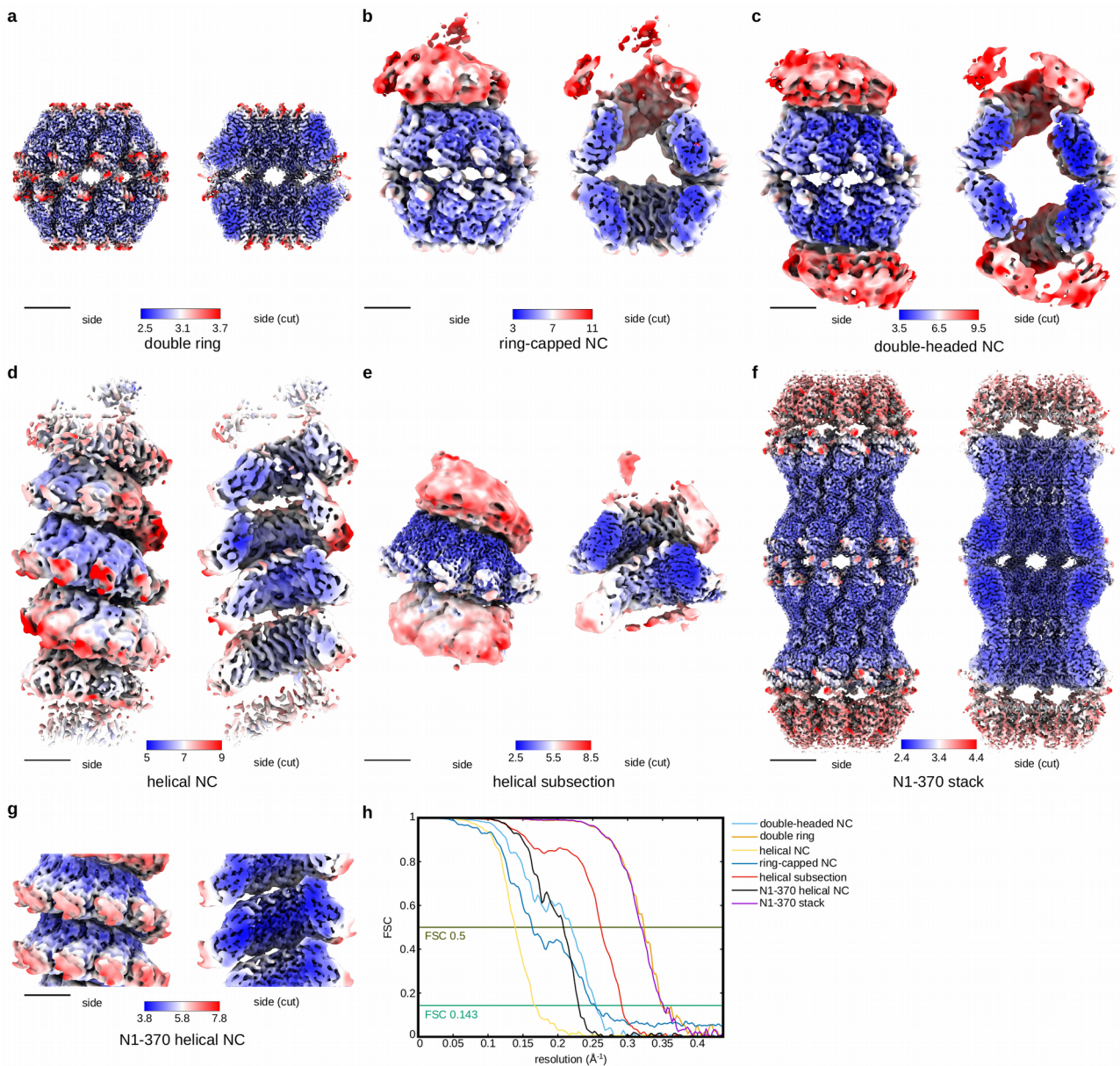
Plasmid name	Primer sequence (5'-3')
pN1-370	Forward ACTAGACTTGtaaGCAGAAGAAGACTAG Reverse ACACTGTAGTTAATCACAC
pNH100E	Forward TGTAACAACAgagCGTCAAGACAT Reverse CTACTCCATTGCTTTTAC
pNH100E-R101D	Forward AACAACAGAGgacCAAGACAT Reverse ACATCTACTCCATTTGCTTTTAC
pNH100E-E122R	Forward CTTAACAACgacATTCAAATCAAC Reverse CTTGCCAATGTTAACACTTC

The pNH100E plasmid was used as a template to generate the plasmids pNH100E-R101D and pNH100E-E122R.

**Supplementary Table 2. Cryo-EM data collection, refinement and validation statistics**

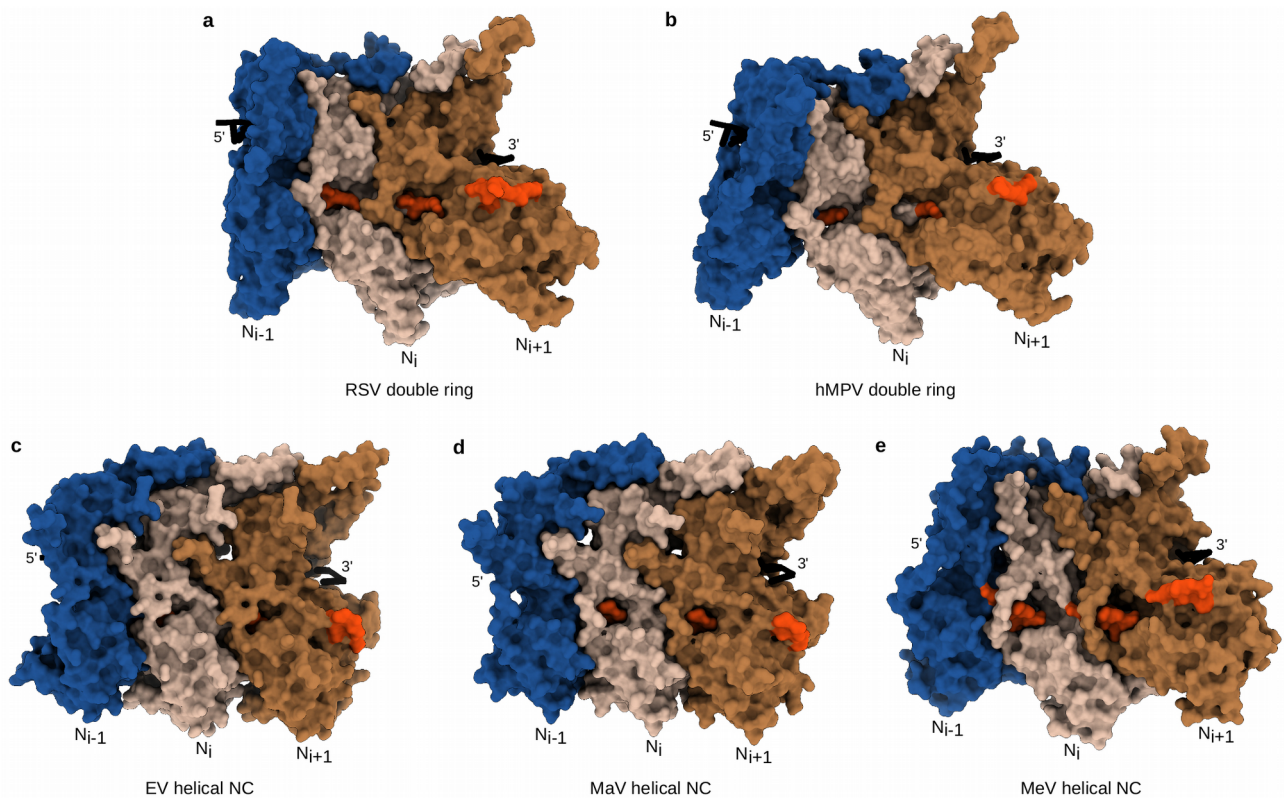
Dataset	WT RSV NC					Mutant 1-370 RSV NC	
	N10 double ring	Helical NC	Ring-capped NC	Double-headed NC	Helical sub-section	Helical NC	Stack
Name of the maps generated in this study	EMDB PDB	EMDB	EMDB	EMDB	EMDB PDB	EMDB	EMDB PDB
<b>Data collection and processing</b>							
Magnification			36,000			36,000	
Voltage (kV)			200			200	
Electron exposure (e-/Å <sup>2</sup> )			42.0			42.0	
Defocus range (µm)			-0.7 – -2.4			-0.7 – -2.4	
Pixel size (Å)			1.145			1.145	
Symmetry imposed	D10	Helical 149.5° 105.3Å	C1	D1	C1	Helical -36° 6.58Å	D10
Initial particle images (no.)	-	1406835	-	-	-	471,549	-
Final particle images (no.)	47,212	389,540	22,162	25,338	389,540	329,706	81,918
Map resolution (Å)	2.9	6.2	3.9	3.8	3.5	4.3	2.8
FSC threshold	0.143	0.143	0.143	0.143	0.143	0.143	0.143
Map resolution range (Å)	2.5-3.7	5-9	3-11	3.5-9.5	2.5-8.5	3.8-7.8	2.4-4.4
<b>Refinement</b>							
Initial model used (PDB code)	2WJ8	-	-	-	2WJ8	-	2WJ8
Model resolution (Å) (masked)	2.9	-	-	-	3.7	-	2.98
FSC threshold	0.5	-	-	-	0.5	-	0.5
Map sharpening <i>B</i> factor (Å <sup>2</sup> )	-96 Å <sup>2</sup>	-	-	-	-94 Å <sup>2</sup>	-	-99 Å <sup>2</sup>
Model composition							
Non-hydrogen atoms	61,800	-	-	-	15,415	-	120,560
Protein residues	7,560	-	-	-	1890	-	14,760
Ligands	0	-	-	-	0	-	0
<i>B</i> factors (Å <sup>2</sup> )							
Protein	38.96	-	-	-	54.50	-	47.85
R.m.s. deviations							
Bond lengths (Å)	0.005	-	-	-	0.007	-	0.005
Bond angles (°)	0.628	-	-	-	1.021	-	0.883
<b>Validation</b>							
MolProbity score	1.50	-	-	-	2.99	-	2.18
Clashscore	8.30	-	-	-	18.34	-	8.64
Poor rotamers (%)	0.00	-	-	-	15.87	-	5.19
<b>Ramachandran plot</b>							
Favoured (%)	97.77	-	-	-	95.48	-	97.00
Allowed (%)	2.23	-	-	-	4.52	-	3.00
Outliers (%)	0.00	-	-	-	0.00	-	0.00



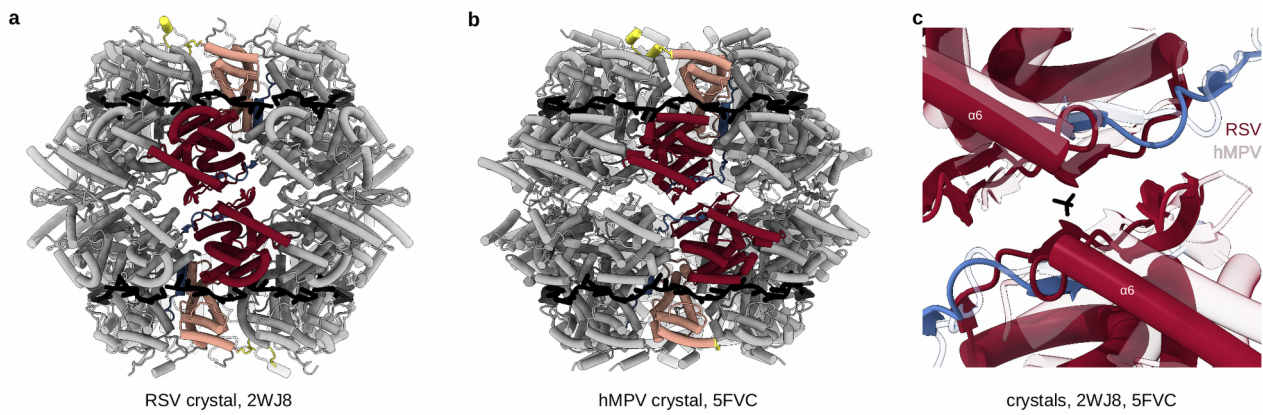


**Supplementary Figure 1. Cryo-EM maps determined in this work and the corresponding FSC curves.** Cryo-EM maps filtered and coloured by local resolution (in Å) for the double ring (a), ring-capped NC (b), double-headed NC (c), helical NC (d), helical subsection (e), N1-370 stack (f) and N1-370 helical NC (g). Contours levels used in ChimeraX to generate the full or cut-out views are 0.264 (a), 0.096 (b), 0.103 (c), 0.117 (d), 0.084 (e), 0.174 (f) and 0.075 (g). Scale bars 50 Å. (h) Masked FSC curves. Scale bars 50 Å.

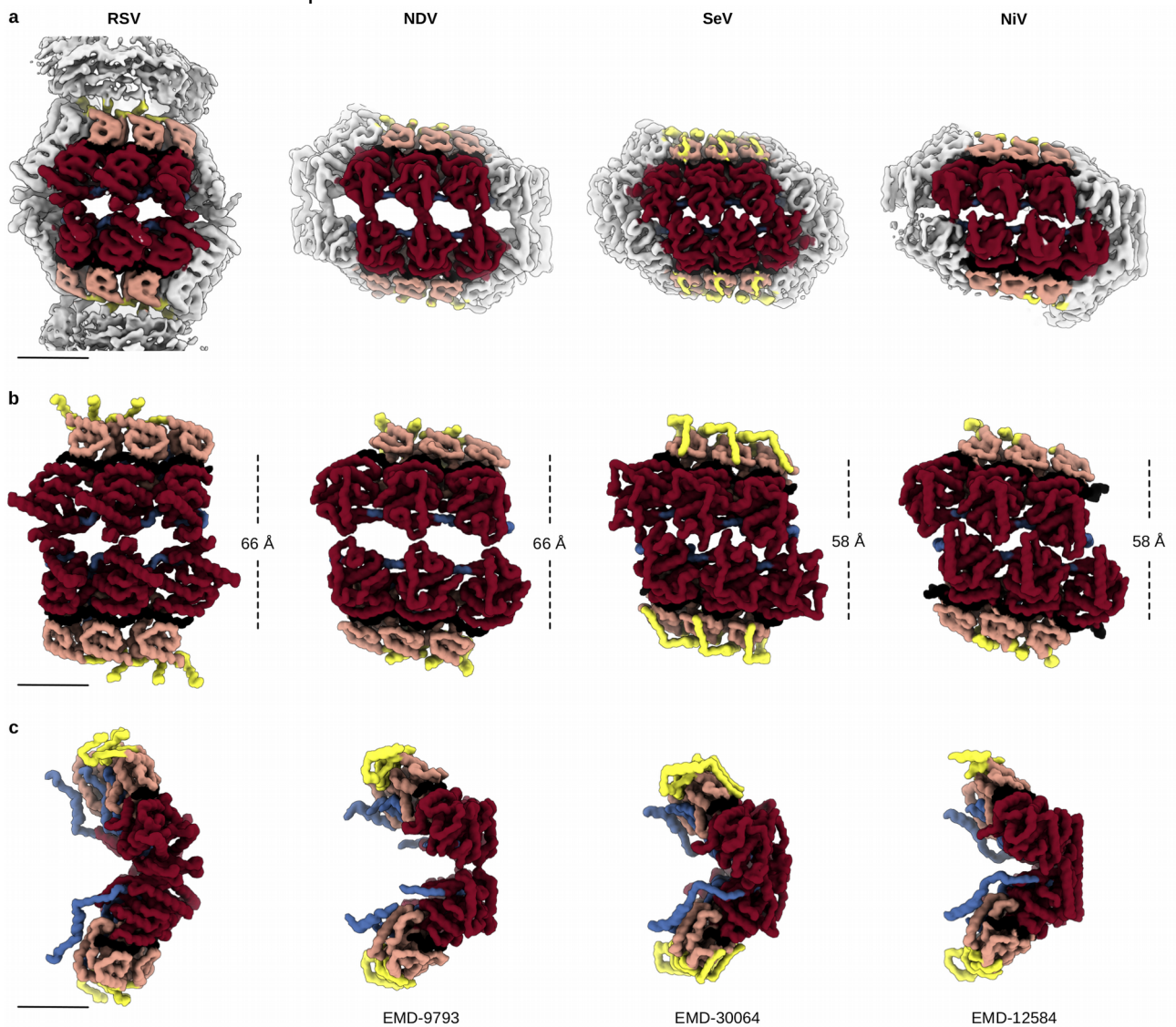




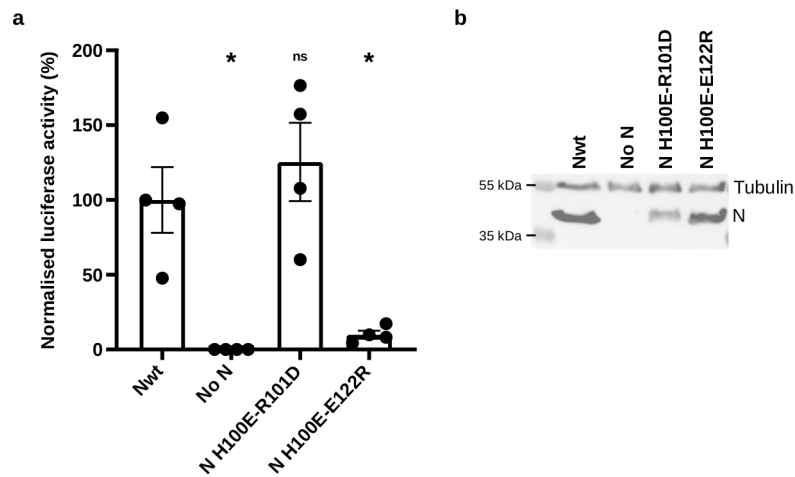
**Supplementary Figure 2. N-hole conservation between *Pneumoviridae*, *Filoviridae* and *Paramyxoviridae* families.** Atomic models of three consecutive promoters of the cryo-EM structure of RSV double ring (a), crystal structure of the hMPV double ring (PDB: 5FVC) (b), Ebola virus helical NC (PDB: 5Z9W) (c), Marburg virus helical NC (PDB: 7F1M) (d), and Measles virus helical NC (PDB: 4UFT) (e) are shown as a surface. The residues coloured in orange correspond to the short loop from the NTD of the  $N_{i-1}$  protruding into the N-hole of  $N_i$ , numbered 230-238 in RSV N (a), 234-238 in hMPV N (b), 221-226 in EV N (c), 203-208 in MaV N (d) and 242-248 in MeV (e). Of note, EV N-hole is less visible because the short loop (in orange) protruding into the N-hole is masked by the loops forming the N-hole. RNA is in black.



**Supplementary Figure 3. Comparison of RSV and hMPV double rings as observed in the respective crystals.** (a) Atomic model of the RSV N<sub>10</sub> double ring (PDB: 2WJ8) is shown as cartoon, coloured as in Figure 1. (b) Atomic model of the hMPV N<sub>10</sub> double ring (PDB: 5FVC). (c) Close-up of the alignment of the RSV and hMPV N<sub>10</sub> double rings. RSV N<sub>10</sub> double ring is coloured as in (a) and hMPV N<sub>10</sub> double ring is in transparent. The borate ion in the interaction site in PDB: 2WJ8 is shown. The 6<sup>th</sup> alpha-helix is labeled for reference.

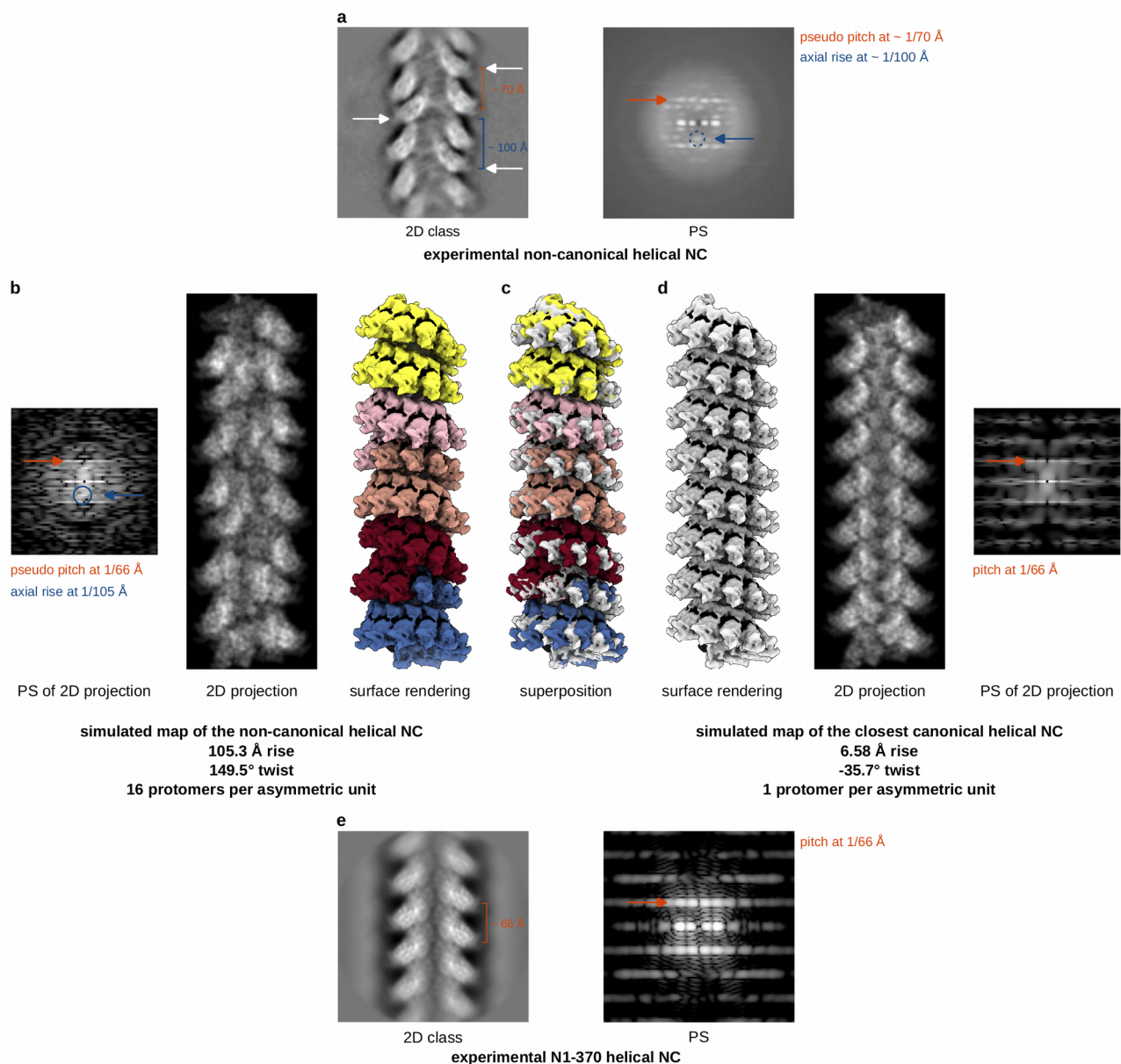


**Supplementary Figure 4. Comparison of double-headed NCs of RSV, NDV, SeV and NiV.** (a) Cryo-EM maps of double-headed NCs of RSV, New-castle disease virus (NDV) (EMD-9793), Sendai virus (SeV) (EMD-30064) and Nipah virus (NiV) (EMD-12584), filtered to 6 Å resolution, scale bar 50 Å. Front (b) and side (c) views of atomic models of three consecutive protomers from the double-headed NCs of RSV, NDV, SeV and NiV, filtered to 6 Å resolution and displayed as surface. Of note, the clam-shaped assemblies of RSV and NDV are both formed in an end-on fashion, without insertion into the opposite inter-protomer grooves and with the centers of gravity of the two spirals separated by 66 Å, as in the cryo-EM structure of the RSV N<sub>10</sub> double ring. In contrast, the SeV and NiV clams adopt a closely nested packing, leading to inter-spiral distances of only 58 and 56 Å respectively, and therefore actually look more reminiscent of the crystal structure of the RSV double ring. A visual comparison of the side views of the central clam-forming protomers, opposite to the helical junction, also reveals that the RSV protomer is notably less tilted from the filament axis than its three paramyxoviral counterparts.

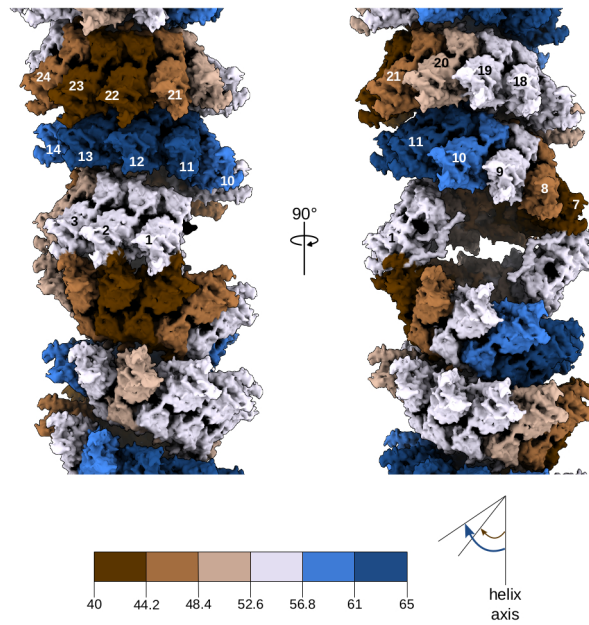


**Supplementary Figure 5. Impact of N mutation on the RSV polymerase activity.** (a) Quantification of the RSV polymerase activity in the presence of wild type N (Nwt), in the absence of N (No N) and for the two N mutants, H100E-R101D and H100E-E122R. Luciferase activities were normalised based on corresponding  $\beta$ -Gal activities, and are representative of three experiments performed in quadruplicates. Data are mean  $\pm$  s.e.m. (standard error of the mean).  $n = 4$  replicates. A two-tailed Mann-Whitney test was used to compare the normalised luciferase activities between the Nwt and the other conditions.  $p < 0.05$  is considered significant. \*,  $p = 0.0286$ . For N H100E-R101D,  $p = 0.3429$  (ns for no significance). (b) Western blot showing the expression of N (WT and mutants) and tubulin in BSRT7/5 cells.





**Supplementary Figure 6. Comparison between the experimental NC, the simulated non-canonical helical NC, the simulated closest canonical helical NC and the N1-370 mutant NC.** (a) A 2D class-average (left) and an average of the PS of the particles in the class (right), representative of the experimental non-canonical helical NCs are shown. The white arrows are indicating the inwards-shifted protomers. (b) A simulated non-canonical helical NC map has been built using the experimentally refined helical parameters as indicated and filtered to 8 Å resolution (each asymmetric unit is coloured in a different colour, right). The corresponding 2D projection (middle) and its PS (left) are shown. (c) Superposition of the simulated maps of the non-canonical helical NC and the closest canonical helical NC. (d) The closest canonical helical NC symmetry parameters were calculated by dividing the non-canonical helical rise and twist by the number of protomers in the asymmetric unit ( $16$ ;  $105.3/16=6.58$  Å rise and a  $-(360-149.5+360)/16=-35.7^\circ$  twist to account for right-handed to left-handed conversion). The corresponding simulated map filtered to 8 Å resolution (left), its 2D projection (middle) and its PS (right) are shown. (e) A 2D class-average (left) and an average of the PS of the particles in the class (right), representative of the canonical helical NC formed by the N1-370 mutant construct.



**Supplementary Figure 7. Model of a long double-headed NC.** A simulated map of long double-headed NCs, filtered to 6 Å resolution, was built from the atomic model of the double-headed NC. Protomers are coloured dependent on their axial tilt determined as described in the method section, following the colour code shown at the schematic underneath, RNA is in black. The protomer numbering follows the convention used for the non-canonical helical NC.



### **3. Initial study of RSV nucleocapsid assembly in infected cells by cryo-electron tomography**

Solving the structures of the purified recombinant helical RSV NC and other N-RNA assemblies by single particle cryo-EM showed the non-canonical symmetry of the RSV helical NC and also highlighted the diversity of N-RNA assemblies that can be formed. In light of the very recent work on NCs of *Mononegavirales* by cryo-ET (Shi et al., 2022; Zhang et al., 2021, bioRxiv preprint), RSV NCs are expected to exhibit conformational variability during the viral cycle. Therefore, we decided to further investigate RSV NCs structure in a native environment, i.e. in infected cells by RSV. My thesis co-director, Irina Gutsche, from the MICA group, is also an associated visiting professor at the University of Umeå in Sweden. In 2021-2022, she was working in the Linda Sandblad's group at the Umeå Centre for Electron Microscopy (UCEM) in the frame of a long-term CNRS mission aimed at establishing cryo-FIB milling and cryo-ET workflows on several projects of the MICA group. Thus, I had an opportunity to spend almost 3 months in Umeå and contribute to developing a protocol to visualise the NC in RSV-infected cells using cryo-ET.

The first challenge was to grow cells on the EM grids with the ideal distribution of 1 cell per grid square, so that the sample layer would not be too thick and the cells stay isolated for good vitrification and FIB milling. We tried two types of cells that are sensitive to RSV infection, the HEp-2 cell line (human cells, derived from HeLa cells) and the BEAS-2B cell line (human cells, derived from bronchial epithelium). Different dilutions of cells were tested in order to reach an optimal number of cells on the grids. These assays led us to conclude that BEAS-2B cells were too large and the ice layer was too thick after plunge freezing for the FIB milling step, whereas HEp-2 cells allowed to obtain the good condition of freezing. Then, an optimisation was performed to find the right MOI (multiplicity of infection) and timing to get 100 % infected cells without inducing cell death. The RSV-mCherry virus (Rameix-Welti et al., 2014) was used, so the infection rate could be assessed by fluorescence microscopy (Figure 29). Several attempts were made until we found the currently best condition, which we are now optimising further, in particular with grid micropatterning.



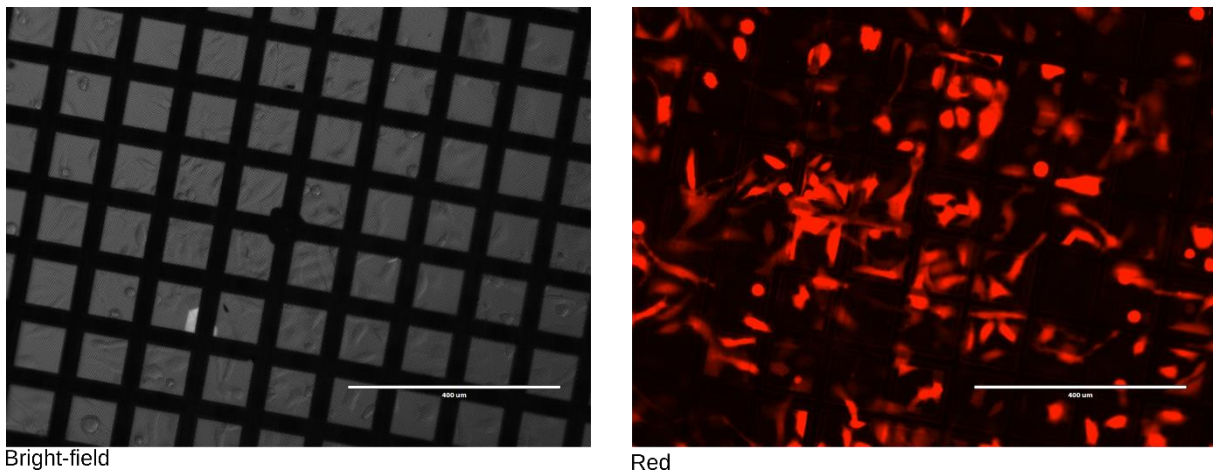


**Figure 29.** Fluorescent microscopy images of HEP-2 cells on grids, infected with RSV-mCherry. Scales bars 400 µm.

Following these settings, several milling patterns were tried to obtain 150-200 nm lamellae. The lamellae tend to break during the milling step and the transfer between the Scios cryo-FIB/SEM and the Krios microscope. Sputter-coating with platinum and introduction of micro-expansion joints could successfully strengthen the lamellae. Cryo-FIB milling is an important bottleneck, especially because automatic milling was not yet available at UCEM, and imaging is limited by the number of lamellae that can be made (maximum 6 per day). It would therefore be necessary to pursue the milling optimisation to obtain thin enough lamellae to perform imaging by cryo-ET without having cracked samples.

Finally, tilt series of the prepared lamellae were collected on the Krios cryo-electron microscope, but we were not able to see any IBs or NCs. IBs are difficult to identify because there are membrane-less organelles and they do not have a specific location in the cytoplasm of the RSV-infected cells. The size of the NCs was also a limitation (approximately 150 Å in diameter). However, we observed that most of the lamella were correctly vitrified and allowed to observe well-preserved organelles.

In order to successfully visualise IBs and thus the NCs in RSV-infected cells, several steps will be optimised or added. First, micropatterning of the grids with fibronectin in order to have evenly spaced cells in the centre of each grid hole will be optimised, giving the opportunity to do more and better lamellae per grid. Second, the RSV-mCherry that we used in this proof-of-concept study expresses the mCherry protein throughout the cytoplasm of infected cells. We therefore plan to use another recombinant RSV expressing the viral M2-1 protein fused to a fluorescent protein, and thus suitable for cryo-correlative approaches. This should allow us to precisely target IBs and thus direct the milling to these areas. The cryo-correlative step could be implemented using a Leica Thunder cryo-fluorescence microscope available at UCEM, so that the milling process can be guided by the fluorescence signal coming from a viral protein in the IBs. Because this microscope does not allow to obtain a sufficient resolution in Z, we may also seek access to the LSM 900 Airyscan microscope available in the Imaging Centre of the EMBL Heidelberg for on-lamella cryo-CLEM.



## Part III: Conclusion and perspectives

The objectives of my PhD project were to characterise the potential specificity of the RSV N protein for RNA using *in vitro* encapsidation assays and to solve the structure of the helical NC by cryo-EM. Some specific goals of these studies were (i) to identify key elements that could explain the regulation of the transition from N<sup>0</sup>-P to N-RNA, and (ii) to obtain structural information on the NC that could help to better understand the functioning of the viral RNA synthesis mechanism by the polymerase L.

Based on the capacity to purify a monomeric RNA-free N protein, my results showed that, while 7-mer RNA was the minimal length to trigger encapsidation, 11-mer RNA was required to achieve stable encapsidation. Given the strong tendency of N to associate with RNA independently of the sequence, we wondered whether the 5' end modification of RNAs could explain the encapsidation of the viral genome and antigenomes that have a 5' ppp end, compared to the 5' 7<sup>m</sup>Gppp end of viral mRNAs that are not encapsidated. However, our approaches did not reveal a difference of encapsidation between the 5' ppp and 5' 7<sup>m</sup>Gppp ends. Nonetheless, this study demonstrates that RNA encapsidation was essential for IBs formation *in vitro* (Gonnin et al., 2022). Of most interest, although the level of N<sup>0</sup> was hypothesised to be critical for the transition from transcription to replication, and as a consequence in the switch from N<sup>0</sup>-P to N-RNA interaction, it was demonstrated that N is necessary for the replication but does not favour replication over transcription (Fearn et al., 1997). Recent studies concerning IBs organisation, composition and nature, as well as the obtaining of the cryo-EM structure of L open new perspectives. First, the identification of sub-compartments, the IBAGs, where M2-1 and viral mRNAs concentrate suggests that the association of M2-1 to mRNAs (Rincheval et al., 2017) could indirectly impair their encapsidation by N. Supporting this hypothesis, our preliminary results revealed that contrary to N, M2-1 can interact with short capped RNA. This mechanism could also be driven and/or facilitated by the spatial organisation of the catalytic domains of L associated with P (Gilman et al., 2019) which could somehow orchestrate the specific recruitment of M2-1 and N<sup>0</sup>.

Nevertheless, one main issue of our work relied on the fact that recombinant N-P40 protein presents a strong propensity to oligomerise in the absence of RNA upon concentration (data not shown). This observation highlights that although RNA encapsidation and N oligomerisation are concomitant, local concentration of N could induce its oligomerisation. By homology with the HMPV N<sup>0</sup>-P complex (Renner et al., 2016), two key elements were identified as necessary to maintain N monomeric and RNA free. First the fixation of P<sub>NTD</sub> on the N<sub>CTD</sub> through hydrophobic interactions. The binding site of P overlaps with the binding site of the N- and C-terminal arms of the neighbouring protomers, impairing oligomerisation. Second, the specific folding of the C-terminal arm of N close to the RNA binding groove blocks the accessibility to RNA (Galloux et al., 2015; Esneau et al., 2019). Our recent results suggest the existence of a third bolt required to maintain the N in monomeric form until the encapsidation of nascent genomes and antigenomes, which remains to be characterised. Given the critical role of the N-terminal arm of N in oligomerisation, we hypothesised that post-translational modifications (PTMs) could be involved in the regulation of the N-terminal arm of N. Preliminary work has been initiated in the BMP team to identify by mass spectrometry potential PTMs on N purified from RSV-infected cells. This analysis revealed that residues on the N-terminal arm are phosphorylated and methylated (data not shown). The current work hypothesis is that methylation and/or phosphorylation of N<sup>0</sup> could impair oligomerisation. Studies are being carried out by Vincent Basse, PhD student in the BMP team, in order to (i) characterise the role of these PTMs, and (ii) identify the cellular partners responsible for these PTMs.

During my PhD, I also managed to purify RSV helical NC by overexpressing N in insect cells, to perform their structural study using cryo-EM. This work led us to solve the structure of the RSV helical NC, along with other N-RNA assemblies, i.e. double-headed NC, ring-capped NC and double-decameric N-RNA ring. Of most interest compared to previous structures of *Mononegavirales* NCs, the RSV helical NC displays a non-canonical symmetry, the helix being composed of a succession of asymmetric units of 16 N protomers (making about one and a half turns). Furthermore, we showed the importance of the C-terminal arm in the flexibility of the helical NC, the truncation of the last 22 amino acids of N inducing a stiffness of the helix which gains a canonical symmetry (Gonnin et al., 2023, bioRxiv preprint).

During RNA synthesis, P mediates the association between the NC and L which uses NC as a template. One of the major unsolved questions is how the catalytic site of the RdRp reaches the RNA. L does not have direct access to the RNA nested in N. This suggests that structural rearrangements are required to expose the RNA. The cryo-EM structures of the RSV and HMPV L-P complexes (Gilman et al., 2019; Pan et al., 2019) showed that the P<sub>OD</sub> and P<sub>CTD</sub> are linked to L, with a different folding structure for each P protomer and each P<sub>CTD</sub> of the tetramer could fulfil a different role. It is noteworthy that in these structures, the last residues of P<sub>CTD</sub> interacting with the NC (Tran et al., 2007; Galloux et al., 2012) are free, suggesting that the P tetramer could bind both L and the NC at the same time. Furthermore, it was previously proposed that the P<sub>CTD</sub> region could be responsible for the NC opening (Renner et al., 2016). Taken together, the proximity of the N and L binding sites on P and the diversity of P<sub>CTD</sub> folding on L (Gilman et al., 2019), support the hypothesis that P<sub>CTD</sub> may be involved in the local structural reorganisation of N to allow access to RNA by L.

Most interestingly, the unique symmetry of the helical NC structure shows that RNA access is variable along the helix: in some parts, the protomers are lying and the above turn is covering the RNA, making it impossible for L to reach the RNA directly, in others, the protomers are standing, exposing the RNA. Although difficult to conclude on the mechanistic implication of this structure, it demonstrates that, as each N protomer has a slightly different angle to the helix axis, the NC allow a certain degree of variability of each N protomer. It could be hypothesised that this flexibility allows local extraction of RNA associated with the remodelling of the N promoters at this location, without disarticulating the whole NC. This flexibility is probably driven by the C-terminal arm of N, as we showed that the truncation of part of the C-terminal arm (after residue 370) changes the NC symmetry and stiffens the NC filament. Similar to the N<sub>tail</sub> of paramyxoviruses and filoviruses, the C-terminal arm of the pneumoviruses confers flexibility to the helical NC. Further work is needed to address this fundamental issue, in particular, solving the structure of the L-P complex associated with NC would be a major advance.

It is also essential to consider that the formation of IBs is critical for L functioning suggesting that the specific environment of these structures could be crucial for protein-protein interactions. Characterisation of the RSV IBs showed that numerous viral and cellular proteins can be found in these structures and that M2-1 clusters with viral mRNA in substructures called IBAGs (Rincheval et al., 2017). However, little is known about how the spatial and temporal organisation of IBs is impacted by L activities and how NCs are generated and further transported from IBs to virion assembly sites. The cryo-ET study of the MuV NC in infected cells allowed the reconstruction by sub-tomogram averaging of NCs displaying two types of condensation induced by stress (Zhang et al., 2021, bioRxiv preprint). Studies on EBOV NCs also showed that the NC can display different degrees of condensation and that the matrix protein VP40 rigidifies the NC (Bharat et al., 2012). The maturation of the filoviruses NCs requires the phosphoprotein VP35 and the membrane-associated protein VP24, and mature NCs are found mainly on the periphery of the IBs (Huang et al., 2002; Noda et al., 2006). In order to better understand the organisation of RSV IBs, and to see if RSV NCs could adopt different condensation states, we initiated work on IBs visualisation in infected cells by cryo-ET and NC characterisation. It will be interesting to explore whether RSV viral proteins and specific cellular proteins can affect the conformation of NCs. In particular, it would be interesting to study whether the structure of the NC changes according to the state of virion assembly and whether viral proteins, such as M, or cellular proteins could influence the structure of the NCs.

Our study revealed a double-headed NC structure for the RSV. Double-headed NCs were already described for the *Paramyxoviridae* family (Song et al., 2019; Zhang et al., 2021; Ker et al., 2021) but their functional role during the viral cycle is still poorly characterised. It would be interesting to decipher if these structures play a role in the packaging of several genomes in the virions and/or in protecting the end of the RNA from host antiviral sensors. Cryo-ET study could help assess their role *in vivo*.

Finally, another issue that remains unresolved is the question of the factors that lead to the formation of N-RNA rings or helices. In prokaryotic cells, overexpression of N induces N-RNA ring formation (Tran et al., 2007; Tawar et al., 2009) whereas, in eukaryotic cells, a mixture of rings and helices is obtained (Bhella et al., 2002; Bakker et al., 2013; Gonnin et al., 2023,



bioRxiv preprint). Observations in RSV-infected cells or in virions reveal the existence of helices (Liljeroos et al., 2011; Kiss et al., 2014), but also recently of rings (Conley et al., 2022; Vijayakrishnan et al., 2022, bioRxiv preprint). Moreover, *in vitro* encapsidation assays showed that N-RNA rings and not helices are formed (Gao et al., 2020; Gonnin et al., 2022) contrary to what is observed for paramyxoviruses (Milles et al., 2016). One hypothesis could be that helices are formed due to spatial and mechanical constraints linked to the IBs environment, however it is unlikely as helices are formed in insect cells by overexpression. A more likely hypothesis is that there are factors present in eukaryotic cells that are necessary for helix formation: PTMs and their regulation, or cellular chaperone proteins already identified as participants in the viral cycle such as HSP70 which are present in IBs (Brown et al., 2005; Noton et al., 2012) or HSP90 which is necessary for virus replication (Geller et al., 2013). The resolution of this issue would allow to perform *in vitro* transcription and replication assays using an encapsidated minigenome. Today the *in vitro* assays are only performed with L-P complex with small non-encapsidated RNAs on which L is not very processive (Braun et al., 2017; Cao et al., 2022; Cressey et al., 2018; Noton et al., 2014, 2012; Shareef et al., 2021). Obtaining a functional L-P-NC complex should give insight in RSV viral RNA synthesis.



## References

- Afonso, C.L., Amarasinghe, G.K., Bányai, K., Bào, Y., Basler, C.F., Bavari, S., Bejerman, N., Blasdel, K.R., Briand, F.-X., Briese, T., Bukreyev, A., Calisher, C.H., Chandran, K., Chéng, J., Clawson, A.N., Collins, P.L., Dietzgen, R.G., Dolnik, O., Domier, L.L., Dürwald, R., Dye, J.M., Easton, A.J., Ebihara, H., Farkas, S.L., Freitas-Astúa, J., Formenty, P., Fouchier, R.A.M., Fù, Y., Ghedin, E., Goodin, M.M., Hewson, R., Horie, M., Hyndman, T.H., Jiāng, D., Kitajima, E.W., Kobinger, G.P., Kondo, H., Kurath, G., Lamb, R.A., Lenardon, S., Leroy, E.M., Li, C.-X., Lin, X.-D., Liú, L., Longdon, B., Marton, S., Maisner, A., Mühlberger, E., Netesov, S.V., Nowotny, N., Patterson, J.L., Payne, S.L., Paweska, J.T., Randall, R.E., Rima, B.K., Rota, P., Rubbenstroth, D., Schwemmler, M., Shi, M., Smither, S.J., Stenglein, M.D., Stone, D.M., Takada, A., Terregino, C., Tesh, R.B., Tian, J.-H., Tomonaga, K., Tordo, N., Towner, J.S., Vasilakis, N., Verbeek, M., Volchkov, V.E., Wahl-Jensen, V., Walsh, J.A., Walker, P.J., Wang, D., Wang, L.-F., Wetzell, T., Whitfield, A.E., Xiè, J., Yuen, K.-Y., Zhang, Y.-Z., Kuhn, J.H., 2016. Taxonomy of the order Mononegavirales: update 2016. *Arch Virol* 161, 2351–2360. <https://doi.org/10.1007/s00705-016-2880-1>
- Aggarwal, M., Leser, G.P., Kors, C.A., Lamb, R.A., 2018. Structure of the Paramyxovirus Parainfluenza Virus 5 Nucleoprotein in Complex with an Amino-Terminal Peptide of the Phosphoprotein. *J Virol* 92, e01304-17. <https://doi.org/10.1128/JVI.01304-17>
- Ahmad, A., Eze, K., Noulin, N., Horvathova, V., Murray, B., Baillet, M., Grey, L., Mori, J., Adda, N., 2022. EDP-938, a Respiratory Syncytial Virus Inhibitor, in a Human Virus Challenge. *N Engl J Med* 386, 655–666. <https://doi.org/10.1056/NEJMoa2108903>
- Alayyoubi, M., Leser, G.P., Kors, C.A., Lamb, R.A., 2015. Structure of the paramyxovirus parainfluenza virus 5 nucleoprotein–RNA complex. *Proc. Natl. Acad. Sci. U.S.A.* 112. <https://doi.org/10.1073/pnas.1503941112>
- Alvarez, R., Elbashir, S., Borland, T., Toudjarska, I., Hadwiger, P., John, M., Roehl, I., Morskaya, S.S., Martinello, R., Kahn, J., Van Ranst, M., Tripp, R.A., DeVincenzo, J.P., Pandey, R., Maier, M., Nechev, L., Manoharan, M., Kotelianski, V., Meyers, R., 2009. RNA Interference-Mediated Silencing of the Respiratory Syncytial Virus Nucleocapsid Defines a Potent Antiviral Strategy. *Antimicrob Agents Chemother* 53, 3952–3962. <https://doi.org/10.1128/AAC.00014-09>
- Asenjo, A., Rodríguez, L., Villanueva, N., 2005. Determination of phosphorylated residues from human respiratory syncytial virus P protein that are dynamically dephosphorylated by cellular phosphatases: a possible role for serine 54. *Journal of General Virology* 86, 1109–1120. <https://doi.org/10.1099/vir.0.80692-0>
- Bächi, T., Howe, C., 1973. Morphogenesis and Ultrastructure of Respiratory Syncytial Virus. *J Virol* 12, 1173–1180. <https://doi.org/10.1128/jvi.12.5.1173-1180.1973>

Bajorek, M., Caly, L., Tran, K.C., Maertens, G.N., Tripp, R.A., Bacharach, E., Teng, M.N., Ghildyal, R., Jans, D.A., 2014. The Thr205 Phosphorylation Site within Respiratory Syncytial Virus Matrix (M) Protein Modulates M Oligomerization and Virus Production. *J Virol* 88, 6380–6393. <https://doi.org/10.1128/JVI.03856-13>

Bajorek, M., Galloux, M., Richard, C.-A., Szekely, O., Rosenzweig, R., Sizun, C., Eleouet, J.-F., 2021. Tetramerization of Phosphoprotein Is Essential for Respiratory Syncytial Virus Budding while Its N-Terminal Region Mediates Direct Interactions with the Matrix Protein. *J Virol* 95, e02217-20. <https://doi.org/10.1128/JVI.02217-20>

Baker, R.E., Park, S.W., Yang, W., Vecchi, G.A., Metcalf, C.J.E., Grenfell, B.T., 2020. The impact of COVID-19 nonpharmaceutical interventions on the future dynamics of endemic infections. *Proc. Natl. Acad. Sci. U.S.A.* 117, 30547–30553. <https://doi.org/10.1073/pnas.2013182117>

Bakker, S.E., Duquerroy, S., Galloux, M., Loney, C., Conner, E., Eléouët, J.-F., Rey, F.A., Bhella, D., 2013. The respiratory syncytial virus nucleoprotein–RNA complex forms a left-handed helical nucleocapsid. *Journal of General Virology* 94, 1734–1738. <https://doi.org/10.1099/vir.0.053025-0>

Barik, S., 1993. The structure of the 5' terminal cap of the respiratory syncytial virus mRNA. *Journal of General Virology* 74, 485–490. <https://doi.org/10.1099/0022-1317-74-3-485>

Barik, S., 1992. Transcription of human respiratory syncytial virus genome RNA in vitro: requirement of cellular factor(s). *J Virol* 66, 6813–6818. <https://doi.org/10.1128/jvi.66.11.6813-6818.1992>

Barik, S., Mclean, T., Dupuy, L.C., 1995. Phosphorylation of Ser232 Directly Regulates the Transcriptional Activity of the P Protein of Human Respiratory Syncytial Virus: Phosphorylation of Ser237 May Play an Accessory Role. *Virology* 213, 405–412. <https://doi.org/10.1006/viro.1995.0013>

Battles, M.B., McLellan, J.S., 2019. Respiratory syncytial virus entry and how to block it. *Nat Rev Microbiol* 17, 233–245. <https://doi.org/10.1038/s41579-019-0149-x>

Beem, M., Wright, F. H., Hamre, D., Egerer, R., & Oehme, M., 1960. Association of the chimpanzee coryza agent with acute respiratory disease in children. *The New England journal of medicine*, 263, 523–530. <https://doi.org/10.1056/NEJM196009152631101>

Behera, A.K., Matsuse, H., Kumar, M., Kong, X., Lockey, R.F., Mohapatra, S.S., 2001. Blocking Intercellular Adhesion Molecule-1 on Human Epithelial Cells Decreases Respiratory Syncytial Virus Infection. *Biochemical and Biophysical Research Communications* 280, 188–195. <https://doi.org/10.1006/bbrc.2000.4093>

Bepler, T., Morin, A., Rapp, M., Brasch, J., Shapiro, L., Noble, A.J., Berger, B., 2019. Positive-unlabeled convolutional neural networks for particle picking in cryo-electron micrographs. *Nat Methods* 16, 1153–1160. <https://doi.org/10.1038/s41592-019-0575-8>

Bermingham, A., Collins, P.L., 1999. The M2-2 protein of human respiratory syncytial virus is a regulatory factor involved in the balance between RNA replication and transcription. *Proc. Natl. Acad. Sci. U.S.A.* 96, 11259–11264. <https://doi.org/10.1073/pnas.96.20.11259>

Bharat, T.A.M., Riches, J.D., Kolesnikova, L., Welsch, S., Krähling, V., Davey, N., Parsy, M.-L., Becker, S., Briggs, J.A.G., 2011. Cryo-Electron Tomography of Marburg Virus Particles and Their Morphogenesis within Infected Cells. *PLoS Biol* 9, e1001196. <https://doi.org/10.1371/journal.pbio.1001196>

Bhella, D., Ralph, A., Murphy, L.B., Yeo, R.P., 2002. Significant differences in nucleocapsid morphology within the Paramyxoviridae. *Journal of General Virology* 83, 1831–1839. <https://doi.org/10.1099/0022-1317-83-8-1831>

Bitko, V., & Barik, S., 2001. An endoplasmic reticulum-specific stress-activated caspase (caspase-12) is implicated in the apoptosis of A549 epithelial cells by respiratory syncytial virus. *Journal of cellular biochemistry*, 80(3), 441–454. [https://doi.org/10.1002/1097-4644\(20010301\)80:3<441::aid-jcb170>3.0.co;2-c](https://doi.org/10.1002/1097-4644(20010301)80:3<441::aid-jcb170>3.0.co;2-c)

Blanchard, E.L., Braun, M.R., Lifland, A.W., Ludeke, B., Noton, S.L., Vanover, D., Zurla, C., Fearn, R., Santangelo, P.J., 2020. Polymerase-tagged respiratory syncytial virus reveals a dynamic rearrangement of the ribonucleocapsid complex during infection. *PLoS Pathog* 16, e1008987. <https://doi.org/10.1371/journal.ppat.1008987>

Blondot, M.-L., Dubosclard, V., Fix, J., Lassoued, S., Aumont-Nicaise, M., Bontems, F., Eléouët, J.-F., Sizun, C., 2012. Structure and Functional Analysis of the RNA- and Viral Phosphoprotein-Binding Domain of Respiratory Syncytial Virus M2-1 Protein. *PLoS Pathog* 8, e1002734. <https://doi.org/10.1371/journal.ppat.1002734>

Bloth, B., Norrby, E., 1967. Electron microscopic analysis of the internal component of respiratory syncytial (RS) virus. *Archiv f Virusforschung* 21, 71–77. <https://doi.org/10.1007/BF01258478>

Blumberg, B.M., Giorgi, C., Kolakofsky, D., 1983. N protein of vesicular stomatitis virus selectively encapsidates leader RNA in vitro. *Cell* 32, 559–567. [https://doi.org/10.1016/0092-8674\(83\)90475-0](https://doi.org/10.1016/0092-8674(83)90475-0)

Bouillier, C., Cosentino, G., Léger, T., Rincheval, V., Richard, C.-A., Desquesnes, A., Sitterlin, D., Blouquit-Laye, S., Eléouët, J.-F., Gault, E., Rameix-Welti, M.-A., 2019. The Interactome analysis of the Respiratory Syncytial Virus protein M2-1 suggests a new role in viral mRNA metabolism post-transcription. *Sci Rep* 9, 15258. <https://doi.org/10.1038/s41598-019-51746-0>

Boyapalle, S., Wong, T., Garay, J., Teng, M., San Juan-Vergara, H., Mohapatra, Subhra, Mohapatra, Shyam, 2012. Respiratory Syncytial Virus NS1 Protein Colocalizes with Mitochondrial Antiviral Signaling Protein MAVS following Infection. *PLoS ONE* 7, e29386. <https://doi.org/10.1371/journal.pone.0029386>

Braun, M.R., Deflubé, L.R., Noton, S.L., Mawhorter, M.E., Tremaglio, C.Z., Fearn, R., 2017. RNA elongation by respiratory syncytial virus polymerase is calibrated by conserved region V. *PLoS Pathog* 13, e1006803. <https://doi.org/10.1371/journal.ppat.1006803>

Braun, M.R., Noton, S.L., Blanchard, E.L., Shareef, A., Santangelo, P.J., Johnson, W.E., Fearn, R., 2021. Respiratory syncytial virus M2-1 protein associates non-specifically with viral messenger RNA and with specific cellular messenger RNA transcripts. *PLoS Pathog* 17, e1009589. <https://doi.org/10.1371/journal.ppat.1009589>

Brock, S.C., Goldenring, J.R., Crowe, J.E., 2003. Apical recycling systems regulate directional budding of respiratory syncytial virus from polarized epithelial cells. *Proc. Natl. Acad. Sci. U.S.A.* 100, 15143–15148. <https://doi.org/10.1073/pnas.2434327100>

Brown, G., Rixon, H.W.McL., Steel, J., McDonald, T.P., Pitt, A.R., Graham, S., Sugrue, R.J., 2005. Evidence for an association between heat shock protein 70 and the respiratory syncytial virus polymerase complex within lipid-raft membranes during virus infection. *Virology* 338, 69–80. <https://doi.org/10.1016/j.virol.2005.05.004>

Bryche, B., Frétaud, M., Saint-Albin Deliot, A., Galloux, M., Sedano, L., Langevin, C., Descamps, D., Rameix-Welti, M., Eléouët, J., Le Goffic, R., Meunier, N., 2020. Respiratory syncytial virus tropism for olfactory sensory neurons in mice. *J. Neurochem.* 155, 137–153. <https://doi.org/10.1111/jnc.14936>

Bukreyev, A., Yang, L., Fricke, J., Cheng, L., Ward, J. M., Murphy, B. R., & Collins, P. L., 2008. The secreted form of respiratory syncytial virus G glycoprotein helps the virus evade antibody-mediated restriction of replication by acting as an antigen decoy and through effects on Fc receptor-bearing leukocytes. *Journal of virology*, 82(24), 12191–12204. <https://doi.org/10.1128/JVI.01604-08>

Bulletin hebdomadaire Bronchiolite, 18/01/2023, Semaine 02, Santé publique France. <https://www.santepubliquefrance.fr/revues/beh/bulletin-epidemiologique-hebdomadaire>

Calain, P., Roux, L., 1993. The rule of six, a basic feature for efficient replication of Sendai virus defective interfering RNA. *J Virol* 67, 4822–4830. <https://doi.org/10.1128/jvi.67.8.4822-4830.1993>

Cao, D., Gao, Y., Roesler, C., Rice, S., D’Cunha, P., Zhuang, L., Slack, J., Domke, M., Antonova, A., Romanelli, S., Keating, S., Forero, G., Juneja, P., Liang, B., 2020. Cryo-EM structure of the respiratory syncytial virus RNA polymerase. *Nat Commun* 11, 368. <https://doi.org/10.1038/s41467-019-14246-3>

Cao, D., Gooneratne, I., Mera, C., Vy, J., Royal, M., Huang, B., Park, Y., Manjunath, A., Liang, B., 2022. Analysis of Template Variations on RNA Synthesis by Respiratory Syncytial Virus Polymerase. *Viruses* 15, 47. <https://doi.org/10.3390/v15010047>

Carlos, T. S., Young, D. F., Schneider, M., Simas, J. P., & Randall, R. E., 2009. Parainfluenza virus 5 genomes are located in viral cytoplasmic bodies whilst the virus dismantles the interferon-induced antiviral state of cells. *The Journal of general virology*, 90(Pt 9), 2147–2156. <https://doi.org/10.1099/vir.0.012047-0>

Cartee, T.L., Wertz, G.W., 2001. Respiratory Syncytial Virus M2-1 Protein Requires Phosphorylation for Efficient Function and Binds Viral RNA during Infection. *J Virol* 75, 12188–12197. <https://doi.org/10.1128/JVI.75.24.12188-12197.2001>

Castagné, N., Barbier, A., Bernard, J., Rezaei, H., Huet, J.-C., Henry, C., Costa, B.D., Eléouët, J.-F., 2004. Biochemical characterization of the respiratory syncytial virus P–P and P–N protein complexes and localization of the P protein oligomerization domain. *Journal of General Virology* 85, 1643–1653. <https://doi.org/10.1099/vir.0.79830-0>

Castaño-Díez, D., Kudryashev, M., Arheit, M., Stahlberg, H., 2012. Dynamo: A flexible, user-friendly development tool for subtomogram averaging of cryo-EM data in high-performance computing environments. *Journal of Structural Biology* 178, 139–151. <https://doi.org/10.1016/j.jsb.2011.12.017>

Challa, S., Scott, A.D., Yuzhakov, O., Zhou, Y., Tiong-Yip, C.L., Gao, N., Thresher, J., Yu, Q., 2015. Mechanism of Action for Respiratory Syncytial Virus Inhibitor RSV604. *Antimicrob Agents Chemother* 59, 1080–1087. <https://doi.org/10.1128/AAC.04119-14>

Chanock, R., Roizman, B., & Myers, R., 1957. Recovery from infants with respiratory illness of a virus related to chimpanzee coryza agent (CCA). I. Isolation, properties and characterization. *American journal of hygiene*, 66(3), 281–290. <https://doi.org/10.1093/oxfordjournals.aje.a119901>



Chen, S., McMullan, G., Faruqi, A.R., Murshudov, G.N., Short, J.M., Scheres, S.H.W., Henderson, R., 2013. High-resolution noise substitution to measure overfitting and validate resolution in 3D structure determination by single particle electron cryomicroscopy. *Ultramicroscopy* 135, 24–35. <https://doi.org/10.1016/j.ultramic.2013.06.004>

Chin, J., Magoffin, R.L., Shearer, L.A., Schieble, J.H., Lennette, E.H., 1969. Field evaluation of a respiratory syncytial virus vaccine and a trivalent parainfluenza virus vaccine in a pediatric population. *American Journal of Epidemiology* 89, 449–463. <https://doi.org/10.1093/oxfordjournals.aje.a120957>

Chirkova, T., Lin, S., Oomens, A.G.P., Gaston, K.A., Boyoglu-Barnum, S., Meng, J., Stobart, C.C., Cotton, C.U., Hartert, T.V., Moore, M.L., Ziady, A.G., Anderson, L.J., 2015. CX3CR1 is an important surface molecule for respiratory syncytial virus infection in human airway epithelial cells. *Journal of General Virology* 96, 2543–2556. <https://doi.org/10.1099/vir.0.000218>

Chu, H.Y., Steinhoff, M.C., Magaret, A., Zaman, K., Roy, E., Langdon, G., Formica, M.A., Walsh, E.E., Englund, J.A., 2014. Respiratory Syncytial Virus Transplacental Antibody Transfer and Kinetics in Mother-Infant Pairs in Bangladesh. *J Infect Dis.* 210, 1582–1589. <https://doi.org/10.1093/infdis/jiu316>

Cifuentes-Muñoz, N., Branttie, J., Slaughter, K.B., Dutch, R.E., 2017. Human Metapneumovirus Induces Formation of Inclusion Bodies for Efficient Genome Replication and Transcription. *J Virol* 91, e01282-17. <https://doi.org/10.1128/JVI.01282-17>

Cochran, W., Crick, F.H., Vand, V., 1952. The structure of synthetic polypeptides. I. The transform of atoms on a helix. *Acta Cryst* 5, 581–586. <https://doi.org/10.1107/S0365110X52001635>

Collins, P.L., Hill, M.G., Camargo, E., Grosfeld, H., Chanock, R.M., Murphy, B.R., 1995. Production of infectious human respiratory syncytial virus from cloned cDNA confirms an essential role for the transcription elongation factor from the 5' proximal open reading frame of the M2 mRNA in gene expression and provides a capability for vaccine development. *Proc. Natl. Acad. Sci. U.S.A.* 92, 11563–11567. <https://doi.org/10.1073/pnas.92.25.11563>

Collins, P.L., Hill, M.G., Cristina, J., Grosfeld, H., 1996. Transcription elongation factor of respiratory syncytial virus, a nonsegmented negative-strand RNA virus. *Proc. Natl. Acad. Sci. U.S.A.* 93, 81–85. <https://doi.org/10.1073/pnas.93.1.81>

Conley, M.J., Short, J.M., Burns, A.M., Streetley, J., Hutchings, J., Bakker, S.E., Power, B.J., Jaffery, H., Haney, J., Zanetti, G., Murcia, P.R., Stewart, M., Fearn, R., Vijayakrishnan, S., Bhella, D., 2022. Helical ordering of envelope-associated proteins and glycoproteins in respiratory syncytial virus. *The EMBO Journal* 41. <https://doi.org/10.15252/emboj.2021109728>

Cox, R., Green, T.J., Qiu, S., Kang, J., Tsao, J., Prevelige, P.E., He, B., Luo, M., 2009. Characterization of a Mumps Virus Nucleocapsidlike Particle. *J Virol* 83, 11402–11406. <https://doi.org/10.1128/JVI.00504-09>

Cressey, T.N., Noton, S.L., Nagendra, K., Braun, M.R., Fearn, R., 2018. Mechanism for de novo initiation at two sites in the respiratory syncytial virus promoter. *Nucleic Acids Research* 46, 6785–6796. <https://doi.org/10.1093/nar/gky480>

Cuesta, I., Geng, X., Asenjo, A., Villanueva, N., 2000. Structural Phosphoprotein M2-1 of the Human Respiratory Syncytial Virus Is an RNA Binding Protein. *J Virol* 74, 9858–9867. <https://doi.org/10.1128/JVI.74.21.9858-9867.2000>

Cunningham, S., Piedra, P. A., Martinon-Torres, F., Szymanski, H., Brackeva, B., Dombrecht, E., Detalle, L., Fleurinck, C., & RESPIRE study group, 2021. Nebulised ALX-0171 for respiratory syncytial virus lower respiratory tract infection in hospitalised children: a double-blind, randomised, placebo-controlled, phase 2b trial. *The Lancet. Respiratory medicine*, 9(1), 21–32. [https://doi.org/10.1016/S2213-2600\(20\)30320-9](https://doi.org/10.1016/S2213-2600(20)30320-9)

Currier, M.G., Lee, S., Stobart, C.C., Hotard, A.L., Villenave, R., Meng, J., Pretto, C.D., Shields, M.D., Nguyen, M.T., Todd, S.O., Chi, M.H., Hammonds, J., Krumm, S.A., Spearman, P., Plemper, R.K., Sakamoto, K., Peebles, R.S., Power, U.F., Moore, M.L., 2016. EGFR Interacts with the Fusion Protein of Respiratory Syncytial Virus Strain 2-20 and Mediates Infection and Mucin Expression. *PLoS Pathog* 12, e1005622. <https://doi.org/10.1371/journal.ppat.1005622>

De Rosier, D.J., Klug, A., 1968. Reconstruction of Three Dimensional Structures from Electron Micrographs. *Nature* 217, 130–134. <https://doi.org/10.1038/217130a0>

Desfosses, A., Goret, G., Farias Estrozi, L., Ruigrok, R.W.H., Gutsche, I., 2011. Nucleoprotein-RNA Orientation in the Measles Virus Nucleocapsid by Three-Dimensional Electron Microscopy. *J Virol* 85, 1391–1395. <https://doi.org/10.1128/JVI.01459-10>

Desfosses, A., Milles, S., Jensen, M.R., Guseva, S., Colletier, J.-P., Maurin, D., Schoehn, G., Gutsche, I., Ruigrok, R.W.H., Blackledge, M., 2019. Assembly and cryo-EM structures of RNA-specific measles virus nucleocapsids provide mechanistic insight into paramyxoviral replication. *Proc. Natl. Acad. Sci. U.S.A.* 116, 4256–4264. <https://doi.org/10.1073/pnas.1816417116>

Detalle, L., Stohr, T., Palomo, C., Piedra, P.A., Gilbert, B.E., Mas, V., Millar, A., Power, U.F., Stortelers, C., Allosery, K., Melero, J.A., Depla, E., 2016. Generation and Characterization of ALX-0171, a Potent Novel Therapeutic Nanobody for the Treatment of Respiratory Syncytial Virus Infection. *Antimicrob Agents Chemother* 60, 6–13. <https://doi.org/10.1128/AAC.01802-15>

Devarkar, S.C., Wang, C., Miller, M.T., Ramanathan, A., Jiang, F., Khan, A.G., Patel, S.S., Marcotrigiano, J., 2016. Structural basis for m7G recognition and 2'-O-methyl discrimination in capped RNAs by the innate immune receptor RIG-I. *Proc. Natl. Acad. Sci. U.S.A.* 113, 596–601. <https://doi.org/10.1073/pnas.1515152113>

DeVincenzo, J. P., Whitley, R. J., Mackman, R. L., Scaglioni-Weinlich, C., Harrison, L., Farrell, E., McBride, S., Lambkin-Williams, R., Jordan, R., Xin, Y., Ramanathan, S., O'Riordan, T., Lewis, S. A., Li, X., Toback, S. L., Lin, S. L., & Chien, J. W., 2014. Oral GS-5806 activity in a respiratory syncytial virus challenge study. *The New England journal of medicine*, 371(8), 711–722. <https://doi.org/10.1056/NEJMoa1401184>

DeVincenzo, J.P., McClure, M.W., Symons, J.A., Fathi, H., Westland, C., Chanda, S., Lambkin-Williams, R., Smith, P., Zhang, Q., Beigelman, L., Blatt, L.M., Fry, J., 2015. Activity of Oral ALS-008176 in a Respiratory Syncytial Virus Challenge Study. *N Engl J Med* 373, 2048–2058. <https://doi.org/10.1056/NEJMoa1413275>

DeVincenzo, J., Cass, L., Murray, A., Woodward, K., Meals, E., Coates, M., Daly, L., Wheeler, V., Mori, J., Brindley, C., Davis, A., McCurdy, M., Ito, K., Murray, B., Strong, P., Rapeport, G., 2022. Safety and Antiviral Effects of Nebulized PC786 in a Respiratory Syncytial Virus Challenge Study. *The Journal of Infectious Diseases* 225, 2087–2096. <https://doi.org/10.1093/infdis/jiaa716>

Diaz, R., Rice, W., J., Stokes, D.L., 2010. Fourier–Bessel Reconstruction of Helical Assemblies, in: *Methods in Enzymology*. Elsevier, pp. 131–165. [https://doi.org/10.1016/S0076-6879\(10\)82005-1](https://doi.org/10.1016/S0076-6879(10)82005-1)

Domachowske, J., Madhi, S. A., Simões, E. A. F., Atanasova, V., Cabañas, F., Furuno, K., Garcia-Garcia, M. L., Grantina, I., Nguyen, K. A., Brooks, D., Chang, Y., Leach, A., Takas, T., Yuan, Y., Griffin, M. P., Mankad, V. S., Villafana, T., & MEDLEY Study Group, 2022. Safety of Nirsevimab for RSV in Infants with Heart or Lung Disease or Prematurity. *The New England journal of medicine*, 386(9), 892–894. <https://doi.org/10.1056/NEJMc2112186>

Dong, J., Basse, V., Bierre, M., Peres De Oliveira, A., Vidalain, P.-O., Sibille, P., Tangy, F., Galloux, M., Eleouet, J.-F., Sizun, C., Bajorek, M., 2022. Respiratory Syncytial Virus NS1 Protein Targets the Transactivator Binding Domain of MED25. *Journal of Molecular Biology* 434, 167763. <https://doi.org/10.1016/j.jmb.2022.167763>

Dong, X., Wang, X., Xie, M., Wu, W., Chen, Z., 2022. Structural Basis of Human Parainfluenza Virus 3 Unassembled Nucleoprotein in Complex with Its Viral Chaperone. *J Virol* 96, e01648-21. <https://doi.org/10.1128/JVI.01648-21>

Donovan-Banfield, I., Milligan, R., Hall, S., Gao, T., Murphy, E., Li, J., Shawli, G.T., Hiscox, J., Zhuang, X., McKeating, J.A., Fearn, R., Matthews, D.A., 2022. Direct RNA sequencing of respiratory syncytial virus infected human cells generates a detailed overview of RSV polycistronic mRNA and transcript abundance. *PLoS ONE* 17, e0276697. <https://doi.org/10.1371/journal.pone.0276697>

Doreleijers, J.F., Langedijk, J.P.M., Hård, K., Boelens, R., Rullmann, J.A.C., Schaaper, W.M., Van Oirschot, J.T., Kaptein, R., 1996. Solution Structure of the Immunodominant Region of Protein G of Bovine Respiratory Syncytial Virus. *Biochemistry* 35, 14684–14688. <https://doi.org/10.1021/bi9621627>

Dubochet, J., Chang, J.-J., Freeman, R., Lepault, J., McDowell, A.W., 1982. Frozen aqueous suspensions. *Ultramicroscopy* 10, 55–61. [https://doi.org/10.1016/0304-3991\(82\)90187-5](https://doi.org/10.1016/0304-3991(82)90187-5)

Dubochet, J., McDowell, A.W., 1981. Vitrification of pure water for electron microscopy. *Journal of Microscopy* 124, 3–4. <https://doi.org/10.1111/j.1365-2818.1981.tb02483.x>

Egelman E. H., 2010. Reconstruction of helical filaments and tubes. *Methods in enzymology*, 482, 167–183. [https://doi.org/10.1016/S0076-6879\(10\)82006-3](https://doi.org/10.1016/S0076-6879(10)82006-3)

El Omari, K., Scott, K., Dhaliwal, B., Ren, J., Abrescia, N.G.A., Budworth, J., Lockyer, M., Powell, K.L., Hawkins, A.R., Stammers, D.K., 2008. Crystallization and preliminary X-ray analysis of the human respiratory syncytial virus nucleocapsid protein. *Acta Crystallogr F Struct Biol Cryst Commun* 64, 1019–1023. <https://doi.org/10.1107/S1744309108031059>

El Saleeby, C.M., Bush, A.J., Harrison, L.M., Aitken, J.A., DeVincenzo, J.P., 2011. Respiratory Syncytial Virus Load, Viral Dynamics, and Disease Severity in Previously Healthy Naturally Infected Children. *The Journal of Infectious Diseases* 204, 996–1002. <https://doi.org/10.1093/infdis/jir494>

Esneau, C., Raynal, B., Roblin, P., Brûlé, S., Richard, C.-A., Fix, J., Eléouët, J.-F., Galloux, M., 2019. Biochemical characterization of the respiratory syncytial virus N0-P complex in solution. *Journal of Biological Chemistry* 294, 3647–3660. <https://doi.org/10.1074/jbc.RA118.006453>

Falsey, A.R., Erdman, D., Anderson, L.J., Walsh, E.E., 2003. Human Metapneumovirus Infections in Young and Elderly Adults. *J INFECT DIS* 187, 785–790. <https://doi.org/10.1086/367901>

Falsey, A.R., Walsh, E.E., House, S., Vandenijck, Y., Ren, X., Keim, S., Kang, D., Peeters, P., Witek, J., Ispas, G., 2021. Risk Factors and Medical Resource Utilization of Respiratory Syncytial Virus, Human Metapneumovirus and Influenza Related Hospitalizations in Adults – A Global Study During the 2017-2019 Epidemic Seasons (Hospitalized Acute Respiratory Tract Infection [HARTI] Study). *Open Forum Infectious Diseases* ofab491. <https://doi.org/10.1093/ofid/ofab491>

Faruqi, A.R., 2009. Principles and prospects of direct high resolution electron image acquisition with CMOS detectors at low energies. *J. Phys.: Condens. Matter* 21, 314004. <https://doi.org/10.1088/0953-8984/21/31/314004>

Fearns, R., Collins, P.L., 1999. Role of the M2-1 Transcription Antitermination Protein of Respiratory Syncytial Virus in Sequential Transcription. *J Virol* 73, 5852–5864. <https://doi.org/10.1128/JVI.73.7.5852-5864.1999>

Fearns, R., Peeples, M.E., Collins, P.L., 1997. Increased Expression of the N Protein of Respiratory Syncytial Virus Stimulates Minigenome Replication but Does Not Alter the Balance between the Synthesis of mRNA and Antigenome. *Virology* 236, 188–201. <https://doi.org/10.1006/viro.1997.8734>

Feldman, S.A., Audet, S., Beeler, J.A., 2000. The Fusion Glycoprotein of Human Respiratory Syncytial Virus Facilitates Virus Attachment and Infectivity via an Interaction with Cellular Heparan Sulfate. *J Virol* 74, 6442–6447. <https://doi.org/10.1128/JVI.74.14.6442-6447.2000>

Feldman, S.A., Hendry, R.M., Beeler, J.A., 1999. Identification of a Linear Heparin Binding Domain for Human Respiratory Syncytial Virus Attachment Glycoprotein G. *J Virol* 73, 6610–6617. <https://doi.org/10.1128/JVI.73.8.6610-6617.1999>

Fernandez-Leiro, R., Scheres, S.H.W., 2016. Unravelling biological macromolecules with cryo-electron microscopy. *Nature* 537, 339–346. <https://doi.org/10.1038/nature19948>

Filipowicz, W., Furuichi, Y., Sierra, J.M., Muthukrishnan, S., Shatkin, A.J., Ochoa, S., 1976. A protein binding the methylated 5'-terminal sequence, m7GpppN, of eukaryotic messenger RNA. *Proc. Natl. Acad. Sci. U.S.A.* 73, 1559–1563. <https://doi.org/10.1073/pnas.73.5.1559>

Förster, A., Maertens, G.N., Farrell, P.J., Bajorek, M., 2015. Dimerization of Matrix Protein Is Required for Budding of Respiratory Syncytial Virus. *J Virol* 89, 4624–4635. <https://doi.org/10.1128/JVI.03500-14>

Frank J., 1975. Averaging of low exposure electron micrographs of non-periodic objects. *Ultramicroscopy*, 1(2), 159–162. [https://doi.org/10.1016/s0304-3991\(75\)80020-9](https://doi.org/10.1016/s0304-3991(75)80020-9)

Fujita-Fujiharu, Y., Sugita, Y., Takamatsu, Y., Houri, K., Igarashi, M., Muramoto, Y., Nakano, M., Tsunoda, Y., Taniguchi, I., Becker, S., Noda, T., 2022. Structural insight into Marburg virus nucleoprotein–RNA complex formation. *Nat Commun* 13, 1191. <https://doi.org/10.1038/s41467-022-28802-x>

Fulginiti, V.A., Eller, J.J., Sieber, O.F., Joyner, J.W., Minamitani, M., Meiklejohn, G., 1969. Respiratory virus immunization. *American Journal of Epidemiology* 89, 435–448. <https://doi.org/10.1093/oxfordjournals.aje.a120956>

Galloux, M., Gabiane, G., Sourimant, J., Richard, C.-A., England, P., Moudjou, M., Aumont-Nicaise, M., Fix, J., Rameix-Welti, M.-A., Eléouët, J.-F., 2015. Identification and Characterization of the Binding Site of the Respiratory Syncytial Virus Phosphoprotein to RNA-Free Nucleoprotein. *J Virol* 89, 3484–3496. <https://doi.org/10.1128/JVI.03666-14>

Galloux, M., Risso-Ballester, J., Richard, C.-A., Fix, J., Rameix-Welti, M.-A., Eléouët, J.-F., 2020. Minimal Elements Required for the Formation of Respiratory Syncytial Virus Cytoplasmic Inclusion Bodies *In Vivo* and *In Vitro*. *mBio* 11, e01202-20. <https://doi.org/10.1128/mBio.01202-20>

Galloux, M., Tarus, B., Blazevic, I., Fix, J., Duquerroy, S., Eléouët, J.-F., 2012. Characterization of a Viral Phosphoprotein Binding Site on the Surface of the Respiratory Syncytial Nucleoprotein. *J Virol* 86, 8375–8387. <https://doi.org/10.1128/JVI.00058-12>

Gan, S.-W., Tan, E., Lin, X., Yu, D., Wang, J., Tan, G.M.-Y., Vararattanavech, A., Yeo, C.Y., Soon, C.H., Soong, T.W., Pervushin, K., Torres, J., 2012. The Small Hydrophobic Protein of the Human Respiratory Syncytial Virus Forms Pentameric Ion Channels. *Journal of Biological Chemistry* 287, 24671–24689. <https://doi.org/10.1074/jbc.M111.332791>

Gao, Y., Cao, D., Ahn, H.M., Swain, A., Hill, S., Ogilvie, C., Kurien, M., Rahmatullah, T., Liang, B., 2020a. In vitro trackable assembly of RNA-specific nucleocapsids of the respiratory syncytial virus. *Journal of Biological Chemistry* 295, 883–895. [https://doi.org/10.1016/S0021-9258\(17\)49942-X](https://doi.org/10.1016/S0021-9258(17)49942-X)

Gao, Y., Cao, D., Pawnikar, S., John, K.P., Ahn, H.M., Hill, S., Ha, J.M., Parikh, P., Ogilvie, C., Swain, A., Yang, A., Bell, A., Salazar, A., Miao, Y., Liang, B., 2020b. Structure of the Human Respiratory Syncytial Virus M2-1 Protein in Complex with a Short Positive-Sense Gene-End RNA. *Structure* 28, 979-990.e4. <https://doi.org/10.1016/j.str.2020.07.001>

García, J., García-Barreno, B., Vivo, A., & Melero, J. A., 1993. Cytoplasmic inclusions of respiratory syncytial virus-infected cells: formation of inclusion bodies in transfected cells that coexpress the nucleoprotein, the phosphoprotein, and the 22K protein. *Virology*, 195(1), 243–247. <https://doi.org/10.1006/viro.1993.1366>

García-Barreno, B., Delgado, T., Melero, J.A., 1996. Identification of protein regions involved in the interaction of human respiratory syncytial virus phosphoprotein and nucleoprotein: significance for nucleocapsid assembly and formation of cytoplasmic inclusions. *J Virol* 70, 801–808. <https://doi.org/10.1128/jvi.70.2.801-808.1996>

Garriga, D., Ferrer-Orta, C., Querol-Audí, J., Oliva, B., Verdaguer, N., 2013. Role of Motif B Loop in Allosteric Regulation of RNA-Dependent RNA Polymerization Activity. *Journal of Molecular Biology* 425, 2279–2287. <https://doi.org/10.1016/j.jmb.2013.03.034>

Geller, R., Andino, R., Frydman, J., 2013. Hsp90 Inhibitors Exhibit Resistance-Free Antiviral Activity against Respiratory Syncytial Virus. *PLoS ONE* 8, e56762. <https://doi.org/10.1371/journal.pone.0056762>

Ghildyal, R., Mills, J., Murray, M., Vardaxis, N., Meanger, J., 2002. Respiratory syncytial virus matrix protein associates with nucleocapsids in infected cells. *Journal of General Virology* 83, 753–757. <https://doi.org/10.1099/0022-1317-83-4-753>

Gilman, M.S.A., Liu, C., Fung, A., Behera, I., Jordan, P., Rigaux, P., Ysebaert, N., Tcherniuk, S., Sourimant, J., Eléouët, J.-F., Sutto-Ortiz, P., Decroly, E., Roymans, D., Jin, Z., McLellan, J.S., 2019. Structure of the Respiratory Syncytial Virus Polymerase Complex. *Cell* 179, 193-204.e14. <https://doi.org/10.1016/j.cell.2019.08.014>

Glezen, W.P., 1986. Risk of Primary Infection and Reinfection With Respiratory Syncytial Virus. *Arch Pediatr Adolesc Med* 140, 543. <https://doi.org/10.1001/archpedi.1986.02140200053026>

Gottlieb, J., Zamora, M. R., Hodges, T., Musk, A. W., Sommerwerk, U., Dilling, D., Arcasoy, S., DeVincenzo, J., Karsten, V., Shah, S., Bettencourt, B. R., Cehelsky, J., Nochur, S., Gollob, J., Vaishnav, A., Simon, A. R., & Glanville, A. R., 2016. ALN-RSV01 for prevention of bronchiolitis obliterans syndrome after respiratory syncytial virus infection in lung transplant recipients. *The Journal of heart and lung transplantation : the official publication of the International Society for Heart Transplantation*, 35(2), 213–221. <https://doi.org/10.1016/j.healun.2015.08.012>

Grant, T., Grigorieff, N., 2015. Measuring the optimal exposure for single particle cryo-EM using a 2.6 Å reconstruction of rotavirus VP6. *eLife* 4, e06980. <https://doi.org/10.7554/eLife.06980>

Grosfeld, H., Hill, M.G., Collins, P.L., 1995. RNA replication by respiratory syncytial virus (RSV) is directed by the N, P, and L proteins; transcription also occurs under these conditions but requires RSV superinfection for efficient synthesis of full-length mRNA. *J Virol* 69, 5677–5686. <https://doi.org/10.1128/jvi.69.9.5677-5686.1995>

Guryanov, S.G., Liljeroos, L., Kasaragod, P., Kajander, T., Butcher, S.J., 2016. Crystal Structure of the Measles Virus Nucleoprotein Core in Complex with an N-Terminal Region of Phosphoprotein. *J Virol* 90, 2849–2857. <https://doi.org/10.1128/JVI.02865-15>

Gutsche, I., Desfosses, A., Effantin, G., Ling, W.L., Haupt, M., Ruigrok, R.W.H., Sachse, C., Schoehn, G., 2015. Near-atomic cryo-EM structure of the helical measles virus nucleocapsid. *Science* 348, 704–707. <https://doi.org/10.1126/science.aaa5137>

Habibi, M.S., Jozwik, A., Makris, S., Dunning, J., Paras, A., DeVincenzo, J.P., De Haan, C.A.M., Wrammert, J., Openshaw, P.J.M., Chiu, C., 2015. Impaired Antibody-mediated Protection and Defective IgA B-Cell Memory in Experimental Infection of Adults with Respiratory Syncytial Virus. *Am J Respir Crit Care Med* 191, 1040–1049. <https://doi.org/10.1164/rccm.201412-2256OC>

Hagen, W.J.H., Wan, W., Briggs, J.A.G., 2017. Implementation of a cryo-electron tomography tilt-scheme optimized for high resolution subtomogram averaging. *Journal of Structural Biology* 197, 191–198. <https://doi.org/10.1016/j.jsb.2016.06.007>

Hall, C.B., Douglas, R.G., 1981. Modes of transmission of respiratory syncytial virus. *The Journal of Pediatrics* 99, 100–103. [https://doi.org/10.1016/S0022-3476\(81\)80969-9](https://doi.org/10.1016/S0022-3476(81)80969-9)

Hall, C.B., Iwane, M.K., Staat, M.A., Poehling, K.A., Grijalva, C.G., Szilagyi, P., 2009. The Burden of Respiratory Syncytial Virus Infection in Young Children. *n engl j med*.

Hall, C.B., Walsh, E.E., Long, C.E., Schnabel, K.C., 1991. Immunity to and Frequency of Reinfection with Respiratory Syncytial Virus. *Journal of Infectious Diseases* 163, 693–698. <https://doi.org/10.1093/infdis/163.4.693>

Hammitt, L.L., Dagan, R., Yuan, Y., Baca-Cots, M., Bosheva, M., Madhi, S.A., Muller, W.J., Zar, H.J., Brooks, D., Grenham, A., Wählby Hamrén, U., Mankad, V.S., Ren, P., Takas, T., Abram, M.E., Leach, A., Griffin, M.P., Villafana, T., 2022. Nirsevimab for Prevention of RSV in Healthy Late-Preterm and Term Infants. *N Engl J Med* 386, 837–846. <https://doi.org/10.1056/NEJMoa2110275>

Hardy, R. W., & Wertz, G. W., 1998. The product of the respiratory syncytial virus M2 gene ORF1 enhances readthrough of intergenic junctions during viral transcription. *Journal of virology*, 72(1), 520–526. <https://doi.org/10.1128/JVI.72.1.520-526.1998>

Hause, B.M., Padmanabhan, A., Pedersen, K., Gidlewski, T., 2016. Feral swine virome is dominated by single-stranded DNA viruses and contains a novel Orthopneumovirus which circulates both in feral and domestic swine. *Journal of General Virology* 97, 2090–2095. <https://doi.org/10.1099/jgv.0.000554>

He, S., Scheres, S.H.W., 2017. Helical reconstruction in RELION. *Journal of Structural Biology* 198, 163–176. <https://doi.org/10.1016/j.jsb.2017.02.003>

Heggeness, M.H., Scheid, A., Choppin, P.W., 1980. Conformation of the helical nucleocapsids of paramyxoviruses and vesicular stomatitis virus: reversible coiling and uncoiling induced by changes in salt concentration. *Proc. Natl. Acad. Sci. U.S.A.* 77, 2631–2635. <https://doi.org/10.1073/pnas.77.5.2631>



Heinrich, B.S., Cureton, D.K., Rahmeh, A.A., Whelan, S.P.J., 2010. Protein Expression Redirects Vesicular Stomatitis Virus RNA Synthesis to Cytoplasmic Inclusions. *PLoS Pathog* 6, e1000958. <https://doi.org/10.1371/journal.ppat.1000958>

Hendricks, D. A., Baradaran, K., McIntosh, K., & Patterson, J. L., 1987. Appearance of a soluble form of the G protein of respiratory syncytial virus in fluids of infected cells. *The Journal of general virology*, 68 (Pt 6), 1705–1714. <https://doi.org/10.1099/0022-1317-68-6-1705>

Himes, B.A., Zhang, P., 2018. emClarity: software for high-resolution cryo-electron tomography and subtomogram averaging. *Nat Methods* 15, 955–961. <https://doi.org/10.1038/s41592-018-0167-z>

Hirano, E., Kobayashi, M., Tsukagoshi, H., Yoshida, L.M., Kuroda, M., Noda, M., Ishioka, T., Kozawa, K., Ishii, H., Yoshida, A., Oishi, K., Ryo, A., Kimura, H., 2014. Molecular evolution of human respiratory syncytial virus attachment glycoprotein (G) gene of new genotype ON1 and ancestor NA1. *Infection, Genetics and Evolution* 28, 183–191. <https://doi.org/10.1016/j.meegid.2014.09.030>

Hoenen, T., Shabman, R.S., Groseth, A., Herwig, A., Weber, M., Schudt, G., Dolnik, O., Basler, C.F., Becker, S., Feldmann, H., 2012. Inclusion Bodies Are a Site of Ebolavirus Replication. *J Virol* 86, 11779–11788. <https://doi.org/10.1128/JVI.01525-12>

Homaira, N., Rawlinson, W., Snelling, T.L., Jaffe, A., 2014. Effectiveness of Palivizumab in Preventing RSV Hospitalization in High Risk Children: A Real-World Perspective. *International Journal of Pediatrics* 2014, 1–13. <https://doi.org/10.1155/2014/571609>

Hornung, V., Ellegast, J., Kim, S., Brzózka, K., Jung, A., Kato, H., Poeck, H., Akira, S., Conzelmann, K. K., Schlee, M., Endres, S., & Hartmann, G., 2006. 5'-Triphosphate RNA is the ligand for RIG-I. *Science (New York, N.Y.)*, 314(5801), 994–997. <https://doi.org/10.1126/science.1132505>

Jácome, R., Becerra, A., Ponce De León, S., Lazcano, A., 2015. Structural Analysis of Monomeric RNA-Dependent Polymerases: Evolutionary and Therapeutic Implications. *PLoS ONE* 10, e0139001. <https://doi.org/10.1371/journal.pone.0139001>

Jeffree, C.E., Brown, G., Aitken, J., Su-Yin, D.Y., Tan, B.-H., Sugrue, R.J., 2007. Ultrastructural analysis of the interaction between F-actin and respiratory syncytial virus during virus assembly. *Virology* 369, 309–323. <https://doi.org/10.1016/j.virol.2007.08.007>

Jenni, S., Horwitz, J.A., Bloyet, L.-M., Whelan, S.P.J., Harrison, S.C., 2022. Visualizing molecular interactions that determine assembly of a bullet-shaped vesicular stomatitis virus particle. *Nat Commun* 13, 4802. <https://doi.org/10.1038/s41467-022-32223-1>

Jeong, K.-I., Piepenhagen, P.A., Kishko, M., DiNapoli, J.M., Groppo, R.P., Zhang, L., Almond, J., Kleanthous, H., Delagrave, S., Parrington, M., 2015. CX3CR1 Is Expressed in Differentiated Human Ciliated Airway Cells and Co-Localizes with Respiratory Syncytial Virus on Cilia in a G Protein-Dependent Manner. *PLoS ONE* 10, e0130517. <https://doi.org/10.1371/journal.pone.0130517>

Jin, H., Cheng, X., Zhou, H.Z.Y., Li, S., Seddiqui, A., 2000. Respiratory Syncytial Virus That Lacks Open Reading Frame 2 of the M2 Gene (M2-2) Has Altered Growth Characteristics and Is Attenuated in Rodents. *J Virol* 74, 74–82. <https://doi.org/10.1128/JVI.74.1.74-82.2000>

Johnson, J.E., Gonzales, R.A., Olson, S.J., Wright, P.F., Graham, B.S., 2007. The histopathology of fatal untreated human respiratory syncytial virus infection. *Modern Pathology* 20, 108–119. <https://doi.org/10.1038/modpathol.3800725>

Johnson, S.M., McNally, B.A., Ioannidis, I., Flano, E., Teng, M.N., Oomens, A.G., Walsh, E.E., Peeples, M.E., 2015. Respiratory Syncytial Virus Uses CX3CR1 as a Receptor on Primary Human Airway Epithelial Cultures. *PLoS Pathog* 11, e1005318. <https://doi.org/10.1371/journal.ppat.1005318>

Jumper, J., Evans, R., Pritzel, A., Green, T., Figurnov, M., Ronneberger, O., Tunyasuvunakool, K., Bates, R., Žídek, A., Potapenko, A., Bridgland, A., Meyer, C., Kohl, S.A.A., Ballard, A.J., Cowie, A., Romera-Paredes, B., Nikolov, S., Jain, R., Adler, J., Back, T., Petersen, S., Reiman, D., Clancy, E., Zielinski, M., Steinegger, M., Pacholska, M., Berghammer, T., Bodenstein, S., Silver, D., Vinyals, O., Senior, A.W., Kavukcuoglu, K., Kohli, P., Hassabis, D., 2021. Highly accurate protein structure prediction with AlphaFold. *Nature* 596, 583–589. <https://doi.org/10.1038/s41586-021-03819-2>

Kapikian, A.Z., Mitchell, R.H., Chanock, R.M., Shvedoff, R.A., Stewart, C.E., 1969. An epidemiologic study of altered clinical reactivity to respiratory syncytial (rs) virus infection in children previously vaccinated with an inactivated rs virus vaccine. *American Journal of Epidemiology* 89, 405–421. <https://doi.org/10.1093/oxfordjournals.aje.a120954>

Karron, R.A., Buonagurio, D.A., Georgiu, A.F., Whitehead, S.S., Adamus, J.E., Clements-Mann, M.L., Harris, D.O., Randolph, V.B., Udem, S.A., Murphy, B.R., Sidhu, M.S., 1997. Respiratory syncytial virus (RSV) SH and G proteins are not essential for viral replication *in vitro*: Clinical evaluation and molecular characterization of a cold-passaged, attenuated RSV subgroup B mutant. *Proc. Natl. Acad. Sci. U.S.A.* 94, 13961–13966. <https://doi.org/10.1073/pnas.94.25.13961>

Ke, Z., Dillard, R., Chirkova, T., Leon, F., Stobart, C., Hampton, C., Strauss, J., Rajan, D., Rostad, C., Taylor, J., Yi, H., Shah, R., Jin, M., Hartert, T., Peebles, R., Graham, B., Moore, M., Anderson, L., Wright, E., 2018. The Morphology and Assembly of Respiratory Syncytial Virus Revealed by Cryo-Electron Tomography. *Viruses* 10, 446. <https://doi.org/10.3390/v10080446>

Ker, D.-S., Jenkins, H.T., Greive, S.J., Antson, A.A., 2021. CryoEM structure of the Nipah virus nucleocapsid assembly. *PLoS Pathog* 17, e1009740. <https://doi.org/10.1371/journal.ppat.1009740>

Khattar, S. K., Yunus, A. S., Collins, P. L., & Samal, S. K., 2001. Deletion and substitution analysis defines regions and residues within the phosphoprotein of bovine respiratory syncytial virus that affect transcription, RNA replication, and interaction with the nucleoprotein. *Virology*, 285(2), 253–269. <https://doi.org/10.1006/viro.2001.0960>

Kim, H.W., Canchola, J.G., Brandt, C.D., Pyles, G., Chanock, R.M., Jensen, K., Parrott, R.H., 1969. Respiratory syncytial virus disease in infants despite prior administration of antigenic inactivated vaccine. *American Journal of Epidemiology* 89, 422–434. <https://doi.org/10.1093/oxfordjournals.aje.a120955>

Kipper, S., Hamad, S., Caly, L., Avraami, D., Bacharach, E., Jans, D.A., Gerber, D., Bajorek, M., 2015. New Host Factors Important for Respiratory Syncytial Virus (RSV) Replication Revealed by a Novel Microfluidics Screen for Interactors of Matrix (M) Protein. *Molecular & Cellular Proteomics* 14, 532–543. <https://doi.org/10.1074/mcp.M114.044107>

Kirchdoerfer, R.N., Abelson, D.M., Li, S., Wood, M.R., Saphire, E.O., 2015. Assembly of the Ebola Virus Nucleoprotein from a Chaperoned VP35 Complex. *Cell Reports* 12, 140–149. <https://doi.org/10.1016/j.celrep.2015.06.003>

Kiss, G., Holl, J.M., Williams, G.M., Alonas, E., Vanover, D., Lifland, A.W., Gudheti, M., Guerrero-Ferreira, R.C., Nair, V., Yi, H., Graham, B.S., Santangelo, P.J., Wright, E.R., 2014. Structural Analysis of Respiratory Syncytial Virus Reveals the Position of M2-1 between the Matrix Protein and the Ribonucleoprotein Complex. *J Virol* 88, 7602–7617. <https://doi.org/10.1128/JVI.00256-14>

Klug, A., Crick, F.H.C., Wyckoff, H.W., 1958. Diffraction by helical structures. *Acta Cryst* 11, 199–213. <https://doi.org/10.1107/S0365110X58000517>

Klumpe, S., Fung, H.K., Goetz, S.K., Zagoriy, I., Hampoelz, B., Zhang, X., Erdmann, P.S., Baumbach, J., Müller, C.W., Beck, M., Plitzko, J.M., Mahamid, J., 2021. A modular platform for automated cryo-FIB workflows. *eLife* 10, e70506. <https://doi.org/10.7554/eLife.70506>

Kolakofsky, D., Pelet, T., Garcin, D., Hausmann, S., Curran, J., Roux, L., 1998. Paramyxovirus RNA Synthesis and the Requirement for Hexamer Genome Length: the Rule of Six Revisited. *J Virol* 72, 891–899. <https://doi.org/10.1128/JVI.72.2.891-899.1998>

Kolesnikova, L., Mühlberger, E., Ryabchikova, E., Becker, S., 2000. Ultrastructural Organization of Recombinant Marburg Virus Nucleoprotein: Comparison with Marburg Virus Inclusions. *J Virol* 74, 3899–3904. <https://doi.org/10.1128/JVI.74.8.3899-3904.2000>

Krusat, T., Streckert, H.-J., 1997. Heparin-dependent attachment of respiratory syncytial virus (RSV) to host cells. *Arch. Virol.* 142, 1247–1254. <https://doi.org/10.1007/s007050050156>

Krzyzaniak, M.A., Zumstein, M.T., Gerez, J.A., Picotti, P., Helenius, A., 2013. Host Cell Entry of Respiratory Syncytial Virus Involves Macropinocytosis Followed by Proteolytic Activation of the F Protein. *PLoS Pathog* 9, e1003309. <https://doi.org/10.1371/journal.ppat.1003309>

Kuo, L., Fearn, R., Collins, P.L., 1997. Analysis of the gene start and gene end signals of human respiratory syncytial virus: quasi-templated initiation at position 1 of the encoded mRNA. *J Virol* 71, 4944–4953. <https://doi.org/10.1128/jvi.71.7.4944-4953.1997>

Kuo, L., Grosfeld, H., Cristina, J., Hill, M.G., Collins, P.L., 1996. Effect of Mutations in the Gene-Start and Gene-End Sequence Motifs on Transcription of Monocistronic and Dicistronic Minigenomes of Respiratory Syncytial Virus. *J. VIROL.* 70.

Lahaye, X., Vidy, A., Pomier, C., Obiang, L., Harper, F., Gaudin, Y., Blondel, D., 2009. Functional Characterization of Negri Bodies (NBs) in Rabies Virus-Infected Cells: Evidence that NBs Are Sites of Viral Transcription and Replication. *J Virol* 83, 7948–7958. <https://doi.org/10.1128/JVI.00554-09>

Langedijk, J.P.M., Schaaper, W.M.M., Meloen, R.H., Van Oirschot, J.T., 1996. Proposed three-dimensional model for the attachment protein G of respiratory syncytial virus. *Journal of General Virology* 77, 1249–1257. <https://doi.org/10.1099/0022-1317-77-6-1249>

Levine, S., Klaiber-Franco, R., & Paradiso, P. R., 1987. Demonstration that glycoprotein G is the attachment protein of respiratory syncytial virus. *The Journal of general virology*, 68 (Pt 9), 2521–2524. <https://doi.org/10.1099/0022-1317-68-9-2521>

Leyrat, C., Renner, M., Harlos, K., Grimes, J.M., 2013. Solution and Crystallographic Structures of the Central Region of the Phosphoprotein from Human Metapneumovirus. *PLoS ONE* 8, e80371. <https://doi.org/10.1371/journal.pone.0080371>

Leyrat, C., Yabukarski, F., Tarbouriech, N., Ribeiro, E.A., Jensen, M.R., Blackledge, M., Ruigrok, R.W.H., Jamin, M., 2011. Structure of the Vesicular Stomatitis Virus N0-P Complex. *PLoS Pathog* 7, e1002248. <https://doi.org/10.1371/journal.ppat.1002248>

Li, D., Jans, D.A., Bardin, P.G., Meanger, J., Mills, J., Ghildyal, R., 2008. Association of Respiratory Syncytial Virus M Protein with Viral Nucleocapsids Is Mediated by the M2-1 Protein. *J Virol* 82, 8863–8870. <https://doi.org/10.1128/JVI.00343-08>

Li, W., Zhang, J., & Tanji, T., 2013. Image processing for phase imperfections in electron holography. *Microscopy* (Oxford, England), 62(6), 583–588. <https://doi.org/10.1093/jmicro/dft034>

Li, Y., Wang, X., Blau, D.M., Caballero, M.T., Feikin, D.R., Gill, C.J., Madhi, S.A., Omer, S.B., Simões, E.A.F., Campbell, H., Pariente, A.B., Bardach, D., Bassat, Q., Casalegno, J.-S., Chakhunashvili, G., Crawford, N., Danilenko, D., Do, L.A.H., Echavarria, M., Gentile, A., Gordon, A., Heikkinen, T., Huang, Q.S., Jullien, S., Krishnan, A., Lopez, E.L., Markić, J., Mira-Iglesias, A., Moore, H.C., Moyes, J., Mwananyanda, L., Nokes, D.J., Noordeen, F., Obodai, E., Palani, N., Romero, C., Salimi, V., Satav, A., Seo, E., Shchomak, Z., Singleton, R., Stolyarov, K., Stoszek, S.K., Von Gottberg, A., Wurzel, D., Yoshida, L.-M., Yung, C.F., Zar, H.J., Nair, H., Abram, M., Aerssens, J., Alafaci, A., Balmaseda, A., Bandeira, T., Barr, I., Batinović, E., Beutels, P., Bhiman, J., Blyth, C.C., Bont, L., Bressler, S.S., Cohen, C., Cohen, R., Costa, A.-M., Crow, R., Daley, A., Dang, D.-A., Demont, C., Desnoyers, C., Díez-Domingo, J., Divarathna, M., Du Plessis, M., Edgoose, M., Ferolla, F.M., Fischer, T.K., Gebremedhin, A., Giaquinto, C., Gillet, Y., Hernandez, R., Horvat, C., Javouhey, E., Karseladze, I., Kubale, J., Kumar, R., Lina, B., Lucion, F., MacGinty, R., Martinon-Torres, F., McMinn, A., Meijer, A., Milić, P., Morel, A., Mulholland, K., Mungun, T., Murunga, N., Newbern, C., Nicol, M.P., Odoom, J.K., Openshaw, P., Ploin, D., Polack, F.P., Pollard, A.J., Prasad, N., Puig-Barberà, J., Reiche, J., Reyes, N., Rizkalla, B., Satao, S., Shi, T., Sistla, S., Snape, M., Song, Y., Soto, G., Tavakoli, F., Toizumi, M., Tsedenbal, N., Van Den Berge, M., Vernhes, C., Von Mollendorf, C., Walaza, S., Walker, G., 2022. Global, regional, and national disease burden estimates of acute lower respiratory infections due to respiratory syncytial virus in children younger than 5 years in 2019: a systematic analysis. *The Lancet* 399, 2047–2064. [https://doi.org/10.1016/S0140-6736\(22\)00478-0](https://doi.org/10.1016/S0140-6736(22)00478-0)

Liang, B., Li, Z., Jenni, S., Rahmeh, A.A., Morin, B.M., Grant, T., Grigorieff, N., Harrison, S.C., Whelan, S.P.J., 2015. Structure of the L Protein of Vesicular Stomatitis Virus from Electron Cryomicroscopy. *Cell* 162, 314–327. <https://doi.org/10.1016/j.cell.2015.06.018>

Lifland, A.W., Jung, J., Alonas, E., Zurla, C., Crowe, J.E., Santangelo, P.J., 2012. Human Respiratory Syncytial Virus Nucleoprotein and Inclusion Bodies Antagonize the Innate Immune Response Mediated by MDA5 and MAVS. *J Virol* 86, 8245–8258. <https://doi.org/10.1128/JVI.00215-12>

Liljeroos, L., Krzyzaniak, M.A., Helenius, A., Butcher, S.J., 2013. Architecture of respiratory syncytial virus revealed by electron cryotomography. *Proc. Natl. Acad. Sci. U.S.A.* 110, 11133–11138. <https://doi.org/10.1073/pnas.1309070110>

Ling, Z., Tran, K.C., Teng, M.N., 2009. Human Respiratory Syncytial Virus Nonstructural Protein NS2 Antagonizes the Activation of Beta Interferon Transcription by Interacting with RIG-I. *J Virol* 83, 3734–3742. <https://doi.org/10.1128/JVI.02434-08>

Liuzzi, M., Mason, S.W., Cartier, M., Lawetz, C., McCollum, R.S., Dansereau, N., Bolger, G., Lapeyre, N., Gaudette, Y., Lagacé, L., Massariol, M.-J., Dô, F., Whitehead, P., Lamarre, L., Scouten, E., Bordeleau, J., Landry, S., Rancourt, J., Fazal, G., Simoneau, B., 2005. Inhibitors of Respiratory Syncytial Virus Replication Target Cotranscriptional mRNA Guanylylation by Viral RNA-Dependent RNA Polymerase. *J Virol* 79, 13105–13115. <https://doi.org/10.1128/JVI.79.20.13105-13115.2005>

Llorente, M.T., García-Barreno, B., Calero, M., Camafeita, E., López, J.A., Longhi, S., Ferrón, F., Varela, P.F., Melero, J.A., 2006. Structural analysis of the human respiratory syncytial virus phosphoprotein: characterization of an  $\alpha$ -helical domain involved in oligomerization. *Journal of General Virology* 87, 159–169. <https://doi.org/10.1099/vir.0.81430-0>

Llorente, M.T., Taylor, I.A., López-Viñas, E., Gomez-Puertas, P., Calder, L.J., García-Barreno, B., Melero, J.A., 2008. Structural properties of the human respiratory syncytial virus P protein: Evidence for an elongated homotetrameric molecule that is the smallest orthologue within the family of paramyxovirus polymerase cofactors: RSV Phosphoprotein Hydrodynamics and Modeling. *Proteins* 72, 946–958. <https://doi.org/10.1002/prot.21988>

Lu, B., Brazas, R., Ma, C.-H., Kristoff, T., Cheng, X., Jin, H., 2002. Identification of Temperature-Sensitive Mutations in the Phosphoprotein of Respiratory Syncytial Virus That Are Likely Involved in Its Interaction with the Nucleoprotein. *J Virol* 76, 2871–2880. <https://doi.org/10.1128/JVI.76.6.2871-2880.2002>

Lukens, M.V., Van De Pol, A.C., Coenjaerts, F.E.J., Jansen, N.J.G., Kamp, V.M., Kimpen, J.L.L., Rossen, J.W.A., Ulfman, L.H., Tacke, C.E.A., Viveen, M.C., Koenderman, L., Wolfs, T.F.W., Van Bleek, G.M., 2010. A Systemic Neutrophil Response Precedes Robust CD8<sup>+</sup> T-Cell Activation during Natural Respiratory Syncytial Virus Infection in Infants. *J Virol* 84, 2374–2383. <https://doi.org/10.1128/JVI.01807-09>

MacLellan, K., Loney, C., Yeo, R.P., Bhella, D., 2007. The 24-Angstrom Structure of Respiratory Syncytial Virus Nucleocapsid Protein-RNA Decameric Rings. *J Virol* 81, 9519–9524. <https://doi.org/10.1128/JVI.00526-07>

Mallipeddi, S.K., Lupiani, B., Samal, S.K., 1996. Mapping the domains on the phosphoprotein of bovine respiratory syncytial virus required for N-P interaction using a two-hybrid system. *Journal of General Virology* 77, 1019–1023. <https://doi.org/10.1099/0022-1317-77-5-1019>

Mallipeddi, S.K., Samal, S.K., 1993. Analysis of the ovine respiratory syncytial virus (RSV) G glycoprotein gene defines a subgroup of ungulate RSV. *Journal of General Virology* 74, 2787–2791. <https://doi.org/10.1099/0022-1317-74-12-2787>

Malloy, A.M.W., Falsey, A.R., Ruckwardt, T.J., 2013. Consequences of Immature and Senescent Immune Responses for Infection with Respiratory Syncytial Virus, in: Anderson, L.J., Graham, B.S. (Eds.), *Challenges and Opportunities for Respiratory Syncytial Virus Vaccines*, Current Topics in Microbiology and Immunology. Springer Berlin Heidelberg, Berlin, Heidelberg, pp. 211–231. [https://doi.org/10.1007/978-3-642-38919-1\\_11](https://doi.org/10.1007/978-3-642-38919-1_11)

Mariani, V., Biasini, M., Barbato, A., Schwede, T., 2013. IDDT: a local superposition-free score for comparing protein structures and models using distance difference tests. *Bioinformatics* 29, 2722–2728. <https://doi.org/10.1093/bioinformatics/btt473>

Marty, A., Meanger, J., Mills, J., Shields, B., & Ghildyal, R., 2004. Association of matrix protein of respiratory syncytial virus with the host cell membrane of infected cells. *Archives of virology*, 149(1), 199–210. <https://doi.org/10.1007/s00705-003-0183-9>

Marty, F.M., Chemaly, R.F., Mullane, K.M., Lee, D.-G., Hirsch, H.H., Small, C.B., Bergeron, A., Shoham, S., Ljungman, P., Waghmare, A., Blanchard, E., Kim, Y.-J., McKeivitt, M., Porter, D.P., Jordan, R., Guo, Y., German, P., Boeckh, M., Watkins, T.R., Chien, J.W., Dadwal, S.S., 2020. A Phase 2b, Randomized, Double-blind, Placebo-Controlled Multicenter Study Evaluating Antiviral Effects, Pharmacokinetics, Safety, and Tolerability of Presatovir in Hematopoietic Cell Transplant Recipients with Respiratory Syncytial Virus Infection of the Lower Respiratory Tract. *Clinical Infectious Diseases* 71, 2787–2795. <https://doi.org/10.1093/cid/ciz1167>

Mason, S.W., Aberg, E., Lawetz, C., DeLong, R., Whitehead, P., Liuzzi, M., 2003. Interaction between Human Respiratory Syncytial Virus (RSV) M2-1 and P Proteins Is Required for Reconstitution of M2-1-Dependent RSV Minigenome Activity. *J Virol* 77, 10670–10676. <https://doi.org/10.1128/JVI.77.19.10670-10676.2003>

Mazumder, B., & Barik, S., 1994. Requirement of casein kinase II-mediated phosphorylation for the transcriptional activity of human respiratory syncytial viral phosphoprotein P: transdominant negative phenotype of phosphorylation-defective P mutants. *Virology*, 205(1), 104–111. <https://doi.org/10.1006/viro.1994.1624>

Mazur, N.I., Terstappen, J., Baral, R., Bardají, A., Beutels, P., Buchholz, U.J., Cohen, C., Crowe, J.E., Cutland, C.L., Eckert, L., Feikin, D., Fitzpatrick, T., Fong, Y., Graham, B.S., Heikkinen, T., Higgins, D., Hirve, S., Klugman, K.P., Kragten-Tabatabaie, L., Lemey, P., Libster, R., Löwensteyn, Y., Mejias, A., Munoz, F.M., Munywoki, P.K., Mwananyanda, L., Nair, H., Nunes, M.C., Ramilo, O., Richmond, P., Ruckwardt, T.J., Sande, C., Srikantiah, P., Thacker, N., Waldstein, K.A., Weinberger, D., Wildenbeest, J., Wiseman, D., Zar, H.J., Zambon, M., Bont, L., 2023. Respiratory syncytial virus prevention within reach: the vaccine and monoclonal antibody landscape. *The Lancet Infectious Diseases* 23, e2–e21. [https://doi.org/10.1016/S1473-3099\(22\)00291-2](https://doi.org/10.1016/S1473-3099(22)00291-2)

McLellan, J.S., Chen, M., Leung, S., Graepel, K.W., Du, X., Yang, Y., Zhou, T., Baxa, U., Yasuda, E., Beaumont, T., Kumar, A., Modjarrad, K., Zheng, Z., Zhao, M., Xia, N., Kwong, P.D., Graham, B.S., 2013. Structure of RSV Fusion Glycoprotein Trimer Bound to a Prefusion-Specific Neutralizing Antibody. *Science* 340, 1113–1117. <https://doi.org/10.1126/science.1234914>

McNamara, P. S., Ritson, P., Selby, A., Hart, C. A., & Smyth, R. L., 2003. Bronchoalveolar lavage cellularity in infants with severe respiratory syncytial virus bronchiolitis. *Archives of disease in childhood*, 88(10), 922–926. <https://doi.org/10.1136/adc.88.10.922>

McNamara, P.S., Flanagan, B.F., Selby, A.M., Hart, C.A., Smyth, R.L., 2004. Pro- and anti-inflammatory responses in respiratory syncytial virus bronchiolitis. *European Respiratory Journal* 23, 106–112. <https://doi.org/10.1183/09031936.03.00048103>

McNamara, P. S., Flanagan, B. F., Hart, C. A., & Smyth, R. L., 2005. Production of chemokines in the lungs of infants with severe respiratory syncytial virus bronchiolitis. *The Journal of infectious diseases*, 191(8), 1225–1232. <https://doi.org/10.1086/428855>

Meshram, C.D., Baviskar, P.S., Ognibene, C.M., Oomens, A.G.P., 2016. The Respiratory Syncytial Virus Phosphoprotein, Matrix Protein, and Fusion Protein Carboxy-Terminal Domain Drive Efficient Filamentous Virus-Like Particle Formation. *J Virol* 90, 10612–10628. <https://doi.org/10.1128/JVI.01193-16>

Meshram, C.D., Oomens, A.G.P., 2019. Identification of a human respiratory syncytial virus phosphoprotein domain required for virus-like-particle formation. *Virology* 532, 48–54. <https://doi.org/10.1016/j.virol.2019.04.001>

Midgley, C.M., Haynes, A.K., Baumgardner, J.L., Chommanard, C., Demas, S.W., Prill, M.M., Abedi, G.R., Curns, A.T., Watson, J.T., Gerber, S.I., 2017. Determining the Seasonality of Respiratory Syncytial Virus in the United States: The Impact of Increased Molecular Testing. *The Journal of Infectious Diseases* 216, 345–355. <https://doi.org/10.1093/infdis/jix275>

Midulla, F., Huang, Y.T., Gilbert, I.A., Cirino, N.M., McFadden, E.R., Panuska, J.R., 1989. Respiratory Syncytial Virus Infection of Human Cord and Adult Blood Monocytes and Alveolar Macrophages. *Am Rev Respir Dis* 140, 771–777. <https://doi.org/10.1164/ajrccm/140.3.771>

Milazzo, A.-C., Moldovan, G., Lanman, J., Jin, L., Bouwer, J.C., Klienfelder, S., Peltier, S.T., Ellisman, M.H., Kirkland, A.I., Xuong, N.-H., 2010. Characterization of a direct detection device imaging camera for transmission electron microscopy. *Ultramicroscopy* 110, 741–744. <https://doi.org/10.1016/j.ultramic.2010.03.007>

Milles, S., Jensen, M.R., Communie, G., Maurin, D., Schoehn, G., Ruigrok, R.W.H., Blackledge, M., 2016. Self-Assembly of Measles Virus Nucleocapsid-like Particles: Kinetics and RNA Sequence Dependence. *Angew. Chem. Int. Ed.* 55, 9356–9360. <https://doi.org/10.1002/anie.201602619>

Mink, M.A., Stec, D.S., Collins, P.L., 1991. Nucleotide sequences of the 3' leader and 5' trailer regions of human respiratory syncytial virus genomic RNA. *Virology* 185, 615–624. [https://doi.org/10.1016/0042-6822\(91\)90532-G](https://doi.org/10.1016/0042-6822(91)90532-G)

Mitra, R., Baviskar, P., Duncan-Decocq, R.R., Patel, D., Oomens, A.G.P., 2012. The Human Respiratory Syncytial Virus Matrix Protein Is Required for Maturation of Viral Filaments. *J Virol* 86, 4432–4443. <https://doi.org/10.1128/JVI.06744-11>

Morris, J. A., Blount, R. E., Savage, R. E., 1956. Recovery of cytopathogenic agent from chimpanzees with coryza. *Proceedings of the Society for Experimental Biology and Medicine. Society for Experimental Biology and Medicine (New York, N.Y.)*, 92(3), 544–549. <https://doi.org/10.3181/00379727-92-22538>



Moyer, S.A., Smallwood-Kentro, S., Haddad, A., Prevec, L., 1991. Assembly and transcription of synthetic vesicular stomatitis virus nucleocapsids. *J Virol* 65, 2170–2178. <https://doi.org/10.1128/jvi.65.5.2170-2178.1991>

Mufson, M. A., Orvell, C., Rafnar, B., & Norrby, E., 1985. Two distinct subtypes of human respiratory syncytial virus. *The Journal of general virology*, 66 (Pt 10), 2111–2124. <https://doi.org/10.1099/0022-1317-66-10-2111>

Munday, D.C., Wu, W., Smith, N., Fix, J., Noton, S.L., Galloux, M., Touzelet, O., Armstrong, S.D., Dawson, J.M., Aljabr, W., Easton, A.J., Rameix-Welti, M.-A., De Oliveira, A.P., Simabuco, F.M., Ventura, A.M., Hughes, D.J., Barr, J.N., Fearn, R., Digard, P., Eléouët, J.-F., Hiscox, J.A., 2015. Interactome Analysis of the Human Respiratory Syncytial Virus RNA Polymerase Complex Identifies Protein Chaperones as Important Cofactors That Promote L-Protein Stability and RNA Synthesis. *J Virol* 89, 917–930. <https://doi.org/10.1128/JVI.01783-14>

Murphy, L.B., Loney, C., Murray, J., Bhella, D., Ashton, P., Yeo, R.P., 2003. Investigations into the amino-terminal domain of the respiratory syncytial virus nucleocapsid protein reveal elements important for nucleocapsid formation and interaction with the phosphoprotein. *Virology* 307, 143–153. [https://doi.org/10.1016/S0042-6822\(02\)00063-6](https://doi.org/10.1016/S0042-6822(02)00063-6)

Navarro, J., Lopez-Otin, C., Villanueva, N., 1991. Location of phosphorylated residues in human respiratory syncytial virus phosphoprotein. *Journal of General Virology* 72, 1455–1459. <https://doi.org/10.1099/0022-1317-72-6-1455>

Nawrocki, J., Olin, K., Holdrege, M.C., Hartsell, J., Meyers, L., Cox, C., Powell, M., Cook, C.V., Jones, J., Robbins, T., Hemmert, A., Ginocchio, C.C., 2021. The Effects of Social Distancing Policies on Non-SARS-CoV-2 Respiratory Pathogens. *Open Forum Infectious Diseases* 8, ofab133. <https://doi.org/10.1093/ofid/ofab133>

Naydenova, K., Jia, P., Russo, C.J., 2020. Cryo-EM with sub-1 Å specimen movement. *Science* 370, 223–226. <https://doi.org/10.1126/science.abb7927>

Neilson, K.A., Yunis, E.J., 1990. Demonstration of Respiratory Syncytial Virus in an Autopsy Series. *Pediatric Pathology* 10, 491–502. <https://doi.org/10.3109/15513819009067138>

Nilsson-Payant, B. E., Blanco-Melo, D., Uhl, S., Escudero-Pérez, B., Olschewski, S., Thibault, P., Panis, M., Rosenthal, M., Muñoz-Fontela, C., Lee, B., & tenOever, B. R., 2021. Reduced Nucleoprotein Availability Impairs Negative-Sense RNA Virus Replication and Promotes Host Recognition. *Journal of virology*, 95(9), e02274-20. <https://doi.org/10.1128/JVI.02274-20>

Nogales, E., Scheres, S.H.W., 2015. Cryo-EM: A Unique Tool for the Visualization of Macromolecular Complexity. *Molecular Cell* 58, 677–689. <https://doi.org/10.1016/j.molcel.2015.02.019>

Norrby, E., Marusyk, H., Örvell, C., 1970. Morphogenesis of Respiratory Syncytial Virus in a Green Monkey Kidney Cell Line (Vero). *J Virol* 6, 237–242. <https://doi.org/10.1128/jvi.6.2.237-242.1970>

Noton, S.L., Aljabr, W., Hiscox, J.A., Matthews, D.A., Fearn, R., 2014. Factors affecting de novo RNA synthesis and back-priming by the respiratory syncytial virus polymerase. *Virology* 462–463, 318–327. <https://doi.org/10.1016/j.virol.2014.05.032>

Noton, S.L., Cowton, V.M., Zack, C.R., McGivern, D.R., Fearn, R., 2010. Evidence that the polymerase of respiratory syncytial virus initiates RNA replication in a nontemplated fashion. *Proc. Natl. Acad. Sci. U.S.A.* 107, 10226–10231. <https://doi.org/10.1073/pnas.0913065107>

Noton, S.L., Deflubé, L.R., Tremaglio, C.Z., Fearn, R., 2012. The Respiratory Syncytial Virus Polymerase Has Multiple RNA Synthesis Activities at the Promoter. *PLoS Pathog* 8, e1002980. <https://doi.org/10.1371/journal.ppat.1002980>

Noton, S.L., Fearn, R., 2011. The first two nucleotides of the respiratory syncytial virus antigenome RNA replication product can be selected independently of the promoter terminus. *RNA* 17, 1895–1906. <https://doi.org/10.1261/rna.2813411>

Noval, M.G., Esperante, S.A., Molina, I.G., Chemes, L.B., Prat-Gay, G.D., 2016. Intrinsic Disorder to Order Transitions in the Scaffold Phosphoprotein P from the Respiratory Syncytial Virus RNA Polymerase Complex. *Biochemistry* 55, 1441–1454. <https://doi.org/10.1021/acs.biochem.5b01332>

Orlova, E.V., Saibil, H.R., 2011. Structural Analysis of Macromolecular Assemblies by Electron Microscopy. *Chem. Rev.* 111, 7710–7748. <https://doi.org/10.1021/cr100353t>

Quizougun-Oubari, M., Pereira, N., Tarus, B., Galloux, M., Lassoued, S., Fix, J., Tortorici, M.A., Hoos, S., Baron, B., England, P., Desmaële, D., Couvreur, P., Bontems, F., Rey, F.A., Eléouët, J.-F., Sizun, C., Slama-Schwok, A., Duquerroy, S., 2015. A Druggable Pocket at the Nucleocapsid/Phosphoprotein Interaction Site of Human Respiratory Syncytial Virus. *J Virol* 89, 11129–11143. <https://doi.org/10.1128/JVI.01612-15>

Pan, J., Qian, X., Lattmann, S., El Sahili, A., Yeo, T.H., Jia, H., Cressey, T., Ludeke, B., Noton, S., Kalocsay, M., Fearn, R., Lescar, J., 2020. Structure of the human metapneumovirus polymerase phosphoprotein complex. *Nature* 577, 275–279. <https://doi.org/10.1038/s41586-019-1759-1>

Paynter, S., 2015. Humidity and respiratory virus transmission in tropical and temperate settings. *Epidemiol. Infect.* 143, 1110–1118. <https://doi.org/10.1017/S0950268814002702>

Pei, J., Beri, N.R., Zou, A.J., Hubel, P., Dorando, H.K., Bergant, V., Andrews, R.D., Pan, J., Andrews, J.M., Sheehan, K.C.F., Pichlmair, A., Amarasinghe, G.K., Brody, S.L., Payton, J.E., Leung, D.W., 2021. Nuclear-localized human respiratory syncytial virus NS1 protein modulates host gene transcription. *Cell Reports* 37, 109803. <https://doi.org/10.1016/j.celrep.2021.109803>

Pereira, N., Cardone, C., Lassoued, S., Galloux, M., Fix, J., Assrir, N., Lescop, E., Bontems, F., Eléouët, J.-F., Sizun, C., 2017. New Insights into Structural Disorder in Human Respiratory Syncytial Virus Phosphoprotein and Implications for Binding of Protein Partners. *Journal of Biological Chemistry* 292, 2120–2131. <https://doi.org/10.1074/jbc.M116.765958>

Piedra, P. A., Jewell, A. M., Cron, S. G., Atmar, R. L., & Glezen, W. P., 2003. Correlates of immunity to respiratory syncytial virus (RSV) associated-hospitalization: establishment of minimum protective threshold levels of serum neutralizing antibodies. *Vaccine*, 21(24), 3479–3482. [https://doi.org/10.1016/s0264-410x\(03\)00355-4](https://doi.org/10.1016/s0264-410x(03)00355-4)

Piedra, F.-A., Qiu, X., Teng, M.N., Avadhanula, V., Machado, A.A., Kim, D.-K., Hixson, J., Bahl, J., Piedra, P.A., 2020. Non-gradient and genotype-dependent patterns of RSV gene expression. *PLoS ONE* 15, e0227558. <https://doi.org/10.1371/journal.pone.0227558>

Poch, O., Sauvaget, I., Delarue, M., Tordo, N., 1989. Identification of four conserved motifs among the RNA-dependent polymerase encoding elements. *The EMBO Journal* 8, 3867–3874. <https://doi.org/10.1002/j.1460-2075.1989.tb08565.x>

Polack, F.P., Teng, M.N., LCollins, P., Prince, G.A., Exner, M., Regele, H., Lirman, D.D., Rabold, R., Hoffman, S.J., Karp, C.L., Kleeberger, S.R., Wills-Karp, M., Karron, R.A., 2002. A Role for Immune Complexes in Enhanced Respiratory Syncytial Virus Disease. *Journal of Experimental Medicine* 196, 859–865. <https://doi.org/10.1084/jem.20020781>

Punjani, A., Rubinstein, J. L., Fleet, D. J., & Brubaker, M. A., 2017. cryoSPARC: algorithms for rapid unsupervised cryo-EM structure determination. *Nature methods*, 14(3), 290–296. <https://doi.org/10.1038/nmeth.4169>

Radhakrishnan, A., Yeo, D., Brown, G., Myaing, M.Z., Iyer, L.R., Fleck, R., Tan, B.-H., Aitken, J., Sanmun, D., Tang, K., Yarwood, A., Brink, J., Sugrue, R.J., 2010. Protein Analysis of Purified Respiratory Syncytial Virus Particles Reveals an Important Role for Heat Shock Protein 90 in Virus Particle Assembly. *Molecular & Cellular Proteomics* 9, 1829–1848. <https://doi.org/10.1074/mcp.M110.001651>

Rahmeh, A.A., Schenk, A.D., Danek, E.I., Kranzusch, P.J., Liang, B., Walz, T., Whelan, S.P.J., 2010. Molecular architecture of the vesicular stomatitis virus RNA polymerase. *Proc. Natl. Acad. Sci. U.S.A.* 107, 20075–20080. <https://doi.org/10.1073/pnas.1013559107>

Rameix-Welti, M. A., Le Goffic, R., Hervé, P. L., Sourimant, J., Rémot, A., Riffault, S., Yu, Q., Galloux, M., Gault, E., & Eléouët, J. F., 2014. Visualizing the replication of respiratory syncytial virus in cells and in living mice. *Nature communications*, 5, 5104. <https://doi.org/10.1038/ncomms6104>

Renner, M., Bertinelli, M., Leyrat, C., Paesen, G.C., Saraiva De Oliveira, L.F., Huiskonen, J.T., Grimes, J.M., 2016. Nucleocapsid assembly in pneumoviruses is regulated by conformational switching of the N protein. *eLife* 5, e12627. <https://doi.org/10.7554/eLife.12627>

Rhodin, M.H.J., McAllister, N.V., Castillo, J., Noton, S.L., Fearn, R., Kim, I.J., Yu, J., Blaisdell, T.P., Panarese, J., Shook, B.C., Or, Y.S., Goodwin, B., Lin, K., 2021. EDP-938, a novel nucleoprotein inhibitor of respiratory syncytial virus, demonstrates potent antiviral activities in vitro and in a non-human primate model. *PLoS Pathog* 17, e1009428. <https://doi.org/10.1371/journal.ppat.1009428>

Richard, C.-A., Hervet, C., Ménard, D., Gutsche, I., Normand, V., Renois, F., Meurens, F., Eléouët, J.-F., 2018a. First demonstration of the circulation of a pneumovirus in French pigs by detection of anti-swine orthopneumovirus nucleoprotein antibodies. *Vet Res* 49, 118. <https://doi.org/10.1186/s13567-018-0615-x>

Richard, C.-A., Rincheval, V., Lassoued, S., Fix, J., Cardone, C., Esneau, C., Nekhai, S., Galloux, M., Rameix-Welti, M.-A., Sizun, C., Eléouët, J.-F., 2018b. RSV hijacks cellular protein phosphatase 1 to regulate M2-1 phosphorylation and viral transcription. *PLoS Pathog* 14, e1006920. <https://doi.org/10.1371/journal.ppat.1006920>

Riedel, C., Vasishtan, D., Pražák, V., Ghanem, A., Conzelmann, K.-K., Rümener, T., 2019. Cryo EM structure of the rabies virus ribonucleoprotein complex. *Sci Rep* 9, 9639. <https://doi.org/10.1038/s41598-019-46126-7>

Rincheval, V., Lelek, M., Gault, E., Bouillier, C., Sitterlin, D., Blouquit-Laye, S., Galloux, M., Zimmer, C., Eléouët, J.-F., Rameix-Welti, M.-A., 2017. Functional organization of cytoplasmic inclusion bodies in cells infected by respiratory syncytial virus. *Nat Commun* 8, 563. <https://doi.org/10.1038/s41467-017-00655-9>

Ringel, M., Heiner, A., Behner, L., Halwe, S., Sauerhering, L., Becker, N., Dietzel, E., Sawatsky, B., Kolesnikova, L., Maisner, A., 2019. Nipah virus induces two inclusion body populations: Identification of novel inclusions at the plasma membrane. *PLoS Pathog* 15, e1007733. <https://doi.org/10.1371/journal.ppat.1007733>

Risso-Ballester, J., Galloux, M., Cao, J., Le Goffic, R., Hontonnou, F., Jobart-Malfait, A., Desquesnes, A., Sake, S.M., Haid, S., Du, M., Zhang, X., Zhang, H., Wang, Z., Rincheval, V., Zhang, Y., Pietschmann, T., Eléouët, J.-F., Rameix-Welti, M.-A., Altmeyer, R., 2021. A condensate-hardening drug blocks RSV replication in vivo. *Nature* 595, 596–599. <https://doi.org/10.1038/s41586-021-03703-z>

Roberts, S.R., Compans, R.W., Wertz, G.W., 1995. Respiratory syncytial virus matures at the apical surfaces of polarized epithelial cells. *J Virol* 69, 2667–2673. <https://doi.org/10.1128/jvi.69.4.2667-2673.1995>

Rohou, A., Grigorieff, N., 2019. CTFFIND4: Fast and accurate defocus estimation from electron micrographs.

Roymans, D., Alnajjar, S.S., Battles, M.B., Sitthicharoenchai, P., Furmanova-Hollenstein, P., Rigaux, P., Berg, J.V.D., Kwanten, L., Ginderen, M.V., Verheyen, N., Vranckx, L., Jaensch, S., Arnoult, E., Voorzaat, R., Gallup, J.M., Larios-Mora, A., Crabbe, M., Huntjens, D., Raboisson, P., Langedijk, J.P., Ackermann, M.R., McLellan, J.S., Vendeuille, S., Koul, A., 2017. Therapeutic efficacy of a respiratory syncytial virus fusion inhibitor. *Nat Commun* 8, 167. <https://doi.org/10.1038/s41467-017-00170-x>

Russell, R.F., McDonald, J.U., Ivanova, M., Zhong, Z., Bukreyev, A., Tregoning, J.S., 2015. Partial Attenuation of Respiratory Syncytial Virus with a Deletion of a Small Hydrophobic Gene Is Associated with Elevated Interleukin-1 $\beta$  Responses. *J Virol* 89, 8974–8981. <https://doi.org/10.1128/JVI.01070-15>

Russo, C.J., Passmore, L.A., 2016. Progress towards an optimal specimen support for electron cryomicroscopy. *Current Opinion in Structural Biology* 37, 81–89. <https://doi.org/10.1016/j.sbi.2015.12.007>

Samal, S.K., Collins, P.L., 1996. RNA replication by a respiratory syncytial virus RNA analog does not obey the rule of six and retains a nonviral trinucleotide extension at the leader end. *J Virol* 70, 5075–5082. <https://doi.org/10.1128/jvi.70.8.5075-5082.1996>

Sanchez-Seco, M.P., Navarro, J., Martinez, R., Villanueva, N., 1995. C-Terminal phosphorylation of human respiratory syncytial virus P protein occurs mainly at serine residue 232. *Journal of General Virology* 76, 425–430. <https://doi.org/10.1099/0022-1317-76-2-425>

Schoehn, G., Mavrakakis, M., Albertini, A., Wade, R., Hoenger, A., Ruigrok, R.W.H., 2004. The 12Å Structure of Trypsin-treated Measles Virus N–RNA. *Journal of Molecular Biology* 339, 301–312. <https://doi.org/10.1016/j.jmb.2004.03.073>

Selvaraj, M., Yegambaram, K., Todd, E.J.A.A., Richard, C.-A., Dods, R.L., Pangratiou, G.M., Trinh, C.H., Moul, S.L., Murphy, J.C., Mankouri, J., Éléouët, J.-F., Barr, J.N., Edwards, T.A., 2018. The Structure of the Human Respiratory Syncytial Virus M2-1 Protein Bound to the Interaction Domain of the Phosphoprotein P Defines the Orientation of the Complex. *mBio* 9, e01554-18. <https://doi.org/10.1128/mBio.01554-18>

Shaikh, F.Y., Cox, R.G., Lifland, A.W., Hotard, A.L., Williams, J.V., Moore, M.L., Santangelo, P.J., Crowe, J.E., 2012. A Critical Phenylalanine Residue in the Respiratory Syncytial Virus Fusion Protein Cytoplasmic Tail Mediates Assembly of Internal Viral Proteins into Viral Filaments and Particles. *mBio* 3, e00270-11. <https://doi.org/10.1128/mBio.00270-11>

Shan, H., Su, X., Li, T., Qin, Y., Zhang, N., Yang, L., Ma, L., Bai, Y., Qi, L., Liu, Y., Shen, Q.-T., 2021. Structural plasticity of mumps virus nucleocapsids with cryo-EM structures. *Commun Biol* 4, 833. <https://doi.org/10.1038/s42003-021-02362-0>

Shapiro, A.B., Gao, N., O'Connell, N., Hu, J., Thresher, J., Gu, R.-F., Overman, R., Hardern, I.M., Sproat, G.G., 2014. Quantitative investigation of the affinity of human respiratory syncytial virus phosphoprotein C-terminus binding to nucleocapsid protein. *Viol J* 11, 191. <https://doi.org/10.1186/s12985-014-0191-2>

Shareef, A.M., Ludeke, B., Jordan, P., Deval, J., Fearn, R., 2021. Comparison of RNA synthesis initiation properties of non-segmented negative strand RNA virus polymerases. *PLoS Pathog* 17, e1010151. <https://doi.org/10.1371/journal.ppat.1010151>

Scheres S. H., 2012. A Bayesian view on cryo-EM structure determination. *Journal of molecular biology*, 415(2), 406–418. <https://doi.org/10.1016/j.jmb.2011.11.010>

Shi, T., Denouel, A., Tietjen, A. K., Campbell, I., Moran, E., Li, X., Campbell, H., Demont, C., Nyawanda, B. O., Chu, H. Y., Stoszek, S. K., Krishnan, A., Openshaw, P., Falsey, A. R., Nair, H., & RESCEU Investigators, 2020. Global Disease Burden Estimates of Respiratory Syncytial Virus-Associated Acute Respiratory Infection in Older Adults in 2015: A Systematic Review and Meta-Analysis. *The Journal of infectious diseases*, 222 (Suppl 7), S577–S583. <https://doi.org/10.1093/infdis/jiz059>

Si, Z., Zhou, K., Tsao, J., Luo, M., & Zhou, Z. H., 2022. Locations and in situ structure of the polymerase complex inside the virion of vesicular stomatitis virus. *Proceedings of the National Academy of Sciences of the United States of America*, 119(18), e2111948119. <https://doi.org/10.1073/pnas.2111948119>

Sigurs, N., Aljassim, F., Kjellman, B., Robinson, P.D., Sigurbergsson, F., Bjarnason, R., Gustafsson, P.M., 2010. Asthma and allergy patterns over 18 years after severe RSV bronchiolitis in the first year of life. *Thorax* 65, 1045–1052. <https://doi.org/10.1136/thx.2009.121582>

Simabuco, F.M., Asara, J.M., Guerrero, M.C., Libermann, T.A., Zerbini, L.F., Ventura, A.M., 2011. Structural analysis of human respiratory syncytial virus P protein: identification of intrinsically disordered domains. *Braz. J. Microbiol.* 42, 340–345. <https://doi.org/10.1590/S1517-83822011000100043>

Slack, M.S., Easton, A.J., 1998. Characterization of the interaction of the human respiratory syncytial virus phosphoprotein and nucleocapsid protein using the two-hybrid system. *Virus Research* 55, 167–176. [https://doi.org/10.1016/S0168-1702\(98\)00042-2](https://doi.org/10.1016/S0168-1702(98)00042-2)

Song, X., Li, Y., Huang, J., Cao, H., Zhou, Q., Sha, X., Zhang, B., 2021. An emerging orthopneumovirus detected from dogs with canine infectious respiratory disease in China. *Transbound Emerg Dis* 68, 3217–3221. <https://doi.org/10.1111/tbed.14291>

Song, X., Shan, H., Zhu, Y., Hu, S., Xue, L., Chen, Y., Ding, W., Niu, T., Gu, J., Ouyang, S., Shen, Q.-T., Liu, Z.-J., 2019. Self-capping of nucleoprotein filaments protects the Newcastle disease virus genome. *eLife* 8, e45057. <https://doi.org/10.7554/eLife.45057>

Spann, K.M., Tran, K.C., Collins, P.L., 2005. Effects of Nonstructural Proteins NS1 and NS2 of Human Respiratory Syncytial Virus on Interferon Regulatory Factor 3, NF- $\kappa$ B, and Proinflammatory Cytokines. *J. VIROL.* 79.

Srinivasakumar, N., Ogra, P.L., Flanagan, T.D., 1991. Characteristics of fusion of respiratory syncytial virus with HEp-2 cells as measured by R18 fluorescence dequenching assay. *J Virol* 65, 4063–4069. <https://doi.org/10.1128/jvi.65.8.4063-4069.1991>

Stevens, M., Rusch, S., DeVincenzo, J., Kim, Y.-I., Harrison, L., Meals, E.A., Boyers, A., Fok-Seang, J., Huntjens, D., Lounis, N., Mariën, K., Remmerie, B., Roymans, D., Koul, A., Verloes, R., 2018. Antiviral Activity of Oral JNJ-53718678 in Healthy Adult Volunteers Challenged With Respiratory Syncytial Virus: A Placebo-Controlled Study. *The Journal of Infectious Diseases* 218, 748–756. <https://doi.org/10.1093/infdis/jiy227>

Sugita, Y., Matsunami, H., Kawaoka, Y., Noda, T., Wolf, M., 2018. Cryo-EM structure of the Ebola virus nucleoprotein–RNA complex at 3.6 Å resolution. *Nature* 563, 137–140. <https://doi.org/10.1038/s41586-018-0630-0>

Sutherland, K. A., Collins, P. L., & Peebles, M. E., 2001. Synergistic effects of gene-end signal mutations and the M2-1 protein on transcription termination by respiratory syncytial virus. *Virology*, 288(2), 295–307. <https://doi.org/10.1006/viro.2001.1105>

Swedan, S., Andrews, J., Majumdar, T., Musiyenko, A., Barik, S., 2011. Multiple Functional Domains and Complexes of the Two Nonstructural Proteins of Human Respiratory Syncytial Virus Contribute to Interferon Suppression and Cellular Location. *J Virol* 85, 10090–10100. <https://doi.org/10.1128/JVI.00413-11>

Tanner, S.J., Ariza, A., Richard, C.-A., Kyle, H.F., Dods, R.L., Blondot, M.-L., Wu, W., Trincão, J., Trinh, C.H., Hiscox, J.A., Carroll, M.W., Silman, N.J., Eléouët, J.-F., Edwards, T.A., Barr, J.N., 2014. Crystal structure of the essential transcription antiterminator M2-1 protein of human respiratory syncytial virus and implications of its phosphorylation. *Proc. Natl. Acad. Sci. U.S.A.* 111, 1580–1585. <https://doi.org/10.1073/pnas.1317262111>

Tawar, R.G., Duquerroy, S., Vornrhein, C., Varela, P.F., Damier-Piolle, L., Castagné, N., MacLellan, K., Bedouelle, H., Bricogne, G., Bhella, D., Eléouët, J.-F., Rey, F.A., 2009. Crystal Structure of a Nucleocapsid-Like Nucleoprotein-RNA Complex of Respiratory Syncytial Virus. *Science* 326, 1279–1283. <https://doi.org/10.1126/science.1177634>

Tayyari, F., Marchant, D., Moraes, T.J., Duan, W., Mastrangelo, P., Hegele, R.G., 2011. Identification of nucleolin as a cellular receptor for human respiratory syncytial virus. *Nat Med* 17, 1132–1135. <https://doi.org/10.1038/nm.2444>

Tegunov, D., Cramer, P., 2018. Real-time cryo-EM data pre-processing with *Warp* (preprint). *Biophysics*. <https://doi.org/10.1101/338558>

Tegunov, D., Xue, L., Dienemann, C., Cramer, P., Mahamid, J., 2021. Multi-particle cryo-EM refinement with M visualizes ribosome-antibiotic complex at 3.5 Å in cells. *Nat Methods* 18, 186–193. <https://doi.org/10.1038/s41592-020-01054-7>

Teng, M.N., Collins, P.L., 1999. Altered Growth Characteristics of Recombinant Respiratory Syncytial Viruses Which Do Not Produce NS2 Protein. *J Virol* 73, 466–473. <https://doi.org/10.1128/JVI.73.1.466-473.1999>

Teng, M.N., Whitehead, S.S., Bermingham, A., St. Claire, M., Elkins, W.R., Murphy, B.R., Collins, P.L., 2000. Recombinant Respiratory Syncytial Virus That Does Not Express the NS1 or M2-2 Protein Is Highly Attenuated and Immunogenic in Chimpanzees. *J Virol* 74, 9317–9321. <https://doi.org/10.1128/JVI.74.19.9317-9321.2000>

The IMPact-RSV Study Group, 1998. Palivizumab, a Humanized Respiratory Syncytial Virus Monoclonal Antibody, Reduces Hospitalization From Respiratory Syncytial Virus Infection in High-risk Infants. *Pediatrics* 102, 531–537. <https://doi.org/10.1542/peds.102.3.531>

Tran, T.-L., Castagné, N., Bhella, D., Varela, P.F., Bernard, J., Chilmonczyk, S., Berkenkamp, S., Benhamo, V., Grznarova, K., Grosclaude, J., Nespoulos, C., Rey, F.A., Eléouët, J.-F., 2007. The nine C-terminal amino acids of the respiratory syncytial virus protein P are necessary and sufficient for binding to ribonucleoprotein complexes in which six ribonucleotides are contacted per N protein protomer. *Journal of General Virology* 88, 196–206. <https://doi.org/10.1099/vir.0.82282-0>



Tran, T.-L., Castagné, N., Dubosclard, V., Noinville, S., Koch, E., Moudjou, M., Henry, C., Bernard, J., Yeo, R.P., Eléouët, J.-F., 2009. The Respiratory Syncytial Virus M2-1 Protein Forms Tetramers and Interacts with RNA and P in a Competitive Manner. *J Virol* 83, 6363–6374. <https://doi.org/10.1128/JVI.00335-09>

Tremaglio, C.Z., Noton, S.L., Deflubé, L.R., Fearn, R., 2013. Respiratory Syncytial Virus Polymerase Can Initiate Transcription from Position 3 of the Leader Promoter. *J Virol* 87, 3196–3207. <https://doi.org/10.1128/JVI.02862-12>

Trento, A., Casas, I., Calderón, A., Garcia-Garcia, M.L., Calvo, C., Perez-Breña, P., Melero, J.A., 2010. Ten Years of Global Evolution of the Human Respiratory Syncytial Virus BA Genotype with a 60-Nucleotide Duplication in the G Protein Gene. *J Virol* 84, 7500–7512. <https://doi.org/10.1128/JVI.00345-10>

Triantafyllou, K., Kar, S., Vakakis, E., Kotecha, S., Triantafyllou, M., 2013. Human respiratory syncytial virus viroporin SH: a viral recognition pathway used by the host to signal inflammasome activation. *Thorax* 68, 66–75. <https://doi.org/10.1136/thoraxjnl-2012-202182>

Tripp, R.A., Jones, L.P., Haynes, L.M., Zheng, H., Murphy, P.M., Anderson, L.J., 2001. CX3C chemokine mimicry by respiratory syncytial virus G glycoprotein. *Nat Immunol* 2, 732–738. <https://doi.org/10.1038/90675>

Turoňová, B., Hagen, W.J.H., Obr, M., Mosalaganti, S., Beugelink, J.W., Zimmerli, C.E., Kräusslich, H.-G., Beck, M., 2020. Benchmarking tomographic acquisition schemes for high-resolution structural biology. *Nat Commun* 11, 876. <https://doi.org/10.1038/s41467-020-14535-2>

Valarcher, J.-F., Taylor, G., 2007. Bovine respiratory syncytial virus infection. *Vet. Res.* 38, 153–180. <https://doi.org/10.1051/vetres:2006053>

Vanover, D., Smith, D.V., Blanchard, E.L., Alonas, E., Kirschman, J.L., Lifland, A.W., Zurla, C., Santangelo, P.J., 2017. RSV glycoprotein and genomic RNA dynamics reveal filament assembly prior to the plasma membrane. *Nat Commun* 8, 667. <https://doi.org/10.1038/s41467-017-00732-z>

Vijayakrishnan, S., Burns, A.M., Blanchard, E.L., Spink, M.C., Gilchrist, J., Howe, A., Darrow, M.C., Harkiolaki, M., Wu, C.-Y., Dutch, R.E., Santangelo, P.J., Fearn, R., Bhella, D., 2022. Ultrastructural characterization of a viral RNA and G-protein containing, membranous organelle formed in respiratory syncytial virus infected cells (preprint). *Microbiology*. <https://doi.org/10.1101/2022.11.28.517999>

Villanueva, N., Hardy, R., Asenjo, A., Yu, Q., Wertz, G., 2000. The bulk of the phosphorylation of human respiratory syncytial virus phosphoprotein is not essential but modulates viral RNA transcription and replication. *Microbiology* 81, 129–133. <https://doi.org/10.1099/0022-1317-81-1-129>

Wagner, T., Merino, F., Stabrin, M., Moriya, T., Antoni, C., Apelbaum, A., Hagel, P., Sitsel, O., Raisch, T., Prumbaum, D., Quentin, D., Roderer, D., Tacke, S., Siebolds, B., Schubert, E., Shaikh, T.R., Lill, P., Gatsogiannis, C., Raunser, S., 2019. SPHIRE-crYOLO is a fast and accurate fully automated particle picker for cryo-EM. *Commun Biol* 2, 218. <https://doi.org/10.1038/s42003-019-0437-z>

Walsh, E.E., Hruska, J., 1983. Monoclonal antibodies to respiratory syncytial virus proteins: identification of the fusion protein. *J Virol* 47, 171–177. <https://doi.org/10.1128/jvi.47.1.171-177.1983>

Wan, W., Kolesnikova, L., Clarke, M., Koehler, A., Noda, T., Becker, S., Briggs, J.A.G., 2017. Structure and assembly of the Ebola virus nucleocapsid. *Nature* 551, 394–397. <https://doi.org/10.1038/nature24490>

Weber, E., Humbert, B., Streckert, H. J., & Werchau, H., 1995. Nonstructural protein 2 (NS2) of respiratory syncytial virus (RSV) detected by an antipeptide serum. *Respiration; international review of thoracic diseases*, 62(1), 27–33. <https://doi.org/10.1159/000196385>

Welliver, T.P., Garofalo, R.P., Hosakote, Y., Hintz, K.H., Avendano, L., Sanchez, K., Velozo, L., Jafri, H., Chavez-Bueno, S., Ogra, P.L., McKinney, L., Reed, J.L., Welliver, Sr., R.C., 2007. Severe Human Lower Respiratory Tract Illness Caused by Respiratory Syncytial Virus and Influenza Virus Is Characterized by the Absence of Pulmonary Cytotoxic Lymphocyte Responses. *J INFECT DIS* 195, 1126–1136. <https://doi.org/10.1086/512615>

Widjaja, I., Wicht, O., Luytjes, W., Leenhouts, K., Rottier, P.J.M., Van Kuppeveld, F.J.M., Haijema, B.J., De Haan, C.A.M., 2016. Characterization of Epitope-Specific Anti-Respiratory Syncytial Virus (Anti-RSV) Antibody Responses after Natural Infection and after Vaccination with Formalin-Inactivated RSV. *J Virol* 90, 5965–5977. <https://doi.org/10.1128/JVI.00235-16>

Yabukarski, F., Lawrence, P., Tarbouriech, N., Bourhis, J.-M., Delaforge, E., Jensen, M.R., Ruigrok, R.W.H., Blackledge, M., Volchkov, V., Jamin, M., 2014. Structure of Nipah virus unassembled nucleoprotein in complex with its viral chaperone. *Nat Struct Mol Biol* 21, 754–759. <https://doi.org/10.1038/nsmb.2868>

Yu, Q., Hardy, R.W., Wertz, G.W., 1995. Functional cDNA clones of the human respiratory syncytial (RS) virus N, P, and L proteins support replication of RS virus genomic RNA analogs and define minimal trans-acting requirements for RNA replication. *J Virol* 69, 2412–2419. <https://doi.org/10.1128/jvi.69.4.2412-2419.1995>

- Zhang, L., Peeples, M.E., Boucher, R.C., Collins, P.L., Pickles, R.J., 2002. Respiratory Syncytial Virus Infection of Human Airway Epithelial Cells Is Polarized, Specific to Ciliated Cells, and without Obvious Cytopathology. *J Virol* 76, 5654–5666. <https://doi.org/10.1128/JVI.76.11.5654-5666.2002>
- Zhang, N., Shan, H., Liu, M., Li, T., Luo, R., Yang, L., Qi, L., Chu, X., Su, X., Wang, R., Liu, Y., Sun, W., Shen, Q.-T., 2021. Structure and assembly of double-headed Sendai virus nucleocapsids. *Commun Biol* 4, 494. <https://doi.org/10.1038/s42003-021-02027-y>
- Zhang, S., Jiang, Y., Cheng, Q., Zhong, Y., Qin, Y., Chen, M., 2017. Inclusion Body Fusion of Human Parainfluenza Virus Type 3 Regulated by Acetylated  $\alpha$ -Tubulin Enhances Viral Replication. *J Virol* 91, e01802-16. <https://doi.org/10.1128/JVI.01802-16>
- Zhang, X., Sridharan, S., Zagoriy, I., Oegema, C. E., Ching, C., Pflaesterer, T., Fung H. K. H., Poser, I., Müller, C. W., Hyman, A. A., Savitski, M. M., Mahamid J., 2022. Molecular mechanisms of stress-induced reactivation in mumps virus condensates (preprint). doi: <https://doi.org/10.1101/2021.07.10.451879>
- Zhao, X., Singh, M., Malashkevich, V.N., Kim, P.S., 2000. Structural characterization of the human respiratory syncytial virus fusion protein core. *Proc. Natl. Acad. Sci. U.S.A.* 97, 14172–14177. <https://doi.org/10.1073/pnas.260499197>
- Zhou, Y., Su, J.M., Samuel, C.E., Ma, D., 2019. Measles Virus Forms Inclusion Bodies with Properties of Liquid Organelles. *J Virol* 93, e00948-19. <https://doi.org/10.1128/JVI.00948-19>
- Zhu, T., Song, H., Peng, R., Shi, Y., Qi, J., Gao, G.F., 2017. Crystal Structure of the Marburg Virus Nucleoprotein Core Domain Chaperoned by a VP35 Peptide Reveals a Conserved Drug Target for Filovirus. *J Virol* 91, e00996-17. <https://doi.org/10.1128/JVI.00996-17>
- Zimmer, G., Budz, L., Herrler, G., 2001. Proteolytic Activation of Respiratory Syncytial Virus Fusion Protein. *Journal of Biological Chemistry* 276, 31642–31650. <https://doi.org/10.1074/jbc.M102633200>
- Zinzula, L., Beck, F., Klumpe, S., Bohn, S., Pfeifer, G., Bollschweiler, D., Nagy, I., Plitzko, J.M., Baumeister, W., 2021. Cryo-EM structure of the cetacean morbillivirus nucleoprotein-RNA complex. *Journal of Structural Biology* 213, 107750. <https://doi.org/10.1016/j.jsb.2021.107750>
- Zivanov, J., Nakane, T., & Scheres, S. H. W., 2019. A Bayesian approach to beam-induced motion correction in cryo-EM single-particle analysis. *IUCrJ*, 6(Pt 1), 5–17. <https://doi.org/10.1107/S205225251801463X>

Züst, R., Cervantes-Barragan, L., Habjan, M., Maier, R., Neuman, B.W., Ziebuhr, J., Szretter, K.J., Baker, S.C., Barchet, W., Diamond, M.S., Siddell, S.G., Ludewig, B., Thiel, V., 2011. Ribose 2'-O-methylation provides a molecular signature for the distinction of self and non-self mRNA dependent on the RNA sensor Mda5. *Nat Immunol* 12, 137–143. <https://doi.org/10.1038/ni.1979>



# Appendix

## Résumé en français de la thèse intitulée : « Étude structurale et fonctionnelle de la nucléocapside du virus respiratoire syncytial »

### **1. Introduction**

#### *1.1. Généralités sur le virus respiratoire syncytial*

Le virus respiratoire syncytial (VRS) a été isolé en 1957 à partir d'échantillons issus de jeunes enfants présentant une infection des voies respiratoires inférieures (Chanock et al., 1957).

Le VRS est la première cause de bronchiolites et de pneumonie chez les jeunes enfants (PERCH study group, 2019), et tous les enfants sont infectés avant l'âge de 2 ans (Glezen et al., 1987). Ainsi en 2019, le VRS a été responsable d'environ 3 million hospitalisations et de 100 000 morts dans le monde chez les enfants de moins de 5 ans. La majorité de ces morts à lieu dans les pays à faibles revenus (Li et al., 2022). Dans les pays à hauts revenus, le taux de mortalité est faible mais le poids des maladies liées au VRS sur les services d'urgences pédiatriques reste élevé (Hall et al., 2009). Chez les enfants plus âgés et les adultes, les réinfections par le VRS sont très communes au cours de la vie et ne causent généralement que des symptômes légers (Hall et al., 1991). En revanche, chez les personnes âgées et immunodéprimées, le VRS peut causer des infections respiratoires sévères (Shi et al., 2020) et le poids des maladies liées au VRS est similaire à celui de la grippe A saisonnière chez ces personnes (Falsey et al., 2021).

Il n'existe aujourd'hui pas de vaccins disponibles contre le VRS, mais de nombreux candidats vaccins sont actuellement en développement. De même, il n'existe pas de traitements curatifs spécifiques contre le VRS, mais là encore de nombreuses molécules sont testées en essais cliniques. Pour les jeunes enfants, les traitements consistent en des soins de support pour traiter les symptômes. Toutefois un traitement préventif est disponible, le palivizumab, anticorps monoclonal humanisé dirigé contre la protéine de fusion F du VRS,

injecté avant la saison de circulation du VRS (The IMpact-RSV Study Group, 1998). Cependant, son efficacité reste limitée et son coût important le restreint aux enfants à risques des pays à hauts revenus (Homaira et al., 2014). Un nouvel anticorps monoclonal, le nirsevimab, présentant une meilleure efficacité (Domachowske et al., 2022 ; Hammit et al., 2022) a reçu l'autorisation de mise sur le marché de la commission européenne en novembre 2022.

Le VRS est un virus enveloppé dont le génome est un ARN simple brin, linéaire, non segmenté de polarité négative, appartenant à l'ordre des *Mononegavirales*. L'ordre des *Mononegavirales* contient de nombreux pathogènes représentant une menace significative en santé humaine et animale, tels que les virus Ebola et Marburg (de la famille des *Filoviridae*), les virus de la rougeole et des oreillons et les virus Nipah et Sendai (de la famille des *Paramyxoviridae*), ou encore le virus de la rage (de la famille des *Rhabdoviridae*). Le VRS appartient à la famille des *Pneumoviridae* qui comporte un autre virus d'importance en santé humaine, le métapneumovirus humain (HMPV), ainsi que le virus respiratoire syncytial bovin qui cause d'importantes pertes économiques dans les élevages (Valarcher et Taylor, 2007).

### 1.2. Organisation de la particule virale et cycle viral du VRS

Le génome du VRS est un ARN d'environ 15,2 kb contenant 10 gènes codant pour 11 protéines virales (Figure 1A). Les particules virales du VRS varient en tailles et en morphologies : généralement filamenteuses (avec une longueur allant de 200 nm à 2 µm), elles peuvent également adopter des formes asymétriques ou sphériques (avec un diamètre allant de 100 nm à 1 µm) (Figure 1B) (Liljeroos et al., 2013).

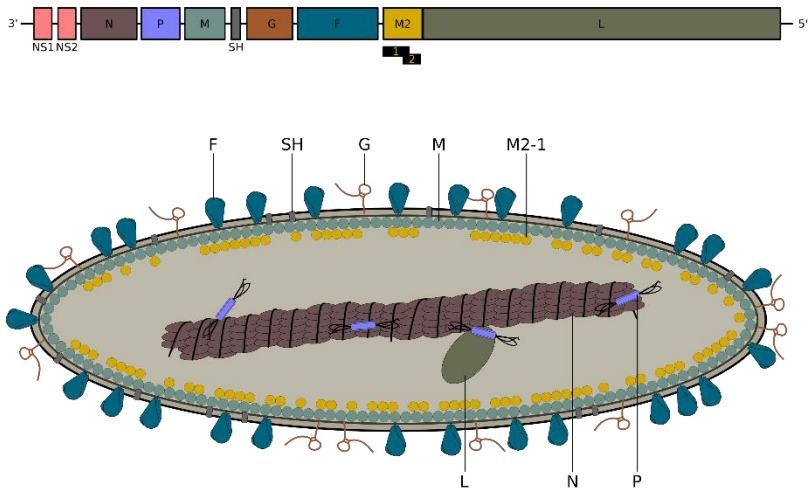
Le VRS possède une enveloppe dérivant de la membrane plasmique de la cellule infectée. Sur cette enveloppe se trouve 3 protéines transmembranaires : la glycoprotéine G, la protéine de fusion F et la petite protéine hydrophobique SH. La face interne de la particule est tapissée par la protéine de matrice M. Le génome ARN du VRS est constamment enveloppé par la nucléoprotéine virale N, formant ainsi une hélice appelée nucléocapside (NC) (Bakker et al., 2013). La NC sert de matrice pour transcription et la réplication du génome par la protéine

virale L. Dans la particule virale, la NC est associée à L et à la phosphoprotéine P, cofacteur essentiel de L (Grosfeld et al., 1995). Le gène M2 code pour 2 protéines : M2-1 qui promeut l'élongation des ARN messagers (ARNm) viraux (Collins et al., 1996), et la protéine M2-2 qui serait impliquée dans la transition entre transcription et réplication virales (Bermingham et Collins, 1999). Le VRS exprime également deux protéines non-structurales NS1 et NS2 qui sont impliquées dans le contrôle de la réponse immunitaire de l'hôte (Spann et al., 2005 ; Swedan et al., 2011).

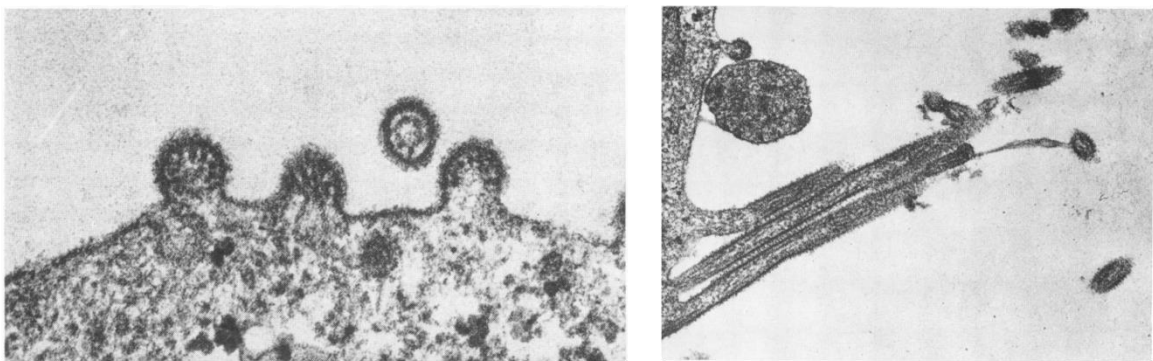
Le cycle viral du VRS se déroule entièrement dans le cytoplasme de la cellule infectée. Il débute par l'attachement de la particule virale sur la cellule cible, puis par la fusion de l'enveloppe virale avec la membrane plasmique de la cellule. Ces étapes sont réalisées par les protéines virales G et F (Levine et al., 1987 ; Walsh et Hruska, 1983). La fusion des membranes permet la libération du complexe ribonucléoprotéique (RNP, complexe formé de la NC et des protéines virales L, P et M2-1) dans le cytoplasme. Ensuite, la transcription des ARNm viraux et la réplication des génomes et antigénomes sont initiés par L, qui porte les 3 activités enzymatiques nécessaires pour la synthèse des ARN viraux : l'ARN polymérase ARN-dépendante, la coiffe et la méthylation des ARNm viraux. Ces étapes se déroulent dans des usines virales, appelées corps d'inclusions (IBs, pour *inclusion bodies*) (Garcia et al., 1993 ; Norrby et al., 1970 ; Rincheval et al., 2017), organelles dépourvues de membrane, formées par séparation des phases liquide-liquide (Galloux et al., 2020 ; Norrby et al., 1970 ; Rincheval et al., 2017 ; Risso-Ballester et al., 2020). Au sein des IBs sont retrouvées les protéines L, P, M2-1 et les NCs, ainsi que certaines protéines cellulaires. Les éléments minimaux pour former des IBs sont N et P (Galloux et al., 2020 ; Garcia et al., 1993 ; Garcia-Barreno et al., 1996). Au cours des étapes de transcription et réplication, alors que les ARN génomiques et antigénomiques sont encapsidés par N et forment des NCs, les ARNm viraux interagissent avec M2-1 et sont retrouvés au sein de sous-structures nommées IBAGs (pour *IB associated granules*). Une fois synthétisés, les ARNm viraux sont exportés hors des IBs pour être traduits en protéines par la machinerie de traduction cellulaire (Figure 1C). En fin de cycle viral, les RNPs sont acheminées vers la membrane plasmique, site d'assemblage des particules virales, où de nouveaux virions sont libérés par bourgeonnement (Figure 1B).



A



B



C

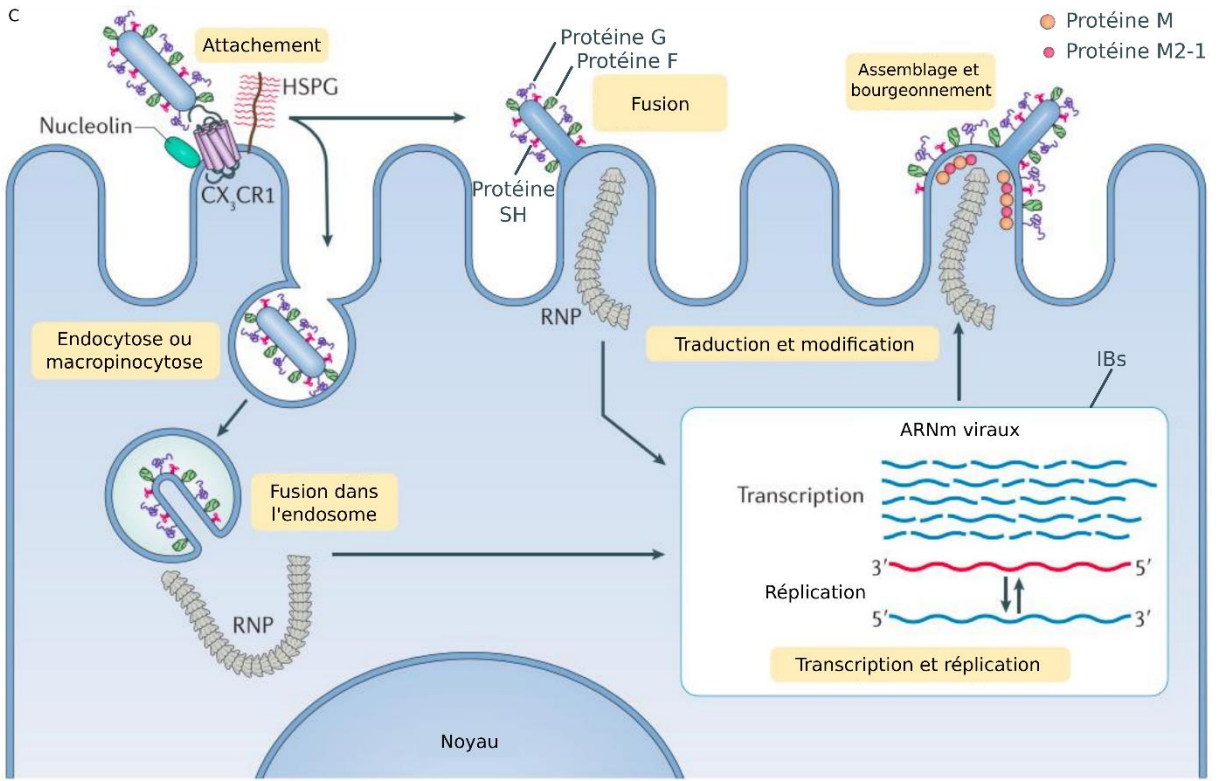


**Figure 1.** (A) Haut, schéma de l'organisation de l'ARN génomique du VRS, chaque boîte représente un gène, et les deux phases ouvertes de lectures du gène M2 sont représentées par des boîtes noires. Bas, schéma d'une particule du VRS, les protéines structurales sont annotées. (B) Images de microscopie électronique en coloration négative de sections montrant le bourgeonnement de particules virales à la surface de cellules infectées par le VRS. Gauche, grossissement 76 000 X. Droite, grossissement 42 000 X. Figure adaptée de Norrby et al., 1970. (C) Schéma illustrant le cycle viral du VRS. RNP, complexe ribonucléoprotéique. IBs, corps d'inclusions. HSPG, héparane sulfate. Figure adaptée de Battles et McLellan, 2019.

### *1.3. La nucléoprotéine et la nucléocapside au cœur cycle viral du VRS*

La nucléoprotéine N du VRS se trouve sous deux formes au cours du cycle viral. Une forme monomérique, appelée  $N^0$ , et une forme oligomérique, liée à l'ARN génomique ou antigénomique et formant la NC.  $N^0$  est synthétisée au cours du cycle viral, et maintenue monomérique et libre d'ARN par son interaction avec P qui joue le rôle de chaperonne moléculaire. Ainsi, P se lie à  $N^0$ , et (i) empêche  $N^0$  de se lier à des ARN cellulaires et (ii) recrute  $N^0$  auprès de L pour encapsider les génomes et antigénomes en cours de synthèse.

Les NCs du VRS observées au microscope électronique présentent une apparence en chevrons. Des NCs recombinantes et purifiées ou natives au sein de virions ont pu être observées par cryo-microscopie électronique (cryo-ME) et cryo-tomographie électronique (cryo-TE) (Bhella et al., 2002 ; Liljeroos et al., 2013 ; Bakker et al., 2013), mais à des résolutions insuffisantes pour caractériser précisément leur structure (Figure 2A).

La structure obtenue en 2009 par cristallographie à rayons X des anneaux N-ARN à une résolution de 3,3 Å (Tawar et al., 2009) a permis d'obtenir des informations sur la structure de N. La protéine N est composée de 2 domaines globulaires, le domaine N-terminal (NTD, résidus 37 à 252), et le domaine C-terminal (CTD, résidus 253 à 359), qui sont principalement composés d'hélices  $\alpha$ . L'interface de ces deux domaines constitue une région charnière où vient se nicher l'ARN. N possède également deux extensions, le bras N-terminal (résidus 1 à 36) en amont du NTD et le bras C-terminal (résidus 360 à 391) en aval du CTD (Figure 2B). Ces 2 bras terminaux sont indispensables pour l'oligomérisation de N sur l'ARN (Esneau et al., 2019 ; Murphy et al.,

2003 ; Tawar et al., 2009). La structure des anneaux N-ARN a permis de révéler que l'ARN se situe à l'extérieur de l'anneau et que chaque protéine N interagit avec 7 nucléotides (Figure 2C).

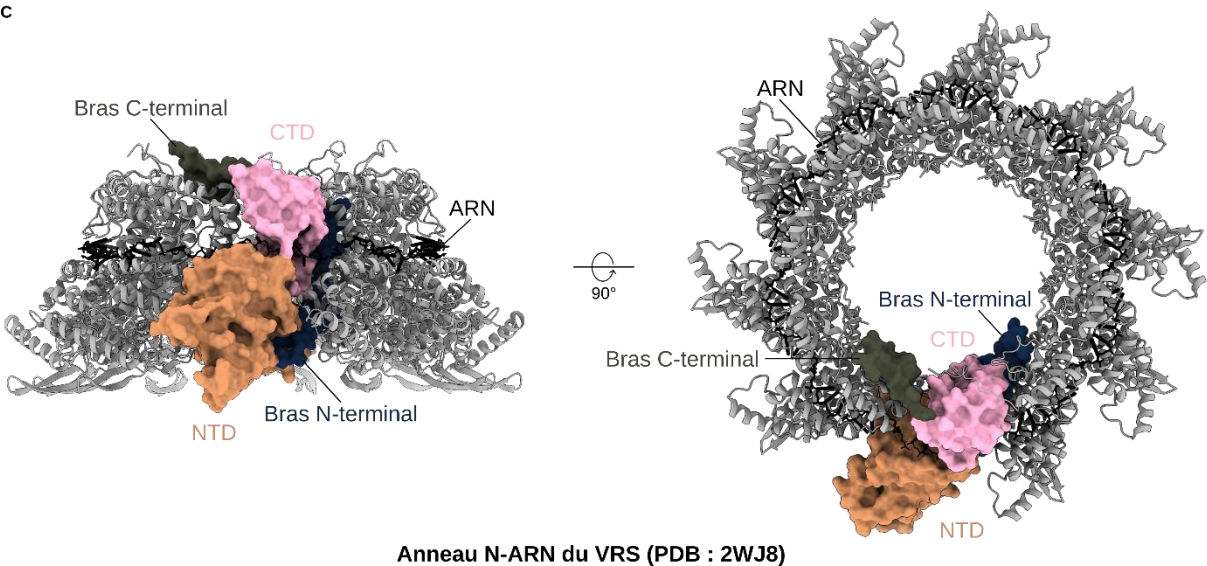
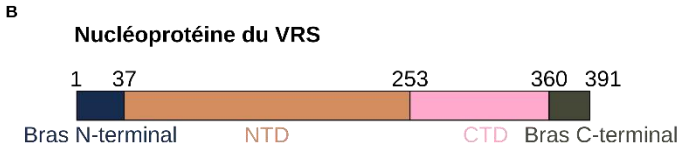
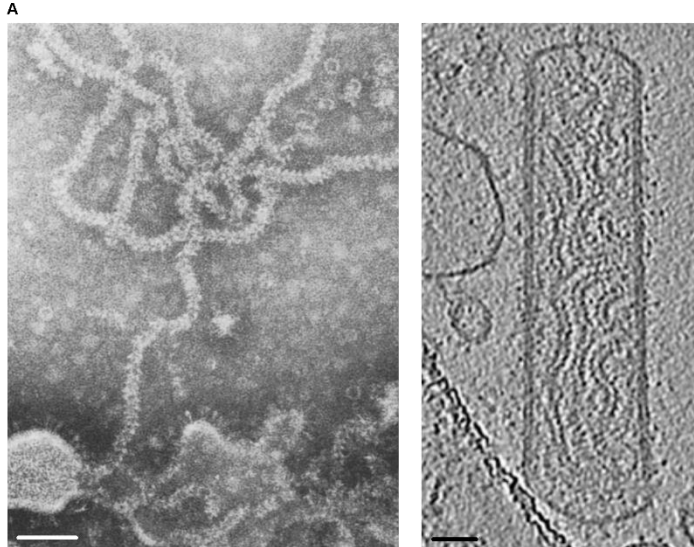


**Figure 2.** (A) Gauche, image de microscopie électronique en coloration négative de NCs issues d'une particule virale du VRS désordonnée. Figure adaptée de Bächli et Howe, 1973. Droite, image issue de coupes de topogrammes d'une particule virale du VRS contenant des NCs. Figure adaptée de Liljeroos et al., 2013. Barres d'échelle, 50 nm. (B) Représentation schématique de la séquence linéaire de la protéine N du VRS. (C) Modèle atomique des anneaux N-ARN du VRS (PDB : 2WJ8, Tawar et al., 2009), un protomère de N est représenté en surface, suivant le code couleur indiqué en B. Les autres protomères sont représentés en rubans et colorés en gris. L'ARN est représenté en bâtons et coloré en noir.

## 2. Les objectifs de la thèse

L'objectif général de ma thèse était d'obtenir des données fonctionnelles et structurales sur la NC du VRS. Plus spécifiquement, une meilleure compréhension de la structure, de l'assemblage et de la fonction des NC permettrait non seulement de comprendre le mécanisme de réplication du virus mais aussi d'ouvrir la voie au développement de nouvelles stratégies antivirales.

Mon projet de thèse était divisé en deux parties complémentaires : (i) l'étude du rôle de l'ARN dans les mécanismes conduisant à la spécificité d'encapsidation des génomes et antigénomes viraux par la protéine N, (ii) la détermination de la structure de la NC par cryo-ME.

Concernant le premier objectif, le but était (i) d'isoler une protéine N recombinante monomérique, fonctionnelle et sans ARN, afin (ii) de réaliser des essais d'encapsidation *in vitro* et de caractériser les complexes N-ARN par des approches biochimiques et biophysiques. Ce travail a été réalisé principalement au cours des deux premières années de ma thèse, en majeure partie au sein de l'équipe BMP de l'INRAE de Jouy-en-Josas, avec la collaboration du groupe Biologie Chimique et chimie des Acides Nucléiques de l'IBMM de Montpellier, qui a fourni l'ensemble des ARNs synthétiques utilisés dans l'étude et du groupe MICA de l'IBS de Grenoble. Ces travaux ont été publiés en août 2022 dans le journal *Journal of Biological Chemistry*.

Le second objectif de ma thèse était d'exprimer la protéine N dans des cellules eucaryotes afin de purifier des NCs et de résoudre leur structure par cryo-ME et obtenir des informations sur l'assemblage N-ARN. Ce travail a conduit à la résolution de 4 assemblages N-ARN différents : la NC hélicoïdale, la NC à deux-têtes, la NC coiffée d'un anneau et les doubles-anneaux N-ARN. Un manuscrit portant sur ces travaux a été soumis au journal *Nature communications*, et actuellement en cours de révision. L'expression et la purification des assemblages N-ARN ont été réalisés au sein de l'équipe BMP. La collecte et le traitement des données ont été réalisés au sein du groupe MICA. J'ai également eu l'opportunité de participer à la mise en place d'un protocole pour résoudre la structure des NCs du VRS en cellules infectées par cryo-TE. Ce travail a été initié au centre de microscopie électronique d'Umeå, au cours de la dernière année de ma thèse.

### **3. Résultats**

#### *3.1. Étude de la spécificité d'encapsidation des ARNs par la nucléoprotéine du VRS*

Au cours de ma première année de thèse, un article portant sur l'étude de l'encapsidation *in vitro* d'ARN par la protéine N du VRS a été publié (Gao et al., 2020). Dans cette étude, les auteurs ont montré leur capacité à obtenir une protéine N<sup>0</sup> stable, non liée à l'ARN et compétente pour l'encapsidation. Leurs résultats mettaient en évidence qu'une longueur de 7 nucléotides permettait de déclencher l'encapsidation, et que l'encapsidation *in vitro* conduisait à la formation d'anneaux N-ARN indépendamment de la longueur de l'ARN utilisé. D'autre part, les auteurs avaient étudié l'importance de la séquence d'ARN pour l'encapsidation, et leurs résultats suggéraient que la position de certains nucléotides favoriserait l'encapsidation.

Lors de notre étude, nous sommes partis du constat qu'au cours du cycle viral, les ARN génomiques et antigénomiques, qui présentent une extrémité 5' ppp sont encapsidés par N, à l'inverse des ARNm viraux qui présentent une coiffe et sont méthylés en 5'. Dans ce contexte outre l'étude de l'importance de la longueur des ARNs pour l'encapsidation, nous avons émis

l'hypothèse selon laquelle les modifications de l'extrémité 5' des ARNs pourraient avoir un impact sur l'encapsidation.

Le premier défi pour pouvoir réaliser des tests d'encapsidation *in vitro* est de purifier une protéine N monomérique, stable, non liée à l'ARN et compétente pour l'encapsidation. En effet, N présente une très forte propension à se lier à l'ARN et à s'oligomériser quand elle est exprimée dans des systèmes recombinants. La stratégie adoptée a été d'exprimer une protéine de fusion composée de la protéine N pleine longueur fusionnée aux 40 premiers acides aminés de la protéine P.

Nous avons pu démontrer dans notre étude que la N encapsidait spécifiquement l'ARN, et que la séquence nucléotidique n'avait pas d'impact majeur sur l'encapsidation (Figure 3A). Nos résultats ont également permis de montrer que si une longueur d'ARN de 7-mer était suffisante pour déclencher l'encapsidation, une longueur de 11-mer était nécessaire pour obtenir une encapsidation stable (Figure 3B). Nous n'avons cependant pas constaté de spécificité d'encapsidation liée à des modifications de l'extrémité 5' de l'ARN. De plus, nous avons montré que, dans nos conditions, l'encapsidation *in vitro* conduits à la formation d'anneaux de N-ARN indépendamment de la taille des ARNs grâce aux images de ME en coloration négative. En outre, nous avons démontré que l'encapsidation de l'ARN est essentielle à la formation d'IBs *in vitro* (Figure 3C) (Gonnin et al., 2022).



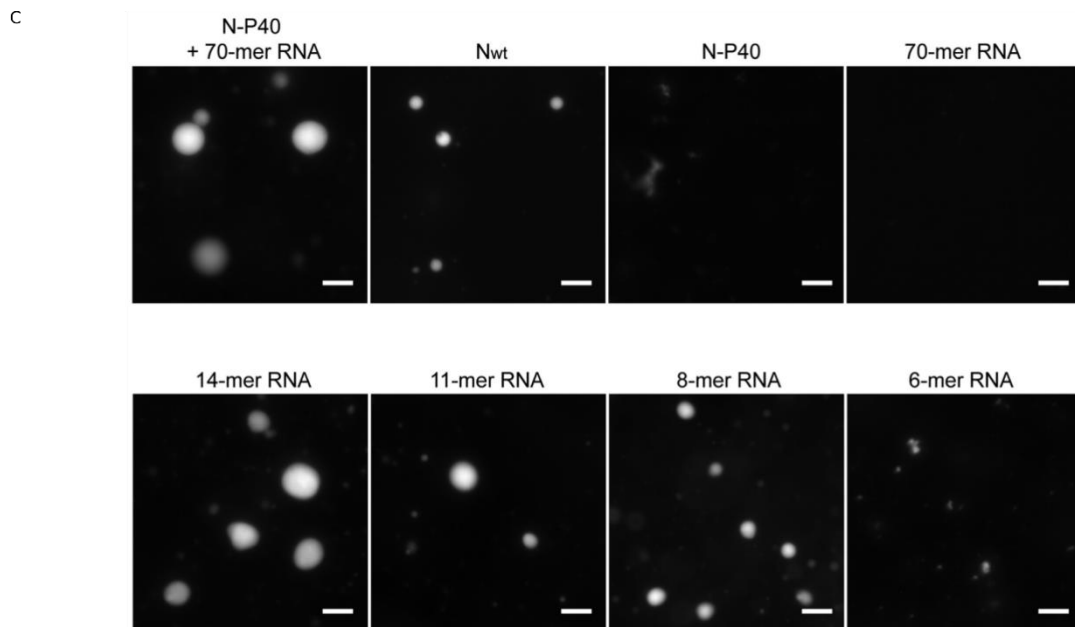
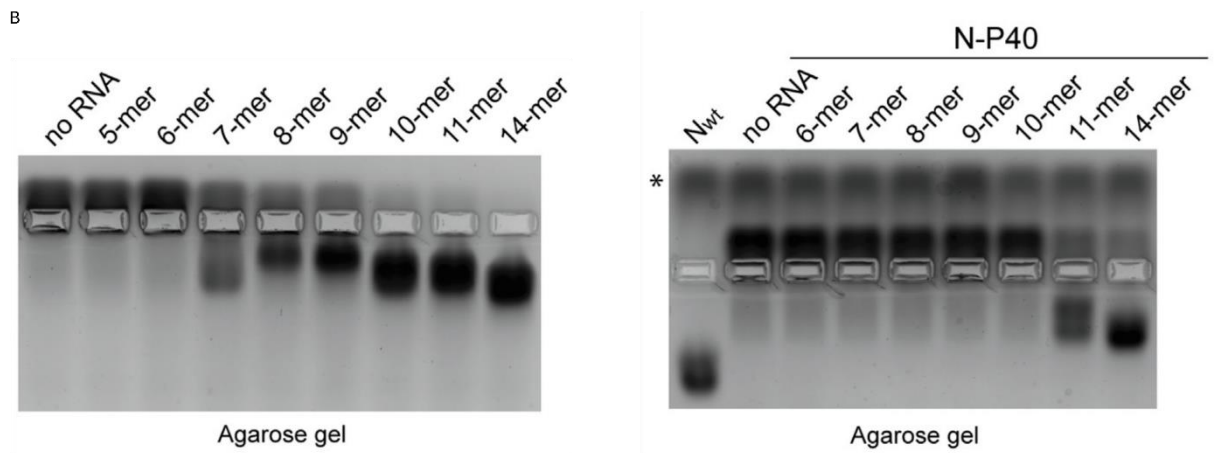
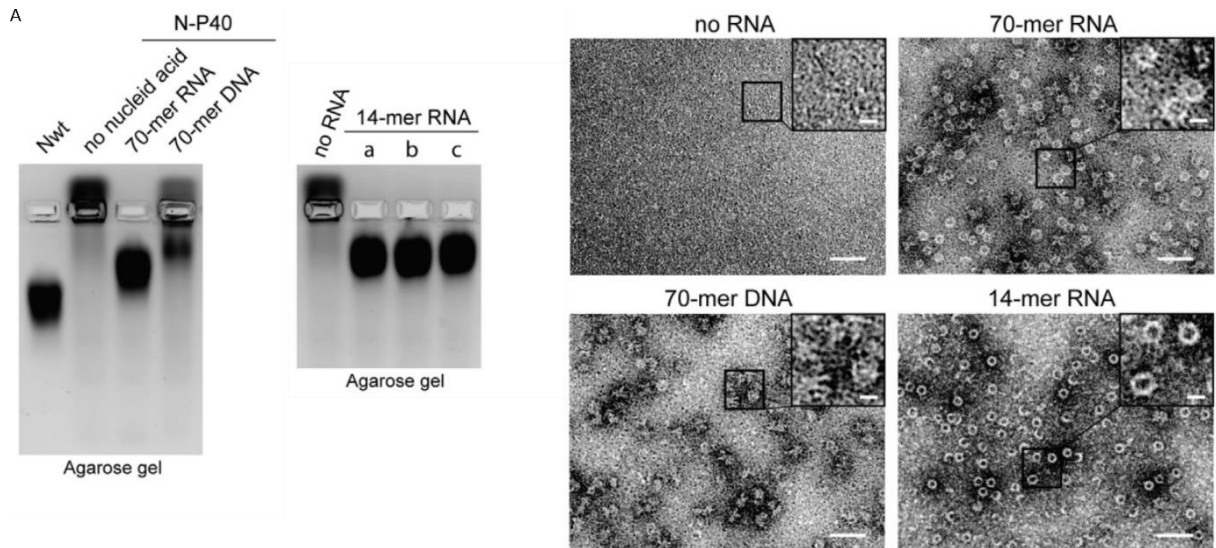


**Figure 3.** (A) Gauche, analyse de la migration de la protéine N-P40 seule ou incubée en présence d'ARN ou d'ADN de 70-mer, ou d'ARN de 14-mer avec des séquences nucléotidiques différentes (a, b c) par électrophorèse sur gel natif d'agarose. Les gels sont colorés à l'amido black. Nwt correspond au anneaux N-ARN utilisés comme contrôle. Droite, images de ME en coloration négative de N-P40 seule ou incubée en présence d'ARN ou d'ADN de 70-mer, ou d'ARN de 14-mer, mettant en évidence la formation d'anneaux de N-ARN, et d'agrégats en présence d'ADN. Barre d'échelle 50 nm et 10 nm pour les panneaux en haut à droites des images. (B) Gauche, analyse de la migration de la protéine N-P40 seule ou incubée en présence d'ARN de 7 à 14-mer par électrophorèse sur gel natif d'agarose. Droite, analyse de la migration de la protéine N-P40 seule ou incubée en présence d'ARN de 7 à 14-mer par électrophorèse sur gel natif d'agarose après traitement à la RNase A. L'astérisque indique la bande correspondant à la RNase A. Les gels sont colorés à l'amido black. Les résultats mettent en évidence une instabilité des anneaux de N-ARN, sensible au traitement par la RNase, en présence d'ARN de taille inférieure à 11 nucléotides (C) Formation de corps d'inclusions *in vitro*. Haut, la protéine recombinante P-BFP (*blue fluorescent protein*) a été incubée en présence de N-P40 pré-incubée avec un ARN de 70-mer, ou en présence de Nwt ou de N-P40 seule ou d'ARN de 70-mer seuls. La formation de pseudo-corps d'inclusion *in vitro* nécessite l'encapsidation de l'ARN. Bas, P-BFP est incubée avec N-P40 pré-incubée avec des ARNs de 14-, 11-, 8- et 6-mer. La formation des gouttelettes est observée par microscopie à fluorescence. Barres d'échelles 10  $\mu$ m. Figure adaptée de Gonnin et al., 2022.

### 3.2. Analyse structurale de la nucléocapside du VRS par cryo-ME

Afin de de déterminer la structure des NCs du VRS par cyro-ME, il a fallu tout d'abord isoler et purifier des NCs. L'expression de la protéine N en cellules procaryotes ne donnant lieu qu'à la formation d'anneaux et non d'hélices (Tran et al., 2007), j'ai exprimé la protéine N dans des cellules eucaryotes en utilisant le système baculovirus. Plusieurs protocoles ont été mis au point afin d'obtenir des NCs en quantité et de qualité suffisante pour mener notre étude. Le protocole qui m'a permis de purifier des hélices de longueur satisfaisante et en bonne quantité est celui avec qui avait été utilisé pour purifier les anneaux N-ARN, à savoir une purification des NCs par affinité pour l'extrémité C-terminal de P (Tawar et al., 2009). Brièvement, la stratégie a consisté à incuber des lysats de cellules exprimant N en présence de billes de purification de la protéine GST-P<sub>CTD</sub> (fusion entre la GST et les 80 résidus C-terminaux de P) exprimée en *E. coli*, suivi d'un clivage de la GST en présence de thrombine.

Différents objets ont pu être observés sur les images de cryo-ME : des NCs hélicoïdales, des doubles-anneaux, des hélices à deux-têtes et des hélices simples coiffées d'un anneau



(Figure 4A). Ces objets ont été étudiés de manière indépendante lors du traitement d'images (Figure 4B). La détermination de la structure 3D de la NC hélicoïdale du VRS a révélé qu'elle présentait une symétrie non-canonique ayant notablement pour conséquence d'induire un accès différentiel à l'ARN le long de l'hélice. Nous avons également démontré que la flexibilité de la NC est dépendante du bras C-terminal de N, en déterminant les structures des NCs du mutant N1-370 qui adopte à la fois un assemblage hélicoïdal et un assemblage particulier de piles de doubles-anneaux (Figure 4C). Ce travail a fait l'objet d'un article, actuellement en cours de révision (Gonnin et al., 2023, bioRxiv preprint).

La résolution des structures des différents assemblages N-ARN par cryo-ME a mis en évidence la diversité des assemblages qui peuvent être formés. A la lumière des travaux très récents sur les NCs de l'ordre des *Mononegavirales* par cryo-TE (Si et al., 2022 ; Zhang et al., 2021 bioRxiv preprint), il est attendu que les NCs du VRS présentent une variabilité conformationnelle au cours du cycle viral. Au cours de ma thèse, nous avons également décidé d'étudier les NCs du VRS dans leur environnement natif, dans les cellules infectées par le VRS. Ma co-directrice de thèse, Irina Gutsche, du groupe MICA de l'IBS, est également professeure invitée associée à l'université d'Umeå. J'ai ainsi eu l'occasion de passer près de 3 mois à Umeå et de contribuer à mettre en place un protocole de visualisation des NCs dans les cellules infectées par le VRS à l'aide de la cryo-TE. Nous avons pu établir un protocole nous permettant de visualiser l'intérieur des cellules infectées, mais nous n'avons pas pu identifier les IBs contenant les NCs, il reste encore un travail important d'optimisation du protocole afin d'observer les NCs natives du VRS et de pouvoir déterminer leur structure 3D.

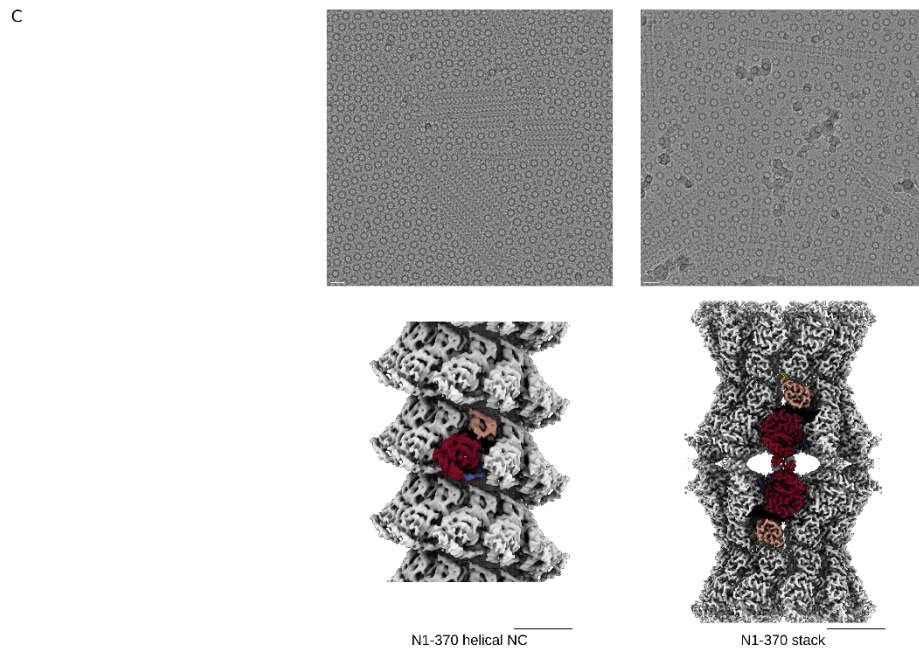
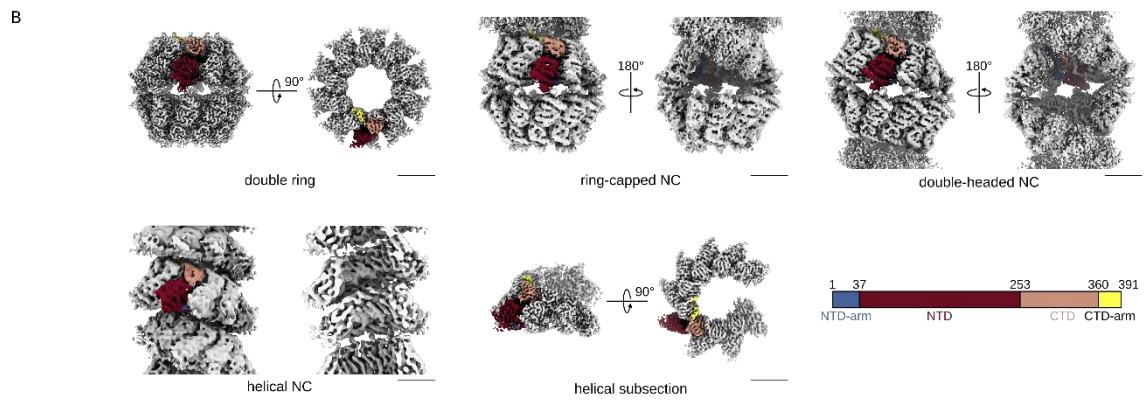
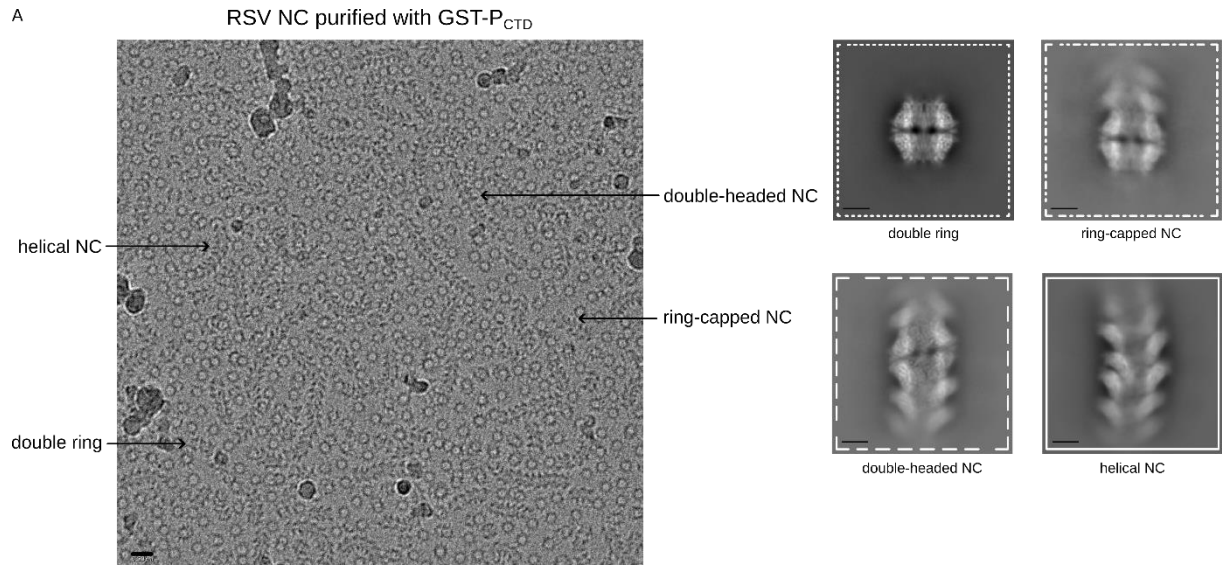


**Figure 4.** (A) Gauche, image de cryo-ME des différents assemblages N-ARN purifiés. Barre d'échelle 20 nm. Droite, classes 2D représentatives des objets observés sur l'image de gauche. (B) Cartes de cryo-ME des doubles anneaux, des hélices simples coiffées d'un anneau, des hélices à deux-têtes et des NCs hélicoïdales. Barres d'échelle 50 Å. Schéma de la séquence protéique de la protéine N du VRS mettant en évidence les sous-domaines structuraux, colorés comme sur les cartes de cryo-ME. (C) Haut, micrographie montrant les NCs hélicoïdales (gauche) et des piles de doubles-anneaux (droite) du mutant N1-370. Barres d'échelle 20 nm. Bas, Cartes de cryo-ME des NCs hélicoïdales (gauche) et des piles de doubles-anneaux (droite) du mutant N1-370. Barres d'échelle 50 Å.

#### 4. Conclusion

Les objectifs de ces études étaient (i) d'identifier les éléments clés qui pourraient expliquer la régulation de la transition N<sup>0</sup>-P vers N-ARN, et (ii) d'obtenir des informations structurales sur la NC qui pourraient permettre de mieux comprendre le fonctionnement de la synthèse des ARNs viraux par L.




Les tests d'encapsidation *in vitro* ont permis de montrer l'importance de la longueur de l'ARN dans la stabilité de l'encapsidation mais nos résultats n'ont pas permis de déchiffrer le rôle des modifications de l'extrémité 5' et de la séquence de l'ARN dans la spécificité d'encapsidation par la protéine N. Des études supplémentaires sont à mener pour comprendre les mécanismes sous-jacents la spécificité d'encapsidation des génomes et antigénomes.

L'étude structure des nucléocapsides par cryo-ME a révélé une diversité d'assemblage N-ARN. L'étude la NC hélicoïdale a révélé une symétrie non canonique impliquant un accès à l'ARN variable le long de l'hélice. Davantage d'étude sont nécessaires, notamment directement au sien de cellules infectées par le VRS, grâce à la cryo-TE afin d'étudier les potentielles différentes conformations de la NC du VRS au cours du cycle viral.

Review: Interactions between the Nucleoprotein and the Phosphoprotein of Pneumoviruses: Structural Insight for Rational Design of Antivirals

Review

# Interactions between the Nucleoprotein and the Phosphoprotein of Pneumoviruses: Structural Insight for Rational Design of Antivirals

Hortense Decool <sup>1,†</sup>, Lorene Gonnin <sup>1,†</sup>, Irina Gutsche <sup>2</sup>, Christina Sizun <sup>3</sup>, Jean-François Eléouët <sup>1,\*</sup> and Marie Galloux <sup>1,\*</sup>

<sup>1</sup> IM, UVSQ, INRAE, Université Paris-Saclay, 78350 Jouy-en-Josas, France; hortense.decool@inrae.fr (H.D.); lorene.gonnin@inrae.fr (L.G.)

<sup>2</sup> IBS, CEA, CNRS, University of Grenoble Alpes, 38044 Grenoble, France; irina.gutsche@ibs.fr

<sup>3</sup> Institut de Chimie des Substances Naturelles, CNRS, Université Paris-Saclay, 91190 Gif-sur-Yvette, France; christina.sizun@cnrs.fr

\* Correspondence: jean-francois.eleouet@inrae.fr (J.-F.E.); marie.galloux@inrae.fr (M.G.)

† These authors contributed equally to this work.

**Abstract:** Pneumoviruses include pathogenic human and animal viruses, the most known and studied being the human respiratory syncytial virus (hRSV) and the metapneumovirus (hMPV), which are the major cause of severe acute respiratory tract illness in young children worldwide, and main pathogens infecting elderly and immune-compromised people. The transcription and replication of these viruses take place in specific cytoplasmic inclusions called inclusion bodies (IBs). These activities depend on viral polymerase L, associated with its cofactor phosphoprotein P, for the recognition of the viral RNA genome encapsidated by the nucleoprotein N, forming the nucleocapsid (NC). The polymerase activities rely on diverse transient protein-protein interactions orchestrated by P playing the hub role. Among these interactions, P interacts with the NC to recruit L to the genome. The P protein also plays the role of chaperone to maintain the neosynthesized N monomeric and RNA-free (called N<sup>0</sup>) before specific encapsidation of the viral genome and antigenome. This review aims at giving an overview of recent structural information obtained for hRSV and hMPV P, N, and more specifically for P-NC and N<sup>0</sup>-P complexes that pave the way for the rational design of new antivirals against those viruses.

**Keywords:** pneumoviruses; RSV; HMPV; nucleoprotein; phosphoprotein; protein-protein interaction; structure; antivirals; nucleocapsid



**Citation:** Decool, H.; Gonnin, L.; Gutsche, I.; Sizun, C.; Eléouët, J.-F.; Galloux, M. Interactions between the Nucleoprotein and the Phosphoprotein of Pneumoviruses: Structural Insight for Rational Design of Antivirals. *Viruses* **2021**, *13*, 2449. <https://doi.org/10.3390/v13122449>

Academic Editor: Akira Ono

Received: 30 October 2021

Accepted: 1 December 2021

Published: 6 December 2021

**Publisher's Note:** MDPI stays neutral with regard to jurisdictional claims in published maps and institutional affiliations.



**Copyright:** © 2021 by the authors. Licensee MDPI, Basel, Switzerland. This article is an open access article distributed under the terms and conditions of the Creative Commons Attribution (CC BY) license (<https://creativecommons.org/licenses/by/4.0/>).

## 1. The *Pneumoviridae* Family

Pneumoviruses belong to the *Mononegavirales* order that includes many pathogenic human or animal viruses in 11 families, such as respiratory syncytial virus (RSV), metapneumovirus (MPV), Measles, Mumps, Rabies, Nipah, Ebola, and Vesicular stomatitis viruses (VSV) [1]. *Mononegavirales* have a non-segmented negative-sense RNA genome ranging from 13.2 to 15.3 kb. They form a large group exhibiting common genome organization and sharing similar replication mechanisms. Recently, the former paramyxoviral subfamily *Pneumovirinae* was elevated to family status *Pneumoviridae* [2]. This “new” family is composed of the two genera, *Metapneumovirus* and *Orthopneumovirus* (Table 1) [3].

The *Metapneumovirus* genus includes human metapneumovirus (hMPV) and avian metapneumovirus (aMPV). The *Orthopneumovirus* genus groups human respiratory syncytial virus (hRSV), bovine respiratory syncytial virus (bRSV), and pneumonia virus of mice (PVM). Although unclassified by the International Committee on Taxonomy of Viruses (ICTV), this taxon also includes ovine respiratory syncytial virus (ORV) and canine pneumovirus (CPV). More recently, an eighth pneumovirus was identified by metagenomic

sequencing of pooled nasal swabs in feral swine in the USA [4]. This newly identified *Orthopneumovirus* shows 93% and 91% protein identities with PVM and CPV, respectively, and was named swine orthopneumovirus (SOV). Amino acid sequence identities between nucleoproteins of SOV and other pneumoviruses are 59.8% for hRSV, 60% for bRSV, 45.7% for hMPV, and 43.3% for aMPV, respectively, indicating that the PVM/SOV group is distinct from *Meta-* and *Ortho-pneumoviruses* and could constitute a third genus.

**Table 1.** Phylogeny of *Pneumoviridae*.

Family	Genus	Viruses
<i>Pneumoviridae</i>	<i>Metapneumovirus</i>	Human metapneumovirus (hMPV) Avian metapneumovirus (aMPV)
	<i>Orthopneumovirus</i> *	Human respiratory syncytial virus (hRSV) Bovine respiratory syncytial virus (bRSV) Pneumonia virus of mice (PVM)

\* Unclassified viruses: Ovine respiratory syncytial virus (ORV), Canine pneumovirus (CPV), Swine orthopneumovirus (SOV).

## 2. Impact of Infections by *Pneumoviridae*

Viruses belonging to the *Pneumoviridae* family cause severe respiratory diseases in humans and animals. Among them, hRSV and hMPV are the main cause of bronchiolitis and pneumonia in young children (<5 years) [5–8]. hRSV infects nearly 100% of children in the first three years of life and is one of the principal causes of child hospitalizations. Worldwide, hRSV is estimated to be responsible for ~33 million acute lower respiratory infections (ALRI), resulting in more than 3.2 million ALRI-related hospitalizations and 118,200 deaths in children under 5 years [9]. In a recent systemic multisite study, hRSV was shown to be the first etiological agent responsible for severe pneumonia (more than 30%) in hospitalized children in Asia and Africa [10]. It is noteworthy that hRSV is also a frequent cause of otitis in infants [11] and that children who suffer from severe hRSV infection are at risk of developing further respiratory complications such as asthma [12].

After hRSV, hMPV is considered the second most common cause of ALRI in young children [7,8,13]. Isolated in 2001 in the Netherlands [14], it is thought to have derived from avian metapneumovirus (aMPV) subgroup C, 200 years ago [15]. The peak age of hospitalization for infants infected by hMPV occurs between 6–12 months, slightly later than the peak of hRSV, which is around 2–3 months. The clinical features and severity of hMPV are similar to those of hRSV. Furthermore, hRSV and hMPV are now recognized as being responsible for significant morbidity and mortality in elderly and immunocompromised persons, such as bone marrow transplant patients (with comparable disease burden to influenza) [16–20]. These viruses are seasonal, the peak of infection typically extending from early fall to early spring. In 2020, the emergence of coronavirus disease (COVID-19) triggered the large-scale implementation of non-pharmaceutical interventions such as confinement, mask-wearing, and extensive handwashing [21]. These preventive public health measures have had an impact on the circulation of diverse pathogens, specifically hRSV, as evidenced by the interseasonal epidemics of hRSV in several countries of the southern hemisphere and late epidemics of hRSV in the USA, Japan, and several European countries [22–25]. For example, the 2020–2021 bronchiolitis epidemic in mainland France lasted 15 weeks, comparable to the previous season, but with a delayed peak, 13 weeks later than that of the previous season, with a much lower amplitude. The proportion of hospitalizations for bronchiolitis has been comparable to that of recent seasons, but notable features of the 2020/21 season were a decrease in the proportion of cases over 65 years of age and an increase in the proportion of cases in children over 3 months and up to 5 years. In addition to the resurgence of hRSV and hMPV infections since March 2021, data indicate more severe illness in younger infants, possibly because of reduced immunity due to lack of exposure to these viruses in the previous season.



Finally, the *Pneumoviridae* family is also an important threat for livestock farming and has a strong economic impact, bRSV, and aMPV causing severe respiratory diseases in calves and poultry, respectively [26,27]. These infections are responsible for important animals' morbidity, leading to high mortality rates, mainly due to opportunistic infections by other viruses or bacteria [28,29]. To limit this, the current care consists of antibiotic administration during epidemics, which represents an indirect risk for animal and human health due to the emergence of resistant bacteria. In addition, the discovery of SOV in the USA suggests that yet unknown pneumoviruses could be responsible for respiratory diseases in other animal species. A recent study suggested a high prevalence of this virus in France [30]. However, further studies are required to determine whether this virus is pathogenic for pigs.

### 3. Treatments against Pneumoviruses

No vaccine is available against hRSV and hMPV. Although several vaccines against bRSV and aMPV are commercialized, their efficacy remains limited [27,31–34]. In this context, the development of antiviral drugs with a wide spectrum represents an alternative to human vaccination. This is especially true because vaccine development against hRSV and hMPV is hampered by the fact that these viruses mostly infect infants who have an immature immune system. Furthermore, as hRSV is 80% fatal to immunocompromised and transplanted patients and a significant cause of death in the elderly, the elaboration of antiviral strategies is a recognized necessity. So far, no specific inhibitors are commercially available against these viruses, ribavirin being used only exceptionally because of its toxicity and poor efficiency. A humanized monoclonal antibody directed against the surface fusion F glycoprotein (palivizumab Synagis®) is also available as a preventive treatment, but its efficiency is limited ( $\approx 50\%$ ), and its high cost restricts its use to high-risk infants [35]. Approximately 6000 children are treated with Synagis each year in France, with a cost of EUR 8000 per child (five injections). There is, therefore, a need for new and cheaper treatments, which implies the critical necessity to better understand the molecular mechanisms of virus replication. To date, most developed antiviral strategies aim at targeting the F protein to impair virus entry [36–39]. The viral polymerase L that is responsible for the enzymatic activities required for viral replication and transcription is the second main target of interest [40,41]. Among the developed compounds, the two fusion inhibitors, GS-5806 and JNJ-53718678, and the polymerase inhibitor ALS-008176, have been tested in humans [38,40,42]. However, the results of phase 2b trials of GS-5806 were disappointing [43,44], and clinical trials of ALS-008176 have recently been halted. The emergence of escape mutants upon treatment represents the main restriction and highlights the necessity to identify new targets and to associate different compounds. The functioning of the viral polymerase depends on different highly conserved transient protein-protein interactions (PPIs) that have no counterparts in cells. These viral PPIs being transient and of low affinity, molecules of high affinity that could compete with them may represent a new class of inhibitors. Furthermore, these interactions are now structurally well-characterized, allowing the rational structure-based design of antivirals.

### 4. Virions and Viral Cycle

Pneumoviruses are enveloped viruses, the virions having pleomorphic but mostly filamentous shapes [45–47]. Their genomes contain 8 to 10 genes that encode 9 and 11 proteins in the case of MPV and RSV, respectively (Figure 1A). The two non-structural proteins NS1 and NS2 of RSV, which are involved in the control of antiviral pathways during infection [48,49], have no counterparts in MPV. The virions present three transmembrane proteins: the glycoprotein (G) involved in virion attachment to the cell surface, the fusion (F) protein responsible for receptor binding and fusion between viral and cellular membranes, and the small hydrophobic protein (SH), a viroporin whose immunomodulatory role still remains unclear [50–52] (Figure 1B). The inner side of the viral membrane is lined by the matrix (M) protein. The viral particles contain the genomic RNA encapsidated

by the N protein, forming the nucleocapsid (NC), which is associated with the P-L-M2-1 proteins.

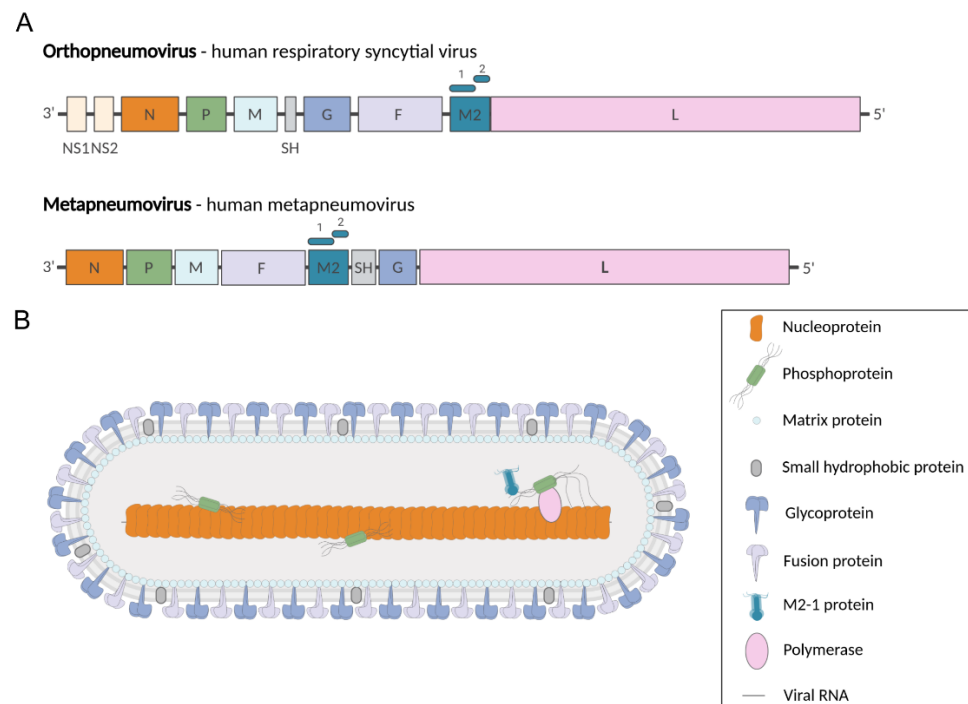


**Figure 1.** *Pneumoviridae* genomes and virion. **(A)** Genome organization of representative members of the *Pneumoviridae* family. Genomic RNAs are presented in sense (coding) orientation (3'-to-5'), with each box representing a gene encoding a separate mRNA drawn approximately to scale. The M2 gene encodes M1-2 and M2-2 proteins (represented by rectangles above M2 gene). **(B)** Representation of pneumovirus viral particle showing the structural proteins. Created with BioRender.com.

After fusion of the viral envelope with the cell membrane, the viral NC penetrates into the cytoplasm, where viral RNA transcription and replication occur (Figure 2). The viral RNA-dependent RNA polymerase (RdRp) L, associated with its cofactor P, is responsible for both activities [5,53]. Transcription of RSV also requires the viral protein M2-1, which acts as an anti-terminator/elongation factor [54,55], whereas MPV M2-1 is not essential for virus replication in cell culture [56]. During transcription, the RdRp has all the activities to transcribe, cap, and poly-adenylate mRNAs. Amplification of the viral genome by the RdRp necessitates the synthesis of an antigenome, which is also encapsidated by N. At the final stage of the viral cycle, NCs assemble with the other structural viral proteins at the cell surface to generate new virions (Figure 2).

More specifically, viral replication and transcription take place in cytoplasmic inclusions bodies (IBs), where all the proteins required for the activities of the RdRp concentrate [57] (Figure 2). These structures, also observed for others *Mononegavirales*, are membrane-less organelles that present liquid-like properties [58,59], and expression of N and P was shown to be sufficient to induce the formation of pseudo-IBs [60,61]. These IBs contain dynamic sub-compartments called IBAGs (IB-associated granules), where viral mRNA and the transcription factor M2-1 specifically accumulate [57] (Figure 2). It is noteworthy that hRSV proteins NS2 and M were also shown to localize to IBs [62–64]. Furthermore, different cellular proteins such as HSP70, actin, actin-associated proteins, translation initiation factors PABP, and eIF4G, as well as the phosphatase PP1, were shown to be recruited to IBs [57,65,66]. In particular, N was shown to interact with proteins involved in innate immune pathways such as MAVS, MDA5, and more recently, the subunit p65 of NF- $\kappa$ B, leading to their sequestration into IBs [67,68]. Thus, there is accumulating evidence that IBs are complex organelles that play a central role in the viral cycle, not



only for viral RNA synthesis but also as platforms for the traffic of NCs from IBs to the plasma membrane and for assembly, as well as in the regulation of cellular innate immune responses to infection.

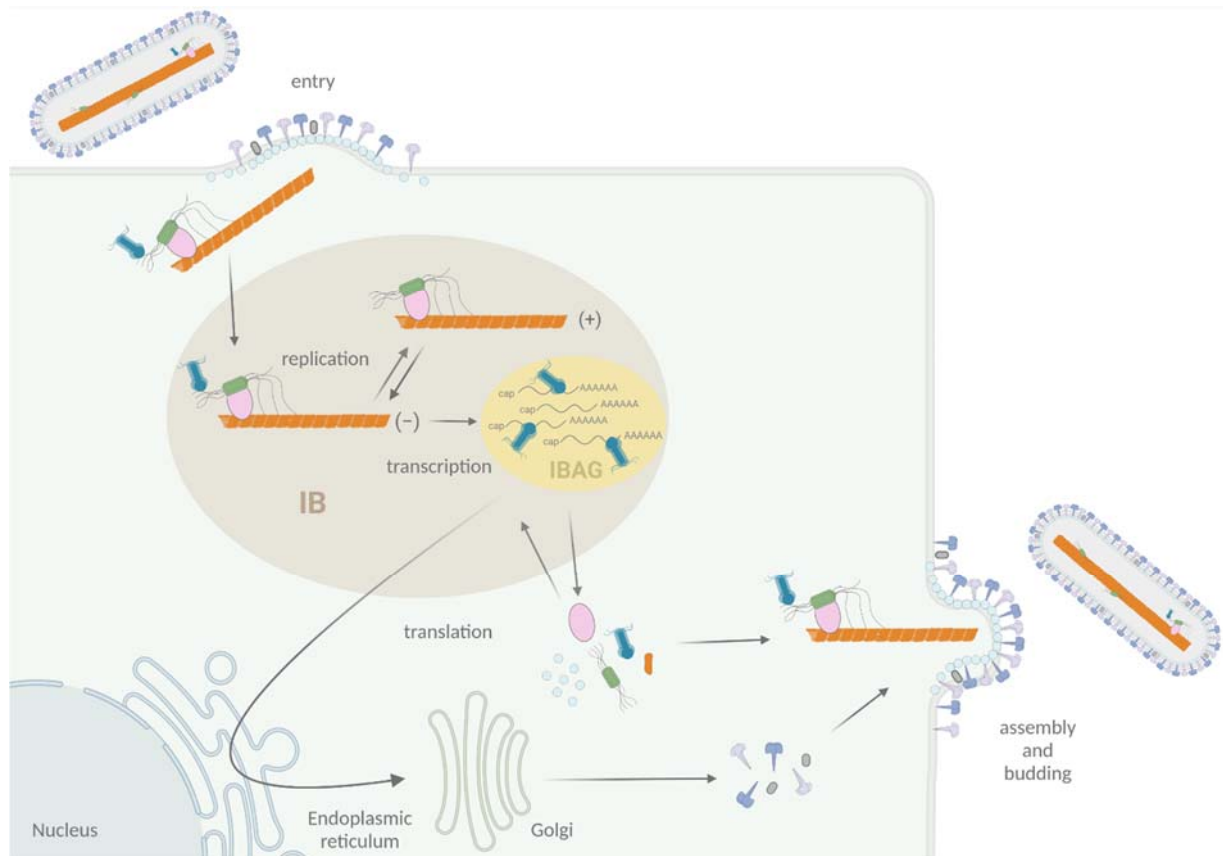


**Figure 2.** Schematic representation of the viral cycle of Pneumoviruses. Virion attachment to the cell is mediated by F and G proteins. The F protein is responsible for the fusion of viral and cell membranes, leading to the delivery in the cytoplasm of the NC complexed with L, P, and M2-1 proteins. Transcription and replication occur in membrane-less organelles called cytoplasmic inclusion bodies (IBs, light brown). Within IBs, M2-1 and viral mRNAs accumulate into sub-structures called inclusion body-associated granules (IBAGs, yellow). After viral protein production and genome replication, assembly and budding of new viral particles take place at the plasma membrane. Adapted from “Replication Cycle”, by BioRender.com (2020). Retrieved from <https://app.biorender.com/biorender-templates> (30 November 2021).

## 5. The Replication/Transcription Machinery of Pneumoviruses

The RdRp functioning depends on different PPIs, with the phosphoprotein P acting as a hub to recruit many partners, and more particularly by interacting with NC, L, M2-1, and the neosynthesized N ( $N^0$ ) (Figure 3).

The last decades were marked by the accumulation of structural and functional information on the pneumoviral RdRp. The main achievement was the recent determination of the 3D structure, although partial, of the L-P complexes of hRSV and hMPV by cryo-electron microscopy [69,70]. These structures revealed strong structural conservation between these two complexes, with a particular mode of P binding to L (see Section 6.1). They allowed establishing a model for the spatial functioning of L [70]. The structure and activities of the L protein will not be discussed extensively here. Briefly, the RdRp recognizes and uses the viral RNA genome as a template exclusively when it is encapsidated by N inside a flexible helical NC (Figure 3). This recognition is mediated by P, which is essential for loading the L polymerase onto the NC template and for keeping it bound to its template in a dynamic fashion during RNA synthesis.

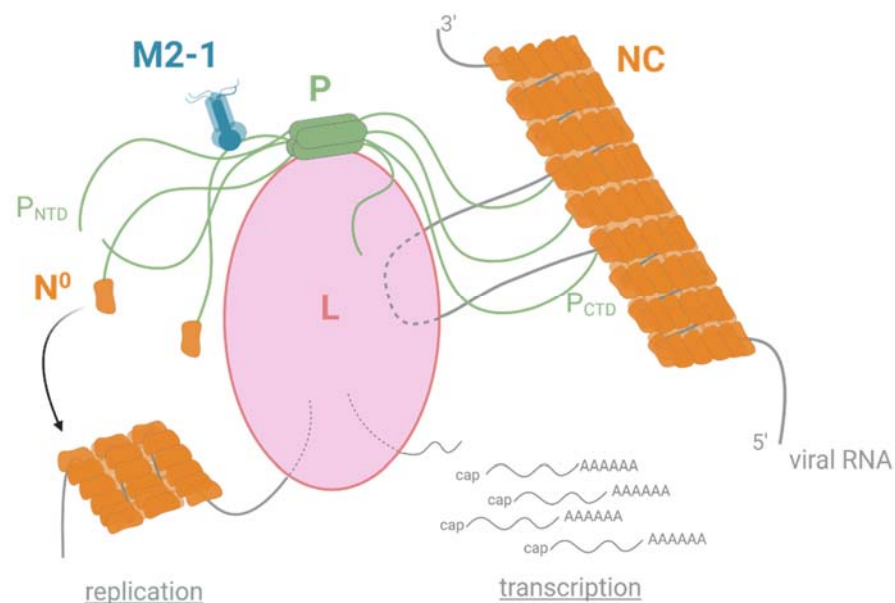


**Figure 3.** Schematic representation of the polymerase functioning of pneumoviruses. The polymerase L is responsible for both viral replication and transcription. The P protein plays a role in the hub by interacting with L and NC through its C-terminal P<sub>CTD</sub> domain and with M2-1 and the monomeric and RNA-free N (N<sup>0</sup>) through its N-terminal P<sub>NTD</sub> domain. Created with BioRender.com (30 November 2021).

The L protein embeds all enzymatic activities required for replication and transcription. The L protein contains an RdRp domain followed by a polyribonucleotidyl-transferase domain (PRNTase or capping domain) and a methyltransferase (MTase) domain. During transcription, the L protein scans the viral RNA, and mRNA synthesis begins at a conserved gene start sequence (GS). When the RNA is about 30 nucleotides long, a GMP moiety, covalently linked to the PRNTase domain of L, is transferred to the 5' end of the nascent viral RNA, forming a cap structure (GpppG-RNA). The cap is subsequently methylated on its 2' O and N7 position (N7GpppGm-RNA) by the MTase activity of L [71]. It is noteworthy that, although the mechanism still remains poorly understood, efficient hRSV transcription requires the recruitment of the M2-1 protein by P [54,55]. During replication, the RdRp synthesises antigenomes and genomes that are concomitantly encapsidated by the N protein. The assembly of new functional viral genomes requires a continuous supply of unassembled N molecules (N<sup>0</sup>). The P protein is an essential co-factor in this process by forming an N<sup>0</sup>-P complex to maintain N in a competent form for the encapsidation of new viral genomes (Figure 3).

## 6. Insights into P and N Protein Structures

The P and N proteins are the two main actors of the polymerase complex. Besides their direct role in viral RNA synthesis, they were shown to be the scaffold proteins responsible for IB morphogenesis [61,72]. This architectural role of P and N for IB formation was recently shown to depend on a liquid-liquid phase separation (LLPS) mechanism, requiring N-P interaction [73]. The LLPS mechanism is now well characterized. It is initiated by scaffold molecules that form condensates through the establishment of a network of interactions, more frequently, proteins and RNA. The archetype of protein architecture sustaining the formation of the LLPS relies on proteins with intrinsically disordered regions (IDRs) presenting multiple interacting motifs of low affinity [74–76] and RNA-interacting domains. The pneumoviruses P proteins, which present different IDRs and interact with NC, appear to be the pivotal element for IB morphogenesis [73].

### 6.1. The Modular Structure of the Phosphoprotein P

Pneumoviral P proteins play a central role during the virus cycle, their high plasticity allowing the establishment of transient and complex interactions with various partners. Both hRSV and hMPV P proteins (of 241 and 294 residues, respectively) form parallel tetramers with a central oligomerization domain ( $P_{OD}$ ) consisting of a helical coiled-coil core, flanked by two intrinsically disordered regions ( $P_{NTD}$  and  $P_{CTD}$ ) (Figure 4A) [77–81]. Sequence alignment of the hRSV and hMPV phosphoproteins indicates a sequence identity and similarity of 28% and 38%, respectively, as calculated with the Sequence Manipulation Suite using an alignment made on the T-coffee server [82].  $P_{OD}$  displays very high conservation with 65% identity and 80% similarity between hRSV and hMPV.  $P_{C\alpha}$ , a subdomain of  $P_{CTD}$  with a high helical propensity, has 41% identity and 52% similarity. The  $P_{NTD}$  domain is longer in hMPV P than in hRSV P, but the N-terminus and the region proximal to the oligomerization domain also present conserved motifs that are likely molecular recognition elements (Figure 4A).

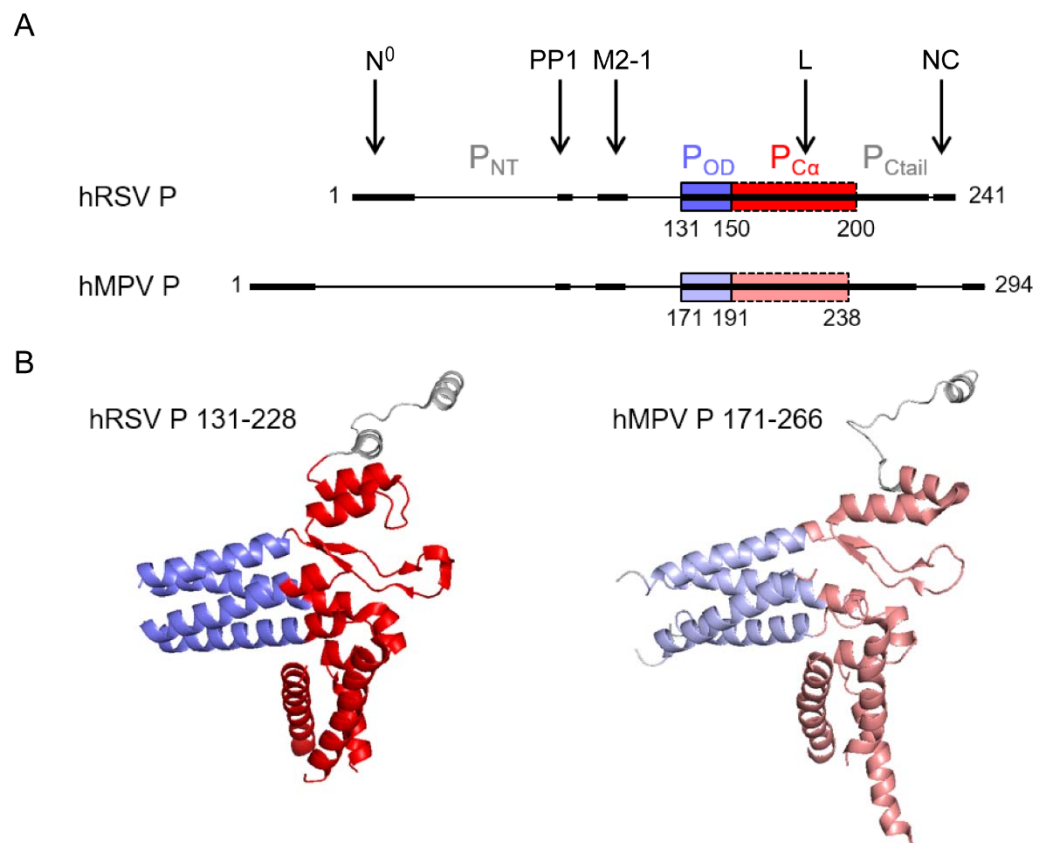


**Figure 4.** Structure of Pneumovirus P proteins. (A) Domain architecture of hRSV and hMPV P proteins, with a fully disordered N-terminal domain,  $P_{NTD}$ , a short tetrameric coiled-coil oligomerization domain,  $P_{OD}$  (blue), and a C-terminal domain,  $P_{CTD}$ , consisting of a domain with a high  $\alpha$ -helical propensity,  $P_{C\alpha}$  (red), and a highly disordered C-terminal tail,  $P_{Ctail}$ . The interaction regions of hRSV P with RdRp, or associated proteins like PP1, are indicated by arrows and bold lines. The corresponding regions in hMPV are also in bold lines. (B) High-resolution cryo-EM structures of the tetrameric L-associated hRSV and hMPV P proteins. Only the  $P_{OD}$  and  $P_{C\alpha}$  domains are observed in the L-P complex structures. Neither  $P_{NTD}$  nor  $P_{Ctail}$ , except for a single protomer, could be observed due to high disorder. Created with Pymol (<https://pymol.org>, 30 November 2021).

NMR proved to be a well-suited tool to obtain structural data of hRSV P alone in solution, and of its intrinsically disordered domains, in particular. This revealed that although these domains were not stably folded, several regions of  $P_{NTD}$  and  $P_{CTD}$  presented a propensity to form transient  $\alpha$ -helices, likely to be involved in various PPIs [83–85]. These

results were confirmed by interaction studies between P and N or M2-1 [65,83,86], but also by resolution of the 3D structures of P fragments in the complex with N<sup>0</sup> [87], M2-1 [88], and L [69,70]. Whereas the interactions with N<sup>0</sup> and M2-1 were shown to involve short linear motifs of the P<sub>NTD</sub> domain that fold into helices upon binding, the recent structures of L-P complexes revealed that both P<sub>OD</sub> and P<sub>CTD</sub>, the latter mostly through P<sub>Cα</sub>, interacts with L [69]. The location of these binding sites is indicated in Figure 4A. Interestingly, each P<sub>CTD</sub> in the P tetramer was shown to adopt a specific and different conformation in contact with L (Figure 4B). However, the conformation of the L-bound hRSV and hMPV P<sub>CTD</sub> tetramers is strikingly similar: structural alignment yields an RMSD of 1.224 Å. Of note, a recent study revealed that the hRSV P-M interaction involves both P<sub>NTD</sub> and P<sub>OD</sub> [64]. In contrast to these extended binding regions, the linear sequence corresponding to the last C-terminal residues of P was shown to be sufficient for binding to NC [89–91].

It is noteworthy that major and minor sites of phosphorylation were identified on hRSV P, with two main clusters of phosphorylated serines S116/S117/S119 and S232/ S237 [92,93]. The phosphorylation status of P was shown to depend on cellular casein kinase II [94] and phosphatases PP1 and PP2A [93]. Although the role of these post-translational modifications during replication and transcription remains unclear [95–97], phosphorylation of hRSV P was shown to regulate its interaction with N and M2-1 [65,93,96,98]. hRSV P protein was also shown to recruit the phosphatase PP1 to IBs [65]. This interaction involves an RVxF-like motif of P located nearby and upstream of the M2-1 binding region (Figure 4A), which is conserved in hMPV P. Through its interaction with hRSV P, PP1 is involved in M2-1 dephosphorylation required for the efficient functioning of M2-1 and viral transcription. Therefore, phosphorylation is critical for the regulation of PPIs within the polymerase complex and efficient functioning.

## 6.2. Structure of Nucleoproteins

The N protein, which is responsible for genome and antigenome encapsidation, is composed of 391 and 394 residues for hRSV and hMPV, respectively. This protein has a high binding affinity for RNA coupled with a strong tendency to oligomerize. The 3D crystal structure of the hRSV N expressed in *E. coli* and purified as annular ribonucleoprotein complexes composed of 10 N proteins bound to RNA (N-RNA rings) was first obtained in 2009 (Figure 5A) [99]. More recently, the structure of oligomeric N of hMPV, also purified as N-RNA rings, was also obtained [87]. These structures revealed strong structural conservation: N proteins have N- and C-terminal globular domains (N<sub>NTD</sub> and N<sub>CTD</sub>, respectively) separated by a hinge region that forms the RNA-binding groove. Two flexible arms located at the N- and C-terminus of the protein bind to adjacent N protomers and rigidify the structure (Figure 5A).

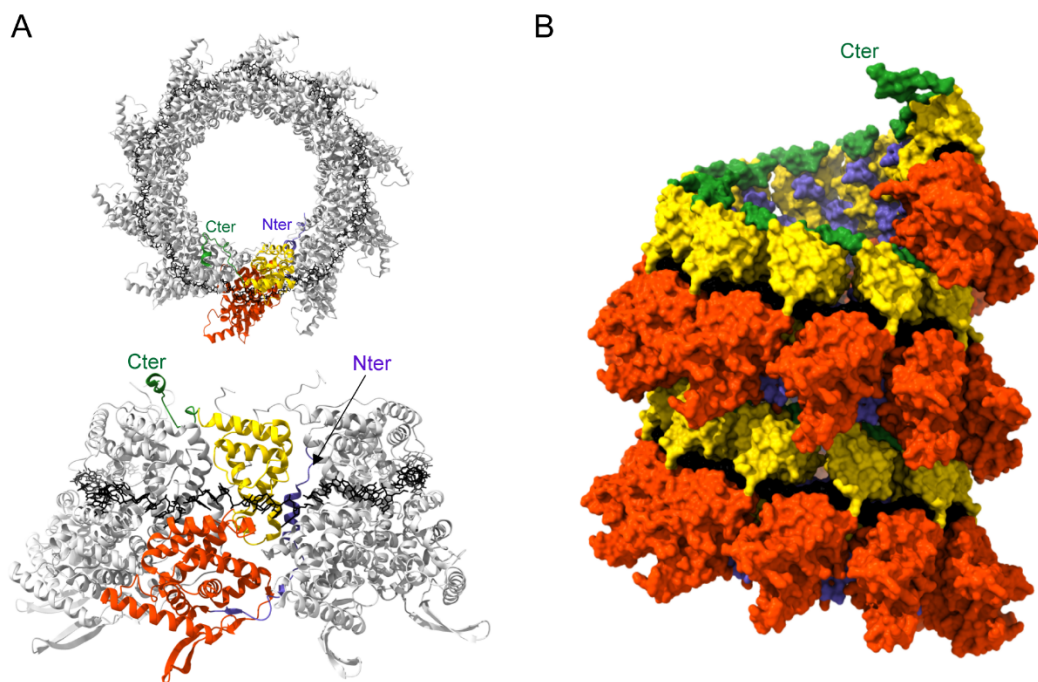


**Figure 5.** Structure of Pneumovirus N proteins. **(A)** Top (upper panel) and side (lower panel) views of hRSV N-RNA rings composed of 10 N proteins bound to RNA, purified from *E. coli* (PDB: 2WJ8 and 5FVC, respectively). N monomers are represented in ribbons; one N subunit is colored with the  $N_{NTD}$  in orange,  $N_{CTD}$  in yellow, and the N- and C-terminal parts in blue and green, respectively. The RNA is represented with the bases in black. N- and C-terminal extremities are indicated. **(B)** Left-handed N-RNA helix model (PDB: 4BKK). N monomers and RNA (black) atoms are shown as surfaces. One N subunit is colored with the  $N_{NTD}$  in orange,  $N_{CTD}$  in yellow, and the N- and C-terminal parts in blue and green, respectively. The C-terminal extremity of the N monomer at the top of the helix model is annotated. Created with UCSF ChimeraX [100].

The RNA wraps around the N protein ring in a basic groove, with seven nucleotides contacting each N monomer. The RNA is constrained and twisted by the N proteins, alternating rows of four and three stacked bases that are exposed and buried within the protein groove, respectively. Surprisingly, N-RNA rings, which were considered artifacts of production/purification, were recently found together with NCs in viral particles [101]. This raises the question of the potential role of these oligomers during the viral cycle. Electron microscopy analysis of hRSV NCs expressed in insect cells as well as cryotomography performed on viral particles revealed that these are left-handed helices [102,103]. Although the resolution of the helix was low, an atomic model of a left-handed RSV NC was generated (Figure 5B). These data allowed us to gain information on the interactions between N protomers of successive helix turns, and more importantly, to reveal that the 3' end of the RSV genome is located at the pointed end of the NC. The structure of NC at high resolution still remains to be established to gain information on the mechanism sustaining the encapsidation of the viral genome and those required to allow genome accessibility to the polymerase.

Finally, during viral replication, the neo-synthesized N is maintained monomeric and RNA-free ( $N^0$ ) by P, which acts as a chaperone (see Section 7.2). Compared to the oligomeric form,  $N^0$  is characterized by a weak rotation of the  $N_{NTD}$  relative to the  $N_{CTD}$  and by the interaction of the N C-arm with the RNA groove, thereby preventing RNA binding.

## 7. N-P Interactions as Targets for New Antiviral Approaches

As previously mentioned, there is still no vaccine nor efficient antivirals against hRSV and hMPV. Most of the molecules under clinical trials target the fusion protein or the enzymatic activities of the L polymerase. However, the emergence of escape mutants upon treatments suggests that the combination of antivirals would be a necessity to prevent/limit



the emergence of resistant viruses. The activity of the RdRp depends on many regulated PPIs. Among those, N-P interactions that are highly specific, of low affinity, and have no counterpart in cells, represent alternative targets for the development of new antivirals against hRSV and hMPV. Of interest, the structural data obtained for these PPIs now allow the rational design of inhibitors.

### 7.1. Interaction of P with NCs and Inhibition

By binding to N, P mediates the attachment of the L protein to the NCs. This interaction was well characterized for hRSV, and was recently shown to be essential for IBs' biogenesis [73]. Using recombinant proteins, it was shown that the nine C-terminal residues of hRSV P are necessary and sufficient for binding to N-RNA rings [89]. More specifically, the C-terminal acidic and hydrophobic residues of P were shown to be critical for this interaction. Using a rational structure-based approach, the domain of hRSV N involved in P<sub>CTD</sub> binding was then identified as N<sub>NTD</sub> [90]. NMR interaction experiments showed that the last 10 C-terminal residues of P were involved in binding to N-RNA rings and N<sub>NTD</sub>, forming fuzzy complexes [83,91]. Residues of N critical for the interaction with P were found in a well-defined pocket composed of hydrophobic residues surrounded by positively charged residues [90]. These results were confirmed by the crystal structure of the N<sub>NTD</sub> domain in the complex with the last two residues of P (P2 peptide in Figure 6) and highlighted the pivotal role of the P C-terminal residue Phe<sup>241</sup>, deeply buried in the N<sub>NTD</sub> pocket [91]. It is noteworthy that this N pocket is accessible at the surface of the modelized helical nucleocapsid [102].

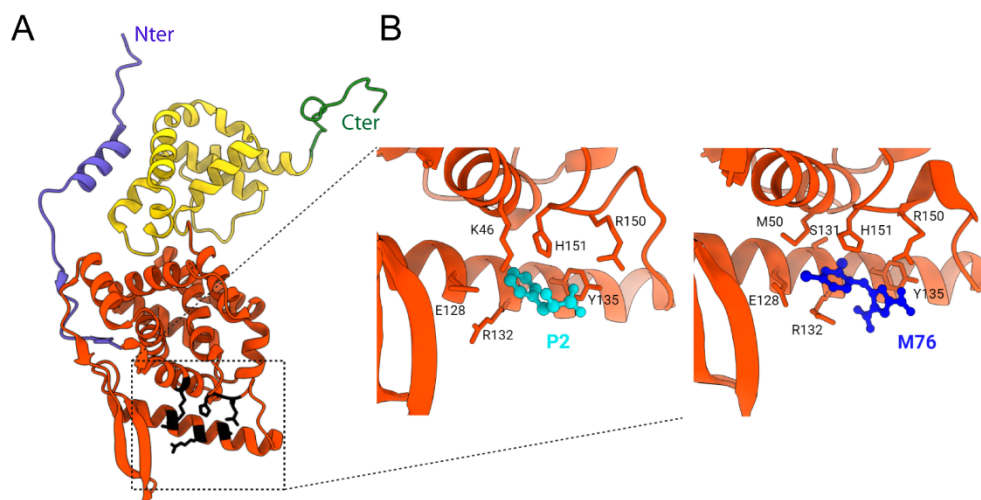


**Figure 6.** X-ray structure of hRSV N protein protomer and of N<sub>NTD</sub> in complex with P2 peptide and M76 compound. (A) An hRSV N protomer taken from the X-ray structure of N-RNA rings (PDB 2WJ8) is represented in ribbons, with the N<sub>NTD</sub> in orange, N<sub>CTD</sub> in yellow, and the N- and C-terminal arms in blue and green, respectively. The residues of N critical for the interaction with P are shown with lateral chains in black. N- and C-terminal extremities are indicated. (B) Zoom into the P2-binding site on N<sub>NTD</sub> (left panel, P2 in cyan) (PDB: 4UCA) and of the M76 compound binding site (right panel, M76 in deep blue) (PDB: 4UCC). The residues of N involved in the interaction with P2 or M76 are indicated. Created with UCSF Chimera [104].

The low affinity of this N-P interaction coupled with the structural characterization of the P binding site on N suggested that small molecules could bind to the pocket of N to impair the P interaction. In silico screening of small compounds was thus performed to identify molecules that could insert into this P binding site. The M76 compound was able to compete in vitro with P for binding to N<sub>NTD</sub> despite its low affinity ( $\mu\text{M}$  range). The crystallographic structure of the N<sub>NTD</sub>-M76 complex revealed that it displayed an optimal charge and shape for N binding (Figure 6B) [91]. However, M76 did not present any antiviral activity on infected cell cultures due to two acidic moieties preventing

cell membrane passage. Further chemical modifications of M76 led to the electrically neutral pH-sensitive prodrug diAM-M76, which was internalized in cells. Although these modifications afforded a molecule with antiviral activity, diAM-M76 displayed a limited activity and important cytotoxicity [91]. Hence, although this approach validated the interest of targeting the P binding pocket of N, further chemical optimization of this compound is required to improve its affinity for N, as well as their cellular delivery and safety.

Other studies confirmed that this N-P interaction represents a potential target to develop antivirals against hRSV. Flavonoids such as hesperetin (Hst) or quercetin were initially shown to inhibit hRSV replication *in vitro* [105]. By coupling experimental and computational approaches, it was recently shown that Hst interacts with N, the aromatic ring of Hst being buried inside the hydrophobic N<sub>NTD</sub> pocket involved in P binding [106], similarly to M76. High-throughput screening of a tailored library also led to the identification of the compound RSV-604 as a specific inhibitor of hRSV replication [107,108]. Further characterization of the mode of action of RSV-604 revealed that this benzodiazepine blocks both *de novo* synthesis of viral RNA and viral infectivity (assembly and release of virions) [109]. However, treatment of hRSV-infected cells with RSV-604 resulted in the emergence of resistant escape mutants, mutations being located in a region of N<sub>NTD</sub> close to the P binding site. Based on these results, the compound EDP-938 has been developed [110]. Compared to RSV-604, EDP-938 displayed improved antiviral activity against hRSV, validated in non-human primates, but escape mutations also occurred on N. As mutations involved in the emergence of resistance concerned residues located close to the P binding site, it is tempting to speculate that these molecules could interfere with the N-P interaction. However, no structural nor experimental data supporting this hypothesis have been reported yet. Finally, a recent study showed that overexpression of P<sub>CTD</sub> in cells inhibits hRSV replication, suggesting that a peptidomimetic approach could be developed to block the P-NC interaction [111].

Until recently, no information was available for the hMPV N-P interaction. Based on the strong structural and functional homologies between hMPV and hRSV N and P proteins, it was expected that N-P interactions could be partially conserved. Using site-directed mutagenesis approaches, coupled with *in vitro* and *in cellula* interaction assays, the last six C-terminal residues of hMPV P protein were shown to be necessary and sufficient for binding to N-RNA rings. Residues of P involved in this interaction, including the last C-terminal residue M<sup>294</sup>, are mostly hydrophobic [112]. Similar to hRSV, residues of N involved in the interaction were found at the surface of N<sub>NTD</sub>, and residues critical for P binding form a pocket mainly composed of hydrophobic residues, surrounded by charged residues [112]. Based on these results, molecular modeling was used to establish a model of binding between the last three C-terminal residues of P and N<sub>NTD</sub>. Altogether, these data confirmed the strong structural homologies between hMPV and hRSV P-N complexes but also highlighted some specificity. Therefore, whereas the hMPV P binding pocket at the N<sub>NTD</sub> surface could also become a target for the rational design of hMPV antivirals, the design of dual inhibitors that could block both hMPV and hRSV N-P interaction is less likely.

## 7.2. The Pneumovirus N<sup>0</sup>-P Complex

The encapsidation process of neosynthesized genome and antigenome by N<sup>0</sup> is an essential step of the viral cycle, the details of which are not yet fully understood. One main issue to gain information on the mechanism involved in the switch from N<sup>0</sup> to N-RNA forms was to isolate and characterize a recombinant monomeric N<sup>0</sup>. Due to the N protein displaying a strong tendency to interact with RNA and to oligomerize, the purification of recombinant N<sup>0</sup> has long been challenging. Different strategies were developed to prevent both RNA interaction and oligomerization of N. Initial approaches consisted in truncation of the N-terminal arm of N to impair N oligomerization [113,114] or substitution of N residues involved in RNA binding [115]. Using co-expression of recombinant mutated

monomeric hRSV N protein with P fragments, the 29 N-terminal residues of P were shown to be sufficient to interact with N<sup>0</sup> [114]. These results confirmed the predictions previously made based on sequence homologies between *Mononegavirales* [116], and the results obtained for its close homolog, the bRSV, showing an interaction between the N-terminus of P and N [117,118]. Moreover, the periodicity of the residues of hRSV P critical for N<sup>0</sup> binding suggested that the stretch spanning residues 11–28 of P could adopt an  $\alpha$ -helical conformation upon binding to N [115].

A major advance was made with the purification of a recombinant chimeric protein corresponding to full-length N fused with the N-terminal domain of P (first 40 residues), which allowed the resolution of the X-ray crystal structure of the hMPV N<sup>0</sup>-P complex (Figure 7) [87]. This structure revealed that the P peptide binds to a hydrophobic surface on N<sub>CTD</sub>. More specifically, residues 12–28 of P form an  $\alpha$ -helix that lies atop N, and the N-terminal residues of P wrap along the N<sub>CTD</sub>. Interestingly, the P peptide binding site on N overlaps with the binding sites of both the N- and C-arms of the N<sub>-i</sub> and N<sub>+i</sub> protomers in the oligomeric form, preventing N self-oligomerization. This structure also revealed that the N<sup>0</sup> form is characterized by a rotation of N<sub>NTD</sub> relatively to N<sub>CTD</sub>, compared to the oligomeric form. Finally, the C-terminal arm of N was shown to fold into the positively charged RNA groove, blocking the binding of RNA.

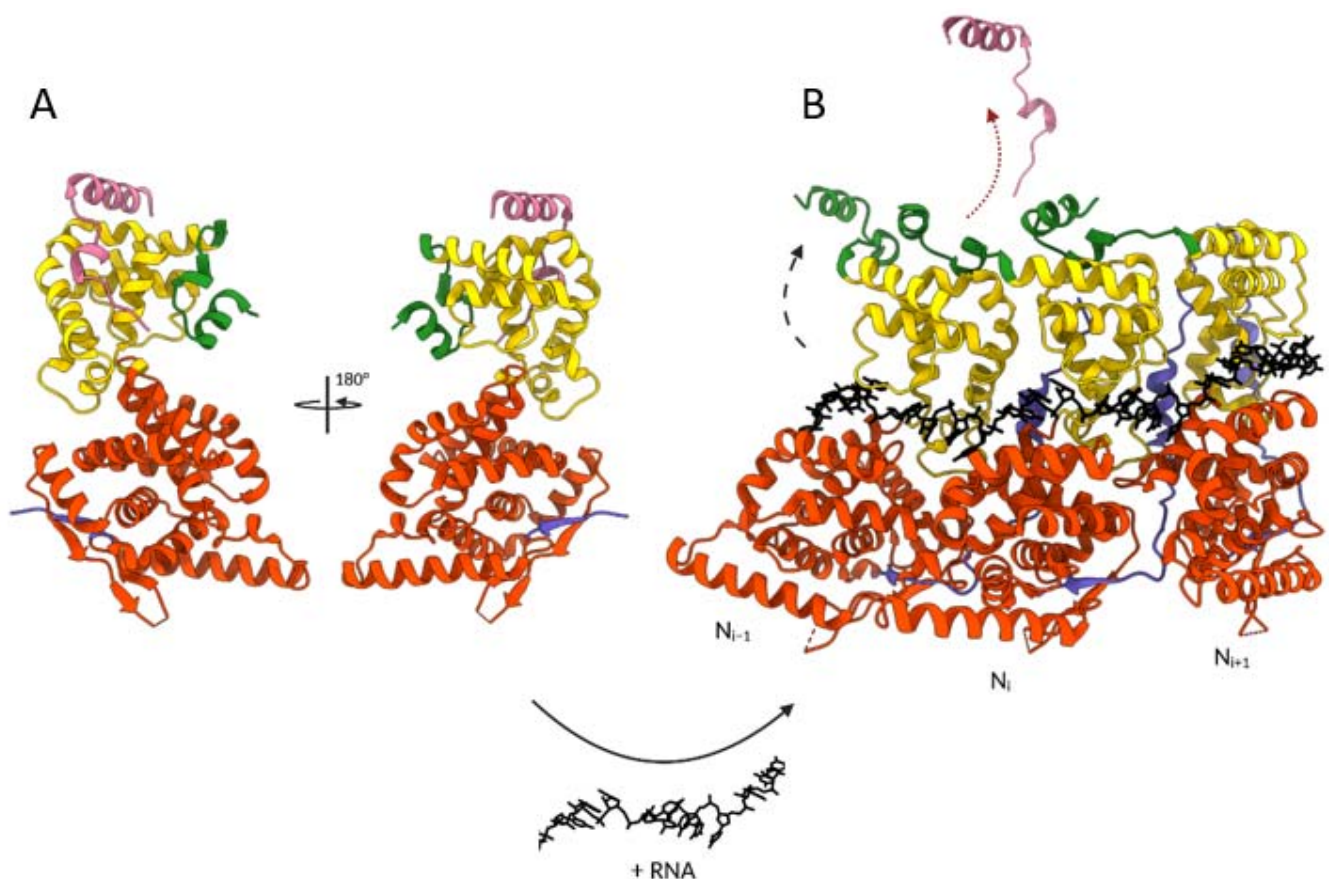


**Figure 7.** Structural changes involved in the transition from hMPV N<sup>0</sup>-P to oligomeric N-RNA forms. The transition requires the presence of RNA, as indicated at the bottom of the figure. (A) Crystal structure of hMPV N<sup>0</sup>-P<sub>1-28</sub> peptide complex (PDB: 5FVD). (B) Representation of a trimer of N in cartoon representation bound to RNA shown in black sticks (PDB: 5FVC). The black and red arrows symbolize the movement of the N C-arm and the release of P<sub>1-28</sub> peptide, respectively, required for N oligomerization. One N subunit is colored with the N<sub>NTD</sub> in orange, N<sub>CTD</sub> in yellow, and the N- and C-terminal parts in blue and green, respectively. The P<sub>1-28</sub> peptide is in pink. The N- and C-terminal extremities of N and the P peptide are indicated. Created with BioRender.com and UCSF ChimeraX [100].



Although the structure of the hRSV N<sup>0</sup>-P complex has not been solved yet, biochemical and biophysical studies confirmed the strong structural homology with hMPV. First, NMR characterization of hRSV P revealed that residues 12–24 present  $\alpha$ -helical propensity [83]. Co-purification of hRSV N protein deleted of the N-arm (N <sub>$\Delta$ 30</sub>) with 40 residues long peptide of P (P40) determined that the P binding site is located on N<sub>CTD</sub> and that the C-arm of N is critical to prevent RNA binding [114]. Based on the biochemical and biophysical characterization of this N <sub>$\Delta$ 30</sub>-P40 complex, the strong homologies between hRSV and hMPV N and P, and in particular, the strong conservation of key residues involved in the N<sup>0</sup>-P interaction, a structural model of the hRSV N<sup>0</sup>-P complex was proposed [114]. In contrast to N<sup>0</sup>-P complexes of other *Mononegavirales*, such as VSV, Nipah, Ebola, and Marburg viruses or parainfluenza 5 (PIV5), for which the binding of P was shown to be sufficient to maintain N<sup>0</sup> [119–125], these observations demonstrated that the stability of pneumoviruses N<sup>0</sup>-P complexes requires a double lock system depending on P binding and on conformational changes of N (Figure 7).

Besides the identification of the hRSV P region involved in N<sup>0</sup> binding, it was shown that the overexpression of a peptide with the corresponding sequence in cells could block the polymerase activity, giving a proof of concept that targeting the N<sup>0</sup>-P complex might be a way to develop novel antivirals against hRSV [114]. Accumulating data confirmed that the region encompassing residues 12–24 of P has a propensity to adopt an  $\alpha$ -helical conformation that is stabilized upon binding [63,114,115]. Based on this observation, a strategy aiming at specifically targeting the N<sup>0</sup>-P interaction using dominant negative peptide inhibitors that mimic the N-terminus of P was recently developed [126]. These inhibitors were synthesized using the stapled peptide technology that constrains short peptides into  $\alpha$ -helical conformation [127–129]. The presence of staples was shown to increase the potency, proteolytic stability, and cellular permeation of peptides. Of note, such a strategy was used to design peptide inhibitors of the hRSV F protein involved in the virus entry [130,131]. Screening of stapled peptides derived from the N-terminal sequence of P allowed identification of peptides derived from residues 7–30 of P, presenting an antiviral activity in cell culture, with an EC<sub>50</sub> of approximately 10  $\mu$ M [126]. Despite limited antiviral activity in cell cultures, the lead peptide was shown to reduce hRSV infection in vivo in a mouse model [126]. Because the N<sup>0</sup>-P interaction is mediated by a large interaction surface and involves a short  $\alpha$ -helix, the stapled peptide approach is of greatest interest compared to small molecules. It is noteworthy that, given the strong structural homologies between hRSV and hMPV N<sup>0</sup>-P complexes, identification of the best combination of peptide length and stapling for hRSV would facilitate the design of peptides specific to hMPV.

## 8. Conclusions

The recent advances in the structure of the viral proteins associated with the L polymerase of pneumoviruses pave the way for the development of new antiviral strategies. Of particular interest, the PPIs required for the polymerase functioning represent potential targets for the design of new classes of antivirals. Indeed, these viral interactions are highly specific and have no cellular counterparts, suggesting that inhibitors should have limited off-target activity. Furthermore, because these interactions are transient and of low affinity, molecules of higher affinity should efficiently compete with the native mimicked sequence. Among these PPIs, the two modes of N-P interactions, which are now well characterized and relatively conserved between hRSV and hMPV, can be targeted using rational structure-based approaches. As described here, the design of potent inhibitors will depend on the nature of the PPIs: whereas small molecules seem promising to target the P binding site on oligomeric N and N-RNA complexes, such as the helical NCs, small peptides seem more adapted to inhibit the N<sup>0</sup>-P interaction. Similar approaches could be used to target L-P or M2-1-P interactions. It is noteworthy that these antiviral strategies could be applied to other *Mononegavirales*. Given the emergence of resistant escape viruses

upon treatment with both anti-F and anti-L inhibitors, combinations of molecules directed against different viral targets may be required for efficient and long-term treatment.

**Author Contributions:** Writing original draft preparation, H.D., L.G., C.S., and M.G.; writing—review and editing, C.S., I.G., J.-F.E., and M.G.; supervision, M.G.; funding acquisition, C.S., J.-F.E. All authors have read and agreed to the published version of the manuscript.

**Funding:** This research was funded by the French Agence Nationale de la Recherche, generic ANR Antibronchio n° ANR-19-CE18-0012-01 and ANR DecRisP n° ANR-19-CE11-0017.

**Institutional Review Board Statement:** Not applicable.

**Informed Consent Statement:** Not applicable.

**Data Availability Statement:** Not applicable.

**Conflicts of Interest:** The authors declare no conflict of interest.

## References

- Rima, B.; Collins, P.; Easton, A.; Fouchier, R.; Kurath, G.; Lamb, R.A.; Lee, B.; Maisner, A.; Rota, P.; Wang, L.F. Problems of classification in the family Paramyxoviridae. *Arch. Virol.* **2018**, *163*, 1395–1404. [[CrossRef](#)]
- Afonso, C.L.; Amarasinghe, G.K.; Banyai, K.; Bao, Y.; Basler, C.F.; Bavari, S.; Bejerman, N.; Blasdel, K.R.; Briand, F.X.; Briese, T.; et al. Taxonomy of the order Mononegavirales: Update 2016. *Arch. Virol.* **2016**, *161*, 2351–2360. [[CrossRef](#)]
- Rima, B.; Collins, P.; Easton, A.; Fouchier, R.; Kurath, G.; Lamb, R.A.; Lee, B.; Maisner, A.; Rota, P.; Wang, L.; et al. ICTV Virus Taxonomy Profile: Pneumoviridae. *J. Gen. Virol.* **2017**, *98*, 2912–2913. [[CrossRef](#)]
- Hause, B.M.; Padmanabhan, A.; Pedersen, K.; Gidlewski, T. Feral swine virome is dominated by single-stranded DNA viruses and contains a novel Orthopneumovirus which circulates both in feral and domestic swine. *J. Gen. Virol.* **2016**, *97*, 2090–2095. [[CrossRef](#)] [[PubMed](#)]
- Collins, P.L.; Crowe, J.E. Respiratory Syncytial Virus and Metapneumovirus. In *Fields Virology*, 5th ed.; Knipe, D.M., Howley, P.M., Eds.; Lippincott Williams & Wilkins: Philadelphia, PA, USA, 2007; pp. 1601–1646.
- Nair, H.; Nokes, D.J.; Gessner, B.D.; Dherani, M.; Madhi, S.A.; Singleton, R.J.; O'Brien, K.L.; Roca, A.; Wright, P.F.; Bruce, N.; et al. Global burden of acute lower respiratory infections due to respiratory syncytial virus in young children: A systematic review and meta-analysis. *Lancet* **2010**, *375*, 1545–1555. [[CrossRef](#)]
- Wang, X.; Li, Y.; Deloria-Knoll, M.; Madhi, S.A.; Cohen, C.; Arguelles, V.L.; Basnet, S.; Bassat, Q.; Brooks, W.A.; Echavarría, M.; et al. Global burden of acute lower respiratory infection associated with human parainfluenza virus in children younger than 5 years for 2018: A systematic review and meta-analysis. *Lancet Glob. Health* **2021**, *9*, e1077–e1087. [[CrossRef](#)]
- van den Hoogen, B.G.; Osterhaus, D.M.; Fouchier, R.A. Clinical impact and diagnosis of human metapneumovirus infection. *Pediatr. Infect. Dis. J.* **2004**, *23* (Suppl. S1), 25–32. [[CrossRef](#)]
- Shi, T.; McAllister, D.A.; O'Brien, K.L.; Simoes, E.A.F.; Madhi, S.A.; Gessner, B.D.; Polack, F.P.; Balsells, E.; Acacio, S.; Aguayo, C.; et al. Global, regional, and national disease burden estimates of acute lower respiratory infections due to respiratory syncytial virus in young children in 2015: A systematic review and modelling study. *Lancet* **2017**, *390*, 946–958. [[CrossRef](#)]
- Pneumonia Etiology Research for Child Health (PERCH) Study Group. Causes of severe pneumonia requiring hospital admission in children without HIV infection from Africa and Asia: The PERCH multi-country case-control study. *Lancet* **2019**, *394*, 757–779.
- Phillips, M.; Finelli, L.; Saiman, L.; Wang, C.; Choi, Y.; Patel, J. Respiratory Syncytial Virus-associated Acute Otitis Media in Infants and Children. *J. Pediatric Infect. Dis. Soc.* **2020**, *9*, 544–550. [[CrossRef](#)]
- Shi, T.; Ooi, Y.; Zaw, E.M.; Utjesanovic, N.; Campbell, H.; Cunningham, S.; Bont, L.; Nair, H.; Investigators, R. Association Between Respiratory Syncytial Virus-Associated Acute Lower Respiratory Infection in Early Life and Recurrent Wheeze and Asthma in Later Childhood. *J. Infect. Dis.* **2020**, *222* (Suppl. 7), 628–633. [[CrossRef](#)]
- Papenburg, J.; Alghounaim, M. Unraveling the Pneumonia Burden Associated with Human Metapneumovirus Infection. *Clin. Infect. Dis.* **2021**, *72*, 118–120. [[CrossRef](#)]
- van den Hoogen, B.G.; de Jong, J.C.; Groen, J.; Kuiken, T.; de Groot, R.; Fouchier, R.A.; Osterhaus, A.D. A newly discovered human pneumovirus isolated from young children with respiratory tract disease. *Nat. Med.* **2001**, *7*, 719–724. [[CrossRef](#)] [[PubMed](#)]
- de Graaf, M.; Osterhaus, A.; Fouchier, R.A.M.; Holmes, E.C. Evolutionary dynamics of human and avian metapneumoviruses. *J. Gen. Virol.* **2008**, *89*, 2933–2942. [[CrossRef](#)]
- Falsey, A.R.; Hennessey, P.A.; Formica, M.A.; Cox, C.; Walsh, E.E. Respiratory syncytial virus infection in elderly and high-risk adults. *N. Engl. J. Med.* **2005**, *352*, 1749–1759. [[CrossRef](#)] [[PubMed](#)]
- Asner, S.; Stephens, D.; Pedulla, P.; Richardson, S.E.; Robinson, J.; Allen, U. Risk factors and outcomes for respiratory syncytial virus-related infections in immunocompromised children. *Pediatr. Infect. Dis. J.* **2013**, *32*, 1073–1076. [[CrossRef](#)] [[PubMed](#)]
- Thompson, W.W.; Shay, D.K.; Weintraub, E.; Brammer, L.; Cox, N.; Anderson, L.J.; Fukuda, K. Mortality associated with influenza and respiratory syncytial virus in the United States. *JAMA* **2003**, *289*, 179–186. [[CrossRef](#)] [[PubMed](#)]

19. Shah, J.N.; Chemaly, R.F. Management of RSV infections in adult recipients of hematopoietic stem cell transplantation. *Blood* **2011**, *117*, 2755–2763. [[CrossRef](#)]
20. Uddin, S.; Thomas, M. *Human Metapneumovirus*; StatPearls: Treasure Island, FL, USA, 2021.
21. Cowling, B.J.; Ali, S.T.; Ng, T.W.Y.; Tsang, T.K.; Li, J.C.M.; Fong, M.W.; Liao, Q.; Kwan, M.Y.; Lee, S.L.; Chiu, S.S.; et al. Impact assessment of non-pharmaceutical interventions against coronavirus disease 2019 and influenza in Hong Kong: An observational study. *Lancet Public Health* **2020**, *5*, e279–e288. [[CrossRef](#)]
22. Foley, D.A.; Phuong, L.K.; Peplinski, J.; Lim, S.M.; Lee, W.H.; Farhat, A.; Minney-Smith, C.A.; Martin, A.C.; Mace, A.O.; Sikazwe, C.T.; et al. Examining the interseasonal resurgence of respiratory syncytial virus in Western Australia. *Arch. Dis. Child.* **2021**, 1–7. [[CrossRef](#)]
23. Agha, R.; Avner, J.R. Delayed Seasonal RSV Surge Observed During the COVID-19 Pandemic. *Pediatrics* **2021**, *148*, e2021052089. [[CrossRef](#)] [[PubMed](#)]
24. Ujiiie, M.; Tsuzuki, S.; Nakamoto, T.; Iwamoto, N. Resurgence of Respiratory Syncytial Virus Infections during COVID-19 Pandemic, Tokyo, Japan. *Emerg. Infect. Dis.* **2021**, *27*, 2969–2970. [[CrossRef](#)]
25. Di Mattia, G.; Nenna, R.; Mancino, E.; Rizzo, V.; Pierangeli, A.; Villani, A.; Midulla, F. During the COVID-19 pandemic where has respiratory syncytial virus gone? *Pediatr. Pulmonol.* **2021**, *56*, 3106–3109. [[CrossRef](#)] [[PubMed](#)]
26. Easton, A.J.; Domachowski, J.B.; Rosenberg, H.F. Animal pneumoviruses: Molecular genetics and pathogenesis. *Clin. Microbiol. Rev* **2004**, *17*, 390–412. [[CrossRef](#)]
27. Valarcher, J.F.; Taylor, G. Bovine respiratory syncytial virus infection. *Vet. Res.* **2007**, *38*, 153–180. [[CrossRef](#)]
28. Giovanardi, D.; Lupini, C.; Pesente, P.; Rossi, G.; Ortali, G.; Catelli, E. Longitudinal field studies of avian metapneumovirus and turkey hemorrhagic enteritis virus in turkeys suffering from colibacillosis associated mortality. *Vet. Res. Commun.* **2014**, *38*, 129–137. [[CrossRef](#)]
29. Makoschey, B.; Berge, A.C. Review on bovine respiratory syncytial virus and bovine parainfluenza—Usual suspects in bovine respiratory disease—A narrative review. *BMC Vet. Res.* **2021**, *17*, 261. [[CrossRef](#)] [[PubMed](#)]
30. Richard, C.A.; Hervet, C.; Menard, D.; Gutsche, I.; Normand, V.; Renois, F.; Meurens, F.; Eleouet, J.F. First demonstration of the circulation of a pneumovirus in French pigs by detection of anti-swine orthopneumovirus nucleoprotein antibodies. *Vet. Res.* **2018**, *49*, 118. [[CrossRef](#)]
31. Ellis, J.A. How efficacious are vaccines against bovine respiratory syncytial virus in cattle? *Vet. Microbiol.* **2017**, *206*, 59–68. [[CrossRef](#)]
32. Valarcher, J.F.; Hagglund, S.; Naslund, K.; Jouneau, L.; Malmstrom, E.; Boulesteix, O.; Pinard, A.; Leguere, D.; Deslis, A.; Gauthier, D.; et al. Single-Shot Vaccines against Bovine Respiratory Syncytial Virus (BRSV): Comparative Evaluation of Long-Term Protection after Immunization in the Presence of BRSV-Specific Maternal Antibodies. *Vaccines* **2021**, *9*, 236. [[CrossRef](#)]
33. Sun, J.; Wei, Y.; Rauf, A.; Zhang, Y.; Ma, Y.; Zhang, X.; Shilo, K.; Yu, Q.; Saif, Y.M.; Lu, X.; et al. Methyltransferase-defective avian metapneumovirus vaccines provide complete protection against challenge with the homologous Colorado strain and the heterologous Minnesota strain. *J. Virol.* **2014**, *88*, 12348–12363. [[CrossRef](#)]
34. Ball, C.; Forrester, A.; Herrmann, A.; Lemiere, S.; Ganapathy, K. Comparative protective immunity provided by live vaccines of Newcastle disease virus or avian metapneumovirus when co-administered alongside classical and variant strains of infectious bronchitis virus in day-old broiler chicks. *Vaccine* **2019**, *37*, 7566–7575. [[CrossRef](#)]
35. Collins, P.L.; Melero, J.A. Progress in understanding and controlling respiratory syncytial virus: Still crazy after all these years. *Virus Res.* **2011**, *162*, 80–99. [[CrossRef](#)] [[PubMed](#)]
36. Cockerill, G.S.; Good, J.A.D.; Mathews, N. State of the Art in Respiratory Syncytial Virus Drug Discovery and Development. *J. Med. Chem.* **2019**, *62*, 3206–3227. [[CrossRef](#)]
37. Detalle, L.; Stohr, T.; Palomo, C.; Piedra, P.A.; Gilbert, B.E.; Mas, V.; Millar, A.; Power, U.F.; Stortelers, C.; Allosery, K.; et al. Generation and Characterization of ALX-0171, a Potent Novel Therapeutic Nanobody for the Treatment of Respiratory Syncytial Virus Infection. *Antimicrob. Agents Chemother.* **2015**, *60*, 6–13. [[CrossRef](#)] [[PubMed](#)]
38. Stevens, M.; Rusch, S.; DeVincenzo, J.; Kim, Y.I.; Harrison, L.; Meals, E.A.; Boyers, A.; Fok-Seang, J.; Huntjens, D.; Lounis, N.; et al. Antiviral Activity of Oral JNJ-53718678 in Healthy Adult Volunteers Challenged With Respiratory Syncytial Virus: A Placebo-Controlled Study. *J. Infect. Dis.* **2018**, *218*, 748–756. [[CrossRef](#)] [[PubMed](#)]
39. Cockerill, G.S. JNJ-5371678, Defining a Role for Fusion Inhibitors in the Treatment of Respiratory Syncytial Virus. *J. Med. Chem.* **2020**, *63*, 8043–8045. [[CrossRef](#)] [[PubMed](#)]
40. DeVincenzo, J.P.; Whitley, R.J.; Mackman, R.L.; Scaglioni-Weinlich, C.; Harrison, L.; Farrell, E.; McBride, S.; Lambkin-Williams, R.; Jordan, R.; Xin, Y.; et al. Oral GS-5806 activity in a respiratory syncytial virus challenge study. *New Engl. J. Med.* **2014**, *371*, 711–722. [[CrossRef](#)]
41. DeVincenzo, J.P.; McClure, M.W.; Symons, J.A.; Fathi, H.; Westland, C.; Chanda, S.; Lambkin-Williams, R.; Smith, P.; Zhang, Q.; Beigelman, L.; et al. Activity of Oral ALS-008176 in a Respiratory Syncytial Virus Challenge Study. *New Engl. J. Med.* **2015**, *373*, 2048–2058. [[CrossRef](#)]
42. Wang, G.; Deval, J.; Hong, J.; Dyatkina, N.; Prhavic, M.; Taylor, J.; Fung, A.; Jin, Z.; Stevens, S.K.; Serebryany, V.; et al. Discovery of 4'-chloromethyl-2'-deoxy-3',5'-di-O-isobutyryl-2'-fluorocytidine (ALS-8176), a first-in-class RSV polymerase inhibitor for treatment of human respiratory syncytial virus infection. *J. Med. Chem.* **2015**, *58*, 1862–1878. [[CrossRef](#)]

43. Chemaly, R.F.; Dadwal, S.S.; Bergeron, A.; Ljungman, P.; Kim, Y.J.; Cheng, G.S.; Pipavath, S.N.; Limaye, A.P.; Blanchard, E.; Winston, D.J.; et al. A Phase 2, Randomized, Double-blind, Placebo-Controlled Trial of Presatovir for the Treatment of Respiratory Syncytial Virus Upper Respiratory Tract Infection in Hematopoietic-Cell Transplant Recipients. *Clin. Infect. Dis.* **2020**, *71*, 2777–2786. [[CrossRef](#)]
44. Marty, F.M.; Chemaly, R.F.; Mullane, K.M.; Lee, D.G.; Hirsch, H.H.; Small, C.B.; Bergeron, A.; Shoham, S.; Ljungman, P.; Waghmare, A.; et al. A Phase 2b, Randomized, Double-blind, Placebo-Controlled Multicenter Study Evaluating Antiviral Effects, Pharmacokinetics, Safety, and Tolerability of Presatovir in Hematopoietic Cell Transplant Recipients with Respiratory Syncytial Virus Infection of the Lower Respiratory Tract. *Clin. Infect. Dis.* **2020**, *71*, 2787–2795. [[PubMed](#)]
45. Kiss, G.; Holl, J.M.; Williams, G.M.; Alonas, E.; Vanover, D.; Lifland, A.W.; Gudheti, M.; Guerrero-Ferreira, R.C.; Nair, V.; Yi, H.; et al. Structural analysis of respiratory syncytial virus reveals the position of M2-1 between the matrix protein and the ribonucleoprotein complex. *J. Virol.* **2014**, *88*, 7602–7617. [[CrossRef](#)]
46. Jeffree, C.E.; Rixon, H.W.; Brown, G.; Aitken, J.; Sugrue, R.J. Distribution of the attachment (G) glycoprotein and GM1 within the envelope of mature respiratory syncytial virus filaments revealed using field emission scanning electron microscopy. *Virology* **2003**, *306*, 254–267. [[CrossRef](#)]
47. Ke, Z.; Dillard, R.S.; Chirkova, T.; Leon, F.; Stobart, C.C.; Hampton, C.M.; Strauss, J.D.; Rajan, D.; Rostad, C.A.; Taylor, J.V.; et al. The Morphology and Assembly of Respiratory Syncytial Virus Revealed by Cryo-Electron Tomography. *Viruses* **2018**, *10*, 446. [[CrossRef](#)]
48. Thornhill, E.M.; Verhoeven, D. Respiratory Syncytial Virus’s Non-structural Proteins: Masters of Interference. *Front. Cell Infect. Microbiol.* **2020**, *10*, 225. [[CrossRef](#)]
49. Sedeyn, K.; Schepens, B.; Saelens, X. Respiratory syncytial virus nonstructural proteins 1 and 2: Exceptional disrupters of innate immune responses. *PLoS Pathog.* **2019**, *15*, e1007984. [[CrossRef](#)]
50. Carter, S.D.; Dent, K.C.; Atkins, E.; Foster, T.L.; Verow, M.; Gorny, P.; Harris, M.; Hiscox, J.A.; Ranson, N.A.; Griffin, S.; et al. Direct visualization of the small hydrophobic protein of human respiratory syncytial virus reveals the structural basis for membrane permeability. *FEBS Lett.* **2010**, *584*, 2786–2790. [[CrossRef](#)]
51. Russell, R.F.; McDonald, J.U.; Ivanova, M.; Zhong, Z.; Bukreyev, A.; Tregoning, J.S. Partial Attenuation of Respiratory Syncytial Virus with a Deletion of a Small Hydrophobic Gene Is Associated with Elevated Interleukin-1beta Responses. *J. Virol.* **2015**, *89*, 8974–8981. [[CrossRef](#)] [[PubMed](#)]
52. Russell, C.D.; Unger, S.A.; Walton, M.; Schwarze, J. The Human Immune Response to Respiratory Syncytial Virus Infection. *Clin. Microbiol. Rev.* **2017**, *30*, 481–502. [[CrossRef](#)]
53. Fearn, R.; Plemper, R.K. Polymerases of paramyxoviruses and pneumoviruses. *Virus Res.* **2017**, *234*, 87–102. [[CrossRef](#)] [[PubMed](#)]
54. Collins, P.L.; Hill, M.G.; Camargo, E.; Grosfeld, H.; Chanock, R.M.; Murphy, B.R. Production of infectious human respiratory syncytial virus from cloned cDNA confirms an essential role for the transcription elongation factor from the 5′ proximal open reading frame of the M2 mRNA in gene expression and provides a capability for vaccine development. *Proc. Natl. Acad. Sci. USA* **1995**, *92*, 11563–11567.
55. Fearn, R.; Collins, P.L. Role of the M2-1 transcription antitermination protein of respiratory syncytial virus in sequential transcription. *J. Virol.* **1999**, *73*, 5852–5864. [[CrossRef](#)]
56. Buchholz, U.J.; Biacchesi, S.; Pham, Q.N.; Tran, K.C.; Yang, L.; Luongo, C.L.; Skiadopoulos, M.H.; Murphy, B.R.; Collins, P.L. Deletion of M2 gene open reading frames 1 and 2 of human metapneumovirus: Effects on RNA synthesis, attenuation, and immunogenicity. *J. Virol.* **2005**, *79*, 6588–6597. [[CrossRef](#)] [[PubMed](#)]
57. Rincheval, V.; Lelek, M.; Gault, E.; Bouillier, C.; Sitterlin, D.; Blouquit-Laye, S.; Galloux, M.; Zimmer, C.; Eleouet, J.F.; Rameix-Welti, M.A. Functional organization of cytoplasmic inclusion bodies in cells infected by respiratory syncytial virus. *Nat. Commun.* **2017**, *8*, 563. [[CrossRef](#)] [[PubMed](#)]
58. Dolnik, O.; Gerresheim, G.K.; Biedenkopf, N. New Perspectives on the Biogenesis of Viral Inclusion Bodies in Negative-Sense RNA Virus Infections. *Cells* **2021**, *10*, 1460. [[CrossRef](#)]
59. Lopez, N.; Camporeale, G.; Salgueiro, M.; Borkosky, S.S.; Visentin, A.; Peralta-Martinez, R.; Loureiro, M.E.; de Prat-Gay, G. Deconstructing virus condensation. *PLoS Pathog.* **2021**, *17*, e1009926. [[CrossRef](#)]
60. Garcia, J.; Garcia-Barreno, B.; Vivo, A.; Melero, J.A. Cytoplasmic inclusions of respiratory syncytial virus-infected cells: Formation of inclusion bodies in transfected cells that coexpress the nucleoprotein, the phosphoprotein, and the 22K protein. *Virology* **1993**, *195*, 243–247. [[CrossRef](#)]
61. Derdowski, A.; Peters, T.R.; Glover, N.; Qian, R.; Utley, T.J.; Burnett, A.; Williams, J.V.; Spearman, P.; Crowe, J.E. Human metapneumovirus nucleoprotein and phosphoprotein interact and provide the minimal requirements for inclusion body formation. *J. Gen. Virol.* **2008**, *89*, 2698–2708. [[CrossRef](#)]
62. Weber, E.; Humbert, B.; Streckert, H.J.; Werchau, H. Nonstructural protein 2 (NS2) of respiratory syncytial virus (RSV) detected by an antipeptide serum. *Respiration* **1995**, *62*, 27–33. [[CrossRef](#)] [[PubMed](#)]
63. Ghildyal, R.; Mills, J.; Murray, M.; Vardaxis, N.; Meanger, J. Respiratory syncytial virus matrix protein associates with nucleocapsids in infected cells. *J. Gen. Virol.* **2002**, *83*, 753–757. [[CrossRef](#)]
64. Bajorek, M.; Galloux, M.; Richard, C.A.; Szekely, O.; Rosenzweig, R.; Sizun, C.; Eleouet, J.F. Tetramerization of Phosphoprotein is Essential for Respiratory Syncytial Virus Budding while its N Terminal Region Mediates Direct Interactions with the Matrix Protein. *J. Virol.* **2021**, *95*, e02217-20. [[CrossRef](#)]



65. Richard, C.A.; Rincheval, V.; Lassoued, S.; Fix, J.; Cardone, C.; Esneau, C.; Nekhai, S.; Galloux, M.; Rameix-Welti, M.A.; Sizun, C.; et al. RSV hijacks cellular protein phosphatase 1 to regulate M2-1 phosphorylation and viral transcription. *PLoS Pathog.* **2018**, *14*, e1006920. [[CrossRef](#)] [[PubMed](#)]
66. Fricke, J.; Koo, L.Y.; Brown, C.R.; Collins, P.L. p38 and OGT sequestration into viral inclusion bodies in cells infected with human respiratory syncytial virus suppresses MK2 activities and stress granule assembly. *J. Virol.* **2013**, *87*, 1333–1347. [[CrossRef](#)]
67. Lifland, A.W.; Jung, J.; Alonas, E.; Zurla, C.; Crowe, J.E., Jr.; Santangelo, P.J. Human respiratory syncytial virus nucleoprotein and inclusion bodies antagonize the innate immune response mediated by MDA5 and MAVS. *J. Virol.* **2012**, *86*, 8245–8258. [[CrossRef](#)]
68. Jobe, F.; Simpson, J.; Hawes, P.; Guzman, E.; Bailey, D. Respiratory Syncytial Virus Sequesters NF-kappaB Subunit p65 to Cytoplasmic Inclusion Bodies To Inhibit Innate Immune Signaling. *J. Virol.* **2020**, *94*, e01380-20. [[CrossRef](#)] [[PubMed](#)]
69. Gilman, M.S.A.; Liu, C.; Fung, A.; Behera, I.; Jordan, P.; Rigaux, P.; Ysebaert, N.; Tcherniuk, S.; Sourimant, J.; Eleouet, J.F.; et al. Structure of the Respiratory Syncytial Virus Polymerase Complex. *Cell* **2019**, *179*, 193–204 e14. [[CrossRef](#)] [[PubMed](#)]
70. Pan, J.; Qian, X.; Lattmann, S.; El Sahili, A.; Yeo, T.H.; Jia, H.; Cressey, T.; Ludeke, B.; Noton, S.; Kalocsay, M.; et al. Structure of the human metapneumovirus polymerase phosphoprotein complex. *Nature* **2020**, *577*, 275–279. [[CrossRef](#)]
71. Sutto-Ortiz, P.; Tcherniuk, S.; Ysebaert, N.; Abeywickrema, P.; Noel, M.; Decombe, A.; Debart, F.; Vasseur, J.J.; Canard, B.; Roymans, D.; et al. The methyltransferase domain of the Respiratory Syncytial Virus L protein catalyzes cap N7 and 2'-O-methylation. *PLoS Pathog.* **2021**, *17*, e1009562. [[CrossRef](#)]
72. Garcia, J.; Garcia-Barreno, B.; Martinez, I.; Melero, J.A. Mapping of monoclonal antibody epitopes of the human respiratory syncytial virus p protein. *Virology* **1993**, *195*, 239–242. [[CrossRef](#)] [[PubMed](#)]
73. Galloux, M.; Risso-Ballester, J.; Richard, C.A.; Fix, J.; Rameix-Welti, M.A.; Eleouet, J.F. Minimal Elements Required for the Formation of Respiratory Syncytial Virus Cytoplasmic Inclusion Bodies In Vivo and In Vitro. *mBio* **2020**, *11*, e01202-20. [[CrossRef](#)] [[PubMed](#)]
74. Banani, S.F.; Lee, H.O.; Hyman, A.A.; Rosen, M.K. Biomolecular condensates: Organizers of cellular biochemistry. *Nat. Rev. Mol. Cell Biol.* **2017**, *18*, 285–298. [[CrossRef](#)]
75. Elbaum-Garfinkle, S.; Kim, Y.; Szczepaniak, K.; Chen, C.C.; Eckmann, C.R.; Myong, S.; Brangwynne, C.P. The disordered P granule protein LAF-1 drives phase separation into droplets with tunable viscosity and dynamics. *Proc. Natl. Acad. Sci. USA* **2015**, *112*, 7189–7194. [[CrossRef](#)] [[PubMed](#)]
76. Nott, T.J.; Petsalaki, E.; Farber, P.; Jervis, D.; Fussner, E.; Plochowitz, A.; Craggs, T.D.; Bazett-Jones, D.P.; Pawson, T.; Forman-Kay, J.D.; et al. Phase transition of a disordered nuage protein generates environmentally responsive membraneless organelles. *Mol. Cell* **2015**, *57*, 936–947. [[CrossRef](#)] [[PubMed](#)]
77. Castagne, N.; Barbier, A.; Bernard, J.; Rezaei, H.; Huet, J.C.; Henry, C.; Da Costa, B.; Eleouet, J.F. Biochemical characterization of the respiratory syncytial virus P-P and P-N protein complexes and localization of the P protein oligomerization domain. *J. Gen. Virol.* **2004**, *85*, 1643–1653. [[CrossRef](#)]
78. Llorente, M.T.; Garcia-Barreno, B.; Calero, M.; Camafeita, E.; Lopez, J.A.; Longhi, S.; Ferron, F.; Varela, P.F.; Melero, J.A. Structural analysis of the human respiratory syncytial virus phosphoprotein: Characterization of an alpha-helical domain involved in oligomerization. *J. Gen. Virol.* **2006**, *87*, 159–169. [[CrossRef](#)]
79. Llorente, M.T.; Taylor, I.A.; Lopez-Vinas, E.; Gomez-Puertas, P.; Calder, L.J.; Garcia-Barreno, B.; Melero, J.A. Structural properties of the human respiratory syncytial virus P protein: Evidence for an elongated homotetrameric molecule that is the smallest orthologue within the family of paramyxovirus polymerase cofactors. *Proteins* **2008**, *72*, 946–958. [[CrossRef](#)]
80. Simabuco, F.M.; Asara, J.M.; Guerrero, M.C.; Libermann, T.A.; Zerbini, L.F.; Ventura, A.M. Structural analysis of human respiratory syncytial virus p protein: Identification of intrinsically disordered domains. *Braz. J. Microbiol.* **2011**, *42*, 340–345. [[CrossRef](#)]
81. Renner, M.; Paesen, G.C.; Grison, C.M.; Granier, S.; Grimes, J.M.; Leyrat, C. Structural dissection of human metapneumovirus phosphoprotein using small angle x-ray scattering. *Sci. Rep.* **2017**, *7*, 14865. [[CrossRef](#)]
82. Di Tommaso, P.; Moretti, S.; Xenarios, I.; Orobittg, M.; Montanyola, A.; Chang, J.M.; Taly, J.F.; Notredame, C. T-Coffee: A web server for the multiple sequence alignment of protein and RNA sequences using structural information and homology extension. *Nucleic Acids Res.* **2011**, *39*, W13–W17. [[CrossRef](#)] [[PubMed](#)]
83. Pereira, N.; Cardone, C.; Lassoued, S.; Galloux, M.; Fix, J.; Assrir, N.; Lescop, E.; Bontems, F.; Eleouet, J.F.; Sizun, C. New Insights into Structural Disorder in Human Respiratory Syncytial Virus Phosphoprotein and Implications for Binding of Protein Partners. *J. Biol. Chem.* **2017**, *292*, 2120–2131. [[CrossRef](#)]
84. Cardone, C.; Caseau, C.M.; Bardiaux, B.; Thureau, A.; Galloux, M.; Bajorek, M.; Eleouet, J.F.; Litaudon, M.; Bontems, F.; Sizun, C. A Structural and Dynamic Analysis of the Partially Disordered Polymerase-Binding Domain in RSV Phosphoprotein. *Biomolecules* **2021**, *11*, 1225. [[CrossRef](#)]
85. Cardone, C.; Caseau, C.M.; Pereira, N.; Sizun, C. Pneumoviral Phosphoprotein, a Multidomain Adaptor-Like Protein of Apparent Low Structural Complexity and High Conformational Versatility. *Int. J. Mol. Sci.* **2021**, *22*, 1537. [[CrossRef](#)]
86. Esperante, S.A.; Paris, G.; de Prat-Gay, G. Modular unfolding and dissociation of the human respiratory syncytial virus phosphoprotein p and its interaction with the m(2-1) antiterminator: A singular tetramer-tetramer interface arrangement. *Biochemistry* **2012**, *51*, 8100–8110. [[CrossRef](#)] [[PubMed](#)]
87. Renner, M.; Bertinelli, M.; Leyrat, C.; Paesen, G.C.; Saraiva de Oliveira, L.F.; Huisken, J.T.; Grimes, J.M. Nucleocapsid assembly in pneumoviruses is regulated by conformational switching of the N protein. *eLife* **2016**, *5*, e12627. [[CrossRef](#)] [[PubMed](#)]

88. Selvaraj, M.; Yegambaram, K.; Todd, E.; Richard, C.A.; Dods, R.L.; Pangratiou, G.M.; Trinh, C.H.; Moul, S.L.; Murphy, J.C.; Mankouri, J.; et al. The Structure of the Human Respiratory Syncytial Virus M2-1 Protein Bound to the Interaction Domain of the Phosphoprotein P Defines the Orientation of the Complex. *mBio* **2018**, *9*, e01554-18. [[CrossRef](#)] [[PubMed](#)]
89. Tran, T.L.; Castagne, N.; Bhella, D.; Varela, P.F.; Bernard, J.; Chilmonczyk, S.; Berkenkamp, S.; Benhamo, V.; Grznarova, K.; Grosclaude, J.; et al. The nine C-terminal amino acids of the respiratory syncytial virus protein P are necessary and sufficient for binding to ribonucleoprotein complexes in which six ribonucleotides are contacted per N protein protomer. *J. Gen. Virol.* **2007**, *88*, 196–206. [[CrossRef](#)]
90. Galloux, M.; Tarus, B.; Blazevic, I.; Fix, J.; Duquerroy, S.; Eleouet, J.F. Characterization of a viral phosphoprotein binding site on the surface of the respiratory syncytial nucleoprotein. *J. Virol.* **2012**, *86*, 8375–8387. [[CrossRef](#)] [[PubMed](#)]
91. Ouizougoun-Oubari, M.; Pereira, N.; Tarus, B.; Galloux, M.; Lassoued, S.; Fix, J.; Tortorici, M.A.; Hoos, S.; Baron, B.; England, P.; et al. A Druggable Pocket at the Nucleocapsid/Phosphoprotein Interaction Site of Human Respiratory Syncytial Virus. *J. Virol.* **2015**, *89*, 11129–11143. [[CrossRef](#)]
92. Navarro, J.; Lopez-Otin, C.; Villanueva, N. Location of phosphorylated residues in human respiratory syncytial virus phosphoprotein. *J. Gen. Virol.* **1991**, *72*, 1455–1459. [[CrossRef](#)]
93. Asenjo, A.; Rodriguez, L.; Villanueva, N. Determination of phosphorylated residues from human respiratory syncytial virus P protein that are dynamically dephosphorylated by cellular phosphatases: A possible role for serine 54. *J. Gen. Virol.* **2005**, *86*, 1109–1120. [[CrossRef](#)]
94. Mazumder, B.; Barik, S. Requirement of casein kinase II-mediated phosphorylation for the transcriptional activity of human respiratory syncytial viral phosphoprotein P: Transdominant negative phenotype of phosphorylation-defective P mutants. *Virology* **1994**, *205*, 104–111. [[CrossRef](#)] [[PubMed](#)]
95. Villanueva, N.; Hardy, R.; Asenjo, A.; Yu, Q.; Wertz, G. The bulk of the phosphorylation of human respiratory syncytial virus phosphoprotein is not essential but modulates viral RNA transcription and replication. *J. Gen. Virol.* **2000**, *81*, 129–133. [[CrossRef](#)]
96. Lu, B.; Ma, C.H.; Brazas, R.; Jin, H. The major phosphorylation sites of the respiratory syncytial virus phosphoprotein are dispensable for virus replication in vitro. *J. Virol.* **2002**, *76*, 10776–10784. [[CrossRef](#)] [[PubMed](#)]
97. Asenjo, A.; Gonzalez-Armas, J.C.; Villanueva, N. Phosphorylation of human respiratory syncytial virus P protein at serine 54 regulates viral uncoating. *Virology* **2008**, *380*, 26–33. [[CrossRef](#)]
98. Shapiro, A.B.; Gao, N.; O’Connell, N.; Hu, J.; Thresher, J.; Gu, R.F.; Overman, R.; Hardern, I.M.; Sproat, G.G. Quantitative investigation of the affinity of human respiratory syncytial virus phosphoprotein C-terminus binding to nucleocapsid protein. *Virol. J.* **2014**, *11*, 191. [[CrossRef](#)]
99. Tawar, R.G.; Duquerroy, S.; Vonrhein, C.; Varela, P.F.; Damier-Piolle, L.; Castagne, N.; MacLellan, K.; Bedouelle, H.; Bricogne, G.; Bhella, D.; et al. Crystal structure of a nucleocapsid-like nucleoprotein-RNA complex of respiratory syncytial virus. *Science* **2009**, *326*, 1279–1283. [[CrossRef](#)]
100. Goddard, T.D.; Huang, C.C.; Meng, E.C.; Pettersen, E.F.; Couch, G.S.; Morris, J.H.; Ferrin, T.E. UCSF ChimeraX: Meeting modern challenges in visualization and analysis. *Protein Sci.* **2018**, *27*, 14–25. [[CrossRef](#)] [[PubMed](#)]
101. Conley, M.J.; Short, J.M.; Hutchings, J.; Burns, A.M.; Streetley, J.; Bakker, S.E.; Jaffery, H.; Stewart, M.; Power, J.; Zanetti, G.; et al. Helical Ordering of Envelope Associated Proteins and Glycoproteins in Respiratory Syncytial Virus Filamentous Virions. *bioRxiv* **2021**. [[CrossRef](#)]
102. Bakker, S.E.; Duquerroy, S.; Galloux, M.; Loney, C.; Conner, E.; Eleouet, J.F.; Rey, F.A.; Bhella, D. The respiratory syncytial virus nucleoprotein-RNA complex forms a left-handed helical nucleocapsid. *J. Gen. Virol.* **2013**, *94*, 1734–1738. [[CrossRef](#)]
103. Liljeroos, L.; Krzyzaniak, M.A.; Helenius, A.; Butcher, S.J. Architecture of respiratory syncytial virus revealed by electron cryotomography. *Proc. Natl. Acad. Sci. USA* **2013**, *110*, 11133–11138. [[CrossRef](#)]
104. Pettersen, E.F.; Goddard, T.D.; Huang, C.C.; Couch, G.S.; Greenblatt, D.M.; Meng, E.C.; Ferrin, T.E. UCSF Chimera—a visualization system for exploratory research and analysis. *J. Comput. Chem.* **2004**, *25*, 1605–1612. [[CrossRef](#)]
105. Kaul, T.N.; Middleton, E., Jr.; Ogra, P.L. Antiviral effect of flavonoids on human viruses. *J. Med. Virol.* **1985**, *15*, 71–79. [[CrossRef](#)]
106. Sa, J.M.; Piloto, J.V.; Cilli, E.M.; Tasic, L.; Fossey, M.A.; Almeida, F.C.L.; Souza, F.P.; Caruso, I.P. Hesperetin targets the hydrophobic pocket of the nucleoprotein/phosphoprotein binding site of human respiratory syncytial virus. *J. Biomol. Struct. Dyn.* **2020**, *20*, 1–13. [[CrossRef](#)]
107. Chapman, J.; Abbott, E.; Alber, D.G.; Baxter, R.C.; Bithell, S.K.; Henderson, E.A.; Carter, M.C.; Chambers, P.; Chubb, A.; Cockerill, G.S.; et al. RSV604, a novel inhibitor of respiratory syncytial virus replication. *Antimicrob. Agents Chemother.* **2007**, *51*, 3346–3353. [[CrossRef](#)] [[PubMed](#)]
108. Henderson, E.A.; Alber, D.G.; Baxter, R.C.; Bithell, S.K.; Budworth, J.; Carter, M.C.; Chubb, A.; Cockerill, G.S.; Dowdell, V.C.; Fraser, I.J.; et al. 1,4-benzodiazepines as inhibitors of respiratory syncytial virus. The identification of a clinical candidate. *J. Med. Chem.* **2007**, *50*, 1685–1692. [[CrossRef](#)]
109. Challa, S.; Scott, A.D.; Yuzhakov, O.; Zhou, Y.; Tiong-Yip, C.L.; Gao, N.; Thresher, J.; Yu, Q. Mechanism of Action for Respiratory Syncytial Virus Inhibitor RSV604. *Antimicrob. Agents Chemother.* **2015**, *59*, 1080–1087. [[CrossRef](#)]
110. Rhodin, M.H.J.; McAllister, N.V.; Castillo, J.; Noton, S.L.; Fearn, R.; Kim, I.J.; Yu, J.M.; Blaisdell, T.P.; Panarese, J.; Shook, B.C.; et al. EDP-938, a novel nucleoprotein inhibitor of respiratory syncytial virus, demonstrates potent antiviral activities in vitro and in a non-human primate model. *PLoS Pathog.* **2021**, *17*, e1009428. [[CrossRef](#)] [[PubMed](#)]

111. Hara, K.; Yaita, K.; Khamrin, P.; Kumthip, K.; Kashiwagi, T.; Eleouet, J.F.; Rameix-Welti, M.A.; Watanabe, H. A small fragmented P protein of respiratory syncytial virus inhibits virus infection by targeting P protein. *J. Gen. Virol.* **2020**, *101*, 21–32. [[CrossRef](#)]
112. Decool, H.; Bardiaux, B.; Checa Ruano, L.; Sperandio, O.; Fix, J.; Gutsche, I.; Richard, C.A.; Bajorek, M.; Eleouet, J.F.; Galloux, M. Characterization of the interaction domains between the phosphoprotein and the nucleoprotein of human Metapneumovirus. *J. Virol.* **2021**, JVI0090921. [[CrossRef](#)] [[PubMed](#)]
113. El Omari, K.; Scott, K.; Dhaliwal, B.; Ren, J.; Abrescia, N.G.A.; Budworth, J.; Lockyer, M.; Powell, K.L.; Hawkins, A.R.; Stammers, D.K. Crystallization and preliminary X-ray analysis of the human respiratory syncytial virus nucleocapsid protein. *Acta Crystallogr. Sect. F-Struct. Biol. Cryst. Comm.* **2008**, *64*, 1019–1023. [[CrossRef](#)]
114. Esneau, C.; Raynal, B.; Roblin, P.; Brule, S.; Richard, C.A.; Fix, J.; Eleouet, J.F.; Galloux, M. Biochemical characterization of the respiratory syncytial virus N(0)-P complex in solution. *J. Biol. Chem.* **2019**, *294*, 3647–3660. [[CrossRef](#)] [[PubMed](#)]
115. Galloux, M.; Gabiane, G.; Sourimant, J.; Richard, C.A.; England, P.; Moudjou, M.; Aumont-Nicaise, M.; Fix, J.; Rameix-Welti, M.A.; Eleouet, J.F. Identification and Characterization of the Binding Site of the Respiratory Syncytial Virus Phosphoprotein to RNA-Free Nucleoprotein. *J. Virol.* **2015**, *89*, 3484–3496. [[CrossRef](#)] [[PubMed](#)]
116. Karlin, D.; Belshaw, R. Detecting remote sequence homology in disordered proteins: Discovery of conserved motifs in the N-termini of Mononegavirales phosphoproteins. *PLoS ONE* **2012**, *7*, e31719.
117. Mallipeddi, S.K.; Lupiani, B.; Samal, S.K. Mapping the domains on the phosphoprotein of bovine respiratory syncytial virus required for N-P interaction using a two-hybrid system. *J. Gen. Virol.* **1996**, *77*, 1019–1023. [[CrossRef](#)] [[PubMed](#)]
118. Khattar, S.K.; Yunus, A.S.; Samal, S.K. Mapping the domains on the phosphoprotein of bovine respiratory syncytial virus required for N-P and P-L interactions using a minigenome system. *J. Gen. Virol.* **2001**, *82*, 775–779. [[CrossRef](#)]
119. Jamin, M.; Yabukarski, F. Nonsegmented Negative-Sense RNA Viruses-Structural Data Bring New Insights Into Nucleocapsid Assembly. *Adv. Virus Res.* **2017**, *97*, 143–185.
120. Leyrat, C.; Yabukarski, F.; Tarbouriech, N.; Ribeiro, E.A., Jr.; Jensen, M.R.; Blackledge, M.; Ruigrok, R.W.; Jamin, M. Structure of the vesicular stomatitis virus N(0)-P complex. *PLoS Pathog.* **2011**, *7*, e1002248. [[CrossRef](#)]
121. Yabukarski, F.; Lawrence, P.; Tarbouriech, N.; Bourhis, J.M.; Delaforge, E.; Jensen, M.R.; Ruigrok, R.W.; Blackledge, M.; Volchkov, V.; Jamin, M. Structure of Nipah virus unassembled nucleoprotein in complex with its viral chaperone. *Nat. Struct. Mol. Biol.* **2014**, *21*, 754–759. [[CrossRef](#)]
122. Guryanov, S.G.; Liljeroos, L.; Kasaragod, P.; Kajander, T.; Butcher, S.J. Crystal Structure of the Measles Virus Nucleoprotein Core in Complex with an N-Terminal Region of Phosphoprotein. *J. Virol.* **2015**, *90*, 2849–2857. [[CrossRef](#)]
123. Kirchdoerfer, R.N.; Abelson, D.M.; Li, S.; Wood, M.R.; Saphire, E.O. Assembly of the Ebola Virus Nucleoprotein from a Chaperoned VP35 Complex. *Cell Rep.* **2015**, *12*, 140–149. [[CrossRef](#)]
124. Zhu, T.; Song, H.; Peng, R.; Shi, Y.; Qi, J.; Gao, G.F. Crystal Structure of the Marburg Virus Nucleoprotein Core Domain Chaperoned by a VP35 Peptide Reveals a Conserved Drug Target for Filovirus. *J. Virol.* **2017**, *91*, e00996-17. [[CrossRef](#)]
125. Aggarwal, M.; Leser, G.P.; Kors, C.A.; Lamb, R.A. Structure of the Paramyxovirus Parainfluenza Virus 5 Nucleoprotein in Complex with an Amino-Terminal Peptide of the Phosphoprotein. *J. Virol.* **2018**, *92*, e01304-17. [[CrossRef](#)] [[PubMed](#)]
126. Galloux, M.; Gsponer, N.; Gaillard, V.; Fenner, B.; Larcher, T.; Vilotte, M.; Riviere, J.; Richard, C.A.; Eleouet, J.F.; Le Goffic, R.; et al. Targeting the Respiratory Syncytial Virus N-0-P Complex with Constrained alpha-Helical Peptides in Cells and Mice. *Antimicrob. Agents Chemother.* **2020**, *64*, e00717-20. [[CrossRef](#)] [[PubMed](#)]
127. Verdine, G.L.; Hilinski, G.J. Stapled peptides for intracellular drug targets. *Methods Enzymol.* **2012**, *503*, 3–33.
128. Kim, Y.W.; Grossmann, T.N.; Verdine, G.L. Synthesis of all-hydrocarbon stapled alpha-helical peptides by ring-closing olefin metathesis. *Nat. Protoc.* **2011**, *6*, 761–771. [[CrossRef](#)]
129. Bird, G.H.; Madani, N.; Perry, A.F.; Princiotta, A.M.; Supko, J.G.; He, X.; Gavathiotis, E.; Sodroski, J.G.; Walensky, L.D. Hydrocarbon double-stapling remedies the proteolytic instability of a lengthy peptide therapeutic. *Proc. Natl. Acad. Sci. USA* **2010**, *107*, 14093–14098. [[CrossRef](#)] [[PubMed](#)]
130. Bird, G.H.; Boyapalle, S.; Wong, T.; Opoku-Nsiah, K.; Bedi, R.; Crannell, W.C.; Perry, A.F.; Nguyen, H.; Sampayo, V.; Devareddy, A.; et al. Mucosal delivery of a double-stapled RSV peptide prevents nasopulmonary infection. *J. Clin. Investig.* **2014**, *124*, 2113–2124. [[CrossRef](#)]
131. Gaillard, V.; Galloux, M.; Garcin, D.; Eleouet, J.F.; Le Goffic, R.; Larcher, T.; Rameix-Welti, M.A.; Boukadiri, A.; Heritier, J.; Segura, J.M.; et al. A Short Double-Stapled Peptide Inhibits Respiratory Syncytial Virus Entry and Spreading. *Antimicrob. Agents Chemother.* **2017**, *61*, e02241-16. [[CrossRef](#)]

Article: Depletion of TAX1BP1 Amplifies Innate Immune Responses during Respiratory Syncytial Virus Infection

This paper includes work I have done on the study of the interaction between the RSV nucleoprotein and the cellular protein TAX1BP1.



1 **Depletion of TAX1BP1 amplifies innate immune responses during respiratory**  
2 **syncytial virus infection**

3

4 **Running title: Revealing the role of TAX1BP1 during RSV infection**

5

6 Delphyne Descamps<sup>1\*</sup>, Andressa Peres de Oliveira<sup>2</sup>, Lorène Gonnin<sup>1</sup>, Sarah Madrières<sup>1</sup>, Jenna Fix<sup>1</sup>,  
7 Carole Drajac<sup>1</sup>, Quentin Marquant<sup>1</sup>, Edwige Bouguyon<sup>1</sup>, Vincent Pietralunga<sup>1</sup>, Hidekatsu Iha<sup>4</sup>, Armando  
8 Morais Ventura<sup>2</sup>, Frédéric Tangy<sup>3</sup>, Pierre-Olivier Vidalain<sup>3,5</sup>, Jean-François Eléouët<sup>1</sup>, and Marie  
9 Galloux<sup>1\*</sup>

10

11 <sup>1</sup> Université Paris-Saclay, INRAE, UVSQ, VIM, 78350, Jouy-en-Josas, France.

12 <sup>2</sup> Departamento de Microbiologia, Instituto de Ciências Biomédicas, Universidade de São Paulo, São  
13 Paulo, Brazil

14 <sup>3</sup> Unité de Génomique Virale et Vaccination, Institut Pasteur, CNRS UMR-3569, 75015 Paris, France.

15 <sup>4</sup> Department of Infectious Diseases, Faculty of Medicine, Oita University Idaiga-oka, Hasama Yufu,  
16 Japan

17 <sup>5</sup> CIRI, Centre International de Recherche en Infectiologie, Univ Lyon, Inserm, U1111, Université Claude  
18 Bernard Lyon 1, CNRS, UMR5308, ENS de Lyon, F-69007, Lyon, France.

19

20 \* Correspondence: [delphyne.descamps@inrae.fr](mailto:delphyne.descamps@inrae.fr) and [marie.galloux@inrae.fr](mailto:marie.galloux@inrae.fr)

21

22 **Keywords:** RSV, TAX1BP1, nucleoprotein, innate immunity, interferons, lung, yeast two-hybrid  
23 screening

24

25

26

27

28

29

30

31 **ABSTRACT**

32 Respiratory syncytial virus (RSV) is the main cause of acute respiratory infections in young children,  
33 and also has a major impact on the elderly and immunocompromised people. In the absence of a  
34 vaccine or efficient treatment, a better understanding of RSV interactions with the host antiviral response  
35 during infection is needed. Previous studies revealed that cytoplasmic inclusion bodies (IBs) where viral  
36 replication and transcription occur could play a major role in the control of innate immunity during  
37 infection by recruiting cellular proteins involved in the host antiviral response. We recently showed that  
38 the morphogenesis of IBs relies on a liquid-liquid phase separation mechanism depending on the  
39 interaction between viral nucleoprotein (N) and phosphoprotein (P). These scaffold proteins are  
40 expected to play a central role in the recruitment of cellular proteins to IBs. Here, we performed a yeast  
41 two-hybrid screen using RSV N protein as a bait, and identified the cellular protein TAX1BP1 as a  
42 potential partner of this viral protein. This interaction was validated by pulldown and immunoprecipitation  
43 assays. We showed that TAX1BP1 suppression has only a limited impact on RSV infection in cell  
44 cultures. However, RSV replication is decreased in TAX1BP1-deficient mice (TAX1BP1<sup>KO</sup>), whereas the  
45 production of inflammatory and antiviral cytokines is enhanced. *In vitro* infection of wild-type or  
46 TAX1BP1<sup>KO</sup> alveolar macrophages confirmed that the innate immune response to RSV infection is  
47 enhanced in the absence of TAX1BP1. Altogether, our results suggest that RSV could hijack TAX1BP1  
48 to restrain the host immune response during infection.

49

50 **Importance**

51 Respiratory syncytial virus (RSV), which is the leading cause of lower respiratory tract illness in infants,  
52 still remains a medical problem in the absence of vaccine or efficient treatment. This virus is also  
53 recognized as a main pathogen in the elderly and immunocompromised people, and the occurrence of  
54 co-infections (with other respiratory viruses and bacteria) amplifies the risks of developing respiratory  
55 distress. In this context, a better understanding of the pathogenesis associated to viral respiratory  
56 infections, which depends on both viral replication and the host immune response, is needed. The  
57 present study reveals that the cellular protein TAX1BP1, which interacts with the RSV nucleoprotein N,  
58 participates in the control of the innate immune response during RSV infection, suggesting that N-  
59 TAX1BP1 interaction represents a new target for the development of antivirals.

60

## 61 INTRODUCTION

62 Respiratory syncytial virus (RSV) is the main pathogen responsible for acute respiratory infections and  
63 bronchiolitis in children (1). Almost all children are infected by the age of two. A systemic multisite study  
64 on the cause of infant's pneumonia in hospitalized children in Asia and Africa recently revealed that RSV  
65 is the main etiological agent of severe pneumonia, accounting for over 30% of infections (2). In the  
66 United States, RSV is estimated to be responsible for the hospitalization of 86,000 children per year,  
67 with a related cost of 394 million dollars (3). Furthermore, RSV infections in early childhood is recognized  
68 to later increase the susceptibility to chronic asthma (4, 5). Reinfections occur throughout life and if  
69 healthy adults generally present symptoms of bad cold, RSV infections are associated with significant  
70 morbidity and mortality in the elderly and immunocompromised people (6-9). Indeed, RSV is estimated  
71 to cause over 17,000 deaths per year in the United States, 78% of which occur in adults over 65 years  
72 of age, and is responsible for 5% of total hospital admissions in the elderly (10). Although RSV has a  
73 major impact on human health and the economy, there is still no vaccine available. The development of  
74 vaccines has been hampered by the repercussions of a failed vaccine trial using a formalin-inactivated  
75 virus in the 1960s, which resulted in an exacerbation of the pathology upon infection and led to two  
76 deaths (11). The current standard of care consists of prophylactic treatment of at-risk infants with a  
77 monoclonal antibody (Palivizumab), but its use is limited by its moderate effectiveness and high cost  
78 (12).

79 The pathology associated with RSV infection results from both viral replication and the host's immune  
80 response (13). RSV infection triggers an early immune response mediated by the production of type I  
81 interferons (IFN-I) which induces the transcription of IFN-stimulating genes (ISG) and the production of  
82 proinflammatory mediators (14-17). On the other hand, RSV has developed multiple strategies to hijack  
83 cellular pathways controlling the IFN-I and NF- $\kappa$ B (Nuclear Factor kappa B) pathway in order to blunt  
84 the host antiviral response (17-19). In particular, the two nonstructural viral proteins NS1 and NS2 are  
85 known to suppress IFN-I production and cell signaling during infection (20). Although IFN-I are major  
86 players in viral clearance and are essential to induce an appropriate immune response (21), they could  
87 also contribute to RSV pathogenesis with potentially different roles in infants and adults (17, 22-26).  
88 Indeed, high levels of IFN-I and inflammatory cytokines usually correlate with severity as this reflects  
89 the inability of the immune response to control the virus. It is thus essential to better characterize the

90 complex interactions between RSV and the host immune response to decipher pathogenesis and design  
91 effective treatments.

92 RSV belongs to the *Mononegavirales* (MNV) order and the *Pneumoviridae* family (27). It is an enveloped  
93 virus with a non-segmented negative strand RNA genome containing 10 genes that encode 11 proteins.  
94 The two surface glycoproteins G and F are involved in the initial steps of infection, *i.e.* attachment and  
95 fusion with the cell membrane. The viral membrane, which also contains the small hydrophobic protein  
96 SH, is lined by the matrix protein M that drives virus assembly. The genome is encapsidated by the  
97 nucleoprotein N, forming a helical nucleocapsid (28). The polymerase complex composed of the large  
98 polymerase (L) and its main cofactor the phosphoprotein P, is associated with this ribonucleoprotein  
99 complex (RNP) which serves as a template for viral transcription and replication (29). The viral  
100 transcription factor M2-1 is also present in the viral particle. After cell entry, RSV replicates in the  
101 cytoplasm of host cells within viro-induced spherical cytoplasmic granules called inclusion bodies (IBs).  
102 These structures are viral factories where all the viral proteins of the polymerase complex concentrate  
103 to perform the replication and transcription of the viral genome (30). These structures also play a role in  
104 viral escape from the innate immune system by limiting the recognition of viral RNAs by cytoplasmic  
105 pattern recognition receptors (PRRs) such as RIG-I (Retinoic acid-Inducible Gene I) and MDA5  
106 (Melanoma Differentiation-Associated gene 5). Once stimulated, these PRRs activate the transcription  
107 factors NF- $\kappa$ B and interferon regulatory factor 3 and 7 (IRF3/7) (31). The function of IBs in the modulation  
108 of the host innate immune response was further supported by a study showing that MDA5 interacts with  
109 the RSV-N protein. In addition, MDA5 and the downstream signaling molecule MAVS (Mitochondrial  
110 AntiViral Signaling) both colocalize to IBs as soon as 12 hours post-infection, leading to downregulation  
111 of *IFN $\beta$*  mRNA expression (32). More recently, a study also revealed the sequestration of the NF- $\kappa$ B  
112 subunit p65 in RSV IBs (33). It is thus now recognized that the recruitment of cellular proteins into IBs  
113 participates not only in viral replication but is also involved in the control of cellular responses (34).

114 We recently showed that RSV IBs display hallmarks of liquid-liquid phase separation, and that the N  
115 and P proteins are at the core of the RSV IBs biogenesis (35). Their role as scaffold proteins suggest  
116 that N and P are directly involved in the partitioning of cellular proteins to IBs. However, their interactions  
117 with cellular factors are still poorly characterized. Here we report the identification of Tax1-binding  
118 protein 1 (TAX1BP1) as an interactor of RSV-N. TAX1BP1 was initially identified as a partner of the Tax  
119 protein from Human T-lymphotropic virus 1 (HTLV-1) (36). Since then, TAX1BP1 was shown to interact

120 with viral proteins from Papillomaviruses (37), measles virus (MeV) (38) and Mammarenaviruses (39).  
121 Among the described activity of TAX1BP1, this protein was involved in the negative regulation of NF- $\kappa$ B  
122 and IRF3 signaling by editing the ubiquitylation of its catalytic partner, the protein A20 (40, 41). We thus  
123 investigated the role of TAX1BP1 in both RSV replication and control the host antiviral response using  
124 *in vitro* and *in vivo* infection models. Altogether our results suggest that TAX1BP1 is recruited by RSV  
125 to inhibit the host antiviral response.

126

## 127 **RESULTS**

### 128 ***Identification of TAX1BP1 interaction with the viral nucleoprotein N***

129 To identify cellular interactors of the RSV-N protein, we first performed a yeast two-hybrid (Y2H) screen.  
130 Yeast cells were transformed with a vector encoding the RSV-N protein fused to GAL4 DNA binding  
131 domain (GAL-BD) in order to use it as bait in the Y2H system. Surprisingly, no yeast clones were  
132 obtained, suggesting that RSV-N is toxic. This could be due to the non-specific RNA-binding properties  
133 of N (42). We thus decided to use as a substitute the N protein harboring the K170A/R185A mutations  
134 that were previously shown to impair the interaction of N with RNA. This mutant is expressed as a  
135 monomeric RNA-free N, named N<sup>mono</sup>, which can mimic the natural N<sup>0</sup> form (42). When yeast cells were  
136 transformed with a vector encoding N<sup>mono</sup> fused to GAL4-BD, growing colonies were obtained on  
137 selective medium as expected. Yeast cells expressing N<sup>mono</sup> were then mated with yeast cells  
138 transformed with a human spleen cDNA library or a normalized library containing 12,000 human ORFs  
139 fused to the GAL4 activation domain (GAL4-AD; prey libraries). Yeast diploids were grown on  
140 appropriate medium for the selection of bait-prey interactions, and positive colonies were analyzed by  
141 PCR and sequencing for identifying human proteins captured by N<sup>mono</sup> in the Y2H system. This screen  
142 allowed us to identify, among others, the protein TAX1BP1 as an interactor of the N<sup>mono</sup> protein (Table  
143 1). For this specific interaction, 40 positive yeast colonies were obtained, and the alignments of the  
144 reads from the PCR products showed that the C-terminal part of TAX1BP1 (residues 401-789), including  
145 half of the central coiled-coil domain involved in TAXBP1 dimerization and the C-terminal zinc fingers  
146 (ZF), is involved in the interaction with N (Figure 1A). None of the cDNA clones expressed full-length  
147 TAX1BP1. This probably reflects the fact that isolated domains often better perform than full length  
148 proteins in the Y2H system as the reconstitution of a functional GAL4 transcription factor is usually  
149 facilitated (43).

150 To validate the interaction between TAX1BP1 and the RSV-N protein, we then performed pulldown  
151 assays using recombinant proteins. Analysis of purified GST-TAX1BP1 by SDS-PAGE stained with  
152 Coomassie blue revealed two main bands of equivalent intensity with apparent MW close to 120 kDa  
153 (Figure 1B). Mass spectrometry analysis of these products allowed to identify the higher migrating band  
154 as full length GST-TAX1BP1 (theoretical mass, 112 kDa). The lower band corresponds to GST-TAX1BP1  
155 deleted from the last 77 residues of TAX1BP1 (data not shown), which include the two C-terminal ZF of  
156 the protein (Figure 1A). This analysis revealed the strong instability of TAX1BP1 C-terminal domain  
157 when expressed alone in bacteria. When co-incubated with Sepharose-glutathione beads bound to  
158 either GST or GST-TAX1BP1, recombinant N protein was specifically captured in the presence of GST-  
159 TAX1BP1 (Figure 1B). This result confirmed that RSV-N and TAX1BP1 can directly interact. Finally, we  
160 investigated the capacity of RSV-N protein to interact with TAX1BP1 in mammalian cells. Cells were co-  
161 transfected with plasmids encoding RSV-N and Flag-tagged TAX1BP1 or the Flag-tag alone as a  
162 control, and an immunoprecipitation assay was performed using an anti-Flag antibody. As shown on  
163 figure 1C, the RSV-N protein co-precipitated specifically with Flag-TAX1BP1. Altogether, if our results  
164 indicate that the RSV-N protein can interact directly with TAX1BP1, further characterization of the  
165 domain of TAX1BP1 involved in the interaction should be required to validate the potential role of the  
166 oligomerization and the ZF domains in N binding.

167

#### 168 ***Downregulation of TAX1BP1 expression has limited impact on RSV replication in human cells***

169 TAX1BP1 was recently shown to control the cellular antiviral response during RSV infection (44). We  
170 thus determined whether downregulation of TAX1BP1 expression has an impact on RSV replication in  
171 cell culture (45). Human epithelial A549 cells were transfected with control siRNA (siCT) or siRNA  
172 targeting TAX1BP1 (siTAX1BP1). After 24 h of culture, cells were infected with recombinant strains of  
173 human RSV expressing either the fluorescent protein mCherry (rHRSV-mCherry) or the bioluminescent  
174 enzyme firefly luciferase (rHRSV-Luc). After 48 h of culture, mCherry and luciferase expression were  
175 determined as a proxy for viral infection. Lower signals were observed in siTAX1BP1-treated cells, thus  
176 suggesting a role of TAX1BP1 in RSV replication (Figure 2A). Western-blot analysis of cell lysates  
177 confirmed that TAX1BP1 expression is suppressed at this time point (Figure 2B). Somewhat  
178 unexpectedly, RSV-N expression in siTAX1BP1-treated cells was similar to control cells (Figure 2B),  
179 suggesting that TAX1BP1 has no major impact on viral replication in this cell culture system. We then

180 further assessed the consequence of TAX1BP1 downregulation on viral shedding by quantifying virions  
181 in culture supernatants of infected cells. As shown on figure 2C, viral titers in supernatants of  
182 siTAX1BP1-treated cells were similar to siCT-treated controls. These results corroborate those of  
183 Martin-Vicente *et al.* (44), showing only a weak reduction of virus titer upon downregulation of TAX1BP1  
184 expression. Altogether, these results led to the conclusion that although a slight decrease of RSV  
185 replication was detected using quantitative approaches based on fluorescent or luminescent reporter  
186 proteins, TAX1BP1 does not have a strong impact on RSV replication. This suggested a more indirect  
187 effect of TAX1BP1 on RSV replication that could depend on its regulatory role on the innate immune  
188 response.

189

### 190 ***Depletion of TAX1BP1 impairs RSV replication in mice***

191 Given the complexity of the immune response triggered upon RSV infection, we assessed the impact of  
192 TAX1BP1 depletion directly *in vivo* using TAX1BP1-deficient (TAX1BP1<sup>KO</sup>) mice. These mice being  
193 generated in 129-strain mice (40), we first investigated the kinetics of rHRSV-Luc replication in this  
194 genetic background. Although luminescence was shown to be correlated to viral replication by direct  
195 measurement on live animals in BALB/c mice using the IVIS system (45, 46), the skin pigmentation of  
196 129 mice impaired luminescence detection. We thus decided to monitor viral replication in infected  
197 animals by measuring the luciferase activity in lung homogenates. Wild-type 129 mice were either instilled  
198 with mock control (Mock) consisting of HEp2 cell culture supernatant, or infected with  $1.87 \times 10^5$  pfu of  
199 rHRSV-Luc *via* intranasal (IN) inoculation. The viral replication was quantified the first 4 days post-infection  
200 (p.i.). The bioluminescence in lung homogenates was detected at day 1 p.i., and viral replication in the  
201 lungs increased from day 2 to day 4 p.i. (Figure 3A, left). In parallel, expression of *N-RSV* gene in the lung  
202 lysates was quantified by qRT-PCR (Figure 3A, right). Data showed that N-RSV mRNA could be detected  
203 from day 2 p.i., and that the peak of infection was reached at day 3 and 4 p.i.. These results revealed a  
204 correlation between bioluminescence intensity and N-RSV mRNA expression in line with previous  
205 reports (45), with a clear detection of RSV replication at day 3 and 4 p.i.. Of note, this kinetics of  
206 replication is similar to the one described in BALB/c mice, a reference mouse strain to study RSV  
207 infection (45, 46).

208 Based on these results, we decided to compare rHRSV-Luc replication in wild-type (WT) and TAX1BP1<sup>KO</sup>  
209 129 mice. We chose to quantify bioluminescence in the lung of mock-treated and HRSV-infected

210 animals at day 2 and day 4 p.i. in order to compare viral replication at an early time point and at the peak  
211 of infection. Our results showed a strong reduction in RSV replication in TAX1BP1<sup>KO</sup> mice compared to  
212 WT mice, at both day 2 p.i. and 4 p.i. (Figure 3B). In order to confirm these results, viral replication in  
213 the lungs of infected mice at day 4 p.i. was assessed by quantification of *N-RSV* gene expression in the  
214 lungs by qRT-PCR, and of virions production in the lungs using a plaque assay approach. As shown in figure  
215 3C, the amount of N-RSV mRNA was significantly lower in TAX1BP1<sup>KO</sup> mice compared to wild-type mice.  
216 Once again, these results reveal that *in vivo* quantification of viral replication by bioluminescence correlate  
217 with viral load, as previously reported (45). However, we didn't manage to recover virus from lungs' lysates  
218 to quantify virions production. Altogether our results revealed a supportive role of TAX1BP1 on RSV  
219 replication *in vivo*.

220

### 221 ***Depletion of TAX1BP1 favors antiviral and inflammatory responses during RSV infection***

222 As mentioned, among the various functions of TAX1BP1, this cellular protein acts as a cofactor of the  
223 A20 protein, which is a negative regulator of NF- $\kappa$ B and IRF3/7 pathways that are respectively involved  
224 in inflammatory and antiviral responses. In the mouse model of RSV infection, the induction of  
225 inflammatory cytokines and IFN-I in the first hours post-exposure to the virus are well documented (47-  
226 50). We thus assessed if the inhibition of RSV replication upon TAX1BP1 depletion could be associated  
227 with a modulation of the antiviral and inflammatory responses in the lungs of infected mice at early time  
228 point post-infection. Mice were mock-treated or infected with  $1.87 \times 10^5$  pfu of rHRSV-Luc and at day 1  
229 p.i., expression levels of IFN-I (IFN- $\alpha$  and IFN- $\beta$ ) and of the inflammatory cytokines IL-6 and TNF- $\alpha$  were  
230 determined from lung lysates of WT or TAX1BP1<sup>KO</sup> mice. As shown on Figure 4, RSV infection of WT  
231 mice induced the production of IFN- $\alpha$  and IFN- $\beta$  in all the animals. Of note, one of the WT infected mice  
232 that presented a strong induction of IFN- $\alpha$  and IFN- $\beta$  also displayed an induction of IL-6 and TNF- $\alpha$ .  
233 TAX1BP1<sup>KO</sup> mice were infected in parallel, and higher levels of IFN- $\alpha$  and TNF- $\alpha$  were detected in the  
234 lungs of TAX1BP1<sup>KO</sup> mice compared to WT mice (Figure 4A and D). On the contrary, IFN- $\beta$  induction by  
235 RSV was unchanged (Figure 4B). Although IL6 was induced in only one of the infected WT animals, this  
236 cytokine was induced in all TAX1BP1<sup>KO</sup> infected mice (Figure 4C). However, IL6 expression levels were  
237 not statistically significant when comparing TAX1BP1<sup>KO</sup> to WT mice. Of note, all groups of animals  
238 showed comparable levels of RSV infection at this early time point (1 d.p.i.) as assessed by  
239 bioluminescence quantification in the lung homogenates (not shown). Because the measurements were



240 performed in whole lung lysates, the quantified cytokines and chemokines are probably produced by  
241 several cell populations (*i.e.* both epithelial and immune cells). We thus decided to specifically focus on  
242 alveolar macrophages (AMs) which are major actors in the antiviral response to RSV (48). AMs were  
243 isolated from WT and TAX1BP1<sup>KO</sup> mice after repeated bronchoalveolar lavages and cultured for 24 h  
244 before incubation for another 24 h in the presence of either rHRSV-mCherry or UV-inactivated rHRSV-  
245 mCherry (MOI = 5). Culture supernatants were collected, and IFN- $\alpha$ , IFN- $\beta$ , IL-6 and TNF- $\alpha$  were  
246 quantified by immunoassay. A strong induction of both anti-viral (Figure 5A and B) and inflammatory  
247 cytokines (Figure 5C and D) was detected in the supernatant of AMs exposed to RSV, whereas a much  
248 weaker induction of these molecules was observed for AMs exposed to inactivated RSV, thus validating  
249 an efficient infection of AMs. Of note, although AMs can be infected by RSV, these cells do not  
250 productively replicate the virus (51). Most interestingly, the production of IFN- $\alpha$ , IFN- $\beta$ , IL-6 and TNF- $\alpha$   
251 was enhanced in AMs derived from TAX1BP1<sup>KO</sup> mice compared to AMs isolated from WT mice (Figure  
252 5). Altogether, these results demonstrate that TAX1BP1 is a key factor involved in the inhibition of the  
253 antiviral and inflammatory responses in the lungs of RSV-infected animals and in isolated AMs.

254

## 255 **DISCUSSION**

256 Previous studies using microarray and proteomic approaches have provided key information on RSV-  
257 host interactions (52, 53), but the interactome of RSV proteins still remains poorly characterized. Due to  
258 their pivotal role during virus entry, replication and assembly, it is expected that components of the viral  
259 polymerase complex, and especially the N protein, are involved in various interactions with cellular  
260 factors. The objective of this study was to find new cellular partners of RSV-N by performing a yeast  
261 two-hybrid screen. Using this approach, we captured 6 cellular proteins using RSV-N as bait, among  
262 which TAX1BP1 was overrepresented. We thus focused on TAX1BP1 as TAX1BP1 depletion has  
263 recently been shown to favor the innate immune response to RSV infection and to impair viral replication  
264 in cell culture (44). In addition, TAX1BP1 is already known to interact with different viral proteins  
265 including the N protein of measles virus that belongs to *Mononegavirales* order (36-39), like RSV,  
266 suggesting that this protein is often hijacked by viruses. TAX1BP1 is a homodimer of about 90 kDa and  
267 is organized into three main structural domains. The N-terminal SKIP carboxyl homology (SKICH)  
268 domain (54) was recently shown to interact with the adaptor protein NAP1, allowing the recruitment of  
269 the TANK-binding kinase 1 (TBK1), which is involved in selective autophagy of invading pathogens and

270 damaged mitochondria but is also critical to the induction of IFN-I by RIG-I, MDA5 and STING (55-59).  
271 It is followed by a LC3-interacting region (LIR) that can bind different LC3/GABARAP orthologs (60)  
272 involved in the recruitment of TAX1BP1 to autophagosomes. The central part of TAX1BP1 exhibits  
273 coiled coils forming the oligomerization domain that interacts with TRAF6 protein (61), and is followed  
274 by two C-terminal zinc fingers (UBZ1 and UBZ2) (62). These zinc fingers were shown to interact with  
275 ubiquitinated proteins, with myosin VI, and with the protein A20 (63-65).

276 Here, the alignment of the PCR reads obtained from the 40 yeast clones that expressed TAX1BP1 in  
277 the two-hybrid screen revealed that the C-terminal part of this protein is involved in the interaction with  
278 RSV-N. Based on our results, it is expected that the TAX1BP1 binding site to RSV-N is located within  
279 the oligomerization domain and/or the C-terminal zinc finger domains. The N-TAX1BP1 interaction was  
280 validated first by pulldown using recombinant TAX1BP1 and RSV-N proteins, and then by  
281 immunoprecipitation when co-expressing the two proteins in human cells. Noteworthy, we managed to  
282 purify the recombinant TAX1BP1 protein to validate the direct interaction with the RSV-N protein.

283 However, the purification of this protein was challenging as TAX1BP1 tends to be cleaved at its C-  
284 terminus, and this hampered affinity study with RSV-N by biophysical approaches. To gain structural  
285 and functional insights on this interaction that could represent a new therapeutic target, a precise  
286 characterization of TAXBP1 binding domains to RSV-N is required. The structure of the C-terminal UBZ  
287 domain of TAXBP1 either alone or in complex with Myosin VI has already been resolved (62, 65). The  
288 crystal structure of RSV nucleocapsid-like structures consisting of rings containing 10 N protomers and  
289 RNA of 70 nucleotides has been determined (66). Recently, a recombinant RSV N<sup>0</sup>-P complex has also  
290 been characterized (67). The reconstitution of a recombinant complex of RSV-N (monomeric or  
291 oligomeric form) bound to the C-terminal fragment of TAX1BP1 could thus provide key structural  
292 information on this interaction. Finally, given the strong homology between the N proteins of RSV and  
293 human Metapneumovirus (hMPV), another pneumovirus also responsible of acute respiratory infections,  
294 the potential interaction between hMPV-N and TAX1BP1, and its functional relevance during infection  
295 should also be investigated.

296 We then investigated the potential role of TAX1BP1 in RSV infection. TAX1BP1 suppression showed a  
297 limited or no impact on viral protein expression in cell culture, and the production of new viral particles  
298 was unaffected. However, a model of RSV-infected TAX1BP1<sup>KO</sup> mice revealed the critical role of  
299 TAX1BP1 in RSV infection *in vivo*, the depletion of TAX1BP1 leading to a nearly 3-fold decrease in viral

300 replication in the lungs of infected mice. We also showed that RSV-infected TAX1BP1<sup>KO</sup> mice present  
301 higher levels of IFN- $\alpha$  and TNF- $\alpha$  in the lungs compared to WT mice at day 1 p.i.. Besides, RSV-infected  
302 AMs isolated from TAX1BP1<sup>KO</sup> mice produced higher levels of IFN-I (IFN- $\alpha$  and  $\beta$ ) and inflammatory  
303 cytokines (IL-6 and TNF- $\alpha$ ) compared to those isolated from WT mice.

304 These results reveal that TAX1BP1 participates to the attenuation of the host antiviral and inflammatory  
305 responses during RSV infection *in vivo* and especially in AMs. Altogether, this suggests that TAXBP1  
306 recruitment by RSV-N indirectly promotes RSV growth by inhibiting the innate immune response. It is  
307 noteworthy that this interaction could compete with the interaction of TAX1BP1 with another partner.  
308 Overall, this conclusion is consistent with the recent study by Martín-Vicente *et al.* (44) but significant  
309 differences should be highlighted. Indeed, they found that the production of infectious RSV particles in  
310 A549 cells decreases when silencing TAX1BP1 or interacting co-factors A20, ABIN1 and ITCH. In our  
311 hands, the effect of TAX1BP1 silencing on RSV infection was striking only *in vivo*. At this point, we don't  
312 have an explanation to this discrepancy as we both used the same *in vitro* model of A549-infected cells.  
313 Besides, they found in their study that A549 cells silenced for TAX1BP1 express higher levels of ISG15,  
314 IL-6 and IL-8 upon RSV infection, but IFN- $\beta$  and TNF- $\alpha$  expression were not significantly affected. On  
315 the contrary, we found that TAX1BP1-deficient AMs express higher level of TNF- $\alpha$ , IL6, IFN- $\beta$  and IFN-  
316  $\alpha$  when infected by RSV. The use of distinct cellular models and TAX1BP1-depletion methods could  
317 account for these differences. Indeed, TAX1BP1 is directly involved in the regulation of innate immune  
318 pathways, but is also an adaptor for autophagy (63) which is required for the induction of an optimal  
319 antiviral response in RSV-infected macrophages (68). Thus, the role of TAX1BP1 in the regulation of  
320 the innate immune response induced upon RSV infection could vary between epithelial and immune  
321 cells depending on the relative contribution of autophagy in the activation of the innate immune  
322 response. Finally, it should be noticed that TAX1BP1 has been previously described to regulate B cell  
323 differentiation (69). It would thus be interesting to study whether TAX1BP1 could also be involved in  
324 acquired immune responses in the context of RSV infection *in vivo*, and in particular the production of  
325 antibodies.

326 As TAX1BP1 works an adaptor protein in different processes, it is essential to characterize TAX1BP1  
327 partners in different cell lines when infected by RSV. During our study, we investigated the cellular  
328 localization of TAX1BP1 in the context of viral infection or overexpression of N, in order to determine in  
329 particular if TAX1BP1 could be recruited to IBs, as previously shown for MDA5 and MAVS (32), or if

330 TAXBP1 could recruit RSV-N to specific cellular compartments. However, we were not able to clearly  
331 detect TAX1BP1 by immunolabeling using commercial antibodies. Furthermore, upon overexpression  
332 of Flag- or GFP-tagged TAX1BP1 in cells, TAX1BP1 was shown to concentrate into cytoplasmic  
333 granules and to induce cell death, thus precluding further analysis (data not shown).

334 In conclusion, we have shown that TAX1BP1 is suppressing the innate immune response to RSV *in vivo*  
335 and in AMs. Results also suggest that RSV hijacks this mechanism through a direct physical interaction  
336 with RSV-N. Although the precise role of TAX1BP1 in RSV infection needs to be further characterized,  
337 this interaction helps understanding the pathology associated with the infection and represents new  
338 target for antiviral approaches.

339

340

## 341 **MATERIALS AND METHODS**

342

### 343 ***Plasmids and siRNA***

344 The plasmid pFlag-TAX1BP1 encoding for TAX1BP1 in fusion with a N-terminal Flag tag was kindly  
345 provided by Dr C. Journo (ENS, Lyon, France). The plasmid pFlag was obtained by inserting a stop  
346 codon in the pFlag-TAX1BP1 vector, using the Quickchange site-directed mutagenesis kit (Stratagene).  
347 The already described p-N (70) was used for cell transfection and immunoprecipitation assay.

348 The pGEX-4T-3 vector was used to produce recombinant Glutathione S-transferase protein (GST). The  
349 pGEX-TAX1BP1 plasmid expressing the GST in fusion with the N-terminus of TAX1BP1 was obtained  
350 by cloning the TAX1BP1 sequence between BamHI and XhoI sites of the pGEX-4T-3 plasmid. For  
351 purification of recombinant N protein, the pET-N and pGEX-PCT plasmids already described (42) were  
352 used. For yeast two-hybrid screening, the DNA sequence encoding the N<sup>mono</sup> (monomeric N mutant  
353 K170A/R185A) was cloned by *in vitro* recombination (Gateway technology; Invitrogen) from pDONR207  
354 into the yeast two-hybrid vector pPC97-GW for expression in fusion downstream of the GAL4 DNA-  
355 binding domain (GAL4-BD). The control siRNA and a pool of TAX1BP1 siRNA (Ambion) were used for  
356 TAX1BP1 silencing experiments.

357

### 358 ***Antibodies***

359 The following primary antibodies were used for immunoprecipitation assay and/or immunoblotting: a

360 mouse anti-Flag and a mouse anti-Flag-HRP antibody (Sigma), a rabbit anti-N antiserum (71), and a  
361 mouse monoclonal anti- $\beta$ -tubulin antibody (Sigma). Secondary antibodies directed against mouse  
362 and rabbit Ig G coupled to HRP (P.A.R.I.S) were used for immunoblotting.

363

### 364 **Cell lines**

365 BHK-21 cells (clone BSRT7/5), hamster kidney cells constitutively expressing the T7 RNA polymerase  
366 (72), HEp-2 cells (ATCC number CCL-23), and human lung carcinoma epithelial A549 cells were grown  
367 in Dulbecco Modified Essential Medium (Lonza) supplemented with 10% fetal calf serum (FCS), 2 mM  
368 glutamine, and 1% penicillin-streptomycin. The transformed human bronchial epithelial cell line BEAS-  
369 2B (ATCC) was maintained in RPMI 1640 medium (Invitrogen) supplemented with 10% fetal bovine  
370 serum (FBS, Invitrogen), 1% L-glutamine, and 1% penicillin-streptomycin.

371

### 372 **Viruses**

373 Recombinant RSV viruses rHRSV-mCherry and rHRSV-Luc corresponding to RSV Long strain  
374 expressing either the mCherry or the Luciferase proteins were amplified on HEp-2 cells and titrated  
375 using a plaque assay procedure as previously described (45). Briefly for titration cells were infected with  
376 serial 10-fold dilutions of viral supernatant in complete minimum essential medium (MEM). The overlay  
377 was prepared with microcrystalline cellulose Avicel RC581 (FMC Biopolymer) at a final concentration of  
378 0.6% in complete MEM containing 1% foetal calf serum. After 6 days at 37°C and 5% CO<sub>2</sub>, plaques  
379 were revealed by 0.5% crystal violet with 20% ethanol solution staining of the cell layers, and the number  
380 of plaque-forming unit (pfu) per well was counted.

381

### 382 **Yeast Two-Hybrid Screening**

383 Yeast two-hybrid screens were performed following the protocol described in Vidalain et al. (73). AH109  
384 yeast cells (Clontech; Takara, Mountain View, CA, USA) were transformed with pGAL4-BD-N<sup>mono</sup> using  
385 a standard lithium-acetate protocol. Screens were performed on a synthetic medium lacking histidine (-  
386 His) and supplemented with 3-amino-1,2,4-triazole (3-AT) at 10 mM. A mating strategy was used to  
387 screen two different prey libraries with distinct characteristics: a human spleen cDNA library, and a  
388 normalized library containing 12,000 human ORFs (74). All libraries were established in the yeast two-  
389 hybrid expression plasmid pPC86 to express prey proteins in fusion downstream of the GAL4

390 transactivation domain (GAL4-AD). After six days of culture, colonies were picked, replica plated, and  
391 incubated over three weeks on selective medium to eliminate potential contamination with false  
392 positives. Prey proteins from selected yeast colonies were identified by PCR amplification using primers  
393 that hybridize within the pPC86 regions flanking the cDNA inserts. PCR products were sequenced, and  
394 cellular interactors were identified by multi-parallel BLAST analysis.

395

### 396 ***Expression and purification of recombinant proteins***

397 *E. coli* BL21 bacteria (DE3) (Novagen, Madison, WI) transformed with pGEX-4T-3 and pGEX-TAX1BP1  
398 plasmids were grown at 37°C for 2-3 h in 200 mL of Luria Bertani (LB) medium containing 100 µg/mL  
399 ampicillin until the OD<sub>600nm</sub> reached 0.6. Protein expression was then induced by addition of 1 mM of  
400 isopropyl-β-D-thio-galactoside (IPTG) in the presence of 50 mM ZnSO<sub>4</sub> during 4 h at 37°C before  
401 harvesting by centrifugation. Expression and purification of the recombinant N protein was previously  
402 described (66, 75). Briefly, BL21 bacteria co-transformed with pET-N- pGEX-PCT plasmids were grown  
403 in LB medium containing kanamycin (50 µg/mL) and ampicillin for 8 h at 37°C. Then, the same volume  
404 of fresh LB was added and protein expression was induced by adding IPTG at 80 µg/ml to the culture.  
405 The bacteria were incubated for 15 h at 28°C and then harvested by centrifugation. For GST-fusion  
406 proteins purification, bacterial pellets were re-suspended in lysis buffer (50 mM Tris-HCl pH 7.8, 60 mM  
407 NaCl, 1 mM EDTA, 2 mM DTT, 0.2% Triton X-100, 1 mg/mL lysozyme) supplemented with complete  
408 protease inhibitor cocktail (Roche, Mannheim, Germany), incubated for 1 hour on ice, sonicated, and  
409 centrifuged at 4°C for 30 min at 10,000 g. Glutathione-Sepharose 4B beads (GE Healthcare, Uppsala,  
410 Sweden) were added to clarified supernatants and incubated at 4°C for 15 h. Beads were then washed  
411 two times in lysis buffer and three times in PBS 1X, then stored at 4°C in an equal volume of PBS. To  
412 isolate the recombinant N protein, beads containing bound GST-PCT+N complex were incubated with  
413 thrombin (Novagen) for 16 h at 20°C. Purified recombinant N proteins were loaded onto a Superdex 200  
414 16/30 column (GE Healthcare) and eluted in 20 mM Tris/HCl pH 8.5, 150 mM NaCl.

415

416 **Pull-down assays.** Purified recombinant N protein was incubated in the presence of GST or the GST-  
417 TAX1BP1 fusion protein fixed on beads in a final volume of 100 µL in buffer Tris 20 mM, pH 8.5, NaCl  
418 150 mM. After 1 h under agitation at 4°C, the beads were extensively washed with 20 mM Tris (pH 8.5)–

419 150 mM NaCl, boiled in 30  $\mu$ L Laemmli buffer, and analyzed by SDS-PAGE and Coomassie blue  
420 staining.

421

422 **Coimmunoprecipitation assay.** BSRT-7 cells were cotransfected with pFlag or pFlag-TAX1BP1 and  
423 pN for 36 h. Transfected cells were then lysed for 30 min at 4°C in ice-cold lysis buffer (Tris HCl 50 mM,  
424 pH 7.4, EDTA 2 mM, NaCl 150 mM, 0.5% NP-40) with a complete protease inhibitor cocktail (Roche),  
425 and coimmunoprecipitation experiments were performed on cytosolic extracts. Cell lysates were  
426 incubated for 4 h at 4°C with an anti-Flag antibody coupled to agarose beads (Euromedex). The beads  
427 were then washed 3 times with lysis buffer and 1 time with PBS, and proteins were eluted in Laemmli  
428 buffer at 95°C for 5 min and then subjected to SDS-PAGE and immunoblotting.

429

#### 430 **siRNA transfection and infection**

431 Freshly passaged A549 cells were transfected with the indicated siRNA at a final concentration of 10  
432 nM by reverse transfection into 48 wells plates, using Lipofectamine RNAiMAX (ThermoFischer)  
433 according to the manufacturer's instructions. Briefly, a mixture containing Opti-MEM (Invitrogen),  
434 lipofectamine RNAiMAX and siRNA was incubated for 5 min at room temperature before depositing at  
435 the bottom of the wells. The cells in DMEM medium without antibiotics were then added dropwise before  
436 incubation at 37°C, 5% CO<sub>2</sub>. After 24 h of transfection in the presence of siRNA, the medium was  
437 removed and the cells were infected with recombinant rHRSV-mCherry or rHRSV-Luc viruses at a MOI  
438 of 0.5 in DMEM medium without phenol red and without SVF, for 2 h at 37°C. The medium was then  
439 replaced by DMEM supplemented with 2% SVF and the cells were incubated for 48 h at 37°C. For cells  
440 infected with the rHRSV-mCherry virus, the quantification of replication was performed by measuring  
441 the mCherry fluorescence (excitation: 580 nm, emission: 620 nm) using a Tecan Infinite M200 Pro  
442 luminometer. For HRSV-Luc replication quantification, cells were lysed in luciferase lysis buffer (30 mM  
443 Tris pH 7.9, 10 mM MgCl<sub>2</sub>, 1 mM DTT, 1% Triton X-100, and 15% glycerol). After addition of luciferase  
444 assay reagent (Promega), luminescence was measured using a Tecan Infinite M200 Pro luminometer.  
445 Non-infected A549 cells were used as standards for fluorescence or luminescence background levels.  
446 Each experiment was performed in triplicates and repeated at least three times. For each experiment,  
447 cells treated in the same conditions were lysed and protein expression was analyzed by Western  
448 blotting.

449

450 **RSV infection of mice and luciferase measurement.**

451 TAX1BP1-deficient (TAX1BP1<sup>KO</sup>) 129 mice were created by gene targeting, as previously described  
452 (40). TAX1BP1<sup>KO</sup> mice and wild-type 129 co-housed control animals were bred and housed under SPF  
453 conditions in our animal facilities (IERP, INRAE, Jouy-en-Josas). Wild type (WT) and TAX1BP1<sup>KO</sup>  
454 female and male mice at 8 weeks of age (n=11 per group) were anesthetized with of a mixture of  
455 ketamine and xylazine (1 and 0.2 mg per mouse, respectively) and infected by intranasal administration  
456 of 80 µL of recombinant RSV expressing luciferase (rHRSV-Luc, 2.34 x 10<sup>6</sup> pfu/mL) (45, 76, 77) or cell  
457 culture media as mock-infection control. Mice were then sacrificed at different timepoints by  
458 intraperitoneal (I.P.) injection of pentobarbital and lungs were frozen.

459

460 **Viral *N-RNA* gene expression by RT-qPCR**

461 Frozen lungs were homogenized in NucleoSpin®RNA XS Kit (Macherey-Nagel) lysis buffer with a  
462 Precellys 24 bead grinder homogenizer (Bertin Technologies, St Quentin en Yvelines, France). Total  
463 RNA was extracted from lungs or infected cells using NucleoSpin® RNA kit (Macherey-Nagel) and  
464 reverse transcribed using the iScript™ Reverse Transcription Supermix for RT-qPCR kit (Bio-Rad)  
465 according to the manufacturer's instructions. The primers (Sigma-Aldrich) used are listed below. The  
466 qPCRs were performed with the MasterCycler RealPlex (Eppendorf) and SYBRGreen PCR Master Mix  
467 (Eurogenetec) and data analyzed with the Realplex software (Eppendorf) to determine the cycle  
468 threshold (Ct) values. Results were determined with the formula  $2^{-\Delta Ct}$  with  $\Delta Ct = Ct_{gene} - Ct_{HPRT}$ . The  
469 primers (Sigma-Aldrich) used are listed below: HPRT (hypoxanthine-guanine  
470 phosphoribosyltransferase), Forward primer 5'-CAGGCCAGACTTTGTTGGAT-3' and Reverse primer  
471 5'- TTGCGCTCATCTTAGGCTTT-3'; and N-RSV, Forward primer 5'-  
472 AGATCAACTTCTGTCATCCAGCAA-3' and Reverse primer 5'-  
473 TTCTGCACATCATAATTAGGAGTATCAAT-3'.

474

475 **Luciferase expression in lung lysates**

476 Frozen lungs were weighed and then homogenized in 300 µL of Passive Lysis Buffer (PLB) (1 mM Tris  
477 pH 7.9; 1 mM MgCl<sub>2</sub>; 1% Triton × 100; 2% glycerol; 1 mM DTT) with a Precellys 24 bead grinder  
478 homogenizer (Bertin Technologies, St Quentin en Yvelines, France) and a cycle of 2 × 15 s at 4 m/s.



479 Lung homogenates were clarified by centrifugation 5 min at 2000 g and distributed on microplates (50  
480  $\mu\text{L}$ ). Then, 50  $\mu\text{L}$  of luciferase assay reagent (Promega) were added on each well. The detection of  
481 firefly luciferase activity was measured by photon emission using an *In Vivo* Imaging System (IVIS-200,  
482 Xenogen, Advanced Molecular Vision) and Live Imaging software (version 4.0, Caliper Life Sciences).  
483 Data were expressed in radiance (photons/sec/cm<sup>2</sup>/sr) and normalized to weight lungs.

484

#### 485 **RSV infection of AMs**

486 A cannula was inserted in trachea from mice and repeated bronchoalveolar lavages (BALs) were made  
487 with PBS. AMs were isolated after centrifugations of the BALs of 5 mice per group, pooled, and  $1 \times 10^5$   
488 AMs were plated in 96-well cell culture plates in RPMI supplemented with L-glutamine 2 mM, FCS 5%  
489 and antibiotics for 24 h to allow for adhesion, as previously described (78). AMs were then exposed to  
490 rHRSV-mCherry or ultra-violet (UV)-inactivated rHRSV-mCherry (the same batch exposed 20 min to  
491 UV) at MOI 5 or Hep2 cell culture supernatant (Mock). After 24 h, supernatants were collected and were  
492 frozen for cytokine quantification.

493

#### 494 **Cytokine quantification**

495 IFN- $\alpha$  and IFN- $\beta$  or IL-6 and TNF- $\alpha$  were measured in supernatants of AMs or lung lysates using IFN  
496 alpha/IFN beta 2-Plex Mouse ProcartaPlex™ immunoassay (ebiosciences) or Milliplex MAP Mouse™  
497 assay (Merck), respectively. Data were acquired using a MagPix multiplex system (Merck) in order to  
498 determine the mean of fluorescent intensities (MFIs) and results were analyzed on Bio-Plex Manager™  
499 software. The concentrations were normalized to lungs weight.

500

501 **Ethics statement.** The *in vivo* work of is study was carried out in accordance with INRAE guidelines in  
502 compliance with European animal welfare regulation. The protocols were approved by the Animal Care  
503 and Use Committee at “Centre de Recherche de Jouy-en-Josas” (COMETHEA) under relevant  
504 institutional authorization (“Ministère de l’éducation nationale, de l’enseignement supérieur et de la  
505 recherche”), under authorization number 2015060414241349\_v1 (APAFIS#600). All experimental  
506 procedures were performed in a Biosafety level 2 facility.

507

#### 508 **Statistical analysis**

509 Nonparametric Mann-Whitney (comparison of two groups,  $n \geq 4$ ) was used to compare unpaired values  
510 (GraphPad Prism software). Significance is represented: \* $p < 0.05$ ; \*\* $p < 0.01$  and \*\*\* $p < 0.001$ .

511

512

### 513 **Acknowledgments**

514 We thank Dr. Sabine Riffault (INRAE, Jouy-en-Josas) for helpful discussion and critical reading of the  
515 manuscript. We are grateful to Chloé Journo (ENS-Lyon, France) for providing the pFlag-TAX1BP1  
516 plasmid, Céline Urien (INRAE, Jouy-en-Josas) for mice genotyping, Fortune Bidossessi (INRAE, Jouy-  
517 en-Josas) for qPCR, and the Infectiology of fishes and rodent facility (IERP, INRAE, doi:  
518 10.15454/1.5572427140471238E12) to animals' facilities and for birth management. We thank the  
519 Emerg'in platform for access to IVIS200 that was financed by the Region Ile De France (SESAME and  
520 DIMOneHealth), and the Plateforme d'Analyse Protéomique de Paris Sud-Ouest (PAPPSO,INRAE) for  
521 mass spectrometry analysis. C. Drajac. and Q. Marquant were recipients of a Ph.D. and Post-doctoral  
522 fellowship of the Région Ile-de-France (DIM-Malinf and DIM-OneHealth, respectively), A. Peres de  
523 Oliveira was recipient of post-doctoral fellowship (CAPES-Brazil 14809-13-3/ CAPES-COFECUB 769-  
524 13). This study was supported in part by Grants-in-Aid for scientific research from the Ministry of  
525 Education, Culture, Sports, Science, and Technology, Japan to H.Iha, and with the financial support of  
526 the French Agence Nationale de la Recherche, specific program ANR Blanc 2013 "Respisyncycell"  
527 (ANR-13-IVS3-0007 and FAPESP-Brazil/ANR - BLANC - RESPISYNCELL 2013/50299-2).

528

529 **Conflict of interest:** The authors declare that they have no conflicts of interest with the contents of this  
530 article.

531

532 **Author contributions:** DD, AMV, JFE, POV and MG designed experiments. APO, SM, LG, JF, FB and  
533 MG performed molecular and cellular assays. SM, CD, VP, QM, EB, HI and DD performed mice  
534 experiments, samples' treatment and analysis of *in vivo* experiments. APO, FT and POV performed two  
535 hybrid screens. MG, DD, POV and JFE wrote the paper. MG edited the manuscript. All authors  
536 commented on the manuscript.

537

### 538 **REFERENCES**

- 539 1. Shi T, McAllister DA, O'Brien KL, Simoes EAF, Madhi SA, Gessner BD, Polack FP,  
540 Balsells E, Acacio S, Aguayo C, Alassani I, Ali A, Antonio M, Awasthi S, Awori JO,  
541 Azziz-Baumgartner E, Baggett HC, Baillie VL, Balmaseda A, Barahona A, Basnet S,  
542 Bassat Q, Basualdo W, Bigogo G, Bont L, Breiman RF, Brooks WA, Broor S, Bruce N,  
543 Bruden D, Buchy P, Campbell S, Carosone-Link P, Chadha M, Chipeta J, Chou M,  
544 Clara W, Cohen C, de Cuellar E, Dang DA, Dash-Yandag B, Deloria-Knoll M, Dherani  
545 M, Eap T, Ebruke BE, Echavarria M, de Freitas Lazaro Emediato CC, Fasce RA, Feikin  
546 DR, Feng L, et al. 2017. Global, regional, and national disease burden estimates of acute  
547 lower respiratory infections due to respiratory syncytial virus in young children in 2015:  
548 a systematic review and modelling study. *Lancet* 390:946-958.
- 549 2. Pneumonia Etiology Research for Child Health Study G. 2019. Causes of severe  
550 pneumonia requiring hospital admission in children without HIV infection from Africa  
551 and Asia: the PERCH multi-country case-control study. *Lancet* 394:757-779.
- 552 3. Olszewska W, Openshaw P. 2009. Emerging drugs for respiratory syncytial virus  
553 infection. *Exp Op on emerging drugs* 14:207-17.
- 554 4. Backman K, Piippo-Savolainen E, Ollikainen H, Koskela H, Korppi M. 2014. Adults  
555 face increased asthma risk after infant RSV bronchiolitis and reduced respiratory health-  
556 related quality of life after RSV pneumonia. *Acta Paediatr* 103:850-5.
- 557 5. Griffiths C, Drews SJ, Marchant DJ. 2017. Respiratory Syncytial Virus: Infection,  
558 Detection, and New Options for Prevention and Treatment. *Clin Microbiol Rev* 30:277-  
559 319.
- 560 6. Asner S, Stephens D, Pedulla P, Richardson SE, Robinson J, Allen U. 2013. Risk factors  
561 and outcomes for respiratory syncytial virus-related infections in immunocompromised  
562 children. *Pediatr Infect Dis J* 32:1073-6.
- 563 7. Falsey AR, Hennessey PA, Formica MA, Cox C, Walsh EE. 2005. Respiratory syncytial  
564 virus infection in elderly and high-risk adults. *N Engl J Med* 352:1749-59.
- 565 8. Fleming DM, Taylor RJ, Lustig RL, Schuck-Paim C, Haguinet F, Webb DJ, Logie J,  
566 Matias G, Taylor S. 2015. Modelling estimates of the burden of Respiratory Syncytial  
567 virus infection in adults and the elderly in the United Kingdom. *BMC Infect Dis* 15:443.
- 568 9. Shah JN, Chemaly RF. 2011. Management of RSV infections in adult recipients of  
569 hematopoietic stem cell transplantation. *Blood* 117:2755-63.
- 570 10. Thompson WW, Shay DK, Weintraub E, Brammer L, Cox N, Anderson LJ, Fukuda K.  
571 2003. Mortality associated with influenza and respiratory syncytial virus in the United  
572 States. *JAMA* 289:179-86.
- 573 11. Kim HW, Canchola JG, Brandt CD, Pyles G, Chanock RM, Jensen K, Parrott RH. 1969.  
574 Respiratory syncytial virus disease in infants despite prior administration of antigenic  
575 inactivated vaccine. *Am J Epidemiol* 89:422-34.
- 576 12. Mac S, Sumner A, Duchesne-Belanger S, Stirling R, Tunis M, Sander B. 2019. Cost-  
577 effectiveness of Palivizumab for Respiratory Syncytial Virus: A Systematic Review.  
578 *Pediatrics* 143.
- 579 13. Walsh EE, McConnochie KM, Long CE, Hall CB. 1997. Severity of respiratory  
580 syncytial virus infection is related to virus strain. *J Infect Dis* 175:814-20.
- 581 14. Durbin RK, Kolenko SV, Durbin JE. 2013. Interferon induction and function at the  
582 mucosal surface. *Immunol Rev* 255:25-39.
- 583 15. Gibbert K, Schlaak JF, Yang D, Dittmer U. 2013. IFN-alpha subtypes: distinct  
584 biological activities in anti-viral therapy. *Br J Pharmacol* 168:1048-58.
- 585 16. Russell CD, Unger SA, Walton M, Schwarze J. 2017. The Human Immune Response  
586 to Respiratory Syncytial Virus Infection. *Clin Microbiol Rev* 30:481-502.

- 587 17. Hijano DR, Vu LD, Kauvar LM, Tripp RA, Polack FP, Cormier SA. 2019. Role of Type  
588 I Interferon (IFN) in the Respiratory Syncytial Virus (RSV) Immune Response and  
589 Disease Severity. *Front Immunol* 10:566.
- 590 18. Isaacs D. 1989. Production of interferon in respiratory syncytial virus bronchiolitis.  
591 *Arch Dis Child* 64:92-5.
- 592 19. Taylor CE, Webb MS, Milner AD, Milner PD, Morgan LA, Scott R, Stokes GM,  
593 Swarbrick AS, Toms GL. 1989. Interferon alfa, infectious virus, and virus antigen  
594 secretion in respiratory syncytial virus infections of graded severity. *Arch Dis Child*  
595 64:1656-60.
- 596 20. Sedeyn K, Schepens B, Saelens X. 2019. Respiratory syncytial virus nonstructural  
597 proteins 1 and 2: Exceptional disrupters of innate immune responses. *PLoS Pathog*  
598 15:e1007984.
- 599 21. Stephens LM, Varga SM. 2020. Function and Modulation of Type I Interferons during  
600 Respiratory Syncytial Virus Infection. *Vaccines (Basel)* 8:177.
- 601 22. Drajac C, Laubreton D, Riffault S, Descamps D. 2017. Pulmonary Susceptibility of  
602 Neonates to Respiratory Syncytial Virus Infection: A Problem of Innate Immunity? *J*  
603 *Immunol Res* 2017:8734504.
- 604 23. McIntosh K. 1978. Interferon in nasal secretions from infants with viral respiratory tract  
605 infections. *J Pediatr* 93:33-6.
- 606 24. Remot A, Descamps D, Jouneau L, Laubreton D, Dubuquoy C, Bouet S, Lecardonnel  
607 J, Rebours E, Petit-Camurdan A, Riffault S. 2016. Flt3 ligand improves the innate  
608 response to respiratory syncytial virus and limits lung disease upon RSV reexposure in  
609 neonate mice. *Eur J Immunol* 46:874-84.
- 610 25. Cormier SA, Shrestha B, Saravia J, Lee GI, Shen L, DeVincenzo JP, Kim YI, You D.  
611 2014. Limited type I interferons and plasmacytoid dendritic cells during neonatal  
612 respiratory syncytial virus infection permit immunopathogenesis upon reinfection. *J*  
613 *Virology* 88:9350-60.
- 614 26. Hall CB, Douglas RG, Jr., Simons RL, Geiman JM. 1978. Interferon production in  
615 children with respiratory syncytial, influenza, and parainfluenza virus infections. *J*  
616 *Pediatr* 93:28-32.
- 617 27. Afonso CL, Amarasinghe GK, Banyai K, Bao Y, Basler CF, Bavari S, Bejerman N,  
618 Blasdel KR, Briand FX, Briesse T, Bukreyev A, Calisher CH, Chandran K, Cheng J,  
619 Clawson AN, Collins PL, Dietzgen RG, Dolnik O, Domier LL, Durrwald R, Dye JM,  
620 Easton AJ, Ebihara H, Farkas SL, Freitas-Astua J, Formenty P, Fouchier RA, Fu Y,  
621 Ghedin E, Goodin MM, Hewson R, Horie M, Hyndman TH, Jiang D, Kitajima EW,  
622 Kobinger GP, Kondo H, Kurath G, Lamb RA, Lenardon S, Leroy EM, Li CX, Lin XD,  
623 Liu L, Longdon B, Marton S, Maisner A, Muhlberger E, Netesov SV, Nowotny N, et  
624 al. 2016. Taxonomy of the order Mononegavirales: update 2016. *Arch Virol* 161:2351-  
625 60.
- 626 28. Bakker SE, Duquerroy S, Galloux M, Loney C, Conner E, Eleouet JF, Rey FA, Bhella  
627 D. 2013. The respiratory syncytial virus nucleoprotein-RNA complex forms a left-  
628 handed helical nucleocapsid. *J Gen Virol* 94:1734-1738.
- 629 29. Collins PL, Melero JA. 2011. Progress in understanding and controlling respiratory  
630 syncytial virus: still crazy after all these years. *Virus Res* 162:80-99.
- 631 30. Rincheval V, Lelek M, Gault E, Bouillier C, Sitterlin D, Blouquit-Laye S, Galloux M,  
632 Zimmer C, Eleouet JF, Rameix-Welti MA. 2017. Functional organization of  
633 cytoplasmic inclusion bodies in cells infected by respiratory syncytial virus. *Nature*  
634 *Commun* 8.
- 635 31. Mogensen TH. 2009. Pathogen recognition and inflammatory signaling in innate  
636 immune defenses. *Clin Microbiol Rev* 22:240-73.

- 637 32. Lifland AW, Jung J, Alonas E, Zurla C, Crowe JE, Jr., Santangelo PJ. 2012. Human  
638 respiratory syncytial virus nucleoprotein and inclusion bodies antagonize the innate  
639 immune response mediated by MDA5 and MAVS. *J Virol* 86:8245-58.
- 640 33. Jobe F, Simpson J, Hawes P, Guzman E, Bailey D. 2020. Respiratory Syncytial Virus  
641 Sequesters NF-kappaB Subunit p65 to Cytoplasmic Inclusion Bodies To Inhibit Innate  
642 Immune Signaling. *J Virol* 94:e01380-20.
- 643 34. Dolnik O, Gerresheim GK, Biedenkopf N. 2021. New Perspectives on the Biogenesis  
644 of Viral Inclusion Bodies in Negative-Sense RNA Virus Infections. *Cells* 10.
- 645 35. Galloux M, Risso-Ballester J, Richard CA, Fix J, Rameix-Welti MA, Eleouet JF. 2020.  
646 Minimal Elements Required for the Formation of Respiratory Syncytial Virus  
647 Cytoplasmic Inclusion Bodies In Vivo and In Vitro. *mBio* 11:e01202-20.
- 648 36. Gachon F, Peleraux A, Thebault S, Dick J, Lemasson I, Devaux C, Mesnard JM. 1998.  
649 CREB-2, a cellular CRE-dependent transcription repressor, functions in association  
650 with Tax as an activator of the human T-cell leukemia virus type 1 promoter. *J Virol*  
651 72:8332-7.
- 652 37. Wang X, Naidu SR, Sverdrup F, Androphy EJ. 2009. Tax1BP1 interacts with  
653 papillomavirus E2 and regulates E2-dependent transcription and stability. *J Virol*  
654 83:2274-84.
- 655 38. Petkova DS, Verlhac P, Rozieres A, Baguet J, Claviere M, Kretz-Remy C, Mahieux R,  
656 Viret C, Faure M. 2017. Distinct Contributions of Autophagy Receptors in Measles  
657 Virus Replication. *Viruses* 9:123.
- 658 39. Baillet N, Krieger S, Journeaux A, Caro V, Tangy F, Vidalain PO, Baize S. 2019.  
659 Autophagy Promotes Infectious Particle Production of Mopeia and Lassa Viruses.  
660 *Viruses* 11:293.
- 661 40. Iha H, Peloponese JM, Verstrepen L, Zapart G, Ikeda F, Smith CD, Starost MF,  
662 Yedavalli V, Heyninck K, Dikic I, Beyaert R, Jeang KT. 2008. Inflammatory cardiac  
663 valvulitis in TAX1BP1-deficient mice through selective NF-kappaB activation. *EMBO*  
664 *J* 27:629-41.
- 665 41. Verstrepen L, Verhelst K, Carpentier I, Beyaert R. 2011. TAX1BP1, a ubiquitin-binding  
666 adaptor protein in innate immunity and beyond. *Trends Biochem Sci* 36:347-54.
- 667 42. Galloux M, Gabiane G, Sourimant J, Richard CA, England P, Moudjou M, Aumont-  
668 Nicaise M, Fix J, Rameix-Welti MA, Eleouet JF. 2015. Identification and  
669 Characterization of the Binding Site of the Respiratory Syncytial Virus Phosphoprotein  
670 to RNA-Free Nucleoprotein. *J Virol* 89:3484-96.
- 671 43. Boxem M, Maliga Z, Klitgord N, Li N, Lemmens I, Mana M, de Lichtervelde L, Mul  
672 JD, van de Peut D, Devos M, Simonis N, Yildirim MA, Cokol M, Kao HL, de Smet AS,  
673 Wang H, Schlaitz AL, Hao T, Milstein S, Fan C, Tipsword M, Drew K, Galli M,  
674 Rhrissorakkrai K, Drechsel D, Koller D, Roth FP, Iakoucheva LM, Dunker AK,  
675 Bonneau R, Gunsalus KC, Hill DE, Piano F, Tavernier J, van den Heuvel S, Hyman  
676 AA, Vidal M. 2008. A protein domain-based interactome network for *C. elegans* early  
677 embryogenesis. *Cell* 134:534-45.
- 678 44. Martin-Vicente M, Gonzalez-Sanz R, Cuesta I, Monzon S, Resino S, Martinez I. 2020.  
679 Downregulation of A20 Expression Increases the Immune Response and Apoptosis and  
680 Reduces Virus Production in Cells Infected by the Human Respiratory Syncytial Virus.  
681 *Vaccines (Basel)* 8:100.
- 682 45. Rameix-Welti MA, Le Goffic R, Herve PL, Sourimant J, Remot A, Riffault S, Yu Q,  
683 Galloux M, Gault E, Eleouet JF. 2014. Visualizing the replication of respiratory  
684 syncytial virus in cells and in living mice. *Nature Commun* 5:5104.
- 685 46. Prince GA, Horswood RL, Berndt J, Suffin SC, Chanock RM. 1979. Respiratory  
686 syncytial virus infection in inbred mice. *Infect Immun* 26:764-6.

- 687 47. Goritzka M, Durant LR, Pereira C, Salek-Ardakani S, Openshaw PJ, Johansson C. 2014.  
688 Alpha/beta interferon receptor signaling amplifies early proinflammatory cytokine  
689 production in the lung during respiratory syncytial virus infection. *J Virol* 88:6128-36.
- 690 48. Goritzka M, Makris S, Kausar F, Durant LR, Pereira C, Kumagai Y, Culley FJ, Mack  
691 M, Akira S, Johansson C. 2015. Alveolar macrophage-derived type I interferons  
692 orchestrate innate immunity to RSV through recruitment of antiviral monocytes. *J Exp*  
693 *Med* 212:699-714.
- 694 49. Harker JA, Yamaguchi Y, Culley FJ, Tregoning JS, Openshaw PJ. 2014. Delayed  
695 sequelae of neonatal respiratory syncytial virus infection are dependent on cells of the  
696 innate immune system. *J Virol* 88:604-11.
- 697 50. Pribul PK, Harker J, Wang B, Wang H, Tregoning JS, Schwarze J, Openshaw PJ. 2008.  
698 Alveolar macrophages are a major determinant of early responses to viral lung infection  
699 but do not influence subsequent disease development. *J Virol* 82:4441-8.
- 700 51. Makris S, Bajorek M, Culley FJ, Goritzka M, Johansson C. 2016. Alveolar  
701 Macrophages Can Control Respiratory Syncytial Virus Infection in the Absence of Type  
702 I Interferons. *J Innate Immun* 8:452-63.
- 703 52. Rouka E, Hatzoglou C, Gourgoulianis KI, Zarogiannis SG. 2020. Interactome networks  
704 between the human respiratory syncytial virus (HRSV), the human metapneumovirus  
705 (EtaMPV), and their host: In silico investigation and comparative functional enrichment  
706 analysis. *Microb Pathog* 141:104000.
- 707 53. Dapat C, Oshitani H. 2016. Novel insights into human respiratory syncytial virus-host  
708 factor interactions through integrated proteomics and transcriptomics analysis. *Expert*  
709 *Rev Anti Infect Ther* 14:285-97.
- 710 54. Yang Y, Wang G, Huang X, Du Z. 2014. Expression, purification and crystallization of  
711 the SKICH domain of human TAX1BP1. *Acta Crystallogr F Struct Biol Commun*  
712 70:619-23.
- 713 55. Shembade N, Pujari R, Harhaj NS, Abbott DW, Harhaj EW. 2011. The kinase IKKalpha  
714 inhibits activation of the transcription factor NF-kappaB by phosphorylating the  
715 regulatory molecule TAX1BP1. *Nat Immunol* 12:834-43.
- 716 56. Fu T, Liu J, Wang Y, Xie X, Hu S, Pan L. 2018. Mechanistic insights into the  
717 interactions of NAP1 with the SKICH domains of NDP52 and TAX1BP1. *Proc Natl*  
718 *Acad Sci U S A* 115:E11651-E11660.
- 719 57. Lazarou M, Sliter DA, Kane LA, Sarraf SA, Wang C, Burman JL, Sideris DP, Fogel  
720 AI, Youle RJ. 2015. The ubiquitin kinase PINK1 recruits autophagy receptors to induce  
721 mitophagy. *Nature* 524:309-314.
- 722 58. Moore AS, Holzbaur EL. 2016. Dynamic recruitment and activation of ALS-associated  
723 TBK1 with its target optineurin are required for efficient mitophagy. *Proc Natl Acad*  
724 *Sci U S A* 113:E3349-58.
- 725 59. Thurston TL, Boyle KB, Allen M, Ravenhill BJ, Karpievich M, Bloor S, Kaul A, Noad  
726 J, Foeglein A, Matthews SA, Komander D, Bycroft M, Randow F. 2016. Recruitment  
727 of TBK1 to cytosol-invading *Salmonella* induces WIPI2-dependent antibacterial  
728 autophagy. *EMBO J* 35:1779-92.
- 729 60. Tumbarello DA, Manna PT, Allen M, Bycroft M, Arden SD, Kendrick-Jones J, Buss F.  
730 2015. The Autophagy Receptor TAX1BP1 and the Molecular Motor Myosin VI Are  
731 Required for Clearance of *Salmonella Typhimurium* by Autophagy. *PLoS Pathog*  
732 11:e1005174.
- 733 61. Ling L, Goeddel DV. 2000. T6BP, a TRAF6-interacting protein involved in IL-1  
734 signaling. *Proc Natl Acad Sci U S A* 97:9567-72.

- 735 62. Ceregido MA, Spinola Amilibia M, Buts L, Rivera-Torres J, Garcia-Pino A, Bravo J,  
736 van Nuland NA. 2014. The structure of TAX1BP1 UBZ1+2 provides insight into target  
737 specificity and adaptability. *J Mol Biol* 426:674-90.
- 738 63. Tumbarello DA, Waxse BJ, Arden SD, Bright NA, Kendrick-Jones J, Buss F. 2012.  
739 Autophagy receptors link myosin VI to autophagosomes to mediate Tom1-dependent  
740 autophagosome maturation and fusion with the lysosome. *Nat Cell Biol* 14:1024-35.
- 741 64. Xie X, et al. (2015) Molecular basis of ubiquitin recognition by the autophagy  
742 receptorCALCOCO2. *Autophagy* 11:1775-1789.
- 743 65. Hu S, Wang Y, Gong Y, Liu J, Li Y, Pan L. 2018. Mechanistic Insights into  
744 Recognitions of Ubiquitin and Myosin VI by Autophagy Receptor TAX1BP1. *J Mol*  
745 *Biol* 430:3283-3296.
- 746 66. Tawar RG, Duquerroy S, Vonrhein C, Varela PF, Damier-Piolle L, Castagne N,  
747 MacLellan K, Bedouelle H, Bricogne G, Bhella D, Eleouet JF, Rey FA. 2009. Crystal  
748 structure of a nucleocapsid-like nucleoprotein-RNA complex of respiratory syncytial  
749 virus. *Science* 326:1279-83.
- 750 67. Esneau C, Raynal B, Roblin P, Brule S, Richard CA, Fix J, Eleouet JF, Galloux M.  
751 2019. Biochemical characterization of the respiratory syncytial virus N(0)-P complex  
752 in solution. *J Biol Chem* 294:3647-3660.
- 753 68. Pokharel SM, Shil NK, Bose S. 2016. Autophagy, TGF-beta, and SMAD-2/3 Signaling  
754 Regulates Interferon-beta Response in Respiratory Syncytial Virus Infected  
755 Macrophages. *Front Cell Infect Microbiol* 6:174.
- 756 69. Matsushita N, Suzuki M, Ikebe E, Nagashima S, Inatome R, Asano K, Tanaka M,  
757 Matsushita M, Kondo E, Iha H, Yanagi S. 2016. Regulation of B cell differentiation by  
758 the ubiquitin-binding protein TAX1BP1. *Sci Rep* 6:31266.
- 759 70. Tran TL, Castagne N, Bhella D, Varela PF, Bernard J, Chilmonczyk S, Berkenkamp S,  
760 Benhamo V, Grznarova K, Grosclaude J, Nespoulos C, Rey FA, Eleouet JF. 2007. The  
761 nine C-terminal amino acids of the respiratory syncytial virus protein P are necessary  
762 and sufficient for binding to ribonucleoprotein complexes in which six ribonucleotides  
763 are contacted per N protein protomer. *J Gen Virol* 88:196-206.
- 764 71. Castagne N, Barbier A, Bernard J, Rezaei H, Huet JC, Henry C, Da Costa B, Eleouet  
765 JF. 2004. Biochemical characterization of the respiratory syncytial virus P-P and P-N  
766 protein complexes and localization of the P protein oligomerization domain. *J Gen Virol*  
767 85:1643-53.
- 768 72. Buchholz UJ, Finke S, Conzelmann KK. 1999. Generation of bovine respiratory  
769 syncytial virus (BRSV) from cDNA: BRSV NS2 is not essential for virus replication in  
770 tissue culture, and the human RSV leader region acts as a functional BRSV genome  
771 promoter. *J Virol* 73:251-9.
- 772 73. Vidalain PO, Jacob Y, Hagemeyer MC, Jones LM, Neveu G, Roussarie JP, Rottier PJ,  
773 Tangy F, de Haan CA. 2015. A field-proven yeast two-hybrid protocol used to identify  
774 coronavirus-host protein-protein interactions. *Methods Mol Biol* 1282:213-29.
- 775 74. Bourai M, Lucas-Hourani M, Gad HH, Drosten C, Jacob Y, Tafforeau L, Cassonnet P,  
776 Jones LM, Judith D, Couderc T, Lecuit M, Andre P, Kummerer BM, Lotteau V, Despres  
777 P, Tangy F, Vidalain PO. 2012. Mapping of Chikungunya virus interactions with host  
778 proteins identified nsP2 as a highly connected viral component. *J Virol* 86:3121-34.
- 779 75. Galloux M, Tarus B, Blazevic I, Fix J, Duquerroy S, Eleouet JF. 2012. Characterization  
780 of a viral phosphoprotein binding site on the surface of the respiratory syncytial  
781 nucleoprotein. *J Virol* 86:8375-87.
- 782 76. Cagno V, Andreozzi P, D'Alicarnasso M, Jacob Silva P, Mueller M, Galloux M, Le  
783 Goffic R, Jones ST, Vallino M, Hodek J, Weber J, Sen S, Janecek ER, Bekdemir A,  
784 Sanavio B, Martinelli C, Donalisio M, Rameix Welti MA, Eleouet JF, Han Y, Kaiser L,

- 785 Vukovic L, Tapparel C, Kral P, Krol S, Lembo D, Stellacci F. 2018. Broad-spectrum  
786 non-toxic antiviral nanoparticles with a virucidal inhibition mechanism. *Nat Mater*  
787 17:195-203.
- 788 77. Gaillard V, Galloux M, Garcin D, Eleouet JF, Le Goffic R, Larcher T, Rameix-Welti  
789 MA, Boukadiri A, Heritier J, Segura JM, Baechler E, Arrell M, Mottet-Osman G,  
790 Nyanguile O. 2017. A Short Double-Stapled Peptide Inhibits Respiratory Syncytial  
791 Virus Entry and Spreading. *Antimicrob Agents Chemother* 61.
- 792 78. Descamps D, Le Gars M, Balloy V, Barbier D, Maschalidi S, Tohme M, Chignard M,  
793 Ramphal R, Manoury B, Sallenave JM. 2012. Toll-like receptor 5 (TLR5), IL-1beta  
794 secretion, and asparagine endopeptidase are critical factors for alveolar macrophage  
795 phagocytosis and bacterial killing. *Proc Natl Acad Sci U S A* 109:1619-24.
- 796 79. The Gene Ontology C. 2019. The Gene Ontology Resource: 20 years and still GOing  
797 strong. *Nucleic Acids Res* 47:D330-D338.
- 798 80. Ashburner M, Ball CA, Blake JA, Botstein D, Butler H, Cherry JM, Davis AP, Dolinski  
799 K, Dwight SS, Eppig JT, Harris MA, Hill DP, Issel-Tarver L, Kasarskis A, Lewis S,  
800 Matese JC, Richardson JE, Ringwald M, Rubin GM, Sherlock G. 2000. Gene ontology:  
801 tool for the unification of biology. The Gene Ontology Consortium. *Nat Genet* 25:25-9.  
802

803  
804  
805  
806  
807  
808  
809

## Figure legends

810 **Figure 1: Identification and validation of TAX1BP1-N interaction. (A)** Multiple alignment of  
811 sequencing reads obtained from the 40 yeast colonies matching TAXBP1. As the cDNA library used in  
812 the screen was built by oligo-dT priming, TAX1BP1 fragments captured in the screen extend from the  
813 beginning of the sequencing reads (thick green line) to the end of the TAX1BP1 sequence. The shortest  
814 TAX1BP1 fragment captured with N<sup>mono</sup> is depicted in blue. Below the alignment, a scheme of TAX1BP1  
815 structural organization is presented, with numbers indicating residues of TAX1BP1: SKIP carboxyl  
816 homology domain (SKICH), LC3-interacting region (LIR), central coiled coils constituting the  
817 oligomerization domain, and the two C-terminal zinc fingers (ZF). **(B)** Validation of N-TAX1BP1  
818 interaction by GST-pulldown with recombinant proteins. GST and GST-TAX1BP1 proteins were purified  
819 on glutathione-Sepharose beads and incubated in the presence of recombinant N protein, and  
820 interactions was analyzed by SDS-PAGE and Coomassie blue staining. The asterisks indicate the  
821 product of degradation of GST-TAX1BP1 corresponding to the deletion of the C-terminal domain.  
822 Molecular masses (MW) corresponding to the ladder's bands are indicated. **(C)** Western blot analysis  
823 of the TAX1BP1-N interaction after immunoprecipitation assay. Cells were transiently transfected with  
824 constructs allowing the expression of Flag tag alone or the Flag-TAX1BP1 fusion protein with N protein.  
825 Immunoprecipitations (IP) were performed with an anti-Flag antibody.



826  
827 **Figure 2: Impact of TAX1BP1 depletion on RSV replication in cells.** A549 cells were transfected with  
828 siRNAs control (siCT) or targeting TAX1BP1 (siTAX1BP1) and then infected 24 h later with either rHRSV-  
829 mCherry or rHRSV-Luc, at a MOI of 0.5. **(A)** RSV replication was quantified 48 h post-infection by  
830 measurement of fluorescence (left) and luminescence (right) expressed in arbitrary unit (A.U.) in cell  
831 lysates. Data are representative of three experiments made in quadruplicates. Data are mean  $\pm$  SEM, \* $p$   
832  $< 0.05$ . **(B)** Western blot analysis of TAX1BP1 silencing and RSV N expression in cells infected with  
833 either rHRSV-mCherry or rHRSV-Luc, 48 h post-infection. **(C)** Titration of virions released in the culture  
834 media of cells treated with siCT (left) and siTAX1BP1 (right) and infected with rHRSV-mCherry (upper  
835 panel) or rHRSV-Luc (lower panel). Calculated viral titers in plaque-forming unit per ml (pfu/ml) are  
836 indicated.

837  
838 **Figure 3: TAX1BP1-deficient mice infected with RSV present a reduced virus replication in the lungs.**  
839 **(A)** Kinetics of RSV infection in 129 mice. Wild-type (WT) strain 129 mice were infected with Hep2-  
840 supernatant (Mock,  $n = 1$ ) or rHRSV-Luc ( $n = 4$ ). (Left) Luciferase activity associated to viral replication was  
841 measured at different days post-infection (d.p.i.) in lung lysates, by quantification of photon emission  
842 (radiance in photon/sec/cm<sup>2</sup>/sr) and normalized to the amount of lysed tissue. (Right) In parallel, *N-RSV*  
843 gene expression was measured in the lung lysates by RT-qPCR and calculated by the formula  $2^{-\Delta Ct}$  with  $\Delta Ct$   
844  $= Ct_{N-RSV} - Ct_{HPRT}$ . Data are mean  $\pm$  SEM, \* $p < 0.05$ . **(B)** WT or TAX1BP1<sup>KO</sup> 129 mice were infected with  
845 HEp2-supernatant (Mock) or rHRSV-Luc. Luciferase activity associated to viral replication was measured at  
846 2 or 4 d.p.i. (left and right respectively) in lung lysates, by quantification of photon emission (radiance in  
847 photon/sec/cm<sup>2</sup>/sr) and normalized to the amount of lysed tissue. Data are mean  $\pm$  SEM from two  
848 independent experiments with  $n = 7$  for RSV infected WT mice and  $n = 11$  for RSV infected TAX1BP1<sup>KO</sup> mice.  
849 **(C)** Quantification of *N-RSV* gene expression at 4 d.p.i. in RSV-infected WT or TAX1BP1<sup>KO</sup> mice ( $n = 4$ ).  
850 *N-RSV* gene expression was measured in the lung lysates by RT-qPCR and calculated by the formula  $2^{-\Delta Ct}$   
851 with  $\Delta Ct = Ct_{N-RSV} - Ct_{HPRT}$  (right). Data are mean  $\pm$  SEM, \* $p < 0.05$ .

852  
853 **Figure 4: Study of antiviral/inflammatory immune responses in the lungs of infected TAX1BP1<sup>KO</sup>**  
854 **mice.** WT or TAX1BP1<sup>KO</sup> mice were infected with HEp2-supernatant (Mock) or rHRSV-Luc. **(A, B)** The  
855 productions of IFN- $\alpha$  and IFN- $\beta$  were measured 24 h post-infection in lung lysates using ProcartaPlex  
856 immunoassay. **(C, D)** The productions of IL-6 and TNF- $\alpha$  were measured 24 h post-infection in lung lysates

857 using MilliPlex MAP immunoassay. The concentrations were normalized to weight lungs. Data are mean  
 858  $\pm$  SEM, \* $p < 0.05$ ; \*\* $p < 0.01$ , and are representative of two independent experiments with  $n = 5-6$  mice per  
 859 group.

860

861 **Figure 5: Deletion of TAX1BP1 enhances the production of type I IFN and inflammatory cytokines in**  
 862 **AMs following RSV infection.** AMs from WT or TAX1BP1<sup>KO</sup> mice were either not infected (mock, black  
 863 triangle) or exposed to rHRSV-mCherry (RSV, inverted black triangle symbol) or UV-inactivated rHRSV-  
 864 mCherry (UV-RSV, white circle) at MOI of 5 for 2 h. (A, B) The productions of IFN- $\alpha$  and IFN- $\beta$  were measured  
 865 24h post-infection in supernatants using ProcartaPlex immunoassay. (C, D) The productions of IL-6 and  
 866 TNF- $\alpha$  were measured 24 h post-infection in supernatants using MilliPlex MAP immunoassay. Data are mean  
 867  $\pm$  SEM from two independent experiments, \*\*\* $p < 0.001$ .

868

869

870 **Table 1. Cellular proteins interacting with RSV N<sup>mono</sup> identified by Y2H screening.**

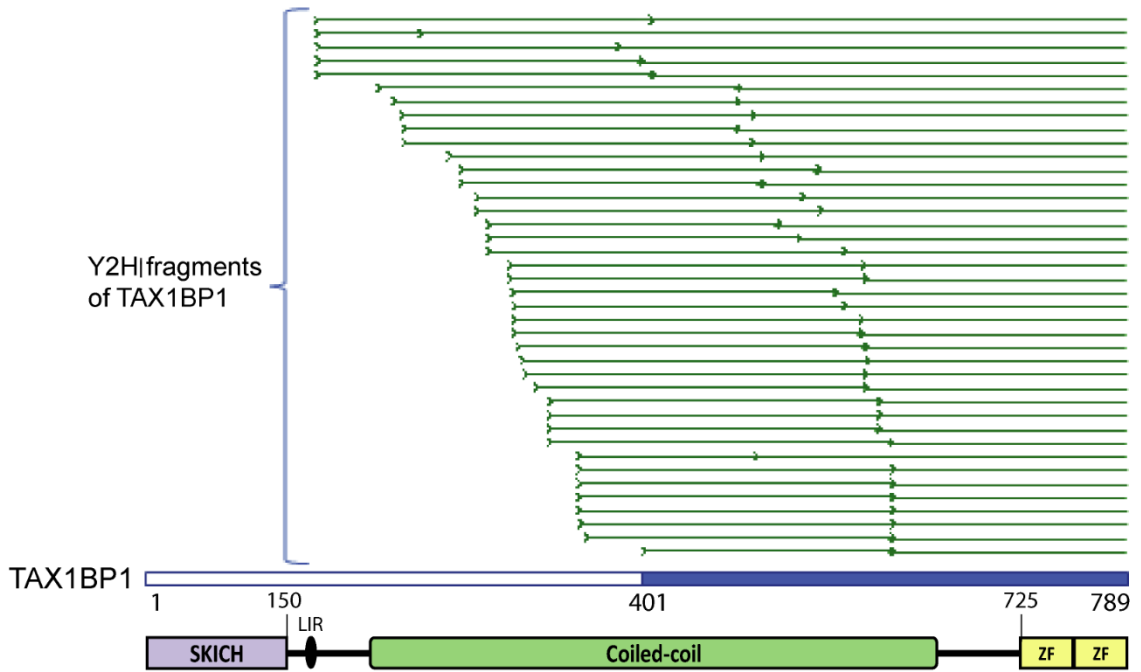
Gene	Gene ID	Hits	Functional annotation (GO Biological process)
MAGEA11	4110	2/67	Undetermined
TAX1BP1	8887	40/0	Negative regulation of NF- $\kappa$ B transcription factor activity Negative regulation of type I interferon production Negative regulation of apoptotic process
TMCC3	57458	11/0	Undetermined
IHO1	339834	5/0	Synapsis Regulation of homologous chromosome segregation DNA recombination Spermatogenesis Oogenesis Meiotic DNA double-strand break formation
BEND7	222389	0/4	Undetermined
CCDC102B	79839	4/0	Undetermined

871 The first and second columns correspond respectively to the canonical gene names and gene IDs of interacting  
 872 cellular proteins. Column 3 shows the number of positive yeast colonies (Hits) obtained for each cellular protein  
 873 when screening the human spleen cDNA or the human ORFeome library. Column 4 provides information on the  
 874 roles of the corresponding proteins using the Gene Ontology annotation (79, 80).  
 875

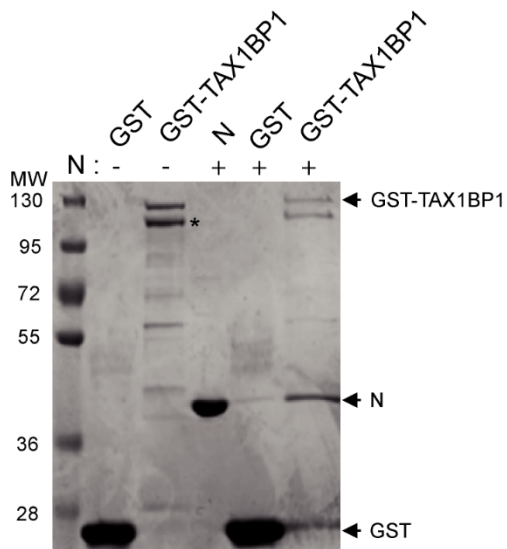
876

877 **Figure 1**

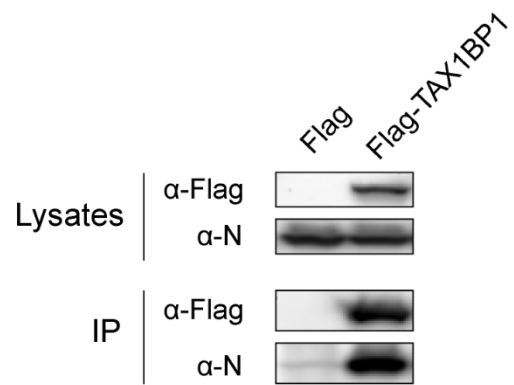
**A**



**B**



**C**



878

879

880

881

882

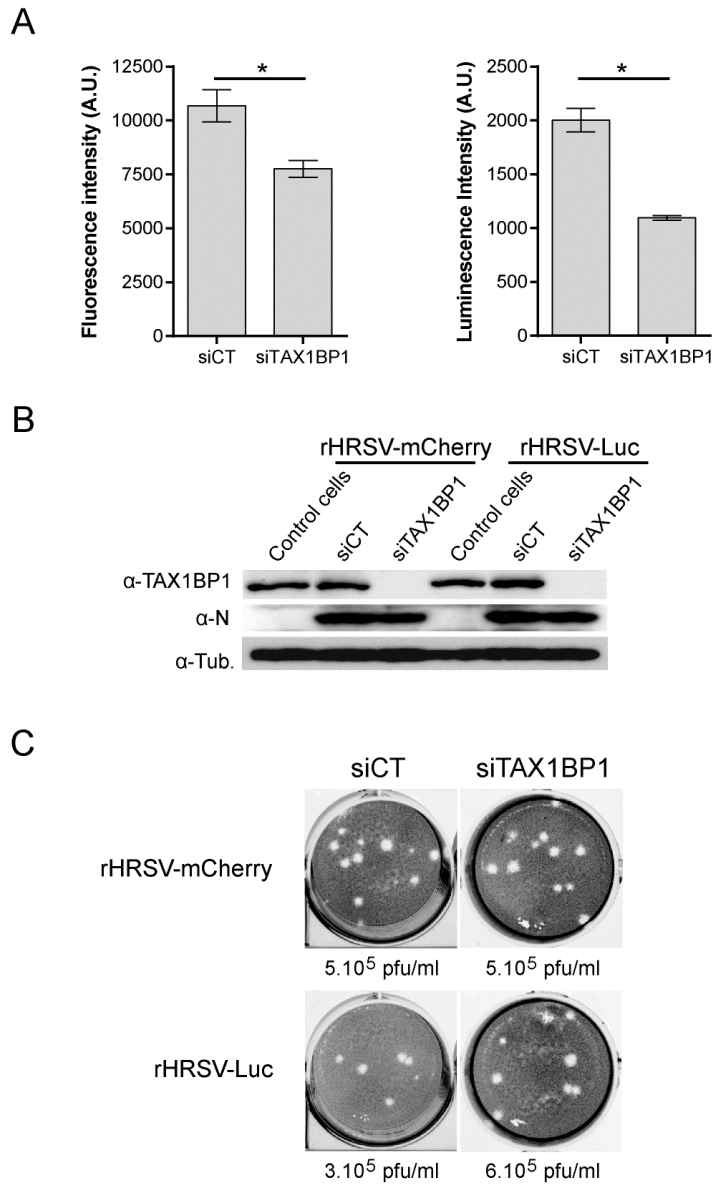
883

884

885

886

887 **Figure 2**



888

889

890

891

892

893

894

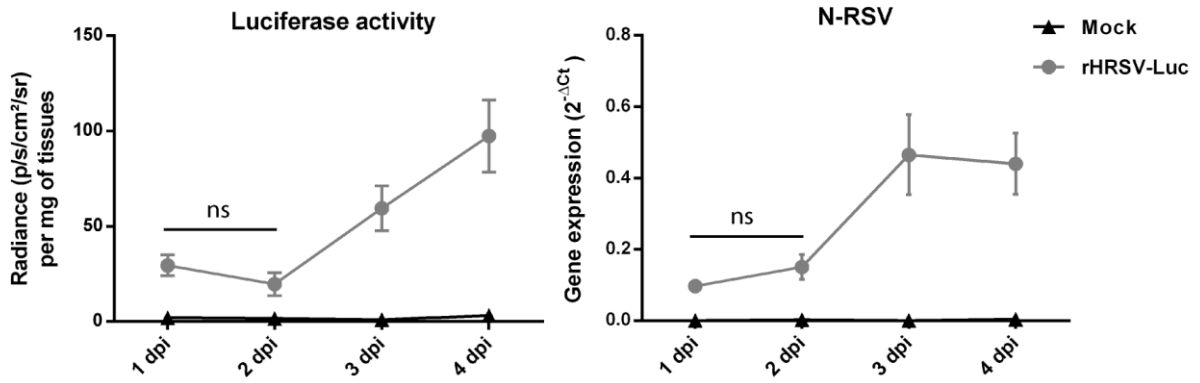
895

896

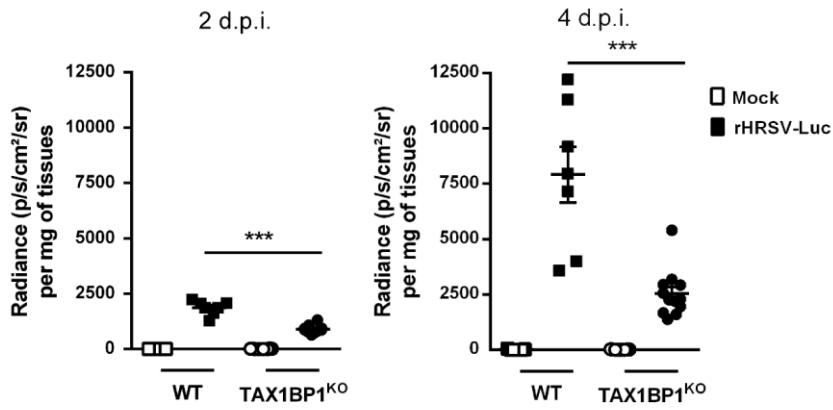
897

898 **Figure 3**

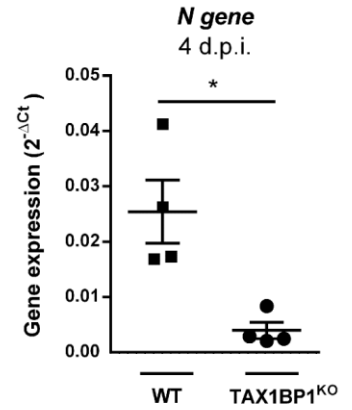
**A**



**B**



**C**



899

900

901

902

903

904

905

906

907

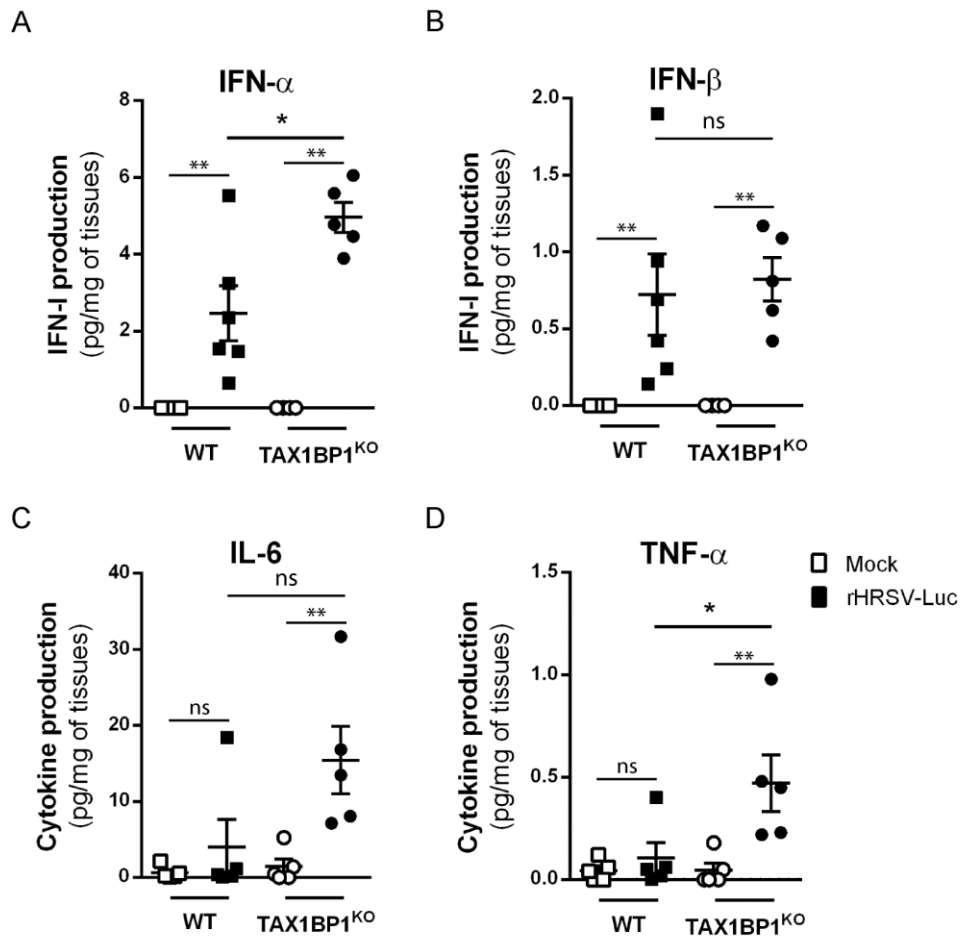
908

909

910

911

912



914  
 915  
 916  
 917  
 918  
 919  
 920  
 921  
 922  
 923  
 924  
 925  
 926

